UNIVERSIDAD AUTÓNOMA DE NUEVO LEÓN

FACULTAD DE INGENIERÍA MECÁNICA Y ELÉCTRICA

SUBDIRECCIÓN DE ESTUDIOS DE POSGRADO

‘‘ULTRASONIC SPRAY DEPOSITION OF PEROVSKITE-INSPIRED LEAD-FREE CESIUM BISMUTH IODIDE THIN FILMS FOR OPTOELECTRONICS’’

POR

SEBIN DEVASIA

1988528

COMO REQUISITO PARCIAL PARA OBTENER EL GRADO DE

DOCTOR EN INGINERIA DE MATERIALES

January 2023

UNIVERSIDAD AUTÓNOMA DE NUEVO LEÓN

FACULTAD DE INGENIERÍA MECÁNICA Y ELÉCTRICA

SUBDIRECCIÓN DE ESTUDIOS DE POSGRADO

‘‘ULTRASONIC SPRAY DEPOSITION OF PEROVSKITE-INSPIRED LEAD-FREE CESIUM BISMUTH IODIDE THIN FILMS FOR OPTOELECTRONICS’’

POR

SEBIN DEVASIA

1988528

COMO REQUISITO PARCIAL PARA OBTENER EL GRADO DE

DOCTOR EN INGINERIA DE MATERIALES

January 2023

To,

Ansamma Devasia & K. J. Devasia

And all of the reasons why I am.

CONTENTS

ACKNOWLEDGMENTS

I am eternally grateful to God, the supreme power that constantly reflects and reciprocates my consciousness, for guiding and blessing me throughout the journey of completing this work.

I am grateful to Facultad de Ingeniería Mecánica y Eléctrica (FIME), Universidad Autónoma de Nuevo León (UANL) for allowing me to pursue my dream to become a researcher and providing all the facilities to conduct my scientific investigations. I am extremely thankful to Consejo Nacional de Ciencia y Tecnología (CONACYT), Mexico, for the economic support throughout this doctoral program. I also benefitted greatly from the research project C.B-2016: No. 284800, funded by CONACYT. Besides, I thank the Centro de Investigación e Innovación en Ingeniería Aeronáutica (CIIIA) for the X-ray diffraction studies, the Centro de Innovación, Investigación y Desarrollo en Ingeniería y Tecnología (CIIDIT) for the Raman spectroscopy and the Centro de Investigación en Materiales Avanzados (CIMAV) for helping with energy dispersive spectroscopy.

My most profound appreciation and gratitude go to Dr. Bindu Krishnan, my doctoral advisor, for accepting me as a doctoral student in her research group. I am thankful for her invaluable guidance, support and encouragement throughout the course of this research work. I would like to thank Dr. Sadasivan Shaji and Dr. David Avellaneda Avellaneda for their constant motivation, wisdom and help during this entire period, especially for their services during the COVID-19 pandemic.

My gratitude to Dr. Sofía Vázquez Rodríguez, Dr. Edén A. Rodríguez Castellanos, Dr. Marco Antonio Garza Navarro, Dr. Beatriz Cristina López Walle and the committee members for their insightful comments and suggestions, which have greatly contributed to the improvement of this thesis. I am thankful to Dr. Josué Amilcar Aguilar Martínez for sharing the X-ray diffraction facilities and the discussions. I would also like to thank the program coordinators during the period, Dr. Marco Antonio Loudovic Hernández Rodríguez and Dr. Azael Martinez de la Cruz and the subdirector of postgraduate studies, Dr. Simón Martínez Martínez, for their support. I thank M.A. Olga Hernández Tovar for

the timely reminders to complete various academic procedures. My sincere gratitude to Dr. E.I. Anila for suggesting me this Ph.D. position in Mexico and for her continuous support.

Special thanks to all my friends in Mexico and India who have stood by my side and helped me on this journey. I am particularly grateful to Anjali, Joseph, Katia, Aiswarya, Akshana, Surya, Sreed, Albert, Paulosutty, Denis, Dr. Arturo, and Lalo for their friendship and assistance.

Thanks to all the Malayali families in Mexico for sharing the happy moments.

I am extremely thankful to Ms. Maria Magdalena Garza Ruiz and Ing. Jaime Emilio Cantu Diaz and their entire family for accepting me as one of their own and providing me with boundless love and affection during my time in Mexico.

My gratitude to all my family and relatives who have been a motivation and support on this journey. I am grateful to my brothers Albin Devasia and Bibin Devasia for being there for me all the time. Aleena, for her understanding during the time I spent working on this thesis.

Finally, to the most important people in my life who are the reason for all that I am today, my parents, Ansamma Devasia and K. J. Devasia. I am grateful for the freedom and opportunities you have given me to pursue my dreams and follow my heart's desires. Your unwavering trust and support in my choices have meant everything to me.

ABSTRACT

Semiconductor thin films have been outstanding in revolutionizing the optoelectronic industry over the past years. Recently, a particular class of semiconductor materials called perovskites has been found to have exciting light-matter interaction that can be beneficial for highly performing optoelectronic devices. These organic lead halide materials have pushed the photovoltaic power conversion efficiency from 3 % to 25.7 % in just fourteen years and have demonstrated excellent photodetection properties with detectivities reaching ~10^{13} Jones. Besides, they are finding applications in LEDs, photocatalysis and lasers. However, the perovskite materials have demonstrated various instability issues to ambient conditions and most importantly, the presence of lead (Pb) makes them toxic materials. In this aspect, lead-free materials that are derived from perovskite structures are of great interest.

Cesium bismuth iodide ($Cs_3Bi_2I_9$) is a non-toxic and stable perovskite derivative with a band gap of ~2 eV. It presents an absorption coefficient in the order of 10^4-10^5 cm^{-1} and has an exciton binding energy of 270-300 meV. This high molecular mass material demonstrates excellent photoresponse with high resistivity, which makes them ideal for hard radiation detectors. Besides, photodetectors with exceptionally good detection properties are reported based on $Cs_3Bi_2I_9$ single crystals and nanocrystal thin films. Until now, $Cs_3Bi_2I_9$ thin film deposition depended only on the spin-coating of DMF/DMSO based precursor solution followed by annealing. Interestingly, a scalable deposition technique called ultrasonic spray deposition in ambient conditions is used in our study for the *in situ* deposition of $Cs_3Bi_2I_9$ thin films.

Our investigations are mainly focused on the scaling up of $Cs_3Bi_2I_9$ thin film deposition using less toxic solvents, like ethanol and acetone, and deeply understanding their semiconducting properties through various characterization techniques. Using the MedeA software, VASP-based density functional theory calculations are used in hand with the experiments to explain the observed properties better. The ultrasonic spray deposition is used to deposit BiI_3, $Cs_3Bi_2I_9$, Bi_2S_3 and $Cs_3Bi_2I_9$:Bi_2S_3 thin films. Further, various characterization techniques such as XRD, Raman spectroscopy, SEM, XPS, EDX, UV-

Vis-NIR spectroscopy, I-V and photocurrent measurements are used to understand their structure, morphology, chemical states, composition, optical, electrical and optoelectronic properties. The BiI_3 thin films are deposited using an ethanol-based low-concentration solution and the influence of substrate temperature on its properties is analyzed. Later, CsI is sprayed over this BiI_3 layer to obtain phase pure $Cs_3Bi_2I_9$ thin films. Here, the CsI concentration and deposition numbers varied from 0.003 to 0.021 M and 5-15 times, respectively. The thin film displayed photodetection characteristics and formed heterojunction with n-ZnO in a glass/FTO/n-ZnO/p-$Cs_3Bi_2I_9$/C-Ag structure. The glass/FTO/n-CdS/p-$Cs_3Bi_2I_9$/C-Ag structure demonstrated a photovoltaic performance with V_{oc} of 300 mV and J_{sc} of 0.003 $mAcm^{-2}$.

Further, $Cs_3Bi_2I_9$ thin films are fabricated in a single step using a DMF-based precursor solution. The control of substrate temperature on the growth mechanism of $Cs_3Bi_2I_9$ during the deposition is explored. Interestingly, the $Cs_3Bi_2I_9$ thin films exhibited self-powered detection with a detectivity of 5.93×10^8 Jones and a responsivity of 0.0051 mAW^{-1} under a 405 nm laser source. Furthermore, Bi_2S_3 nanorods incorporated $Cs_3Bi_2I_9$ composite thin films are developed by solution engineering the acetone-based $Cs_3Bi_2I_9$ precursor solution with thioacetamide. Our findings show a real-time growth of Bi_2S_3 nanorods vertically in the $Cs_3Bi_2I_9$ grain boundaries. These composite films exhibit broad spectral photodetection (405-1064 nm). The glass/FTO/n-CdS/$Cs_3Bi_2I_9$:Bi_2S_3/C-Ag photodetector yielded an improved detectivity of 8.18×10^9 Jones and a responsivity of 0.59 mAW^{-1}.

For the first time in the literature, we use the scalable ultrasonic spray deposition to grow $Cs_3Bi_2I_9$ thin films and fabricate their self-powered photodetectors. The detailed synthesis procedures, characterization, analysis, and fabrication of devices and their properties are discussed in the following chapters. The scientific data provided will help in a deep understanding of the properties of the $Cs_3Bi_2I_9$ thin films and their engineering to motivate further research and improve the device performance. Most importantly, the novel methodologies can be adopted by various other perovskite systems to overcome their current limitations.

RESUMEN

Las películas delgadas de semiconductores se han destacado por revolucionar la industria optoelectrónica en los últimos años. Recientemente, se descubrió que una clase particular de materiales semiconductores llamados perovskitas tienen una interesante interacción luz-materia, que puede ser beneficiosa para dispositivos optoelectrónicos de alto rendimiento. Estos materiales orgánicos de haluro de plomo han aumentado la eficiencia de conversión de energía fotovoltaica del 3 % al 25,7 % en solo catorce años y han demostrado excelentes propiedades de fotodetección, con detectividades que alcanzan los ~10^{13} Jones. Además, están encontrando aplicaciones en LEDs, fotocatálisis y láseres. Sin embargo, los materiales de perovskita han demostrado diversos problemas de inestabilidad en condiciones ambientales y, lo que es más importante, la presencia de plomo (Pb) los hace muy tóxicos. En este aspecto, los materiales sin plomo que se derivan de estructuras de perovskita son de gran interés.

El yoduro de bismuto y cesio ($Cs_3Bi_2I_9$) es un derivado de perovskita no tóxico y estable con una banda prohibida de ~2 eV. Presenta un coeficiente de absorción del orden de 10^4 – 10^5 cm^{-1} y tiene una energía de enlace de excitón de 270-300 meV. Este material de alta masa molecular demuestra una excelente fotorrespuesta con alta resistividad, lo que los hace ideales para detectores de radiación dura. Además, se reportan fotodetectores con propiedades de detección excepcionalmente buenas, basados en monocristales de $Cs_3Bi_2I_9$ y películas delgadas de nanocristales. Hasta ahora, el depósito de películas delgadas de $Cs_3Bi_2I_9$ dependía únicamente del recubrimiento por rotación de la solución precursora basada en DMF/DMSO seguida del tratamiento térmico. De manera interesante, en nuestro estudio se utiliza una técnica de deposición escalable llamada: deposición por pulverización ultrasónica en condiciones ambientales, para la deposición in situ de películas delgadas de $Cs_3Bi_2I_9$.

Nuestras investigaciones se centran principalmente en el escalamiento del depósito de las películas delgadas de $Cs_3Bi_2I_9$ utilizando disolventes menos tóxicos, como etanol y acetona, además de la comprensión profunda de sus propiedades semiconductoras a través de diversas técnicas de caracterización. Usando el software MedeA, los cálculos de la teoría

funcional de la densidad basados en VASP se usan junto con los experimentos para explicar mejor las propiedades observadas. La deposición por pulverización ultrasónica se utiliza para depositar películas delgadas de BiI_3, $Cs_3Bi_2I_9$, Bi_2S_3 y $Cs_3Bi_2I_9$:Bi_2S_3. Además, se utilizan diversas técnicas de caracterización como XRD, espectroscopia Raman, SEM, XPS, EDX, espectroscopia UV-Vis-NIR, mediciones I-V y fotocorriente para comprender su estructura, morfología, estados químicos, composición, propiedades ópticas, eléctricas y optoelectrónicas. Las películas delgadas de BiI_3 se depositan utilizando una solución de baja concentración a base de etanol y se analiza la influencia de la temperatura del sustrato en sus propiedades. Posteriormente, se rocía CsI sobre esta capa de BiI_3 para obtener películas delgadas de $Cs_3Bi_2I_9$ de fase pura. Aquí, la concentración de CsI y el número de depósitos variaron de 0,003 a 0,021 M y de 5 a 15, respectivamente. La película delgada mostró características de fotodetección y se formó una heterounión con n-ZnO en una estructura de tipo: vidrio/FTO/n-ZnO/p-$Cs_3Bi_2I_9$/C-Ag, la cual demostró un desempeño fotovoltaico con V_{oc} de 300 mV y J_{sc} de 0.003 $mAcm^{-2}$.

Además, las películas delgadas de $Cs_3Bi_2I_9$ se fabrican en un solo paso utilizando una solución precursora basada en DMF. Se explora el control de la temperatura del sustrato sobre el mecanismo de crecimiento de $Cs_3Bi_2I_9$ durante la deposición. Curiosamente, las películas delgadas $Cs_3Bi_2I_9$ exhibieron una detección autoalimentada con una detectividad de $5{,}93 \times 10^8$ Jones y una capacidad de respuesta de 0,0051 mAW^{-1} bajo una fuente láser de 405 nm. Además, las películas delgadas compuestas de $Cs_3Bi_2I_9$ incorporadas en nanobarras de Bi_2S_3 se desarrollan mediante la ingeniería de la solución precursora de $Cs_3Bi_2I_9$ a base de acetona con tioacetamida. Nuestros hallazgos muestran un crecimiento en tiempo real de nanorods verticales de Bi_2S_3 en los límites de grano con el $Cs_3Bi_2I_9$. Estas películas compuestas muestran una fotodetección de amplio espectro (405-1064 nm). El fotodetector de vidrio/FTO/n-CdS/$Cs_3Bi_2I_9$:Bi_2S_3/C-Ag produjo una detección mejorada de $8{,}18 \times 10^9$ Jones y una capacidad de respuesta de 0,59 mAW^{-1}.

Por primera vez en la literatura, utilizamos la deposición por pulverización ultrasónica escalable para hacer crecer películas delgadas de $Cs_3Bi_2I_9$ y fabricar sus fotodetectores autoalimentados. Los procedimientos de síntesis detallados, caracterización, análisis, y fabricación de dispositivos, así como sus propiedades, se discuten en los siguientes

capítulos. Los datos científicos proporcionados ayudarán a una comprensión profunda de las propiedades de las películas delgadas $Cs_3Bi_2I_9$ y su ingeniería para motivar más investigaciones y mejorar el rendimiento del dispositivo. Lo que es más importante, las metodologías novedosas pueden ser adoptadas por diversos sistemas de perovskita para superar sus limitaciones actuales.

LIST OF PUBLICATIONS

1. **S. Devasia**, S. Shaji, D.A. Avellaneda, J.A. Aguilar Martinez, B. Krishnan, "Ultrasonically sprayed $Cs_3Bi_2I_9$ thin film based self-powered photodetector", *Mater. Chem. Phys*. (2023) 127295. https://doi.org/10.1016/j.matchemphys.2023.127295.
2. **S. Devasia**, S. Shaji, D.A. Avellaneda, J.A.A. Martinez, B. Krishnan, "In situ crystallization of 0D perovskite derivative $Cs_3Bi_2I_9$ thin films via ultrasonic spray", *J. Alloys Compd*. 893 (2021) 162294. https://doi.org/10.1016/j.jallcom.2021.162294.
3. **S. Devasia**, S. Shaji, D.A. Avellaneda, J.A. Aguilar Martinez, B. Krishnan, Tin antimony sulfide ($Sn_6Sb_{10}S_{21}$) thin films by heating chemically deposited Sb_2S_3/SnS layers: Studies on the structure and their optoelectronic properties, *J. Alloys Comp*d. 827 (2020) 154256. https://doi.org/10.1016/j.jallcom.2020.154256.
4. A. Nadukkandy, **S. Devasia**, P. Abraham, S. Shaji, D.A. Avellaneda, J.A. Aguilar-Martínez, E.G. Martinez, R.F. Cienfuegos-Pelaes, B. Krishnan, "Monoclinic $AgSbS_2$ thin films for photovoltaic applications: Computation, growth and characterization approaches", *Mater. Sci. Semicond. Process*. 135 (2021) 106074. https://doi.org/10.1016/j.mssp.2021.106074.
5. A.A. Ramachandran, B. Krishnan, **S. Devasia**, D.A. Avellaneda, M.I. Mendivil Palma, J.A. Aguilar Martinez, S. Shaji, "Photosensitive antimony triiodide thin films by rapid iodization of chemically deposited antimony sulfide," *Mater. Res. Bull.* 142 (2021) 111382. https://doi.org/10.1016/j.materresbull.2021.111382.
6. **S. Devasia**, A. A.Ramachandran, S. Shaji, D.A. Avellaneda, J.A. Aguilar Martinez, B. Krishnan, "Bismuth triiodide: Ab-initio simulations to spray cast thin films for optoelectronic applications," *Scientia*. 15 (2019) 98–111. http://www.scientia.mercycollege.edu.in/pdf/scientia-15.pdf#page=99

PRESENTATION IN CONFERENCES

1. "Bismuth sulfide nanorods decorated cesium bismuth iodide composite thin films by ultrasonic spray pyrolysis," Sebin Devasia, S. Shaji, D. A. Avellaneda, J. A. Aguilar Martinez, and B. Krishnan, XV International Conference on Surfaces, Materials and Vacuum, Puerto Vallarta, Mexico, 26-29 September 2022. (Oral presentation)
2. "Perovskite-inspired $Cs_3Bi_2I_9$ films via ultrasonic spray for self-powered photodetectors", Sebin Devasia, S. Shaji, D. A. Avellaneda, J. A. Aguilar Martinez, and B. Krishnan, XXX International Materials Research Congress (IMRC) Cancun, Mexico, 14-19 August 2022. (Oral presentation)
3. "Effect of source-substrate distance on the transparent electrode properties of spray pyrolysed aluminium doped zinc oxide thin films," International Conference on Recent Advances in Materials and Manufacturing (ICRAMM), 25-26 November 2021, Kolhapur, Maharashtra, India.
4. "Ultrasonically spray deposited cesium bismuth iodide thin films: Structure, morphology and photophysical properties," Sebin Devasia, S. Shaji, D. A. Avellaneda, J. A. Aguilar Martinez, and B. Krishnan, XXIX International Materials Research Congress (IMRC) Cancun, Mexico, 15-19 August 2021. (Oral presentation)
5. "Ultrasonic Spray deposited BiI_3 thin films for Optoelectronic applications", Progress and promises in chemical sciences (PPCS-2021), Sebin Devasia, S. Shaji, D. A. Avellaneda, J. A. Aguilar Martinez, and B. Krishnan, 22 March 2021, Christ (deemed to be university), Bengaluru (Bengaluru (Bangalore)), India. (Oral presentation)
6. "*Ab initio* simulations to ultrasonically sprayed thin films of bismuth triiodide", Sebin Devasia, S. Shaji, D. A. Avellaneda, J. A. Aguilar Martinez and B. Krishnan, 12^{th} international conference on Hybrid and organic photovoltaics (HOPV20 online conference), 26 - 29^{th} May 2020. (Poster presentation)
7. "Bismuth triiodide: *Ab initio* simulations to spray-cast thin films," Sebin Devasia, S. Shaji, D. A. Avellaneda, J. A. Aguilar Martinez and B. Krishnan, RSC Twitter conference, 3 March 2020. (Poster presentation).

LIST OF FIGURES

LIST OF TABLES

ABBREVIATIONS

ALP	:	All-inorganic Lead-free Perovskite
A.U.	:	Arbitrary Unit
BCP	:	Bathocuproine
B.E.	:	Binding Energy
CdS	:	Cadmium sulfide
CBD	:	Chemical Bath Deposition
CBM	:	Conduction Band Minimum
CBI	:	Cesium Bismuth Iodide
DFT	:	Density Functional Theory
DMF	:	Dimethyl formamide
DMSO	:	Dimethyl sulfoxide
EDX	:	Energy Dispersive X-ray
ETL	:	Electron Transport Layer
EQE	:	External Quantum Efficiency
FA	:	Formamidinium
FTO	:	Fluorine doped tin oxide
HTL	:	Hole Transport Layer
ICDD	:	International Centre for Diffraction Data
ITO	:	Indium doped tin oxide
I-V	:	Current-Voltage
J-V	:	Current Density-Voltage
JCPDS	:	Joint Committee on Powder Diffraction Standards
LED	:	Light Emitting Diode
MA	:	Methylammonium
NIR	:	Near Infrared

OLED	:	Organic Light Emitting Diode
P3HT	:	Poly(3-hexylthiophene-2,5-diyl)
PCBM	:	[6,6]-Phenyl C_{61} butyric acid methyl ester
PCE	:	Power Conversion Efficiency
PEDOT:PSS	:	Poly(3,4-ethylenedioxythiophene) poly(styrenesulfonate)
PeLEDs	:	Perovskite Light Emitting Diodes
PSCs	:	Perovskite Solar Cells
PTAA	:	Poly(triaryl amine)
PV	:	Photovoltaic
RTP	:	Rapid Thermal Processing
SEM	:	Scanning Electron Microscopy
Spiro-OMeTAD	:	2,2',7,7'-Tetrakis[N,N-di(4-methoxyphenyl)amino]-9,9'-spirobifluorene
TA	:	Thioacetamide
USD	:	Ultrasonic Spray Deposition
UV	:	Ultraviolet
VASP	:	Vienna Ab-initio Simulation Package
VBM	:	Valence Band Maximum
Vis	:	Visible
XPS	:	X-ray photoelectron spectroscopy
XRD	:	X-ray diffraction
ZnO	:	Zinc oxide

CHAPTER 1

PEROVSKITE-INSPIRED LEAD-FREE SEMICONDUCTORS

Perovskite materials have made revolutionary developments in photovoltaics, LEDs, photodetectors, lasers, and other optoelectronic devices. However, the long-term instability and lead toxicity in hybrid halide perovskites demand deeper atomic/electronic investigations and engineering in hand with advanced strategies to improve the device performance.

1.1. Introduction

Semiconducting materials have led to unprecedented developments in the electronic industry and expedited advanced technologies in ways we could have never imagined. Global energy crisis and technology demands are pushing the research to engineer them for designing advanced and novel materials with superior properties for efficient and cost-effective devices. In particular, the light-matter interactions in these materials have paved the way for vast optoelectronic applications. They are used in embedded systems, thermoelectric, lighting and LED (light emitting diodes) displays, photovoltaics, photocatalysis, supercapacitors, electrodes, sensors, and batteries.

This chapter introduces the most celebrated class of semiconductors namely hybrid organic lead halide perovskites and their applications. Further, it discusses the necessity for considering perovskite's toxicity due to the presence of lead and instability issues. Finally, the importance of the proposed investigations of this thesis based on non-toxic and stable perovskite-inspired cesium bismuth iodide is explained.

1.2. Lead-halide perovskites

The intriguing light-matter interactions and energy conversion in perovskite materials leading to exciting device performance have gained major attention from material scientists in recent times [1–5]. In addition to the excellent optoelectronic properties, the feasibility to synthesize high-quality halide perovskites by solution process at low temperatures from earth-abundant materials indicate facile commercialization to deliver cost-effective devices. Besides, the low-temperature synthesis allows these photo-absorbers to be engineered for lightweight, flexible and semi-transparent devices [6]. The perovskites are continuously outperforming most of the current semiconductors in photovoltaic technology. Moreover, they demonstrate excellent photoluminescence quantum efficiencies, narrow emissions and tunable colors, thus can be exceptional as light-emitting materials [7–11]. Until now, perovskites have found a vast pool of applications and improved the performance of semiconductor lasers [12,13], photodetectors [14], and thermoelectric systems [15].

1.2.1. Structure

The perovskite materials have a general chemical structure of AMH_3 as seen in **Figure 1.1**a, where A = $CH_3NH_3^+$ (MA^+)/$HCNH_3^+$ (FA^+)/ Cs^+/Rb^+ ; M = Pb^{2+}/Sn^{2+}/Ge^{2+}/Sb^{3+}/Bi^{3+} and H = Cl^-/Br^-/ I^-. In the cubic structure, the H anions are octahedrally coordinated to the M cation in the center, while the A cations occupy the corners. A repetition of such octahedra generates the molecular perovskite structure, as seen in **Figure 1.1**b**.**

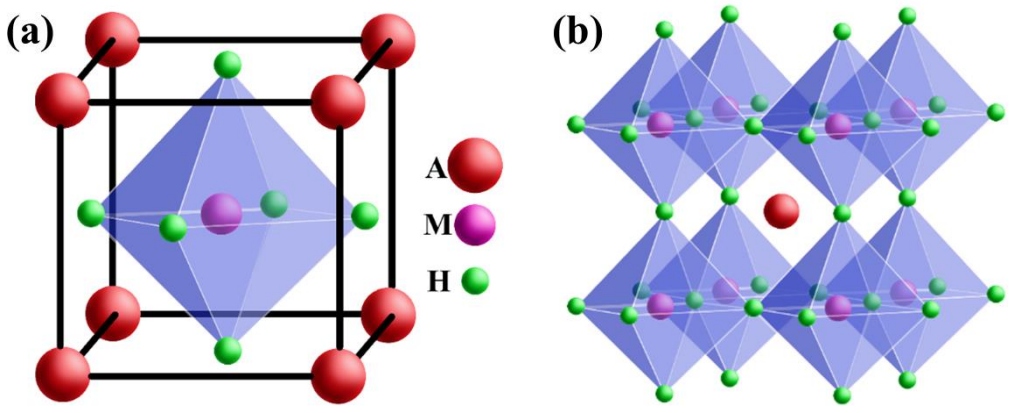

Figure 1.1. The general cubic structure of AMH_3 perovskite.

The highly performing organic–inorganic hybrid perovskites generally have methylammonium ($CH_3NH_3^+$) or formamidinium ($HCNH_3^+$) cation at the *A* site, Pb^{2+} at the *M* site and I^- halogen-anion at the *H* site due to the excellent photophysical properties with a band gap in the range of 1.5-1.7 eV [16]. The crystal structure of methylammonium lead iodide ($CH_3NH_3PbI_3$) is presented in Figure 1.2.

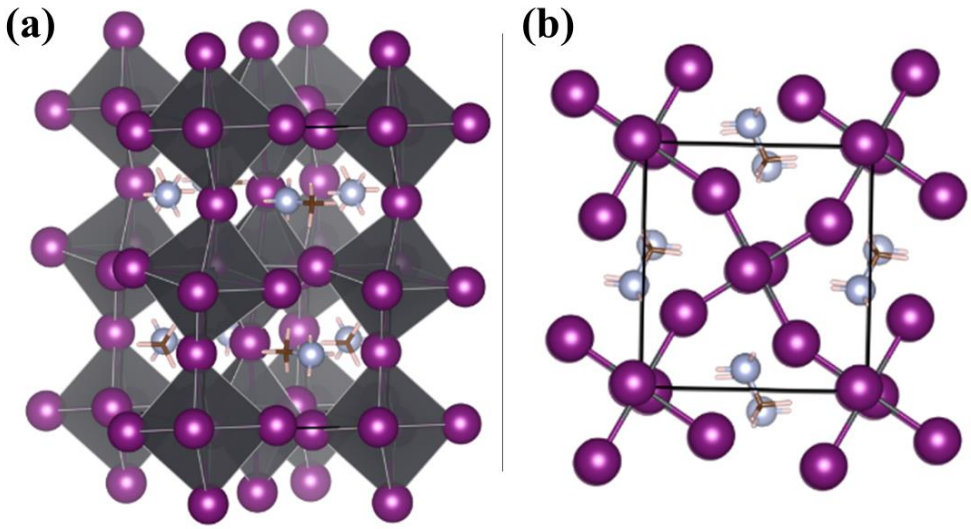

Figure 1.2. (a) The structure of $CH_3NH_3PbI_3$. (b) A view from the top.

1.2.2. Electronic properties

The exciting optoelectronic performance of the hybrid lead halide perovskites originates from the suitable optical band gap, high absorption coefficient, bipolar and high charge carrier mobility, excellent carrier transport, low defect density, long carrier diffusion lengths, form factor and photon recycling ability [17,18]. A band gap in the range of 1.4–1.6 eV with high absorption coefficients in the order of ~10^5 cm^{-1} makes them excellent photoabsorbers [19]. It has a long charge carrier diffusion length of 100-1000 nm in polycrystalline films, while it is even up to 100 μm in single crystals. Promising open circuit voltages up to 1.18 V and short circuit current up to 23.8 mA/cm^2 have been achieved in solar cells [20,21]. High light extinction coefficients were displayed by the material in device structures [22]. $CH_3NH_3PbI_3$ has very low excitonic and electron-phonon coupling effects (~50 meV), a sharp absorption edge with a low Urbach energy (~15 meV) and a high-frequency dielectric constant of 5.8 [23]. They have large mobility

lifetime products in the order of ~10^{-2} cm^2V^{-1} as a result of small electron effective mass and low trap density [24].

1.2.3. Major Application

Photodetectors and X-ray detectors

Perovskites have been used as photodetectors of outstanding responsivity, detectivity and rise-decay times. Especially, they have demonstrated self-powered photodetection (**Table 1-1**) which is crucial in developing durable sensors for imaging, structural monitoring as well as biomedical and optical communication systems.

Table 1-1. Device performance of lead-based perovskite photodetectors.

Device structure	R (AW^{-1})	EQE (%)	D^* (Jones) $\times10^{10}$	On/off ratio	τ_r/τ_d	Ref.
Self-powered photodetectors						
ITO/PEDOT:PSS/$CsPbI_2Br$/C_{60}/BCP/Ag (655 nm)		12 %	2.43			[25]
ITO/SnO_2/5%Cs/15%Cs/Spiro/Au	0.258	56.91	244	28	80/99 µs	[26]
FTO/TiO_2/$Cs_{0.05}MA_{0.16}FA_{0.79}Pb(I_{0.9}Br_{0.1})_3$/Spiro/Au (585 nm LED, 37 $mWcm^{-2}$)	0.52	~ 80	880	7.3×10^5	19/21 µs	[27]
ITO/$CsPbBr_3$:ZnO/Ag (405 nm, 10 mW)	0.0115			12.86	409/17.9 ms	[28]
ITO/TiO_2/$MAPbI_3$/P3HT/Ag (550 nm, 2.75 µWcm^{-2})	0.16			4.89	1.2/0.2 s	[29]
ITO/SnO_2/$CsPbBr_3$(MC)/Spiro/Au (473 nm, 100 mW)	0.172		480	1.3×10^5	140/120 µs	[30]
FTO/CdS/$MAPbI_3$/Spiro/Ag	0.48		2100		5.4/2.2 ms	[31]
FTO/C60/$MAPbI_3$/GaN/In	0.198		796	5×10^3	45/63 ms	[32]

Moreover, they are exciting for the detection of hard radiations like X-rays and Gamma rays (**Table 1-2**) since the organic lead halide single crystals demonstrate excellent mobilities (µ) and carrier lifetimes (τ). In addition, the large atomic number of the constituent elements leads to higher attenuation coefficients (α, = Z^4/E^3, where E is the

photon energy) for X-ray absorption. This gives it a higher hand to the perovskites as compared to commercialized silicon single-crystal detectors and α-Se X-ray detectors [24,33].

Table 1-2. Radiation detection parameters of various perovskites.

Device structure	μτ product (cm^2V^{-1})	Lowest Dose rate ($\mu Gy_{air}\ s^{-1}$)	Sensitivity ($\mu CGy^{-1}_{air}\ cm^{-2}$)	Ref.
Ag or Au/BCP/C_{60}/$MAPbBr_3$/Au	1.2×10^{-2}	0.5	80	[33]
Ag/$(NH_4)_3Bi_2I_9$/Ag (parallel)		0.21	8.2×10^3	[34]
Ag/$(NH_4)_3Bi_2I_9$/Ag (vertical)		0.055	803	
Si/$MAPbBr_3$/C_{60}/BCP/Au			2.1×10^4	[24]

Perovskite Solar Cells (PSCs)

The excellent absorption and transport properties of the perovskites make them the most celebrated material in solar cell research (**Table 1-3**). The single-junction perovskite solar cell has reached 25.8 % power conversion efficiency (PCE) from 3.8 % in 2009 [1,2,35]. Here, the Cl-bonded SnO_2 layer (ETL) with the Cl-containing perovskite layer could overcome the interfacial defects to achieve the highest 25.8 % efficiency [35].

Table 1-3. Some of the high-performance hybrid organic lead halide perovskite solar cells.

Device structure	V_{OC} (V)	J_{SC} (mA/cm^2)	FF	PCE (%)	Ref.
ITO/PTAA/SC-$MAPbI_3$/C60/Bathocuproine (BCP)/Cu	1.076	23.46	83.5	21.09	[36]
ITO/PTAA/SC-$MAPbI_3$/C60/Bathocuproine (BCP)/Cu	1.144	23.68	81	21.93	[37]
Glass/ITO/PEDOT:EVA/perovskite/PCBM/BCP/Ag	1.18	22.91	82	22.16	[20]
FTO/c-TiO_2/Li-doped m-TiO_2: perovskite composite /$FA_{0.97}MA_{0.03}PbI_{2.9}1Br_{0.09}$/2,5-thophenedicarboxylic acid/ Spiro-OMeTAD/Au	1.17	25.2	79.1	23.4	[38]
FTO/TiO_2(Si)/$MAPbI_3$/Spiro-OMeTAD/Au	1.036	23.8	85.7	21.1	[21]
FTO/SnO_2/PCBM/$MAPbI_3$/Spiro-OMeTAD/Au	1.12	23.3	77.7	20.28	[39]
FTO/SnO_2/$FASnCl_3$/$FAPbI_3$/Spiro-OMeTAD/Au	1.189	25.71	84.43	25.83	[35]

Perovskite technology has already outperformed the existing technologies based on CIGS (23.4 %) or CdTe (22.1 %) and even silicon heterostructures (26.7 %) leveling with the

single junction GaAs (29.1 %) thin film crystal photovoltaic devices [3,5,6,26]. Recently, perovskite-silicon tandem solar cells, shown in **Figure 1.3**, (planar as well as textured devices) have broken the PCE barrier of 30 % [41]. Furthermore, the emerging chalcogenide perovskite ($Ba(Zr,Ti)S_3$)/c-Si tandem solar cell may help us to push the efficiency over 38 %, as predicted by the theoretical calculations [42].

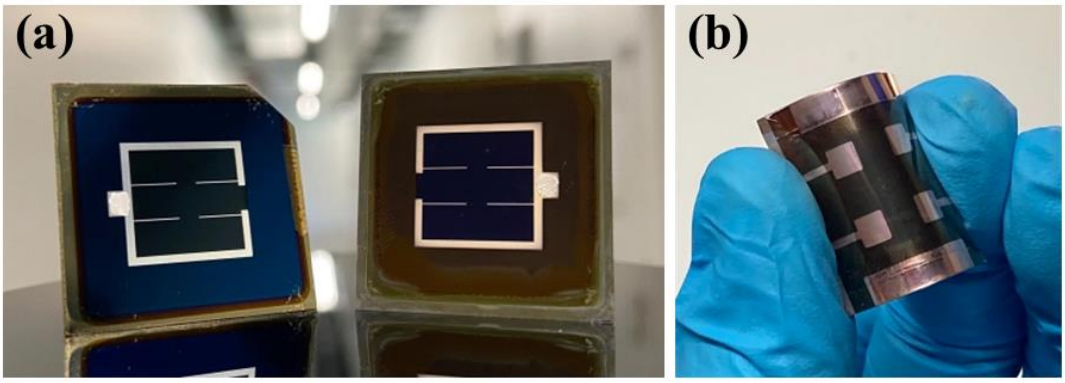

Figure 1.3. (a) Si/Per tandem cells with more than 30 % efficiency. Credit: D. Türkay/C. Wolff / EPFL/F. Sahli/Q. Jeangros/CSEM (2022). (b) Flexible all-perovskite tandem solar cell with 23.8 % efficiency [6]. Image: Federal Laboratories for Materials Science and Technology.

Perovskite Light Emitting Diodes (PeLEDs)

Owing to their high defect tolerance, tunable band gap in the visible spectrum, narrow emission bandwidth and high photoluminescence quantum yield, photoluminescent and electroluminescent perovskite materials are finding their way to the market through display industries [43]. Perovskites with low organic components are hardly prone to “pixel-burnout” which is a major issue observed in modern organic light-emitting diodes (OLED). External quantum efficiencies of up to 22 %, comparable to OLEDs, have been achieved with photoluminescent perovskites [44]. The five times higher absorption of perovskites as compared to InP prevents blue light leakage which impacts the performance in ‘in-pixel’ structures enabling cheap thinner devices. Moreover, the overlap between absorption and emission spectra in perovskites provides space for photon recycling that can contribute to 30-70% of the electroluminescence [44].

Lasers

The high fluorescence yield and wavelength tunability in addition to long carrier lifetime (10^{1-2} ns) and diffusion length (~10^{-6} m) make the perovskites an ideal candidate for lasing application. Moreover, perovskite thin films, nanowires and nanoplates have demonstrated excellent waveguiding characteristics. In most cases, the requirement of high threshold carrier density limits the application of these materials to be incorporated into devices with electrically driven lasing and also Auger recombination losses. However, recent developments have led to low lasing thresholds, wide tunability, high-quality factors and quantum yields [45].

Other applications

The conductivity changes in perovskites due to the ionic-electronic coupling can be used for creating memristive synapses for energy-efficient neuromorphic computation [46].

1.2.4. Challenges and solutions

Chemical Instability

Though great improvement has been made, the organic-inorganic hybrid perovskites degrade upon prolonged exposure to external stresses, like light, moisture, heat, and electric field which are practically quite imperative in the commercialization [19]. To be viable for commercialization, optoelectronic devices need to pass harsh environments such as humidity freeze, damp heat and thermal cycling tests preferably in accordance with the IEC61215:2016 standard test method [47].

The chemical instability originates from the volatile organic cation in the case of organic lead halides [19]. On the other hand, the rattling behavior of Cs cations which barely bonds with I and high octahedral distortion may lead to instabilities in the inorganic lead halides [48]. Besides, the instability of halogen anions also deteriorates the device performance. The long light exposures cause halide segregation forming gradient band gap regions that can behave as trap states [49]. The migration of halides to the transport layer interface or metal electrodes to form resistive contacts due to the very weak hydrogen bonding of octahedral PbI_2 with monovalent organic cation [19,50–52]. In addition, the electric field

induced hysteresis arising from ion migration, non-radiative recombination at the interfaces and ferroelectric polarization in PSCs can result in the unstable and deteriorating performance of devices [53].

Various strategies to overcome instabilities were adopted by researchers such as encapsulation for a pressure-tight environment [54] and partial replacement of organic cations with inorganic cations to stabilize the metal halide octahedra [55]. The light-induced halide segregation can be controlled by increasing the grain size, lowering carrier diffusion lengths, partial substitution of Sn at Pb and Cl at I/Br sites or A cation alloying as well as the application of external pressure or Br alloying up to a certain limit can also stabilize the structure [56]. Introduction of metal cations (K^+, Sr^{2+}, Mn^{2+}, etc.), different deposition techniques, solvent engineering and thermal treatments were employed to improve the crystal growth with low trap densities.

The hysteresis can be mitigated by growing large grains and mesoporous TiO_2 in a normal mesoscopic structure. While interface engineering of the perovskite layer near the HTL/ETL has been an effective way, bulk defect engineering also shows great promise in solving these issues. Charge accumulation is higher in the perovskite-TiO_2/Spiro-OMeTAD interface as compared to PEDOT:PSS or PCBM. Besides, some reports suggest that the presence of TiO_2 may be a reason for the hysteresis in PSCs [57].

Table 1-4. The photovoltaic performance of all-inorganic lead halide perovskite solar cells.

Device structure	Absorber band gap (eV)	V_{OC} (V)	J_{SC} (mA/cm^2)	FF (%)	PCE (%)	Ref.
FTO/c-TiO_2/CHI-$CsPbI_3$(β)/Spiro-OMeTAD/Ag		1.11	20.03	82	18.4	[58]
FTO/Cs:ZnO/γ-$CsPb_{0.99}Cd_{0.01}I_{2.5}Br_{0.5}$/P3HT/Au	1.7	1.258	19.98	78.58	19.75	[59]

Scalability

Finding suitable deposition techniques for large-scale production of the solution-derivable perovskite devices while maintaining the quality of the devices and their cost is crucial in their commercialization. The largest module with appreciable efficiency reported was an all-perovskite tandem solar mini-module, fabricated by blade coating and vacuum

deposition, with a 12.25 cm^2 aperture area which showed a power conversion efficiency of 19.1 %, shown in **Figure 1.4**. It uses a 1.78 eV $FA_{0.8}$ $Cs_{0.2}(I_{0.6}Br_{0.4})_3$ as top subcell and a narrower 1.26 eV $Cs_x(FA_{0.83}MA_{0.17})_{(1-x)}Sn_{0.5}Pb_{0.5}I_3$ as the bottom subcell [60].

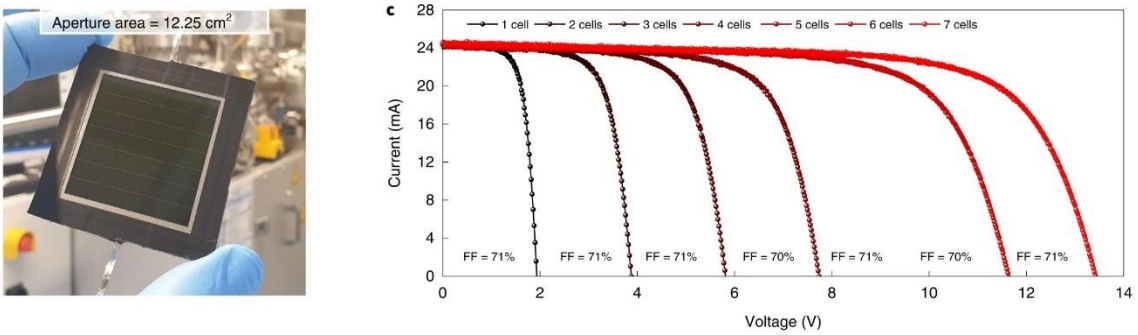

Figure 1.4. The 12.25 cm^2 perovskite solar module with 19.1 % efficiency [60]. Nature Energy (Nat Energy) ISSN 2058-7546 (Open access).

Lead toxicity

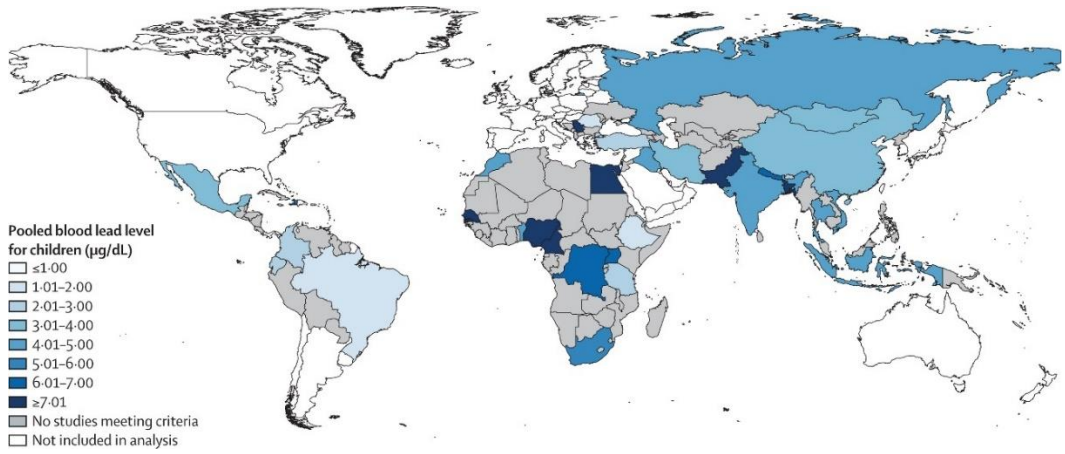

Figure 1.5. The blood lead levels among children (<14 years) in different countries [61] | Open access.

Even though performing exceptionally well in optoelectronic devices, the presence of lead (Pb) in the hybrid perovskites rises serious concerns about its toxicity [19,50]. The World Health Organization, the European Environment Agency and the United States Environmental Protection Agency all refer to Pb and Cd as potentially toxic elements and demand avoiding their presence even in small doses. Particularly, the presence of Pb, which has been referred to as *"one of the most toxic elements in existence"* [62], in the environment presents impending health hazards to the ecosystem. Lead in many widely

used commodities has already lead-poisoned millions of people, among whom largely affected are the children and middle class (Figure 1.5) and can be accounted only from the anthropogenic contamination [61].

Therefore, intensive investigations on engineering perovskite materials are necessary to improve the stability, safety, sustainability, scalability, and storage, but most importantly, the toxicity of LEAD (Pb) must be addressed [63].

1.3. Lead-free perovskites

The most suitable candidates for replacing Pb in the perovskite structure are the homovalent Sn and Ge in the same group as well as heterovalent Bi and Sb.

1.3.1. Sn and Ge-based perovskites

Tin (Sn) is the most investigated replacement for Pb in perovskites due to its comparable electrical and optical properties as observed in the studies of $FASnI_3$, $CsSnI_3$ and Cs_2SnI_6 [64,65]. However, the major problem is the instability of Sn^{2+} state which gets oxidized easily to a stable Sn^{4+} state when exposed to air and moisture. This leads to the creation of more Sn- vacancies and thereby adding to the self p-doping [66,67]. In addition, the absence of a sharp absorption at the band gap due to the lower DOS that may be polarized can lead to low photogenerated charge density in the band gap region [68].

On the other hand, Ge-based perovskites have low absorption coefficients, large carrier effective masses, dielectric constants as well as photoconductivity [69]. Although $CsGeI_3$ have a stable rhombohedral structure, their limited performance in PSCs with only 0.11% PCE, in addition to the high cost have limited their potential for applications [70].

1.3.2. Sb-based perovskites

Similar to the Sn-based perovskites, the absence of a sharp absorption in the Sb-based perovskites greatly limits its power conversion efficiency [68]. Recently, a Dion-Jacobson perovskite $CsSbCl_4$ has been proposed as a potential replacement for organic lead halide perovskites based on the first-principles calculations and screening. The material is expected to have an optimum 1.4 eV band gap with an absorption coefficient of ~10^5 cm^{-1}

and carrier mobility of ~10^2-10^4 $cm^2V^{-1}s^{-1}$. Besides, the absorber proposes to yield a 20.07% efficiency in TiO_2/$CsSbCl_4$/spiro-OMeTAD structure [71].

1.3.3. Developing Bi-based perovskites

Non-toxic bismuth (Bi^{3+}) cation has an ionic radius of 0.103 nm much closer to the 0.119 nm of Pb^{2+}. Moreover, it has an electronic configuration of $[Xe]4f^{14}5d^{10}6s^26p^0$ which is isoelectronic with Pb^{2+}. The vacant 6p orbitals account for the conduction band (CB) and filled 6s orbitals to the valence band (VB) along with the I^- 5p orbitals. The antibonding VB character of the material can lead to shallow defect states and longer carrier lifetime. In addition, strong absorption can be expected owing to the high p orbital density of states in the conduction band minimum (CBM) [72].

Table 1-5. The performance of $(CH_3NH_3)_3Bi_2I_9$ solar cells.

PV structure	Absorber E_g (eV)	V_{OC} (V)	J_{SC} (mA/cm^2)	FF	PCE (%)	Ref.
FTO/c-TiO_2/m-TiO_2/$(CH_3NH_3)_3Bi_2I_9$/HTM/Ag	2.1	0.68	0.52	0.33	0.12	[73]
(ITO/PEDOT/$(CH_3NH_3)_3Bi_2I_9$/PCBM/Ca/Al	2.94	0.66	0.22	0.49	0.1	[74]
FTO/TiO_2/$(CH_3NH_3)_3Bi_2I_9$/Spiro-OMeTAD/Au	2.26	0.721	0.491	0.318	0.11	[75]
FTO/TiO_2-BL/TiO_2-mpl+MBI+P3HT/Au	2.11	0.354	1.157	0.464	0.19	[76]
FTO/c-TiO_2/m-TiO_2/$(CH_3NH_3)_3Bi_2I_9$/Spiro-OMeTAD/MoO_3/Ag		0.67	1.00	0.624	0.42	[77]
FTO/bl-TiO_2/m-TiO_2/$(CH_3NH_3)_3Bi_2I_9$/Spiro-OMeTAD/Au	2.11	0.653	1.10	0.496	0.356	[78]
FTO/cp-TiO_2/mp-TiO_2/$(CH_3NH_3)_3Bi_2I_9$/C	2.17	0.895	0.255	24	0.054	[79]
FTO/TiO_2/$(CH_3NH_3)_3Bi_2I_9$/Spiro-OMeTAD/Ag		0.686	0.372	0.32	0.082	[80]
FTO/c-TiO_2/m-TiO_2/$(CH_3NH_3)_3Bi_2I_9$/Spiro-OMeTAD/Ag		0.51	0.94	0.61	0.31	[81]
FTO/d-TiO_2/m-TiO_2/$(CH_3NH_3)_3Bi_2I_9$/Spiro-OMeTAD/Au		0.81	2.95	0.69	1.64	[82]
ITO/FPDI/$(CH_3NH_3)_3Bi_2I_9$/ Spiro-OMeTAD/MoO_3/Ag		0.61	0.37	0.277	0.063	[83]
FTO/c-TiO_2/m-TiO_2/$(CH_3NH_3)_3Bi_2I_9$ /P3HT/		1.01	4.02	0.78	3.17	[84]

However, substituting Pb^{2+} with Bi^{3+} leads to perovskite materials of $A_3Bi_2H_9$ composition different from AMH_3 due to their different valence states [85]. Earlier, Bi was proposed to replace Pb in organic perovskites to obtain $CH_3NH_3BiI_3$. Besides, Bi-based multiferroic perovskites (like $BiFeO_3$) have been of great interest lately due to their spontaneous electric

polarization that can drive photoexcited carriers and photovoltage greater than band gaps with PCE up to 8% [86,87]. The improved PSCs of solar cells based on methylammonium bismuth iodide thin films formed by treating vapor deposited BiI_3 thin films in the MAI vapor showed promises of Bi as a potential replacement [84].

1.4. The perovskite-derived Cesium bismuth iodide

The all-inorganic cesium bismuth iodide ($Cs_3Bi_2I_9$) has received extensive attention due to its stable and non-toxic nature along with good light absorption and photosensitivity.

1.4.1. Structure

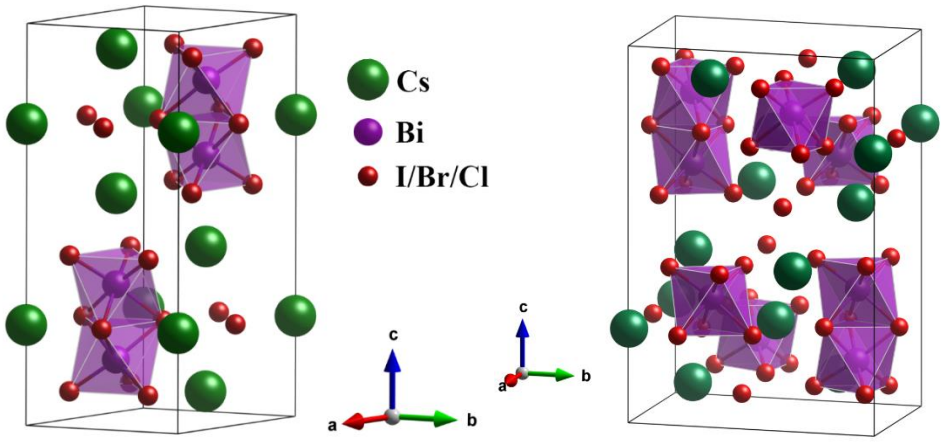

Figure 1.6. The hexagonal $P6_3/mmc$ and monoclinic C12/c1 structures of $Cs_3Bi_2I_9$.

The structural studies on $Cs_3Bi_2I_9$ go back to 1968 and 1978 [88,89]. At low temperatures, $Cs_3Bi_2I_9$ has a monoclinic structure (space group: C12/c1 (15)) which transforms to room temperature hexagonal phase (space group: $P6_3/mmc$(194)) at the transition temperature of 218 K [90]. The hexagonal $Cs_3Bi_2I_9$ has face sharing $(Bi_2I_9)^{3-}$ clusters surrounded by Cs^+ cations occupying the voids between the bioctahedral layers (D_{6h} point group) with lattice parameters of a=b=8.41 Å, c=21.20 Å, α=β=90° and γ=120° [17,73,85,91,92]. The face-sharing metal halide octahedra are layered along the c-axis with weak van der Waals interaction between the neighboring $(Bi_2I_9)^{3-}$ units explaining the sometimes flake-like appearance [93]. Unlike the corner-sharing MI_6 octahedra to form the 3D structure in Pb-based perovskite, the face-sharing anions lead to a zero-dimensional (0D) molecular salt crystal structure in $Cs_3Bi_2I_9$ as illustrated in **Figure 1.6** [94]. The large optical and electrical

anisotropy arises due to the density differences in the arrangement of these discrete dimers [91].

1.4.2. Optical and electrical properties

This defect halide compound is a p-type semiconductor in the family of ternary $A_3Bi_2I_9$-type perovskites [14]. The valence band maximum consists of filled Bi 6s orbital hybridized with iodine 5 p orbitals, whereas, the vacant Bi 6p orbitals constitute the conduction band minimum. The high density of states of the p orbitals in the conduction band minimum can favor strong absorption properties in the material [72]. Moreover, the directional transport properties studied by DFT suggest low electron effective masses in the *ab* plane for $Cs_3Bi_2I_9$ and $MA_3Bi_2I_9$ ($m_e^* = 1$ and 3.66, respectively) as compared to the high values along the c-axis ($m_e^* = 3.46$ and 119, respectively) [95]. The Calculated direct and indirect band gaps are in the range of 2.17 and 2 eV for $Cs_3Bi_2I_9$ [95].

Optical studies indicate band gaps in the range of 1.9 - 2.2 eV [92,96–98] and absorption coefficients around ~10^4-10^5 cm^{-1} at 450 nm, compared to the 1.55 eV and ~2×10^5 cm^{-1} of $MAPbI_3$, respectively [73,99]. Strong excitonic behavior is common for such low dimensional perovskites arising due to the quantum confinement effect of 0D-$[Bi_2I_9]^{3-}$ bi-octahedra. The exciton peak energies observed were in the range of 2.30-2.85 eV and has a high exciton binding energy of ~270 meV (30.8 nm grains)/ 300 meV [100] compared to the 25-50 meV of lead halide perovskites [73,99]. Experimental ionization energy between 5.6-6.2 eV is also reported for $Cs_3Bi_2I_9$ [98]. The charge transport properties have shown that they have time constants in the range of 1.3-1.5 ns and a recombination lifetime of 180-240 ps [72]. The photoluminescence and Raman spectra measurements suggest strong electron-phonon coupling and high polarizability in these compounds [92]. High resistivities and photoresponse signify that this compound can be used for hard radiation detection applications [92]. Theoretical analysis shows that the $Cs_3Bi_2I_9$ with $P\bar{3}m1$ symmetry has a lower band gap (1.74 eV) as compared to the $P6_3/mmc$ symmetry (2.25 eV) [97]. The ionization energy or the valence band maximum with respect to the vacuum is determined to be 5.6 – 6.2 eV [98].

1.4.3. State of the art

Technologically important materials in their thin film form demonstrate fascinating properties especially optical and electrical properties as compared to the bulk. This has initiated the development of thin film technology for advanced optoelectronic and microelectronic device fabrication that yields cheaper, more efficient, durable, and portable devices. There are various chemical and physical methods commonly used in the fabrication of thin films. Some of the widely used techniques are chemical bath deposition, dip coating, thermal evaporation, magnetron sputtering, slot-die coating, blade coating, spin-coating, electrodeposition, plasma deposition, chemical vapor deposition – Plasma enhanced (PECVD) and metal-organic (MOCVD), atomic layer deposition and spray deposition [101].

Mostly, $Cs_3Bi_2I_9$ thin films were fabricated by spin coating method [73,102–108] based on DMF [107], DMF+DMSO [73,103,105,106] or GBL+DMSO [104] precursor solutions. The method uses highly concentrated solutions prepared over long stirring durations [103,106,107] and sometimes in N_2-filled gloveboxes [105]. The deposited films were annealed on a separate hot plate at 80-200 ℃ for the evaporation of solvent and crystallization [73,102,103,105,107]. At times, anti-solvents like chlorobenzene were used before annealing for effective and rapid solvent removal at low temperatures (100 ℃) [106]. In addition, dissolution-recrystallization of spin-coated films using a solvent mixture of DMF and methanol was also effective in the fabrication of $Cs_3Bi_2I_9$ thin films composed of ultrathin nanosheets [107,108]. Besides, $Cs_3Bi_2I_9$ nanocrystals were synthesized using a modulated colloidal synthetic method and their dispersions were spin-coated for devices [109].

Furthermore, a chemical vapor deposition (CVD) furnace filled with hydrogen and argon was used to deposit $Cs_3Bi_2I_9$ films on mica substrates by heating the chamber containing CsI and BiI_3 mixture to 600 ℃ [94].

1.4.4. Applications

Photodetectors

$Cs_3Bi_2I_9$ has shown excellent photodetection properties in a broad electromagnetic spectrum. Especially, their single crystals have demonstrated significant improvement in the detection properties in the broad spectrum. The photodetector constructed from $Cs_3Bi_2I_9$ nanoplates could suppress dark current below 50 pA yielding a high responsivity of 33.1 mAW^{-1}, even higher than the hybrid lead halide perovskites [103]. The low trap density and high carrier mobility of $Cs_3Bi_2I_9$ single crystal thin film photodetectors demonstrated an ON/OFF ratio as high as 11000 which was stable for 1000 h (50% RH) [14]. Besides, the excellent transport properties of 2D materials such as graphene and MoS_2 were utilized in improving the $Cs_3Bi_2I_9$ devices yielding specific detectivities in the order of 10^{11} and 10^{13} Jones, respectively [110].

The photodetector based on $Cs_3Bi_2I_9$ micro-crystal thin film displayed excellent photosensitivity in a broad spectrum of 450-950 nm with a dark current as low as 0.46 pA. The photo-switching characteristics of the device were stable and reproducible up to 2000 cycles and the thin film was even stable for three months in moist conditions (75 % RH) [104]. The composition engineering in $Cs_3Bi_2I_9$ using Br anions obtained the $Cs_3Bi_2I_6Br_3$ thin film which exhibited photodetection in the 300-600 nm spectral range. The photodetector performed with an average dark current of 145 pA and photocurrent of 4.7 μA at zero bias [105]. The interfacial tunneling effect induced by a thin Al_2O_3 layer helped in suppressing the dark current resulting in a 20-fold increase in the ON/OFF ratio of $Cs_3Bi_2I_9$ thin film photodetectors. These PDs could maintain 90% of their performance after 30 days with a perspective of application in diffuse reflection mode imaging systems [106]. Most interestingly, the $Cs_3Bi_2I_9$ nanocrystals-based PD exhibited very good detectivities in a very broad spectrum of 254-1064 nm. This device constructed on a p-Si substrate and a graphene top layer achieved the highest detectivity of 1.75×10^{13} Jones. These nanocrystals were also used to fabricate flexible photodetectors with appreciable detection properties [109]. Furthermore, a semi-transparent $Cs_3Bi_2I_9$ photodetector in self-powered operation was demonstrated using the interesting electrical and optical properties of Au/ITO electrodes [111].

Radiation detectors (X-rays, Gamma-ray and nuclear radiations)

All inorganic $Cs_3Bi_2I_9$ is a high resistivity material with a large band gap and photoresponse with an average atomic number of 57.7 which makes them suitable for radiation detection [91]. More importantly, the absence of organic parts makes them durable [91]. The $Cs_3Bi_2I_9$ has excellent sensitivity to hard radiations such as X-rays and gamma rays due to the high atomic mass of the constituent elements, high density, wide band gap and structural anisotropy [34,112]. The centimeter-sized SCs have low trap densities and suppressed ion migration which helped design X-ray detectors with a sensitivity of 1652.3 μC Gy_{air}^{-1} cm^{-2} that detect doses as low as 130 $nGy_{air}^{-1}s^{-1}$. These detectors were stable for 13 h of continuous operation and stable responses could be observed even at 100℃ [113].

On the other hand, the organic $(CH_3NH_3)_3Bi_2I_9$ single crystals demonstrated excellent response to X-ray with a sensitivity of 1947 μC Gy_{air}^{-1} cm^{-2}. The response time of 23.3 ms and the low detection limit of 83 nGy_{air} s^{-1} suggest the potential for high-resolution X-ray imaging systems [114]. The 2D layered $(NH_4)_3Bi_2I_9$ single crystal based detectors showed a detection limit as low as 55 $nGy_{air}^{-1}s^{-1}$ and it was stable for up to 60 days [34]. The 99% X-ray attenuation of these SCs (for 0.9 mm of $(NH_4)_3Bi_2I_9$) is far better than Si or $MAPbBr_3$-based devices and is very close to CdTe [34]. The mobility-lifetime (μτ) product and mobility in parallel direction were 1.1×10^{-2} cm^2V^{-1} and 213 $cm^2V^{-1}s^{-1}$, whereas, it was 1.1×10^{-2} cm^2V^{-1} and 11 $cm^2V^{-1}s^{-1}$ in the perpendicular direction [34]. The parallel direction device displayed sensitivity as high as 0.8×10^4 μC $Gy_{air}^{-1}cm^{-2}$ which is three orders higher than conventional α-Se detectors [34,115]. However, the lowest detection limit was observed in the case of a perpendicular device (803 μC $Gy_{air}^{-1}cm^{-2}$) due to the high SNR value of 6.5 mm^{-1} [34]. Further, they have activation energies of 0.72 eV (parallel) and 0.91 eV (perpendicular) suggesting effective suppression of ionic migration as compared to the 3D perovskites [34].

The $Cs_3Bi_2I_9$ SC Am@5.49 MeV α-particle detectors performed with an energy resolution of 32 % whereas the X-ray detectors had a sensitivity of 111.9 μC $Gy_{air}^{-1}cm^{-2}$ [91]. The electron mobility and mobility lifetime product calculated were 6.10 $cm^2V^{-1}s^{-1}$ and 2.03×10^{-5} cm^2V^{-1} [91]. In another report, the ^{241}Am α-particles (5.5 MeV) interaction with

high-quality crystals of $Cs_3Bi_2I_9$ and $Rb_3Bi_2I_9$ showed a good response. The $(\mu\tau)_e$ product and μ_e of $Cs_3Bi_2I_9$ were 5.4×10^{-5} cm^2V^{-1} and 4.3 $cm^2V^{-1}s^{-1}$, whereas its $(\mu\tau)_h$ product and μ_h were 1.8×10^{-5} cm^2V^{-1} and 1.7 $cm^2V^{-1}s^{-1}$ [112].

Photovoltaics

Perovskite-derived compounds containing bismuth have a comparatively large band gap with good absorption which makes it ideal for tandem solar cells as the top cell [116]. Even though much effort was taken to fabricate binary bismuth iodide (BiI_3) based solar cells (**Table 1-6**), the highest efficiency achieved so far is only 1.33 % [117]. The solar cell used high-quality BiI_3 thin films of 1 μm grain size obtained by the iodization of BiSI thin films. The device was stable for over 100 days with an 8.1 % decline in PCE [117].

Table 1-6. The photovoltaic performance of BiI_3-based solar cells.

PV structure	Absorber E_g (eV)	V_{OC} (V)	J_{SC} (mA/cm^2)	FF (%)	PCE (%)	Ref.
glass/FTO/d-TiO_2/BiI_3/PIDT-DFBT/Au	1.8	0.42	1.70	45	0.32	[118]
Glass/FTO/TiO_2/BiI_3/V_2O_5/Au	1.83		5.0	29.9	1.0	[119]
FTO/c-TiO_2/m-TiO_2/BiI_3/P3HT/Ag		0.17	1.39	30	0.07	[93]
FTO/c-TiO_2/m-TiO_2/BiI_3/P3HT/		0.28	2.71	45	0.34	[84]
ITO/SnO_2/BiSI/BiI_3/organic HTM/Au	1.7	0.33	12.6	29	1.21	[120]
ITO/V_2O_5/BiI_3/ZnO/Ag	1.83	0.601	5.57	39.8	1.33	[117]

While considering bismuth-based organic and inorganic iodides, the $Cs_3Bi_2I_9$ performed with a 1.09 % as compared to 0.12 % and 0.003 % for $MA_3Bi_2I_9$ and $MA_3Bi_2I_9Cl_x$ [73]. Even though the toxicity and stability issues can be solved by developing all-inorganic cesium bismuth iodide, their poor performance (**Table 1-7**) in photovoltaic devices needs tremendous attention.

The highest efficiency reported for the photovoltaic cell purely based on a $Cs_3Bi_2I_9$ absorber is 3.2 %. For this, the morphology of the $Cs_3Bi_2I_9$ thin film was modified to obtain ultrathin nanosheets through a recrystallization process by adding DMF drops and with a top CuI hole transporting layer [107]. Besides, a mixed-phase absorber layer of $Cs_3Bi_2I_9$

and $Ag_3Bi_2I_9$ performed better in a solar cell yielding a PCE of 3.59 % [121]. A $Cs_3Bi_2I_9$ planar-type solar cell demonstrated 8 % PCE with more than 500 h of stability at 65°C (RH ~ 60-70 %) under continuous 1 sun illumination. The excellent crystallinity of these DMF+HI derived films may have contributed to the improved efficiency and thermal stability [122]. Furthermore, the numerical calculations achieved 13.82 % efficiency for 1400 nm $Cs_3Bi_2I_9$-based solar cells with TiO_2 as ETL and NiO as the HTL [123].

Table 1-7. All-inorganic cesium bismuth iodide based perovskite solar cells.

PV structure	Absorber E_g (eV)	V_{OC} (V)	J_{SC} (mA/cm^2)	FF	PCE (%)	Ref.
FTO/c-TiO_2/m-TiO_2/$Cs_3Bi_2I_9$/HTM/Ag	2.2	0.85	2.15	0.60	1.09	[73]
FTO/c-TiO_2/m-TiO_2/$CsBi_3I_{10}$/P3HT/Ag	1.77	0.31	3.40	0.38	0.40	[93]
FTO/c-TiO_2/m-TiO_2/$Cs_3Bi_2I_9$/P3HT/Ag		0.26	0.18	0.37	0.02	
FTO/b-TiO_2/m-TiO_2/ZrO_2/ $CsBi_3I_{10}$/C	1.76	0.46	4.75	0.69	1.51	[124]
FTO/c-TiO_2/m-TiO_2/ $CsBi_3I_{10}$/TQ1/Ag	1.77	0.54	1.7	0.59	0.55	[125]
FTO/m-TiO_2/$Cs_3Bi_2I_9$/Spiro-OMeTAD/Au		0.49	0.67	0.636	0.21	[99]
FTO/c-TiO_2/$Cs_3Bi_2I_9$/CuI/Au		0.86	5.78	0.64	3.20	[107]
FTO/c-TiO_2/$Cs_3Bi_2I_9$/ Spiro-OMeTAD /Au		0.79	4.45	50	1.77	[107]
FTO/c-TiO_2/$Cs_3Bi_2I_9$/ PTAA /Au		0.83	4.82	57	2.30	[107]
FTO/TiO_2/$Cs_3Bi_2I_9$/PTAA/Au	2.1				8.0	[122]
FTO/c-TiO_2/m-TiO_2/$CsBi_3I_{10}$/Spiro-OMeTAD/Ag	1.78	0.55	4.45	0.42	1.03	[126]
ITO/NiO_X/ $Cs_3Bi_2I_9$/PCBM/Ag	2.08	0.74	3.42	0.51	1.26	[96]
AZO/c-TiO_2/$Cs_3Bi_2I_9$/CuSCN/graphite	2.1	0.37	1.43	0.32	0.17	[102]
FTO/c-TiO_2/$Cs_3Bi_2I_9$-$Ag_3Bi_2I_9$/PDBD-T/Au		0.60	7.65	78	3.59	[121]
FTO/c-TiO_2/m-TiO_2/ $Cs_3Bi_2I_9$ -KI/C		1.01	3.60	77	2.81	[127]

On the other hand, an extended photoconversion spectrum was observed in the case of $CsBi_3I_{10}$ phase ($CsI:BiI_3$ = 1:3) thin films which yielded 0.40 % PCE outperforming the $Cs_3Bi_2I_9$ or BiI_3 thin films [93]. The improvements in surface morphology and high absorption coefficients of $CsBi_3I_{10}$ as compared to $Cs_3Bi_2I_9$ had resulted in better charge transport and reduced the recombination losses thus yielding better J_{sc} and FF values to obtain the highest 1.51% PCE [124]. Further, the solvent annealed (160°C) $CsBi_3I_{10}$ thin films have demonstrated a hysteris-free reproduceable PCE of 1.01% with good stability.

The relatively lower charge carrier density and the poor conductivity of mobile charge carriers due to the depletion width are proposed for the poor performance of the device [126].

Light emitting diodes

The $Cs_3Bi_2I_9$ quantum dots have also demonstrated appreciable photoluminescence quantum yield of up to 2.3 % [128]. However, other halides such as $Cs_3Bi_2Cl_9$ and $Cs_3Bi_2Br_9$ yielded better PLQYs as compared to iodides. The nanocrystals of $Cs_3Bi_2Br_9$ displayed a photoluminescence quantum yield of 0.2% which was improved to 4.5% by using oleic acid as a surfactant to passivate the trap states [129]. Employing octylammonium bromide and oleic acid as ligands, 22% PLQY was achieved with $Cs_3Bi_2Br_9$ quantum dots that were also stable at 180℃. In addition, the $Cs_3Bi_2Cl_9$ QDs prepared in the same method had a PLQY of 62% [128].

Photocatalysis

$Cs_3Bi_2I_9$ has also demonstrated photocatalytic activity in efficiently reducing Rhodamine B (RhB) by 93% after 180 minutes of visible light irradiation [130]. The charge separation and carrier transport were improved by depositing $Cs_3Bi_2I_9$ over a graphitic carbon nitride (g-C_3N_4) layer to form a composite through the nitrogen-iodine bonds. The band alignment between the layers and material interaction enhanced the visible light photocatalytic degradation of organic compounds like Rhodamine B, methylene blue and methyl orange [131]. Besides, $Cs_3Bi_2I_9/Bi_2WO_6$ heterostructures showed strong redox ability in the CO_2-to-CO reduction with a CO yield of 66 μmol g^{-1} along with water oxidation, while the pristine $Cs_3Bi_2I_9$ yielded 15.2 μmol g^{-1} CO after photocatalysis (9 h irradiation) [132]. The structures maintained cyclic photocatalytic stability for up to 3 cycles and the material retained its initial crystallinity after photocatalytic reduction [132].

Valleytronics

Valleytronics is an energy-efficient information technology that operates at a low electric field with no net charge thus not causing ion migration in perovskites due to the electric

field. Interestingly, the 2D derivatives of $Cs_3Bi_2I_9$ with odd layers have shown stable valley polarization that can be leveraged in solid-state information devices [94].

Electrode applications

Moreover, $Cs_3Bi_2I_9$ has been used as an active electrode material in supercapacitors and achieved a specific capacitance of 280 Fg^{-1} and an areal capacitance of 2.4 Fcm^{-2}. The device retained 88% of its capacitance values even after 5000 galvanostatic charge-discharge cycles promising long-term stability [133]. Light-absorbing properties of $Cs_3Bi_2I_9$ were leveraged in bifunctional devices as well. $Cs_3Bi_2I_9$ nanosheets were used as photoelectrodes for rechargeable lead-free perovskite Li-ion batteries. In its first discharge, these photo-batteries achieved ~0.43 % of photo-conversion efficiency and under illumination, the capacity improved from 410 to 975 $mAhg^{-1}$ [128,134].

Resistive switching Random Access Memory devices

The iodide vacancy-mediated migration in $CsBi_3I_{10}$ thin films under an electric field can offer trapping and detrapping which is utilized in the ReRAM application of the material [52]. The ReRAM devices demonstrated significantly high on/off ratios (10^3), high endurance (150 cycles) and reliable retention (10^4 s) with excellent stability over 60 days in ambient conditions (25°C, 60% RH) [52]. Flexible memristors were fabricated from ultrathin $Cs_3Bi_2I_9$ nanosheets with an excellent R_{on}/R_{off} ratio of ~10^3 and data retention for more than 10^4 s at a low voltage of 0.3 V [108].

1.4.5. Limitations of 0-D $Cs_3Bi_2I_9$ in optoelectronic devices

Even though $Cs_3Bi_2I_9$ has a band gap of around 2 eV and reasonable absorption coefficients, the non-radiative defects and poor photocurrent density limit their performance in photodetectors and solar cells [99]. The high Urbach energy explains the structural disorder and short-range crystallinity in $Cs_3Bi_2I_9$ which lead to the smearing of local energy bands and high spin-orbit coupling [135]. Besides, the broad photoluminescence spectra suggest that small polarons induced from the strong electron-phonon interactions lead to self-trapped excitons in these materials [92]. The carrier interactions with phonons in bismuth-based compounds lead to carrier localization which

severely reduces the carrier mobilities (~0.024 cm^2/Vs) and significantly limits the extent of absorption [136,137]. On the other hand, localized carriers can act as radiative recombination centers for luminescence and as phosphors in white light-emitting diodes [138]. $Cs_3Bi_2I_9$ has high exciton binding energy and deep energy defects prohibiting charge separation [132]. In addition, the large energy level mismatch with common charge transport materials, as seen in Figure 1.7, leads to inefficient interface charge extraction [98,136,137].

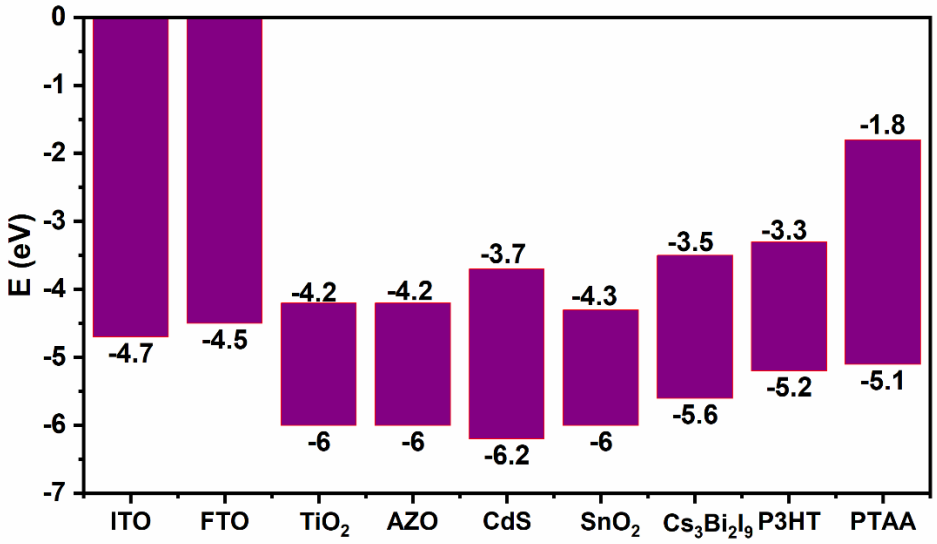

Figure 1.7. Band level diagram of some $A_3Bi_2I_9$ compounds with common charge transport layers.

The limited device efficiencies observed are ascribed to the rapid photocarrier recombinations due to the high density of defect states in the material as well as in the interfaces. In addition, the rough morphology with pin holes seen in the $Cs_3Bi_2I_9$ thin films might be adding to the deterioration of PSCs. Therefore, advanced techniques are required to fabricate dense homogeneous films. Besides, $Cs_3Bi_2I_9$-based solar cells exhibited J-V hysteresis after prolonged storage due to the migration of ions from charge transport layers, especially organic HTLs [73].

1.4.6. Strategies to improve the performance

Various strategies to hurdle these limitations were explored by researchers. The passivation of intrinsic defects or structural disorder by adding 20% excess of BiI_3 in the precursor

solution had improved photocurrent density in $Cs_3Bi_2I_9$ mesoscopic solar cells [99]. Applying a mild external pressure to $Cs_3Bi_2I_9$ led to the contraction of Bi-I bonds and reduced Bi-I-Bi angles to overlap atomic orbitals thus increasing the exciton binding energy. This enhanced the emission properties with the reduction in band gap from 2.05 eV (1 atm) to an optimum 1.12 eV at 12.1 GPa. Further compression metalized $Cs_3Bi_2I_9$ with a 33Ω measured at 28 GPa [139].

Doping or dual cation

Density functional theory (DFT) calculations suggest a dual cation approach using trivalent metals can be employed for engineering the band gap in $Cs_3Bi_2I_9$. Among many cations, the Cs_3BiGaI_9 (direct E_g: 1.60 eV) and Cs_3BiInI_9 (1.90 eV) have shown great promise with the highest absorption coefficients and comparable transport properties. More reduced band gaps by ~0.5 eV were observed using $P\bar{3}m1$ symmetry [97]. Various cations like Rb, K, Cs have been examined at the A cation site in the enneahalogenidometallate phase $A_3Bi_2X_9$ to reveal that the band gaps are insensitive to the A cations. In comparison to the lead halides, they have lower VBM levels and require proper HTMs to match the band positions to obtain high V_{oc} values. Moreover, the band dispersion is not profound as seen in related perovskites. The high DOS along with strong p-character is effective for strong light absorption [98]. Partial substitution of Bi^{3+} with Ru^{3+} created defects in $Cs_3Bi_2I_9$ and enhanced the electron-phonon coupling to result in narrowed band gap and upshifted band structure [100].

Double Perovskites (Cs_2PBiX_6)

Double perovskite structures by considering the two unit cells of ABX_3 perovskite to form A_2PBX_6 (A = Cs, P = Ag/Cu/In/Ga, B = Bi/Sb, X =I/Cl/Br) structure by substituting heterovalent atoms in the B site is an effective way to preserve the 3-D nature of the perovskite structure. The $Cs_2AgBiBr_6$ perovskite PD achieves detectivity up to 1.87×10^{11} Jones with a switching ratio of 1.66×10^4, while the flexible device yields 8.04×10^{11} Jones [140]. The device fabricated from $Cs_2AgBiBr_6$ single crystals has detected X-rays of a dose rate as low as 59.7 $nGy_{air}^{-1}s^{-1}$ with a sensitivity of 105 μC Gy_{air}^{-1} cm^{-2} [141].

The performance of double perovskites in solar cell research is given in **Table 1-8**. $Cs_2AgBiBr_6$ thin films by ultrasonic spray technique yielded PCE the same as that of the spin coating route in solar cells with low hysteresis. The better coverage and uniformity of spray-coated thin films and low electron trap density in the intermediate energy levels enhanced the V_{oc} from 0.82 (spin) to 1.09 V (spray) [116]. Besides, the electrochemical impedance spectroscopy (EIS) suggested that the interfacial recombination rate ($Cs_2AgBiBr_6$/Spiro-OMeTAD) was higher for the spin-coated films which can increase the diffusion current that usually lead to low V_{oc} [116]. Furthermore, the selective contact resistance was low for spin-coated devices pointing to better charge collection as compared to spray-coated devices [116].

Table 1-8. Photovoltaic performance of $Cs_2AgBiBr_6$ double perovskites.

PV structure	Absorber E_g (eV)	V_{OC} (V)	J_{SC} (mA/cm^2)	FF	PCE (%)	Ref.
FTO/c-TiO_2/m-TiO_2/$Cs_2AgBiBr_6$/Spiro-OMeTAD/Au	2.2	0.98	3.93	0.63	2.43	[142]
ITO/SnO_2/$Cs_2AgBiBr_6$/P3HT/Au	2.05	1.04	1.78	0.78	1.44	[143]
ITO/SnO_2/$Cs_2AgBiBr_6$/Au		0.95	1.50	0.60	0.86	
FTO/TiO_2/$Cs_2AgBiBr_6$/Spiro-OMeTAD/Ag	1.98	0.87	1.24	0.65	0.70	[144]
FTO/c-TiO_2/m-TiO_2/$Cs_2AgBiBr_6$/Spiro-OMeTAD/Au	1.9	1.09	3.1	0.70	2.3	[116]
FTO/c-TiO_2/m-TiO_2/$Cs_2AgBiBr_6$/Spiro-OMeTAD/Ag	2.09	1.02	3.22	0.6932	2.28	[145]
FTO/c-TiO_2/m-TiO_2(D149)/$Cs_2AgBiBr_6$/Spiro-OMeTAD/Ag		0.73	8.24	0.7032	4.23	[146]

The highest efficiency of 3.11 % was achieved in $Cs_2AgBiBr_6$ solar cells by engineering the m-TiO_2 ETL with methyl *trans*-3^2-carboxy-pyropheophorbide-a (C-Chl)**.** Its carboxyl group ensured efficient adsorption on m-TiO_2 while the conjugated double bonds enhanced the extinction coefficient pushing the absorption spectrum to 750 nm [145]. The C-Chl-based solar cells showed reduced defects and enhanced charge collection suppressing the charge recombination. However, they only maintained 90 % of their initial PCE at 25°C after 720 h as compared to the C-Chl-free solar cells that retained 93 % of their initial PCE [145]. Later, sensitizing the TiO_2 layer with indoline dyes pushed the PCE to 4.11 % for a

$Cs_2AgBiBr_6$ heterojunction solar cell employing D149 dye. Further on annealing at 200 °C, this was improved to 4.23 % [146].

Layered Double perovskites (Cs_4PBiX_8)

The wide indirect band gap, large carrier effective masses and parity forbidden transitions may again limit the performance of the double perovskites. However, double perovskites with a low-dimensional layered structure (**Figure 1.8**) are a way to tune their electrical and optical properties [147]. Unlike the indirect gap of $Cs_2CuBiBr_6$, monolayer Cs_4CuBiI_8 displayed a direct band gap of 1.54 eV (PBE) which is associated with this reduced dimensionality. The material has a hole effective mass of 0.27 m_0 along the Γ-X direction [147].

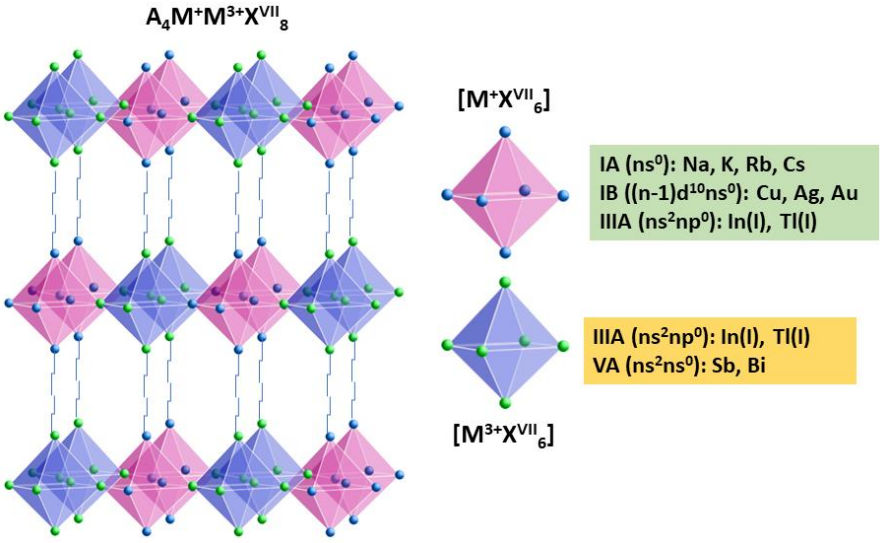

Figure 1.8. The 2-D layered double perovskite structure.

Dual anion engineering by chalcogenides (Cs-Bi-S/Se/Te-X_2)

On top of the suitable band gap and high absorption properties, a continuous 3-D network is another requirement to match the conventional perovskite materials [49]. While substituting Pb with Bi in $CsPbI_3$ the 3-D network may be conserved if suitable anion substitutions are also made simultaneously.

Bismuth-based chalcogenide compounds have a highly anisotropic nature with intriguing semiconducting properties that can be modified to find applications in thermoelectrics

[148–150], photovoltaics [151], γ- ray detection, topological quantum science, second harmonic generation, superconductivity, optical data storage and charge density wave formation [152]. A large number of ternary and quaternary compounds based on bismuth chalcogenides have been realized and studied which belong to A-B-Bi-C systems where A = K/Rb/Cs/Sr/Ba/Eu, B = Sn/Pb/Ag/Cd and C = S/Se/Te [148,151,152]. In such compounds, the corner or edge-sharing BiC_6 octahedra opens possibilities for structure designs with mixed cation sites to form tunneled or layered structures depending on the composition [152]. The studies on single crystals of 2D quaternary chalcogenides like $ACd_xBi_{4-x}C_6$ (A=Cs/Rb/K and C=S/Se) and Cs-Ag-Bi-C suggest that they can provide distinct directions for ion exchange chemistry that may lead to the realization of novel and metastable compounds because of the labile cations in their layers [151,152]. Very recently, a 30 nm PV device of $AgBiS_2$ nanocrystals fabricated using cation disorder engineering achieved 9.17 % efficiency [153].

Table 1-9. The chalcogenide incorporated perovskites.

PV structure	E_g (eV)	V_{OC} (V)	J_{SC} (mA/cm^2)	FF	PCE (%)	Ref.
FTO/c-TiO_2/m-TiO_2/PbSe:$MAPbI_3$/Spiro-OMeTAD/Ag	1.54	0.94	16.7	0.66	10.44	[19]
FTO/c-TiO_2/m-TiO_2/$MASbSI_2$/PCPDTBT/PEDOT:PSS/Au	2.03	0.65	8.12	0.585	3.08	[154]
FTO/c-TiO_2/m-TiO_2/$Ag_3BiI_{5.92}S_{0.04}$/PTAA/Au		0.57	14.7	0.659	5.56	[137]
FTO/c-TiO_2/m-TiO_2/$MA_3Bi_2I_{9-x}S_x$/Spiro-OMeTAD/Au	1.67	0.52	0.58	0.476	0.152	[155]

Thus, band gap tuning with chalcogenides may enhance the optoelectronic properties of the conventional metal halide perovskites while preserving the 3D structure of high-performing $MAPbI_3$ and some of such attempts are given in **Table 1-9** [156,157]. The higher electronegative anions such as Br^-, Cl^- will not be able to form high covalency chemical bonds with Pb^{2+} like I. However, the divalent anions in the structure can improve the electrostatic interaction with the A cations that are held in the metal halide framework leading to enhanced chemical stability in the ambient conditions along with suppressed ion migration [19]. Interestingly, the electronegativity of the anions can significantly affect the covalent nature of the metal halide framework as well as the carrier lifetimes. The carrier

lifetime can be lower in the presence of higher electronegative anions, such as S^{2-} and Se^{-2}, in the structure [19].

While considering a split anion approach in the computational calculations, the chalcogenide incorporation resulted in a narrow band gap in I-III-VI-VII_2 materials. From the HSE+SOC calculations, they obtained a band gap of 1.38 eV for $CH_3NH_3BiSI_2$, which demonstrated stronger absorbance than $CH_3NH_3PbI_3$ below 3 eV. This reduced band gap compared to $CH_3NH_3PbI_3$ is a result of the hybridization of S 3p with I 5p states in the VBM and Bi 6p in the CBM [156]. Besides, sulfur incorporation into $CsSnI_3$ can lead to the $CsSnS_2Cl$ structure with an Sn^{4+} state. This distorted perovskite structure with *I4/mcm* symmetry has a calculated indirect band gap of 0.98 eV. Unlike other indirect solar absorbers, the $CsSnS_2Cl$ shows a sharp increase in absorption at the band gap which might be due to the relatively large density of states at the VBM. Besides, the compound has a direct band gap of 1.11 eV at the Γ-point whereas for Si it is 3.34 eV [156].

In the reported studies, the sulfur-doped MBI thin films by a solvothermal method followed by post-annealing (80-150 ℃) could reduce the band gap from 2.04 eV to 1.45 eV [157]. Further, the Se incorporation into the $MAPbI_3$ by using 10 wt.% PbSe had enhanced its conductivity while the stability was improved by 140 times. The Se-doped films were treated at 100 % RH and 40 ℃ for 72 hours of accelerated aging and found to be stable as compared to the completely degraded pristine $MAPbI_3$ films [19]. The S-incorporated $MASbSI_2$ thin film based solar cells demonstrated a PCE of 3.08 %. with 15-day stability in PV structure retaining 90 % of its PCE in 60% (25℃) humidity[154]. Besides, uniform and dense $MA_3Bi_2I_{9-2x}S_x$ thin films showed a band gap of 1.67 eV with low trap state density (1.9×10^{16} cm^{-3}) which demonstrated a PCE of 0.152 % in solar cell structures [155]. On the other hand, $Ag_aBi_bI_{a+3b-2x}S_x$ thin films were obtained by the incorporation of S into all inorganic perovskite $Ag_aBi_bI_{a+3b}$ by spin-coating. The band gap was observed to be narrowing to 1.76 eV from 1.87 eV due to the upshift of the valence band edge. The solar cells achieved a maximum PCE of 5.56 % (0.16 cm^2) and 4.6% (1.02 cm^2) for 4 at.% S-doped $Ag_3BiI_{5.92}S_{0.04}$ absorber layer with band gap ~1.78 eV [137].

Heterostructures

Heterostructures with 2D materials of excellent transport properties can improve the optoelectronic performance of the $Cs_3Bi_2I_9$, for example, the dark current was suppressed in $MoS_2/Cs_3Bi_2I_9$ and graphene/$Cs_3Bi_2I_9$ photodetectors as compared to $Cs_3Bi_2I_9$ photodetectors [110]. Besides, the $Cs_3Bi_2I_9$ nanocrystals grown on ultrathin bismuth tungsten oxide nanosheets ($Cs_3Bi_2I_9/Bi_2WO_6$) demonstrated enhanced contact and strong electron coupling which promoted interface charge transfer resulting in a fourfold increase in the photocatalytic activity for the CO_2 to CO conversion compared with pristine $Cs_3Bi_2I_9$ nanocrystals [132].

1.5. Ultrasonic Spray Deposition

It is especially important to find low-cost scalable production routes for optoelectronic devices while considering commercialization. The perovskite thin films can be deposited by solution-based cost-effective deposition techniques like slot-die coating, blade coating, inkjet printing, meniscus coating, screen printing, electrodeposition and spray pyrolysis [26]. Among them, the simple and high-throughput spray pyrolysis technique can be used for effective area-selective deposition with efficient material utilization. Spray coating or spray pyrolysis is a processing technique that uses a fine mist of the precursor solution containing the desired elements to deposit higher-density thin films on the surface of a heated substrate [158].

1.5.1. Mechanism of thin film formation

Generally, the mechanism of thin film formation during spray deposition can be explained through the following stages:

(i) *Ultrasonic nebulization process*:

The high frequency ultrasound generated by the ultrasonic nebulizer is passed through the precursor solution, impinging on a liquid-gas interface, which forms an aerosol of micron-sized liquid droplets. The distribution of droplets, the droplet diameters and velocity of aerosols, are controlled by the ultrasonic nebulization process. The ultrasonic nebulization process is best described by the capillary wave mechanism (capillary waves are waves

propagating through the interface between two fluids) and the aerosol formation is a consequence of momentum transfer as described in Figure 1.9 [159]. It was Faraday who discovered the existence of capillary waves on the surface of a fluid when it is supported by a vibrating solid. Therefore, they are often referred to as faraday waves [160]. The liquid droplets are generated when the amplitude of these surface capillary waves is large enough to break the crests off as depicted in Figure 1.9**.** Further, Kelvin formulated the relation between capillary wavelength (λ), fluid depth (h), surface tension (σ), fluid density (ρ), and frequency (f) of the standing waves as given in equation (1.1) [159],

$$\lambda\left[\tanh\left(\frac{2\pi h}{\lambda}\right)\right]^{-1/3} = \left(\frac{2\pi\sigma}{\rho f^2}\right)^{1/3} \quad (1.1)$$

For a deep liquid layer, we can consider $\tanh(2\pi h/\lambda) = 1$, since $h/\lambda \gg 1$. Here, the frequency f of the standing waves is half the excitation frequency (F), $(f = F/2)$, just like in many other oscillators.

The capillary wave mechanism proposes the dependence of droplet size on capillary wavelength which in turn is dependent on the frequency of standing waves. It was R. W. Wood and A. L. Loomis described the droplet formation using ultrasound in 1927 [161], and Lang experimentally established the relationship between average droplet size (D_{avg}) and ultrasonic frequency through the relation in (1.2) [162],

$$D_{avg} = \kappa\lambda = \kappa\left(\frac{8\pi\sigma}{\rho F^2}\right)^{1/3} \quad (1.2)$$

σ = liquid surface tension (Nm^{-1})

ρ = solution density (Kgm^{-3})

$f = F/2$ = ultrasonic frequency (MHz)

The value of κ was determined experimentally for droplets produced by ultrasound of 10-800 kHz by Lang, whereas it was corrected to 0.96 by Yasuda et al. for MHz ranges [163].

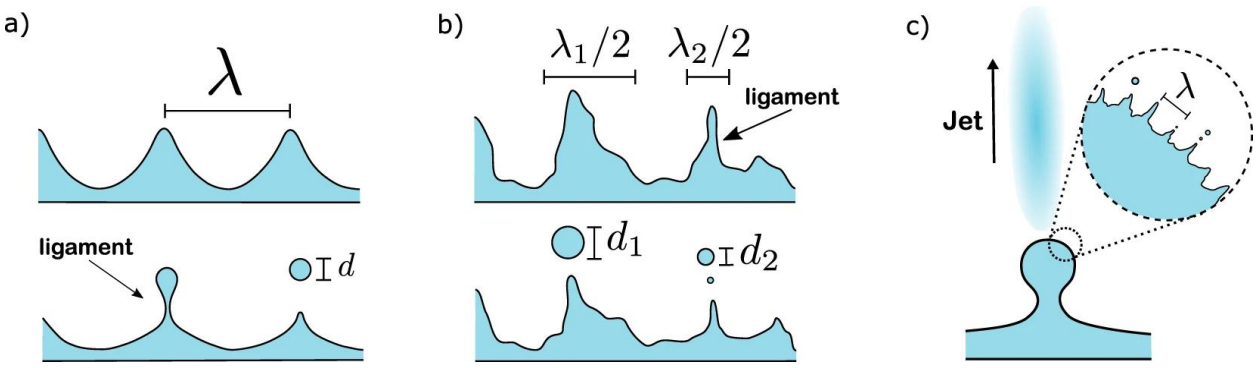

Figure 1.9. (a) Standing capillary waves of wavelength λ. When the amplitude rises above a specific threshold, equal-sized ligaments form, which causes monodisperse droplets of size d~λ to break apart. (b) A perturbed system resulting in large variations in the wavelengths and amplitudes of capillary waves. The average ligament roughness and size distribution leading to a wider range of droplet sizes. (c) Superposition of Faraday waves with larger waves of wavelength similar to that of chip material's wavelength which initiate breakup of the smaller superposed capillary waves | Permission by open access [159].

(ii) Droplet transport and solvent evaporation:

The ultrasonically generated droplets of reaction precursors thus become individual chemical microreactors as they are carried by gas flow onto a heated substrate where reactions occur. It is desirable for most of the droplets to reach the substrate surface and spread to form the film. During this flight of droplets in the aerosols, they may undergo coalescing, spreading, or receding [164]. It is more likely that they interact with the other droplets, the carrier gas and the spraying atmosphere by exchanging heat and energy. These processes involved in droplet transport relates to the distance between nozzle and substrate, droplet size, spray rate and precursor concentration. For the spray deposition with large nozzle to substrate distance and large number of smaller droplets will accelerate these interactions due to the large surface area of the droplets.

In addition, the droplets undergo evaporation in flight that creates a concentration gradient which can lead to surface precipitation when the concentration exceeds solubility limit. As a consequence, porous crust and hollow particles are formed that result in increased film roughness. Moreover, If the precursor concentration is high or the carrier gas flow-rate is low, then solid particles can be formed in a heated atmosphere. However, if the aerosol contains large number of smaller droplets, then the carrier gas will constitute more solvent

vapor and the solute diffusion length will be short. This can lower the evaporation rate and the precipitation will be delayed [165].

(iii) Droplet spreading and diffusion of reactants on the substrate surface:

As the droplets reach the heated substrate surface, a number of processes take place simultaneously. The spreading of the droplets, diffusion and reaction of the constituent elements, evaporation of the solvent, nucleation and crystallization all together lead to the final thin film of the desired compound.

(iv) Escape of any volatile product:

Evaporation of volatile solvent can be followed by chemical reactions either of the remaining solid or, in the presence of high boiling co-solvents or molten salts, in submicron-sized liquid droplets. Such reactions can occur in the interior of the droplet or on the droplet surface [159].

(v) Nucleation and crystallization:

When the solvent starts to evaporate from the preheated substrate surface, nucleation of the compound initiates and further to crystallization. Here, the solvent evaporation rate and crystallization rate have a drastic effect on the properties of the thin films and therefore must be balanced by optimization depending on the application under focus.

The various stages of thin film formation are influenced by the different spray parameters such as type of solvent, substrate temperature, spray rate, the concentration of the precursor solution, number of depositions, etc. The quality, in terms of uniformity and adherence, and thickness of the thin films can be controlled by optimizing these important parameters. Further, fine-tuning of these parameters can be used to change the structure, morphology and optoelectronic properties of thin films.

1.5.2. Spray deposition for perovskite thin films

Researchers have employed ultrasonic spray deposition for fabricating perovskite layers in various optoelectronic devices such as photodetectors, solar cells and LEDs. using solvents like DMF, DMF:DMSO [26] and DMF:GBL [166]. The spray technique enables a fast crystallization of the perovskite film without disturbing the underlying layers which widens

the window for various device architectures such as graded multilayer perovskite photodetectors (PPDs) [26], perovskite light-emitting diodes (PeLEDs) [167], tandem solar cells [168] and even devices on nonplanar surfaces [169]. The underlying mechanism of perovskite layer growth during the spray deposition technique is as follows. At the initial stage of spray deposition, the fast solvent evaporation and crystallization lead to smaller perovskite grains which are soaked and recrystallized by the subsequent depositions to grow into larger crystallites. If the inward flow of solution (f_{in}) is smaller than the outward flow of solvent vapor (f_{out}) then the solution undergoes fast crystallization without dissolving the previous deposition whereas when f_{in} is large, then the solvent is not entirely evaporated and results in dewetting [166].

Particularly, ultrasonic spray deposition has been employed for depositing the active $CH_3NH_3PbI_{(3-x)}Cl_x$ layer in planar heterojunction perovskite solar cells [166,170–172]. Most interestingly, fully sprayed ITO/SnO_2/$CH_3NH_3PbI_{(3-x)}Cl_x$/spiro-OMeTAD/Au solar cells demonstrated power conversion efficiency as high as 19.6 % [170]. The 3.9 μm thick $CsPbI_2Br$ layer deposited via spray method for a narrow band photodetectors yielded a specific detectivity of 2.43×10^{10} Jones at 655 nm [25]. The graded triple cation perovskite-based self-powered PDs developed by spray coating demonstrated excellent detectivity of 2.44×10^{12} $cmHz^{1/2}W^{-1}$ and responsivity of 0.2588 AW^{-1} for broadband detection [26]. Recently, stacked $(PEA)_2(MA)_{n-1}Pb_nI_{n+1}Br_{2n}$ (n=∞/n=50) a 3D/quasi-2D perovskite double layer deposited via a sequential spray deposition demonstrated better stability and efficiency as compared to the single junction 3D perovskite [168].

1.6. Prospects of bismuth halides: perovskites and beyond

The search for lead-free stable perovskite materials has led to semiconductors beyond perovskite structure with prospects for other optoelectronic applications. Among them, the realization of a wide band gap (2.06 eV) Cu_2AgBiI_6 with high absorption coefficients (~10^5 cm^{-1}) is particularly interesting [173,174]. It has an exciton binding energy of 25 meV, a charge carrier mobility of 1.7 $cm^2V^{-1}s^{-1}$ and a photoluminescence lifetime of 33 ns [174].

1.7. Goal of the research

The current research focusses on the development of non-toxic and stable Cs-Bi-halide perovskite thin films by a scalable and simple ultrasonic spray pyrolysis technique and engineer their optoelectronics by incorporating sulfur or noble metals to solve the current limitations faced by the material in their applications.

HYPOTHESIS

Perovskite-inspired and lead-free cesium bismuth iodide ($Cs_3Bi_2I_9$) thin films with tunable properties are formed by ultrasonic spray deposition technique for optoelectronic applications.

OBJECTIVES

General Objective:

To explore the potential of cesium bismuth iodide thin films fabricated by ultrasonic spray deposition technique for optoelectronic applications.

Specific Objectives.

- Setting up an automated ultrasonic spray deposition system for large-area deposition of thin films in atmospheric conditions.
- Begin density functional theory calculations on various Bi-based perovskite systems.
- Determination of equipment conditions to form uniform films by fabricating BiI_3 thin films.
- Optimization of spray parameters such as substrate temperature, spray rate and spray duration for uniform $Cs_3Bi_2I_9$ thin films with pure phase.
- Explore the deposition technique by using non-toxic solvents.
- Incorporation of sulfur into the $Cs_3Bi_2I_9$ films and exploring its optoelectronic properties.
- Fabrication of device structures based on the interesting properties demonstrated by the films.

JUSTIFICATION

The search for better stable and non-toxic perovskite materials through computation and experiments had created a pool of novel materials that require further detailed investigations to understand their optoelectronics and compare them with their unstable and toxic counterparts. Among them, Bi-based compounds are of particular interest, especially, Cs-Bi-halide systems, due to their excellent stability and non-toxic nature. The p-type all inorganic lead-free perovskite (ALP), $Cs_3Bi_2I_9$ has a hexagonal structure composed of $Bi_2I_9^{3-}$ formed by the face-sharing octahedra. This leads to a 0-D structure in contrast to the 3-D structure of well-performing Pb-based perovskites. Besides, various experimental and theoretical studies so far have demonstrated an indirect band gap in the range of 1.9-2.3 eV. They have a high exciton binding energy of 270 meV and have absorption coefficients in the order of 10^5 cm^{-1}.

Most investigations focus on $Cs_3Bi_2I_9$ single crystals or spin-coated thin films, which constricts the production approaches for these materials and reduces their scalability. Since $Cs_3Bi_2I_9$ is a stable compound, it can be fabricated at high substrate temperatures under atmospheric conditions, and the ultrasonic spray deposition is a great tool for scaling up production and examining the impact of different deposition pathways to get beyond the material's current limits.

CHAPTER 2

EXPERIMENTAL METHODS

This chapter describes the processes and methods followed for computational calculations, thin film deposition, post- deposition treatments, device fabrication and characterization.

2.1. Introduction

Computational calculations are a great tool in this new era of materials science which can give in-depth information on properties of interest to make choices from a vast pool of possible materials and experiments to start with, saving a lot of time and energy. Besides, the data from these calculations can be used to understand and explain various optoelectronic phenomena demonstrated by the materials. The optoelectronic performance of semiconductor thin films in devices is directly related to their basic structural, morphological, compositional, optical, and electronic properties. Various characterization techniques and the corresponding equipment used to investigate these properties are briefly described in this chapter along with the computational parameters and the process flow in the calculations.

2.2. Computational methods

2.2.1. Density functional Theory (DFT)

Density functional theory calculations are based on the idea that the total energy of an atomistic system, such as a solid, surface or molecule, depends fundamentally on the ground state electron density of the system. The remarkable theorem formulated by

Hohenberg & Kohn and Kohn & Sham explains the total energy (E) as a function of its electron density defined at each point $\boldsymbol{r}$, ($\rho = \rho(\boldsymbol{r})$) [175,176].

$$E = E(\rho) = E[\rho(r), \{R_\alpha\}] \quad (2.1)$$

Where the $\{R_\alpha\}$ is the set of atomic positions in the system (α) under consideration.

On the other hand, Slater's ideas of electron gas to simplify the widely used Hartree-Fock exchange led to *ad hoc* X_α methods contributing to the development of electronic structure calculations. Later other simplifications in the scattered-wave method with *ab initio* character were also combined into the X_α methods.

The present-day hybrid functional calculations have an *ab initio* character which include wavefunctions based Hartree-Fock concept and DFT. Evidently, solving the Kohn-Sham expression can predict the equilibrium state of a system, the nature of surfaces and adsorption phenomena which are fascinating in materials research.

Vienna Ab initio Simulation Package or VASP is a computer program that uses approximations to solve many-body Schrödinger equation within the density functional theory (DFT) or Hartree-Fock (HF) approximation as well as hybrid calculations including HF approximations and DFT. Here, the plane wave basis sets are used to represent ground state electronic charge density and local potentials. The interactions of electrons with ions are defined by pseudopotentials or the projector-augmented-wave method. Further, for ground electronic state determination iterative matrix diagonalization techniques such as residual minimization methods are employed. Materials design is a software platform for VASP calculations that provide a better user interface with default parameters and potentials.

2.2.2. DFT calculations using MedeA-VASP

The process flow of VASP calculations for structure optimization and electronic structure calculations are given in Figure 2.1. Initially, the hexagonal $Cs_3Bi_2I_9$ structure was relaxed by optimization using the density functional theory via VASP electronic structure method available with the MedeA software package [177–179]. Here, we considered the Purdew-Burke-Ernzerhof for solids (PBEsol) exchange correlation functional in the generalized

gradient approximation (GGA) for representing the electron-nuclei and electron-electron interactions [180]. The projector augmented wave (PAW) potentials for GGA available with MedeA was used while keeping a planewave cutoff of 500 eV to relax all the structural parameters [181].

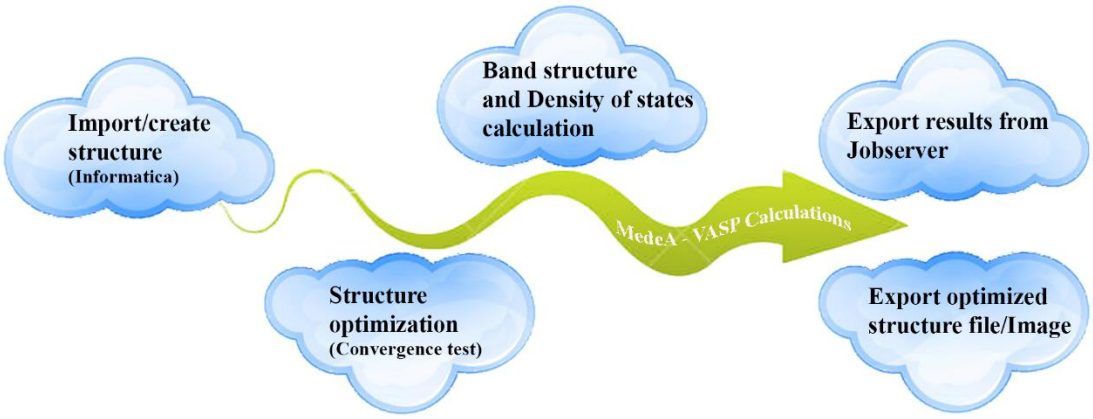

Figure 2.1. The process flow of VASP calculations.

Following a convergence test, the k-mesh for SCF in Brillouin zone was set to 7×7×3 using the Monkhorst-Pack method with origin forced at the Γ-point. This corresponds to a finer k-spacing of 0.125×0.125×0.099 $Å^{-1}$ for accurate calculation of total energies, forces and stress tensors etc. The convergence for ionic relaxation was 0.01 eV/Å, which is the upper limit for residual forces between the atoms. Parallelly, the electronic iterations convergence was set to 1×10^{-6} eV using normal (blocked Davidson) algorithm and real space projection operators. For the integration of electronic density of states, the tetrahedron with Blöchl corrections to the energy scheme was employed which uses a tetrahedra decomposition of the Brillouin zone and an approximated linear interpolation for the integration.

Later, the optimized structure was used for the calculation of band structure and electronic density of states for which the planewave cutoff was 300 eV and k-mesh was 7×7×7.

2.3. Experimental

2.3.1. Ultrasonic Spray Deposition (USD)

The spray pyrolysis technique is a simple and scalable thin film deposition method with efficient material utilization and high throughput [158]. This technique involves spraying a fine mist of precursor solution containing the desired elements onto a heated substrate to deposit high-density thin films as illustrated in Figure 2.2. Due to their resemblance to spray painting in the automobile industry, the technique is commercially scalable and continuous. A wide range of solvents can be utilized in this solution-based technique given they can dissolve the desired chemicals. Besides, a variety of substrates including non-planar substrates can be employed for thin film deposition. Precursor solutions of low concentration and control over the spraying area helps in low and efficient material utilization. The technique has excellent control over stoichiometry which makes it highly useful in doping and fabricating composite thin films. In addition, the influence of various spray parameters on the thin film properties can be explored for specific applications. Furthermore, they are an efficient tool in fabricating graded thin films and tandem devices [182,183].

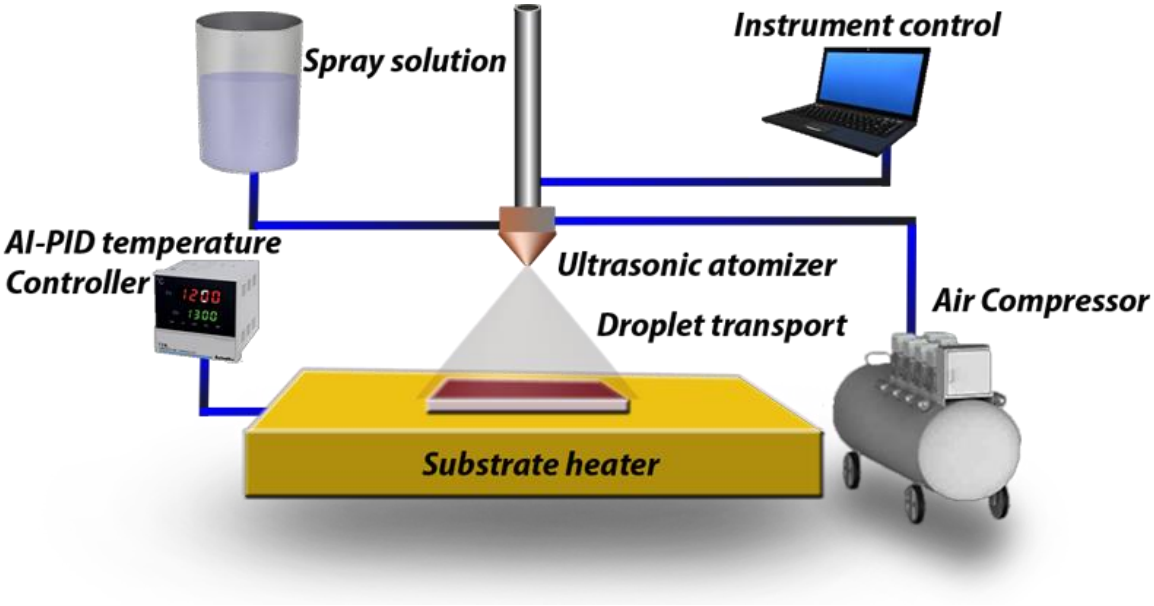

Figure 2.2. The schematic representation of an automated ultrasonic spray pyrolysis system.

The precursor solution is converted to mist or aerosols by different types of atomizers/nebulizers such as pneumatic, ultrasonic, or electrostatic. The pneumatic nebulizer uses a stream of compressed air to break down the solution into fine droplets whereas the ultrasonic nebulizer atomizes the precursor solution with short wavelengths produced by ultrasonic frequencies. The electrostatic nebulizer works with strong electric fields to create spray droplets.

The spray pyrolysis technique was developed by R R Chamberlin and J E Hill in 1964 for depositing conductive films [184,185]. Different types of spray techniques are ultrasonic spray technique, Electric field assisted spray, Hand spray coating, Air assisted spray coating and megasonic spray. Among them, the ultrasonic method has high energy efficiency and is reasonably economic. The controlled inherent low velocity of aerosols facilitates uniform deposition of thin films especially, without disturbing the underlying layer in the case of heterostructures or tandem devices. Besides, a large number of smaller droplets prevents the formation of hollow particles during transport [165].

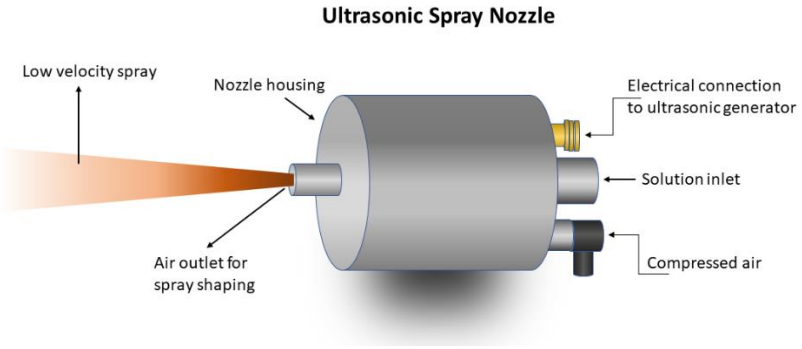

Figure 2.3. The schematic diagram of ultrasonic nozzle for generating spray.

The ultrasonic spray deposition utilizes an ultrasonic nebulizer or nozzle to generate a fine mist of uniform micron-sized droplets as seen in Figure 2.3. A thin, flexible polymer film (e.g., polyethylene, polypropylene, or polytetrafluoroethylene) is used at the base of the reactor reservoir to separate the precursor solutions from the ultrasonic transducer. This configuration allows ultrasound to be effectively transmitted through the polymer membrane into the precursor solution allowing nebulization to occur while sequestering

the solution under an inert or reactive gas. The nebulization vessel is fitted with a gas stream to carry the aerosol to the substrate surface.

2.3.2. Ultrasonic spray deposition equipment

The equipment CY-USP130-A used in this work was purchased from Zhengzhou CY Scientific Instrument Co., Ltd., China which is shown in Figure 2.4 [186]. The equipment uses a 130 W ultrasonic sprayer of 40 kHz which is attached to a nozzle stroke that can move in both x- and y- axis up to 190 mm. The speed of the movement can be regulated between 10-180 mm/s. The substrate heater plate has 150×150 mm area that can be heated up to 500 ℃ with the help of AI-PID temperature controller. A peristatic pump can control the flow rate of the solution in between 0.006 – 41 ml/min into the ultrasonic head from a dispensing tank with a capacity of 50/250 ml. Most importantly, all other parameters can be automated by an available program in the attached PC.

Figure 2.4. The ultrasonic spray pyrolysis equipment (CY-USP130-A) for the deposition of thin films.

2.4. Sample preparation and post deposition treatments

2.4.1. Synthesis of bismuth iodide powder

1 M bismuth nitrate ($Bi(NO_3)_3$, 394.99 gmol^{-1}) and 3 M potassium iodide (KI, 166.0028 gmol^{-1}) are prepared in 50 ml deionized water. The two solutions were then mixed and stirred well to yield BiI_3 precipitate based on the following reaction,

$$3\,KI\,(aq) + Bi(NO_3)_3\,(aq) = BiI_3\,(s) + 3\,KNO_3\,(aq) \qquad (2.2)$$

Figure 2.5. The laboratory synthesized bismuth iodide (BiI_3) powder.

The precipitate is filtered out and washed several times with deionized water. Then, it is dried in a hot air oven for 1 h at 120 ℃. Finally, it is grinded well to obtain the BiI_3 powder as seen in Figure 2.5 [187].

2.4.2. Bismuth iodide thin film

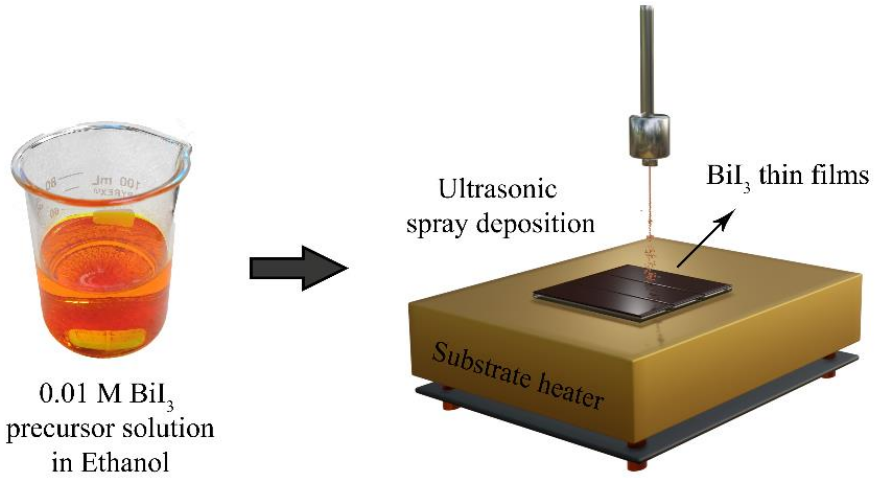

Figure 2.6. The ultrasonic spray deposition of BiI_3 thin films.

The BiI_3 thin films were obtained after several parameter optimizations of the ultrasonic spray deposition technique, as illustrated in **Figure 2.6**. Initially, the glass substrates were

heated on a substrate heater and then a 0.01 M BiI_3 solution (147 mg in 25 ml) in ethanol was sprayed at a spray rate of 0.6 ml/min for 20 mins (20 depositions). The current supply to the ultrasonic nozzle was set to 0.05 A. The compressed air at 0.1 MPa was used to shape and carry the spray generated by the nozzle to the heated substrate surface. The spray head covers an area of 150 ×100 mm^2 with its movements along the x-axis and y-axis at a speed of 50 mm/s and 20 mm/s, respectively. The parameters for the BiI_3 thin film deposition by ultrasonic spray deposition are summarized in **Table 2-1**.

Table 2-1. The optimized spray parameters for BiI_3 thin film deposition.

Substrate temperature	150 ℃	**Number of depositions**	20
Spray rate	0.6 ml/min	**Duration of deposition**	20 minutes
Nozzle current	0.05 A	**Air pressure**	0.1 MPa
Solvent	Ethanol	**Precursor concentration**	0.01 M

Further, the influence of substrate temperature on the properties of spray-deposited BiI_3 thin films was investigated. Thin film samples fabricated at various substrate temperatures are labeled as given in **Table 2-2** and the corresponding results are discussed later in section 4.4.

Table 2-2. The labels of BiI_3 thin films deposited at various substrate temperatures.

Substrate temperature	75 ℃	100 ℃	125 ℃	150 ℃	175 ℃	200 ℃
Sample label	BI75	BI100	BI125	BI150	BI175	BI200

2.4.3. Single-step deposition of $Cs_3Bi_2I_9$ thin films using DMF

In a single-step spray deposition of $Cs_3Bi_2I_9$ thin films, as shown in **Figure 2.7**, dimethyl formamide (DMF) was used as the solvent. DMF has a high boiling point of 153 ℃ and is considered a universal solvent that can effectively dissolve iodide salts. While using DMF, our approach was to obtain uniform $Cs_3Bi_2I_9$ film in a short time by using higher molarity precursor solutions.

Initial experiments

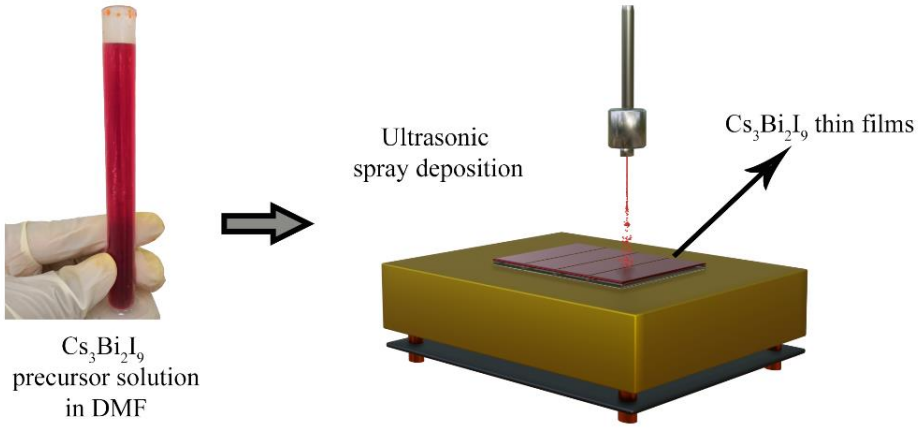

Figure 2.7. Single-step spray deposition and *in situ* crystallization of $Cs_3Bi_2I_9$ thin films.

To understand the influence of various deposition parameters on the film growth and properties, we varied substrate temperature, concentration, spray rate and the number of depositions. Initially, the substrate temperature was varied from 175 to 250 ℃ in steps of 25 ℃. All other parameters were kept the same as described in section 2.4.2. Here, the CsI concentration was 0.015 M (97.4 mg in 25 ml) maintaining the stoichiometric ratio of BiI_3 to CsI in the solution as 2:3.

Table 2-3. The parameters optimized in the initial experiments and the corresponding sample names.

Optimized spray parameters	Substrate temperature	Precursor concentration (BiI_3/CsI) in Molar	Spray rate (ml/min)	Number of depositions
Parameter values and corresponding sample name	175, 200, 225, 250 ℃	0.01/0.015 (M) 0.005/0.0075 (M/2) 0.0025/0.00375 (M/4) 0.00125/0.00187 (M/8)	0.1 (SR0.1) 0.3 (SR0.3) 0.9 (SR0.9)	40 (d40) 50 (d50) 60 (d60)

Further, keeping substrate temperature at 200 ℃, the molarity of BiI_3 was lowered from 0.01 M to 0.00125 M. Afterwards, the spray rate was varied as 0.1 ml/min (SR0.1), 0.3 ml/min (SR0.3), and 0.9 ml/min (SR0.9). In this experiment, the concentration of BiI_3/CsI

was maintained at 0.005/0.0075 M. Later, the number of depositions was increased to 40, 50 and 60 depositions for better coverage. Here, the other parameters, such as substrate temperature, concentration and spray rate, were kept at 200 ℃, 0.005 M/0.0075 M and 0.3 ml/min, respectively, based on the previous depositions. The various thin film samples prepared for the optimization of different spray parameters and the labels used for the discussion are given in **Table 2-3**.

Concentrated precursor solution for $Cs_3Bi_2I_9$ deposition

Here, a concentrated precursor solution was prepared by dissolving 0.368 g of bismuth iodide (0.1 M, BiI_3, section 2.4.1) and 0.244 g of cesium iodide (0.15 M, CsI, Aldrich, 99.9 %) in 6.25 ml DMF by stirring for 1 h at 60 ℃. 4 ml of this solution after filtering was sprayed onto heated glass substrates at 0.3 ml/min in 10 depositions. The substrate temperature was varied as 150, 200, 225, 250, 275, 300, 325, 350 and 400 ℃ and the other parameters are summarized in **Table 2-4**. The influence of temperature on the $Cs_3Bi_2I_9$ film properties is discussed in section 5.3.

Table 2-4. The spray parameters for the deposition of $Cs_3Bi_2I_9$ thin films using DMF solvent.

Substrate temperature	Varied	**Number of depositions**	10
Spray rate	0.3 ml/min	**Duration of deposition**	10 minutes
Nozzle current	0.05 A	**Air pressure**	0.1 MPa
Solvent	DMF	**Precursor concentration (CsI/BiI_3)**	0.15/0.1 M

2.4.4. Two-step deposition of $Cs_3Bi_2I_9$ thin films using ethanol

The ethanol is used as a solvent in the deposition of BiI_3 thin films and its conversion to $Cs_3Bi_2I_9$ thin films by a reactive spray deposition using a CsI solution. Ethanol has a boiling point of 78 ℃ and can have limited solubility for iodide salts. Therefore, low-concentration solutions of BiI_3 and CsI are used in this method.

BiI_3 layer deposition

The BiI_3 layer was deposited using the spray parameters mentioned in section 2.4.2 and **Table 2-1**. The number of depositions were varied according to various experiments.

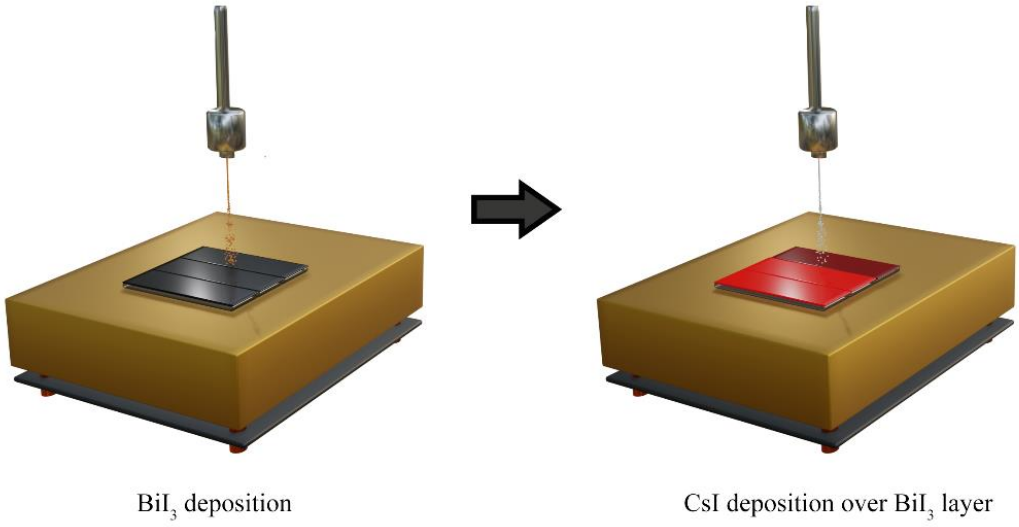

Figure 2.8. Two-step spray deposition of $Cs_3Bi_2I_9$ thin films.

CsI layer deposition

The 0.015 M CsI precursor solution was prepared by dissolving cesium iodide (CsI, Aldrich, 99.9 %) in a solvent mixture of 1 ml deionized water and 24 ml ethanol. The spray parameters for the CsI layer were kept the same as that of BiI_3 film deposition, as given in **Table 2-1**.

2.4.5. $Cs_3Bi_2I_9$ thin films using acetone

The precursor solution was prepared by dissolving 0.147 g (0.005 M) BiI_3 and 0.033 g (0.0025 M) CsI in acetone. The solution was stirred for 2 hours for better dissolution of the salts. For the deposition of thin films, the precursor solution was sprayed using an ultrasonic nozzle (0.07 A) and compressed air at 1 ml/min onto the cleaned glass substrates kept at 200 ℃ for 120 times over an area of 150×100 mm^2.

Table 2-5. The spray parameters for $Cs_3Bi_2I_9$ thin film deposition using acetone solvent.

Substrate temperature	200 ℃	Number of depositions	120
Spray rate	1 ml/min	Duration of deposition	120 minutes
Nozzle current	0.07 A	Air pressure	0.1 MPa
Solvent	Acetone	Precursor concentration (CsI/BiI_3)	2.5/5 mM

2.4.6. Bismuth sulfide thin film

The precursor solution was prepared by dissolving 0.0788 g of bismuth chloride ($BiCl_3$, Aldrich) and 0.150 g of thioacetamide (CH_3CSNH_2, Aldrich) in 50 ml acetone. The solution is ultrasonically sprayed at a spray rate of 1 ml/min onto the glass substrate maintained at 200 ℃. The spray deposition was continued ten times over the same area to obtain uniform films. All other parameters were the same as in other depositions described in **Table 2-5**. The study on the various properties of Bi_2S_3 thin films is discussed in detail in section 7.2.

2.4.7. $Cs_3Bi_2I_9$:Bi_2S_3 composite thin films

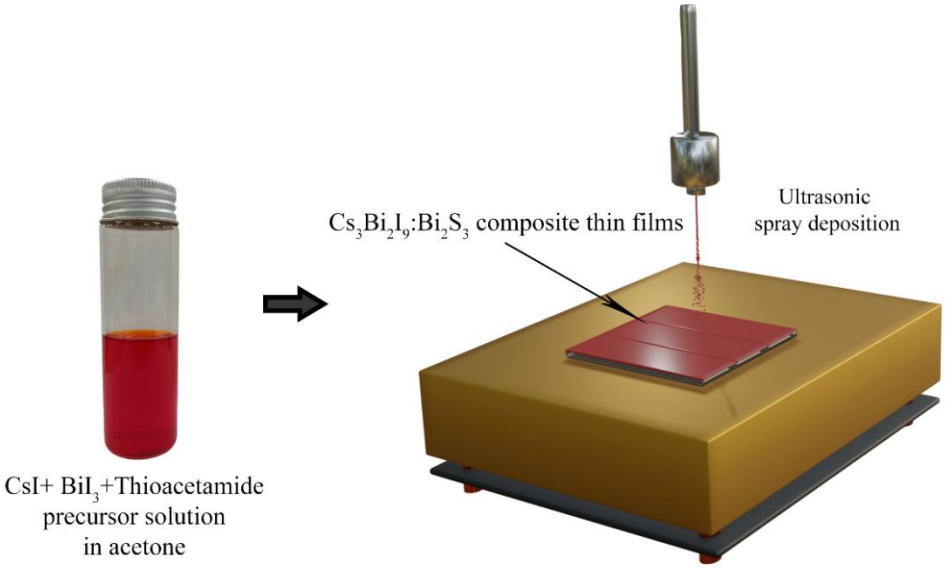

Figure 2.9. The ultrasonic spray deposition of $Cs_3Bi_2I_9$:Bi_2S_3 thin films.

The precursor solution was prepared by dissolving 0.13 g of cesium iodide and 0.59 g of BiI_3 into 200 ml acetone and stirring for 1 hour. Further, thioacetamide (CH_3CSNH_2, Aldrich) was added to this solution to study the effects of sulfur incorporation. The thioacetamide concentration in the precursor solution varied from 0.005, 0.01, 0.03 and 0.05 M. The deposition was carried out at 200 ℃ at a spray rate of 1 ml/min. The spray deposition was repeated 120 times over the same area to get sufficient thickness for the thin films as illustrated in **Figure 2.9**. The thin film samples with different thioacetamide

concentrations are labeled as given in **Table 2-6** and the results are discussed in section 7.3.

Table 2-6. Sample names with thioacetamide concentration.

Thioacetamide concentration	0	0.005 M	0.01 M	0.03 M	0.05 M
Sample name	pCBI	TA05	TA1	TA3	TA5

2.4.8. Post-deposition thermal treatments

Rapid Thermal Processing

Rapid thermal processing of the BiI_3 films at high temperatures (300, 400 and 500 ℃ for 20 s) were performed using the RTP system (***Ecopia RTP-1300***) displayed in Figure 2.10a in a vacuum of 8 - 12 mTorr.

Conventional low vacuum annealing

A ***VBF-1200X, MTI corporation*** furnace, shown in Figure 2.10b, which can maintain a low vacuum in the order of ~10^{-2} torr was used for the thermal treatments.

Figure 2.10. (a) The rapid thermal processing system and (b) the conventional low vacuum annealing oven.

2.5. Characterization techniques and analysis methods

2.5.1. X-ray diffraction (XRD)

X-ray diffraction analysis is a crystallographic technique used to determine the crystallinity and the atomic/molecular structure of materials. The specific atomic arrangements in

crystalline materials will diffract an incoming monochromatic X-ray in different directions which is assessed to picture the electron densities and thereby mean positions of the atoms in the crystal.

Figure 2.11. PANalytical EMPYREAN diffractometer for X-ray diffraction studies.

Here, we employed a ***PANalytical EMPYREAN diffractometer***, shown in Figure 2.11, equipped with Cu K_α radiation (λ=1.5406 Å) for the X-ray diffraction measurements. The measurements were carried out in atmospheric conditions mostly in the 2θ range of 5 – 60°. The current and voltage at which the X-ray source worked was 40 V and 40 mA respectively.

The average crystallite size (D) can be determined from the diffraction data using the Scherrer equation (2.3) [188],

$$D = \frac{K\lambda}{\beta Cos\theta} \qquad (2.3)$$

Where K is the crystallite-shape factor (~0.9 for spherical), λ is the wavelength of Cu K_α radiation (1.5406 Å), β is the full width at half maximum of diffraction peaks in radians and θ is the Bragg angle.

Accurate calculations of crystallite size and stress were made from the Williamson-Hall (W-H) plot using the equation (2.4) [189],

$$\beta Cos\theta = 4\varepsilon\, Sin\theta + \frac{K\lambda}{L} \qquad (2.4)$$

The texture coefficient indicates the preferential orientation of crystallite growth in the thin film which can be calculated using equation (2.5),

$$TC_{hkl} = \frac{I(hkl)/I_0(hkl)}{\sum_{n=0}^{N} I_i(hkl)/I_0(hkl)} \qquad (2.5)$$

Where $I(hkl)$ is the intensity of the peak, $I_0(hkl)$ is the intensity of the corresponding peak in the JCPDS file and N is the number of peaks.

The lattice parameters for the hexagonal structure can be estimated using the equation (2.6) [190].

$$\frac{4}{3}\left(\frac{h^2 + hk + k^2}{a^2}\right) + \frac{l^2}{c^2} = \frac{1}{d_{hkl}^2} \qquad (2.6)$$

Where d_{hkl} is the interplanar distance of the (hkl) planes.

2.5.2. Raman spectroscopy

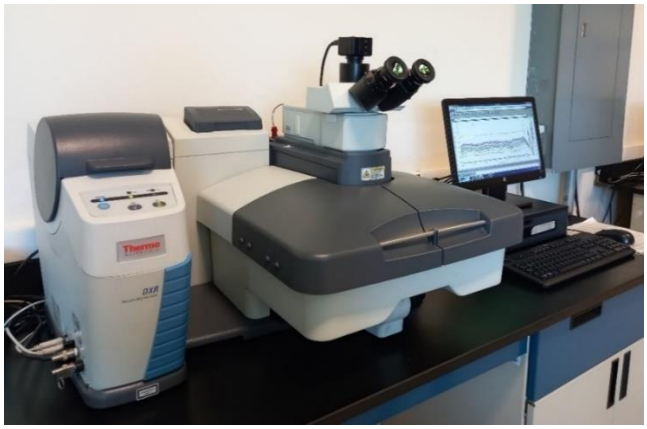

Figure 2.12. The Thermo scientific DXR Raman microscope.

The Raman spectroscopy relies on the inelastic interactions of photons with molecular bonds which helps in determining the chemical structure, molecular interactions, and crystallinity of the materials. Primarily, it probes the various vibrational modes in a

material though other low frequency modes such as rotational and non-bonding interactions may also be noted.

The Raman spectra of the samples were measured using ***Thermo Scientific DXR Raman microscope*** in **Figure 2.12** with a 532 nm excitation laser as the monochromatic light source. The equipment has a spatial resolution of 540 nm and a confocal depth resolution as fine as 1.7 μm. A single exposure captures the spectrum in the range 50-3500 cm^{-1}. Figure 2.13 shows the typical Raman spectrum of glass substrate and c-Si wafer which is used in our studies to compare and distinguish the Raman peaks of our materials of interest.

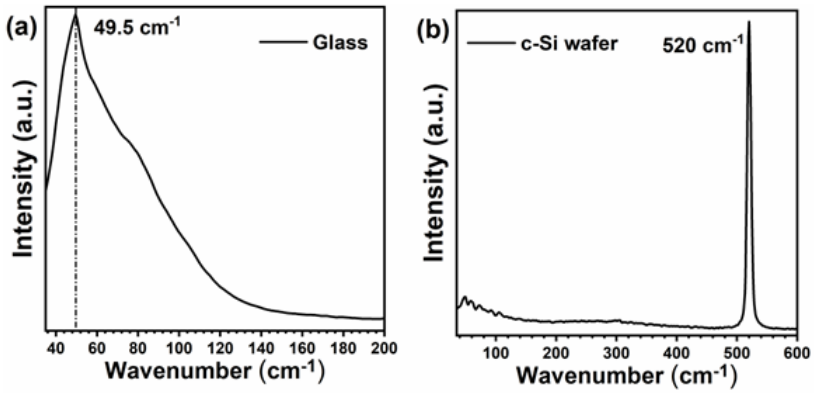

Figure 2.13. Raman spectrum of (a) glass substrate and (b) c-Si wafer.

2.5.3. Scanning electron microscopy (SEM)

Figure 2.14. The HITACHI SU8020 scanning electron microscope.

Scanning electron microscopy uses high energy electrons to scan the surface of materials to probe their morphology. Here, we employed a ***SEM-Hitachi SU8020*** (Figure 2.14) for analyzing the surface morphology of the spray deposited thin films such as their uniformity or coverage as well as the size and shape of the grains. The cross-sectional SEM images provided the nature of vertical growth and thickness of the films.

The acceleration voltage used was between 1 - 3 kV with current 1- 10 μA in the secondary electron (SE) mode.

2.5.4. X-ray photoelectron spectroscopy (XPS)

The photoelectrons emitted by various elements after absorbing X-rays of sufficient energy hold information about the binding energy of core-level electrons in the element which reveals information about the chemical environment and bond structure of the element [191]. In the current investigations, a ***Thermo Scientific K-alpha***, shown in Figure 2.15, was used to obtain X-ray photoelectron spectra of various elements of our interest.

Figure 2.15. The Thermo Scientific K-alpha equipment for X-ray photoelectron spectroscopy.

Thermo Scientific K-alpha can precisely determine the kinetic energy of emitted photoelectrons and correlate it to the binding energy of elements. The thin films were

irradiated with soft Al Kα (=1486.6 eV) X-rays along with a flood gun for charge compensation. Even so, further to the elemental peak positions were calibrated by fixing the adventitious carbon peak at 284.6 eV. The spectra were collected after a soft surface etching of ~1.19 nms^{-1} using 2 keV Ar^{+} ions. The high-resolution peaks were deconvoluted using the Gaussian-Lorentzian sum function while the background was determined by a Shirley type function.

2.5.5. UV-Vis-NIR spectroscopy (UV-Vis-NIR)

The absorption, transmittance, and reflectance spectra of the films were measured using a ***Jasco V770 UV-Visible/NIR spectrophotometer*** displayed in Figure 2.16, with single monochromator design. The UV-Visible range uses a PMT detector while the spectra in NIR region is collected using a Peltier-cooled PbS detector. The equipment can be used to collect absorption and transmittance spectrum in the wavelength range of 200-2500 nm.

Figure 2.16. The Jasco V770 UV-Visible/NIR spectrophotometer.

The optical bandgap can be calculated using the Tauc relation (2.7) given by,

$$B(h\vartheta - E_g)^n = \alpha h\vartheta \qquad (2.7)$$

Where E_g is the optical band gap, h is the planks constant, ϑ is the photon frequency, B is called the band tailing parameter and α is the absorption coefficient. n can have values corresponding to direct allowed $(n = 1/2)$, indirect allowed $(n = 2)$, direct forbidden $(n = 1/3)$ and indirect forbidden $(n = 3)$ transitions.

The absorption coefficient α is estimated from the formula (2.8),

$$\alpha = \frac{1}{t} \times 2.303A \qquad (2.8)$$

Where A is the absorbance and t is the thickness of the thin film.

2.5.6. Electrical measurements

The current-voltage (I-V) characteristics of the thin films and heterojunctions were measured using a ***Keithley 6487 Picoammeter*** controlled by a MATLAB program. Current-time (I-T) measurements under dark and light illumination were done using a 50 W tungsten halogen lamp (Smartlight, 120 V, 60 Hz) or an AM 1.5 illumination (Oriel solar simulator, 100 $mWcm^{-2}$) along with the Keithley 6487 Picoammeter. Furthermore, 405 nm (50 mW) , 532 nm (0 - 100 mW), 785 nm (0 – 100 mW), 840 nm (100 mW), 980 nm (100 mW) and 1064 nm lasers were employed as incident light sources to investigate the photodetection properties of various thin films.

The ideal diode equation can be used to estimate the ideality factor (n) of p-n junction diode which is given by,

$$n = \left(\frac{q}{kT}\right) \times \frac{dV}{dlnI} \qquad (2.9)$$

Where k is the Boltzmann constant (8.617×10^{-5} eVK^{-1}), T is the temperature (300 K) and dV/dlnI is the inverse slope of ln I vs. V curve [192].

Figure of merits of the photodetectors

The **on/off ratio** or **sensitivity (*S*)** is the ratio of photogenerated current (I_{ph}) to the dark current (I_d) in a material and can be calculated by [106],

$$S = \frac{I_{ph}}{I_d} = \frac{I_l - I_d}{I_d} \qquad (2.10)$$

Where I_l is the light current, I_{ph} is the photocurrent ($I_l - I_d$).

The amount of photocurrent generated under an illumination is termed as the **Responsivity** (R) of a photodetector, which can be determined using the relation [193],

$$R = \frac{I_{ph}}{A.P_{\lambda}} \quad (2.11)$$

Where, P_{λ} is the illumination power density and A is the effective area of photodetector.

Detectivity is the extent to which a photodetector can detect the weak signals and therefore is the figure of merit of the photodetector. Detectivity (D) of the photodetector can be calculated from the equation [193],

$$D = \frac{R\sqrt{A}}{\sqrt{2eI_d}} \quad (2.12)$$

Where e is the electronic charge. Therefore, larger the detectivity of a photodetector, higher its detection capability.

Response time: The rise time (τ_{rise}) is the time required for the photocurrent to reach the 90 % of its maximum value from 10 % upon illumination. The decay time (τ_{decay}) is the time in which the photocurrent decay to 10 % from 90 % of its maximum value after the illumination is removed [194].

CHAPTER 3

COMPUTATIONAL DATA ANALYSIS

This chapter explains the computational calculations of bismuth iodide, Cesium bismuth iodide and bismuth sulfide structure using the VASP code available with the MedeA software. The structure is optimized, and the optimized structure is then used for the band structure and density of states calculations.

3.1. Introduction

It is important to have a deeper understanding of the fundamental electronic properties and optical transitions of materials for engineering them into specific device applications in optoelectronics. The density functional theory (DFT) is a quantum-mechanical atomistic simulation method aimed at exploring the wide range of properties related to various atomic systems such as molecules, crystals, interfaces and devices. As one of the most popular first-principles or ab-initio methods, DFT can even predict the properties of unknown systems to design actual experiments.

3.2. Computational calculations

3.2.1. Bismuth iodide (BiI_3): R-3H

The BiI_3 unit cell containing 6 formula units obtained after the geometry optimization by VASP is shown in Figure 3.1**.** It has an R-3H symmetry with 6 Bi atoms at the 6c Wyckoff positions and 18 I atoms filling the 18f Wyckoff positions. The layers of highly ionic Bi-I bonds in the bulk BiI_3 structure are stacked in ABC order with weak van der Waals interactions between them.

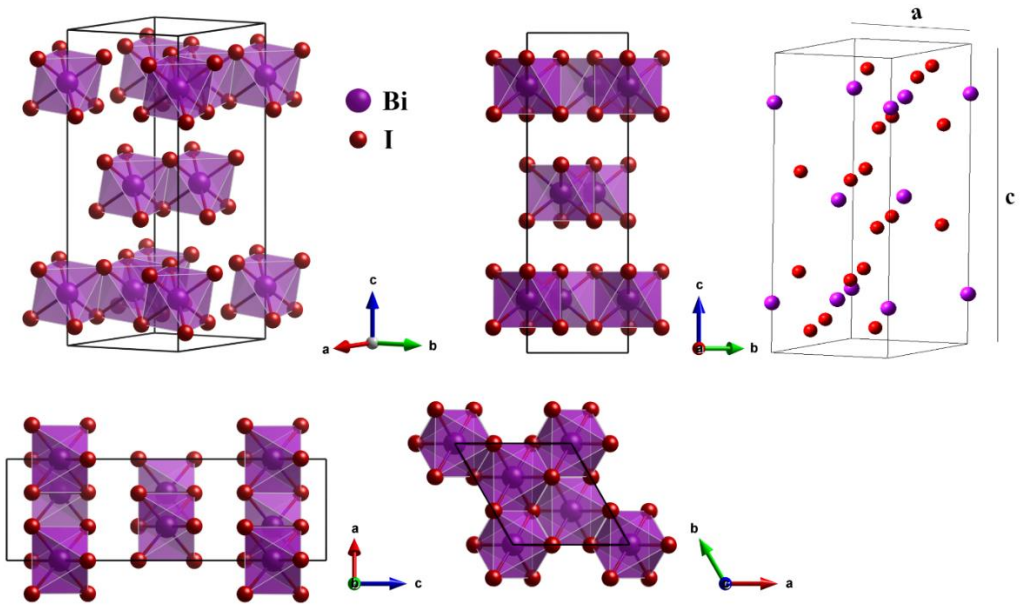

Figure 3.1. The optimized structure of BiI_3 hexagonal unit cell.

Following $(BiI_3)_2$ structure optimizations, the energy was reduced by -0.019026 eV. The unit cell $(BiI_3)_6$ has a final energy of -68.011136 eV and a density of 5.819 gcm^{-3}. Further parameters related to the optimized cell are given in Table 3-1.

Table 3-1. The unit cell parameters realized from the structure optimization of BiI_3.

Parameter	Original (Å)	Change (Å)	Final (Å)	Change (%)
a	7.516	0.007913	7.523913	0.1
b	7.516	0.007913	7.523913	0.1
c	20.718	-0.122948	20.595052	-0.6
α	90	0	90	0
β	90	0	90	0
γ	120	0	120	0
Volume	1013.565929	-3.892215	1009.673714	-0.4

Figure 3.2 (i) & (ii) elucidates the electronic band structure for high symmetry directions in the Brillouin zone for the BiI_3 revealing the spin-orbit coupling (SOC) effects. It is seen from the calculations that the spin-orbit coupling substantially lowers the conduction band minimum, a characteristic of heavy atoms like Bi and I. Without SOC effects, the

calculations have resulted in a large indirect bandgap of 2.387 eV with valence band maximum near (0.20, 0.20, 0.20) at -0.053 eV and conduction band minimum near (0.40, 0.40, 0.40) at 2.334 eV with respect to the Fermi level. On the other hand, the presence of SOC effects for optical band gap calculation revealed a shorter indirect transition of 1.439 eV between the VBM (0.33,0.33,0.33) and CBM (0,0,0) near the Γ- point, in the ZΓ- direction.

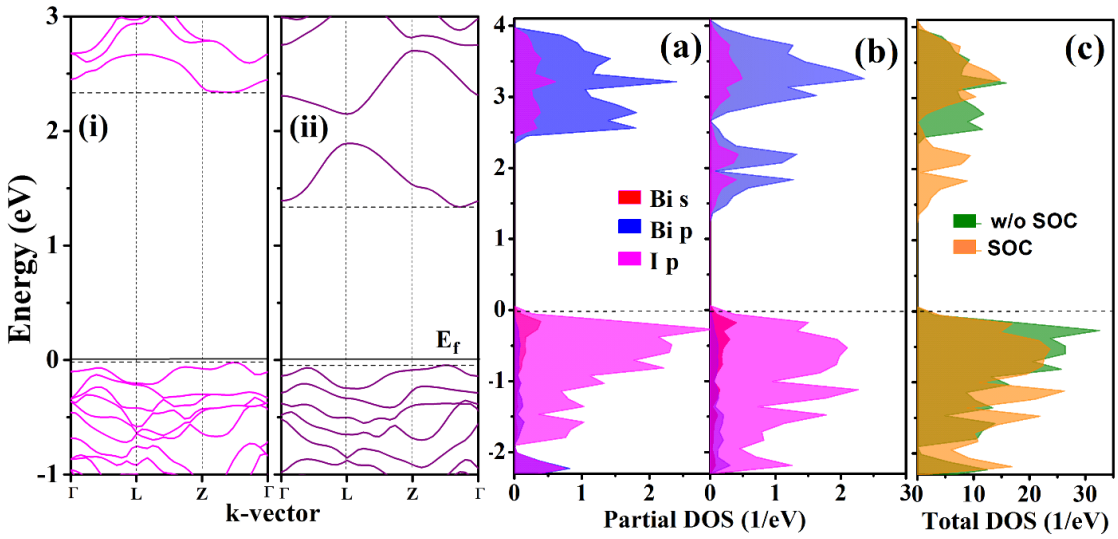

Figure 3.2. The electronic band structure of BiI_3 along the high symmetry directions in the first Brillouin zone (i) without SOC and (ii) with SOC. Related partial density of states (a) without SOC and (b) with SOC as well as their (c) total density of states.

Low band dispersion in VB raises the possibility of additional, slightly higher energy direct transitions in addition to the observed indirect transition. The flat VBM and strong band dispersion in CB point to a low effective mass of electrons relative to holes in BiI_3 [118,195,196]. According to the calculations, the electrons may be more responsible for the material's transport properties [197].

Respectively, the partial and total density of states from the single point calculations are displayed in f

Figure **3.2**(a), (b) and (c). A thorough analysis reveals that the conduction band minimum (CBM) is primarily made up of Bi p states (hybridized with I p states), and the valence band maximum (VBM) is composed of I p states (hybridized with Bi s states). As a result,

light-induced excitation from the valence band to the conduction band occurs mainly from the occupied I p with a little Bi s contribution into the vacant Bi p + I p states [198]. Strong absorption may result from the conduction band minimum's high density of p orbital states. [72] Significantly, two additional broad peaks have emerged in the CB due to the spin-orbit splitting, the first one at ~2.18 eV above E_F with a width of ~0.70 eV and the latter at ~1.83 eV with ~0.60 eV width, predominantly composed of Bi p states in hybridization with I p. We can see from our DFT calculations that the strong spin-orbit coupling due to the heavy elements, Bi and I, is the cause of the low bandgap observed in BiI_3.

3.2.2. Cesium bismuth halides: $Cs_3Bi_2X_9$ (X=I/Br/Cl): $P6_3/mmc$

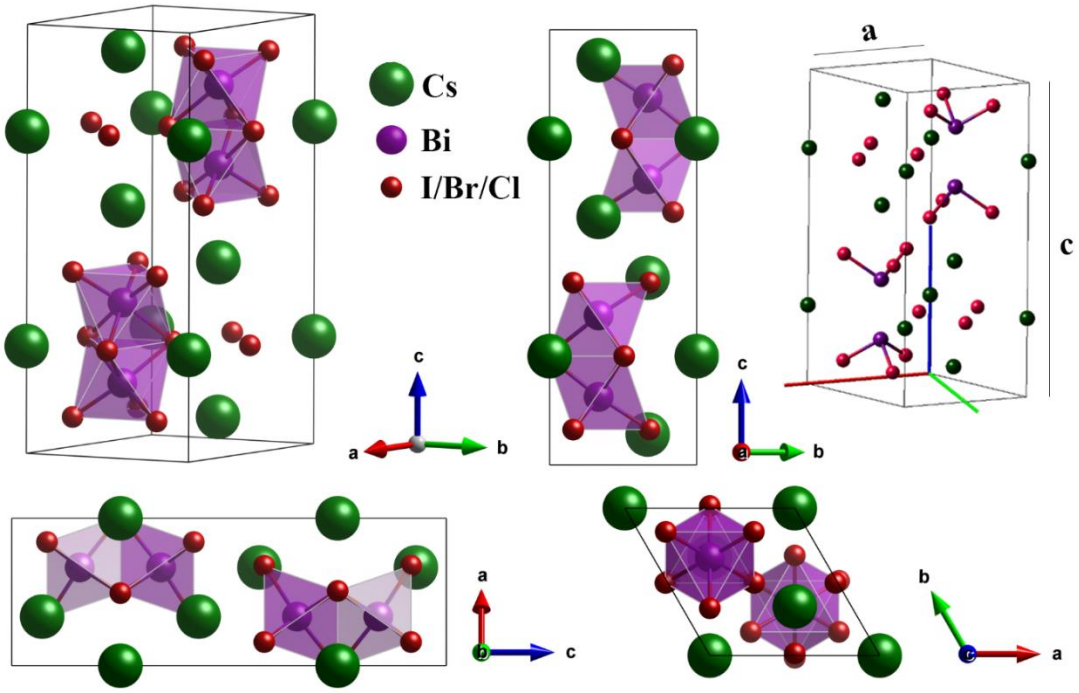

Figure 3.3. The unit cell of $Cs_3Bi_2X_9$ ($P6_3/mmc$) containing 2 formula units after structure optimization by MedeA-VASP.

The PBEsol exchange-correlation functional with a plane wave cutoff energy of 500 eV was used for the structure optimization. The convergence values for forces and energy were set at 0.01 1/Å and 10^{-6} eV, respectively. The 7×7×3 k-mesh was used in the structure optimizations. **Figure 3.3** shows the VASP-optimized structures of cesium bismuth halides and the optimized parameters are listed in **Table 3-2**.

Table 3-2. Structural parameters of hexagonal $Cs_3Bi_2I_9$, $Cs_3Bi_2Br_9$ and $Cs_3Bi_2Cl_9$ obtained through VASP calculations in MedeA.

Unit cell parameters	$Cs_3Bi_2I_9$	$Cs_3Bi_2Br_9$	$Cs_3Bi_2Cl_9$
a (=b) (Å)	8.325	7.796	7.452
c (Å)	21.288	19.987	19.294
α (= β)	90º	90º	90º
γ	120º	120º	120º
Volume ($Å^3$)	1277.77	1052.22	927.99
Density (gcm^{-3})	5.091	4.847	4.065
Energy (eV)	-40.62	-45.575	-50.09

3.2.3. Double perovskites Cs_2AgBiX_6 (X=I/Br/Cl) : *Fm-3m*

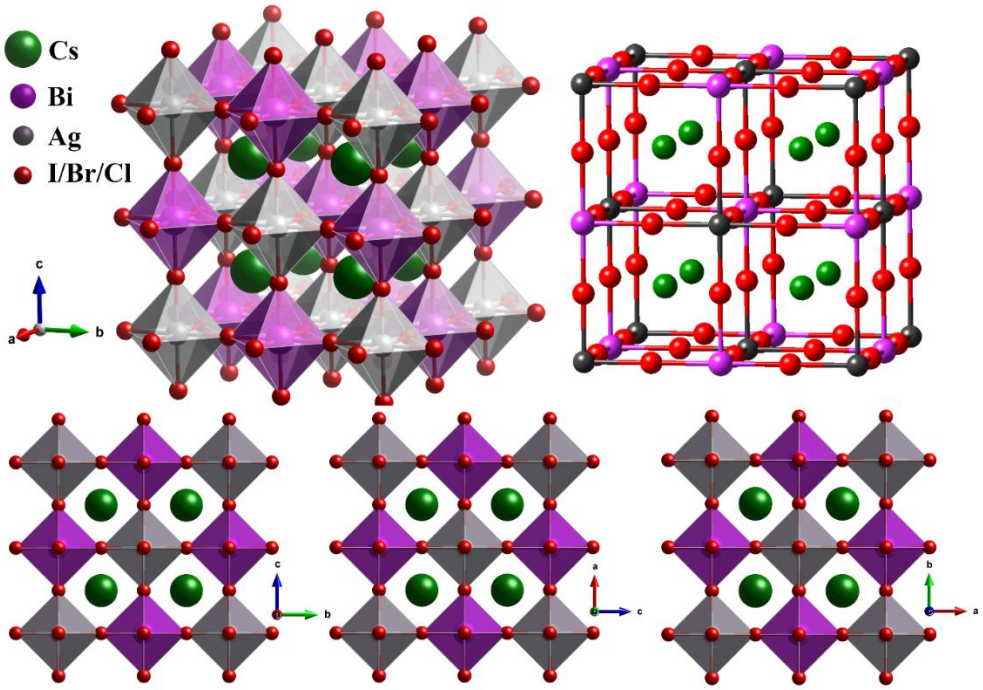

Figure 3.4. Unit cell of the double perovskite Cs_2AgBiX_6 (X=I/Br/Cl).

Two unit cells of 3-D cubic $CsPbI_3$ can be modified to form Ag and Bi substituted Cs_2AgBiX_6 double perovskites with 3-D cubic structure (*Fm-3m*, space group: 225) as displayed in Figure 3.4. The VASP calculations for structure optimization were performed with the GGA-PBEsol exchange-correlation functional and plane wave cutoff energy of

500 eV to ensure that the residual forces converged below 0.01 eV/Å. Electronic iterations convergence was 10^{-6} eV and k-mesh was 7×7×7. The Wyckoff positions of Cs, Ag, Bi and I are 8c, 4a, 4b and 24e, respectively.

Table 3-3. Structural details and the band gap obtained from the structure optimization of Cs_2AgBiX_6 (X=I/Br/Cl) double perovskites.

Unit cell parameters	Cs_2AgBiI_6	$Cs_2AgBiBr_6$	$Cs_2AgBiCl_6$
a (=b=c) (Å)	11.9287	11.1827	10.680
α (= β =γ)	90	90	90
Volume ($Å^3$)	1697.416	1398.44	1218.212
Density (gcm^{-3})	5.260	5.045	4.337
Energy (eV)	-28.549	-31.841	-34.913
Band Gap (eV) indirect	0.756	1.223	1.713

The structural parameters of the optimized structure and an initial band gap prediction based on the calculations are given in Table 3-3.

3.2.4. Chalcohalides $CsBiSX_2$ (X=I/Br/Cl): *P4/mmm*

The large band gap and 0-D structure of hexagonal $Cs_3Bi_2I_9$ may be limiting their application in solar cells as an absorber material. To preserve the 3-D network of metal halide frameworks while replacing Pb with Bi, an anion-splitting approach is proposed. If S^{2-} is used to replace one I^- ion in the structure, a 3-D $CsBiSI_2$ may be formed. For that, we modified a cubic $CsPbI_3$ structure by replacing Pb with Bi and I at the 1b positions to obtain the $CsBiSI_2$ structure as in **Figure 3.5**. The parameters calculated after the structural optimization are presented in **Table 3-4** which shows the effect of halide atoms on the various structural parameters.

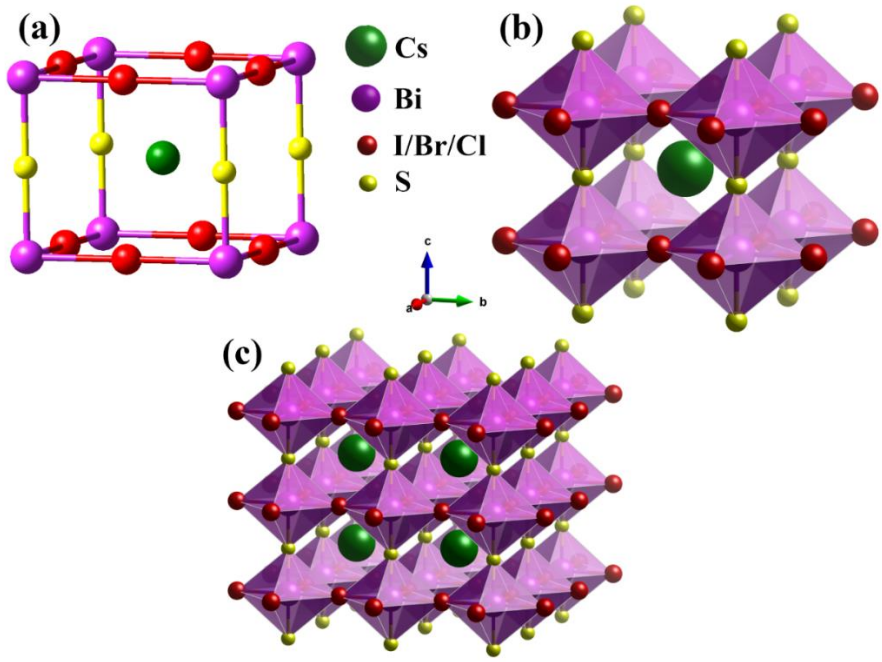

Figure 3.5. (a) & (b) Unit cell and (c) 2×2×2 super cell of tetragonal $CsBiSX_2$ (X=I/Br/Cl).

Table 3-4. Structural details and the band gap obtained from the structure optimization of $CsBiSX_2$ (X=I/Br/Cl).

Unit cell parameters	$CsBiSI_2$	$CsBiSBr_2$	$CsBiSCl_2$
a (=b) (Å)	6.2125	5.798	5.5108
c	5.2738	5.283	5.2989
α (= β =γ)	90	90	90
Volume ($Å^3$)	203.55	177.64	160.929
Density (gcm^{-3})	5.121	4.989	4.590
Energy (eV)	-16.637	-17.873	-18.973
Band Gap (eV)	metal	metal	metal

3.2.5. Cesium bismuth iodide $Cs_3Bi_2I_9$: *$P6_3/mmc$*

Electronic band structure and density of states

The VASP structure optimization yields the relaxed $Cs_3Bi_2I_9$ structure which is shown in Figure 3.7a. The $(Bi_2I_9)^{3-}$ bioctahedra exist in the hexagonal unit cell of $Cs_3Bi_2I_9$ (space

group: *P6₃/mmc*) as distinct anionic units stabilized by the Cs cations, giving rise to its 0D structure. The optimization resulted in the lattice parameters a=b=8.325 Å and c=21.288 Å as well as α=β= 90° and γ=120°. The calculated cell volume and density are respectively 1277.77 $Å^3$ and 5.091 gcm^{-3}.

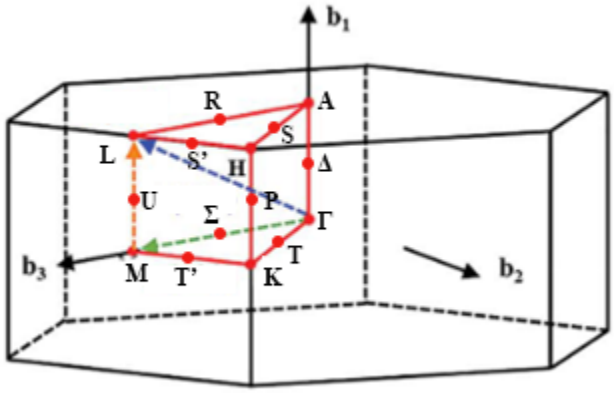

Figure 3.6. The first Brillouin zone of hexagonal structure with high symmetry points and principal directions.

In the hexagonal unit cell with two $Cs_3Bi_2I_9$ formula units, the Cs atoms are located in the 4f and 2b Wyckoff positions. Bi occupies 4f and I inhabit 12k as well as 6h Wyckoff positions resulting in two different bonds of 2.954 Å and 3.196 Å. The high symmetry points and directions in the first Brillouin zone of $Cs_3Bi_2I_9$ are illustrated in **Figure 3.6**. As shown in Figure 3.7b, the band structure calculations revealed a band gap of 1.99 eV, which is consistent with the reported experimental and computational data for the $Cs_3Bi_2I_9$ hexagonal structure [92,96–98]. The fundamental absorption results from the indirect transition, which is explained by the valence band maximum close to the K-point and the conduction band minimum at the Γ -point in the Brillouin zone. Additionally, the lowest observed direct transition with momentum conservation is 2.16 eV along the Γ-point.

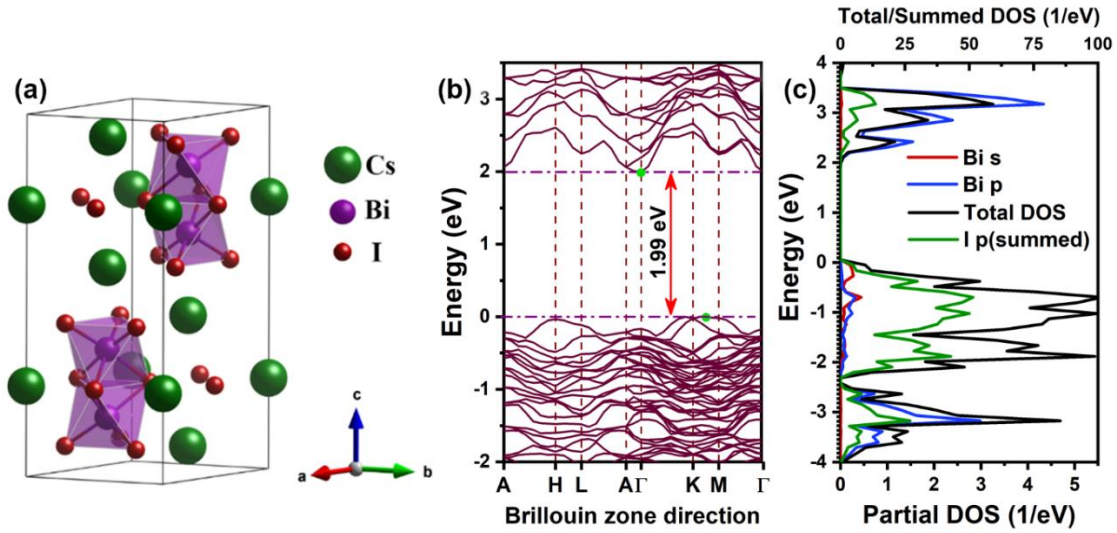

Figure 3.7. (a) The hexagonal unit cell of $Cs_3Bi_2I_9$ following MedeA-VASP structure optimization. (b) Band dispersion in the first Brillouin zone along the high symmetry directions. (c) The respective partial and total density of states.

Previously, the DFT calculation with GGA-PBE functional without including SOC produced an indirect band gap that was overestimated up to 2.24 eV [113]. Using the hybrid functional HSE06 with SOC effects, Lehner et al. and Hong et al. respectively calculated indirect band gaps of 2.32 and 2.12 eV [98,199]. **Figure 3.7**c displays the calculated density of states of the structure. In this case, the individual contributions that I made at two different Wyckoff positions were added up to define the curves. The partial density of states reveal the contributions of I p and Bi s orbitals to the valence band maximum as well as Bi p and I p orbitals to the conduction band minimum [200].

3.3. Conclusions

The structure optimization and electronic band structure calculations suggest that the manipulation of B cation and halogen-anion can tune the band gap of the Cs-Bi-X perovskites. The band structure reveals the possibility of closer energy direct transitions between the VB and CB in $Cs_3Bi_2I_9$, while the density of states shows the influence of absorption properties on the Bi and halide orbitals to the band edges. This gives us more insights into engineering these materials to tune them for specific property enhancements. It is observed that the lattice lengths have increased with larger anions and shifts the band

gap to lower energies. The S substitution may be possible in Cs-Bi-I compounds to maintain the 3-D structure of high-performing Pb-based perovskites. The S 3p states can contribute to the valence band maximum to reduce the band gap as compared to the large band gap of $Cs_3Bi_2I_9$. However, their thermodynamic stability is a major factor in realizing the compound which requires much more investigation and understanding. The computational data on BiI_3 and $Cs_3Bi_2I_9$ aided in understanding the important properties observed in the spray-deposited thin films. Initially, the setting up of the new ultrasonic spray deposition equipment is carried out by optimizing the deposition of BiI_3 thin films to yield films with better coverage and uniformity.

CHAPTER 4

ULTRASONIC SPRAY DEPOSITION OF BISMUTH IODIDE THIN FILMS

Bismuth iodide thin films are fabricated by ultrasonic spray deposition using ethanol solvent. Besides, a study on the influence of substrate temperature on the properties of BiI_3 thin films is presented.

4.1. Introduction

This chapter describes the properties of BiI_3 thin films from laboratory-synthesized BiI_3 powder by the ultrasonic spray deposition to help us in optimizing the equipment settings and understanding its relationship to the quality of metal halide films which usually crystallize at low temperatures. Later, we investigate the effects of substrate temperature on the properties of BiI_3 films which is one of the most influential parameters in spray deposition. The structure, morphology, composition, absorption and photoresponse of these binary thin films are studied in detail. The film possessed dendritic-like morphology with an indirect bandgap of 1.42 eV. Moreover, it displays a very good response to the illumination from white light and LEDs with a sensitivity of up to 4890 %.

4.2. Bismuth iodide powder

4.2.1. Structure

X-ray diffraction (XRD)

Figure 4.1 displays the X-ray diffraction (XRD) pattern for the synthesized BiI_3 powder. The diffraction peaks closely match the BiI_3 data in JCPDS file 48-1795. Nonetheless, two weakly intense peaks at 29.64 and 31.64° correspond to the (102) and (110) planes of the

tetragonal BiOI phase (10-0445). Here, the rhombohedral structure of the polycrystalline BiI_3 has the space group R-3, which usually represents the R-centered hexagonal unit cell. The intense and sharp (113) peak located at 26.97° indicates the preferred orientation of crystallite growth in synthesized powder. Other significant peaks noted at 12.79, 35.25 and 41.57°, are from (003), (111) and (300) planes respectively.

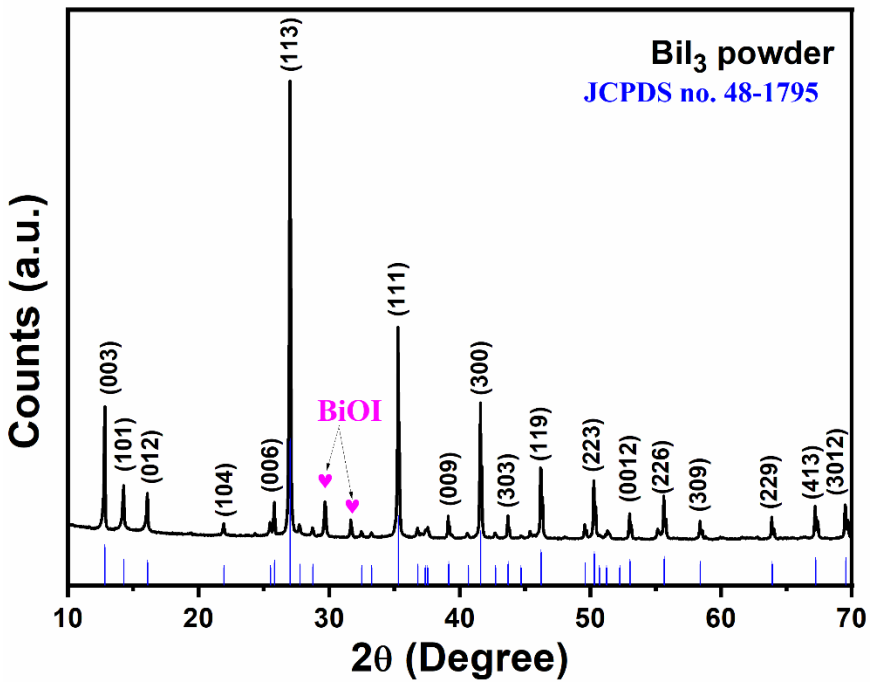

Figure 4.1. The XRD pattern of BiI_3 powder synthesized in laboratory. The heart shape represents the peaks of BiOI phase in the powder.

4.2.2. Chemical states

X-ray photoelectron spectroscopy (XPS)

The BiI_3 powder was dissolved in acetone and then drop-cast on a glass slide for XPS measurements. The surface survey spectrum in Figure 4.2 distinguishes the presence of Bi, I, O and C and verifies the absence of K, nitrates, or any other type of impurities.

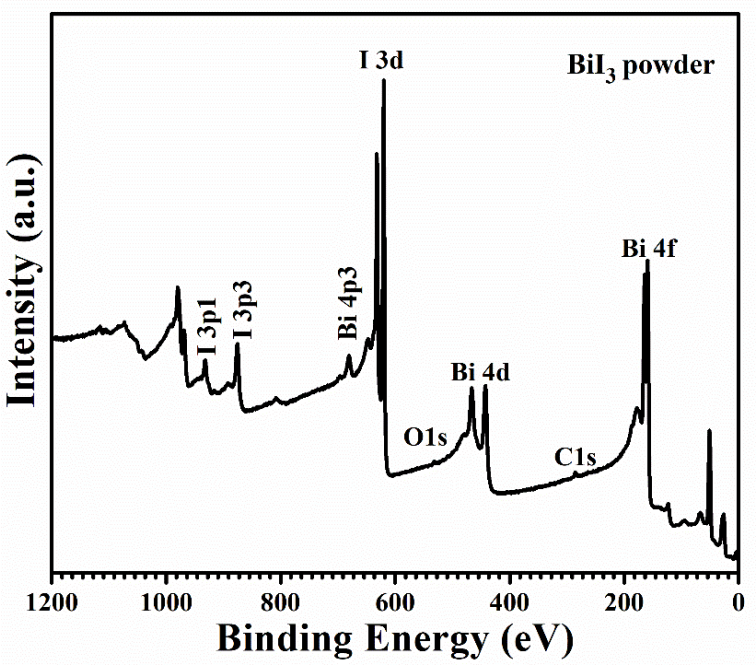

Figure 4.2. Survey spectrum obtained from the surface of BiI_3 powder drop-cast on a glass substrate.

Figure 4.3 displays the high-resolution core-level spectra of Bi and I in BiI_3 powder. Bismuth 4f scan shows two peaks at 159.06 and 164.37 eV with a spin-orbit splitting of 5.31 eV which correspond to $4f_{7/2}$ and $4f_{5/2}$ levels in agreement with Bi^{3+} state in BiI_3 [201]. The I $3d_{5/2}$ and I $3d_{3/2}$ at the binding energies of 619.36 eV and 630.85 eV with energy splitting of 11.49 eV are associated with the I^{2-} state in BiI_3 [201]. The O 1s peak is deconvoluted to identify peaks located at 530.28, 531.86 and 533.03 eV. The peak at 533.03 eV is due to the glass substrate whereas the peak at 531.86 eV may signify the presence of C-O, C-O-O or O-H on the surface. Further, the peak at 530.28 eV corresponds to the Bi-O in bismuth oxyiodide [201,202]. Thus, the XRD and XPS results together conclude the BiI_3 phase in the powder synthesized in the laboratory along with little oxide impurities.

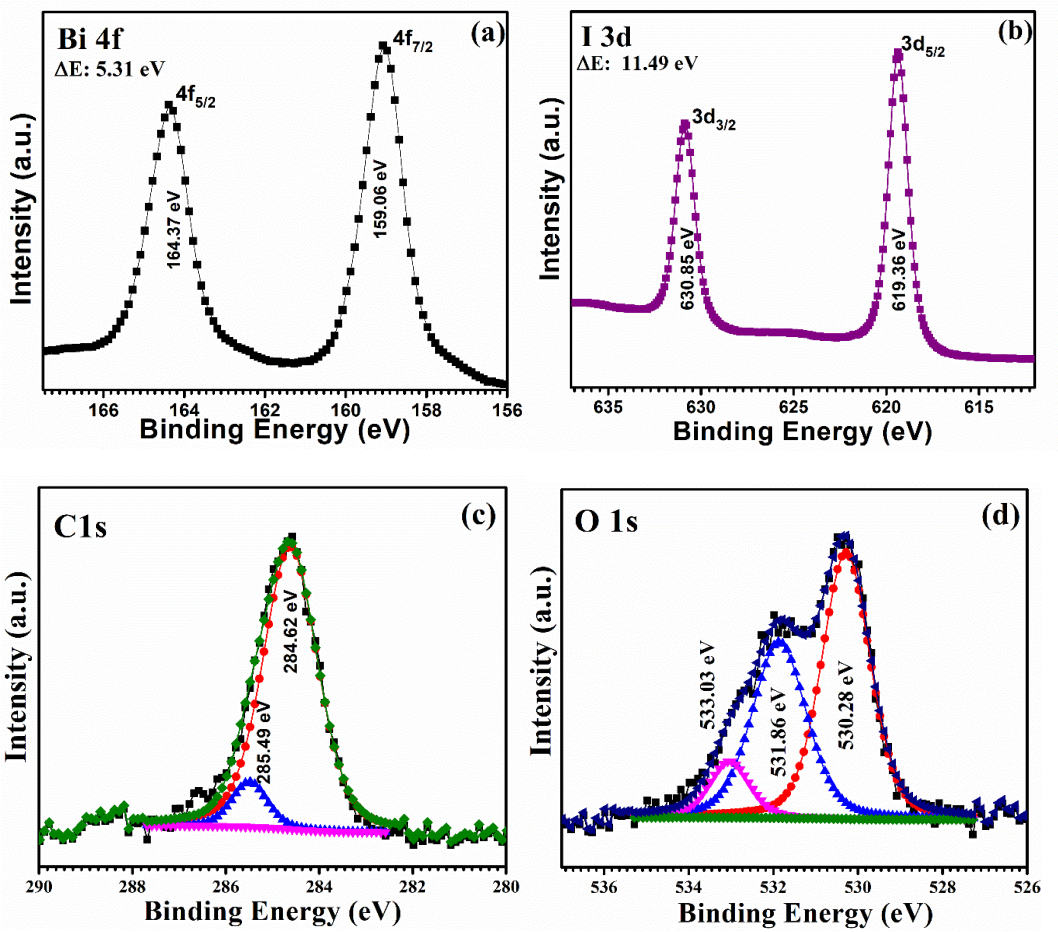

Figure 4.3. The high-resolution core-level spectra of (a) Bi 4f and (b) I 3d (c) C 1s and (d) O 1s.

4.3. Ultrasonic spray deposition of BiI_3 thin film

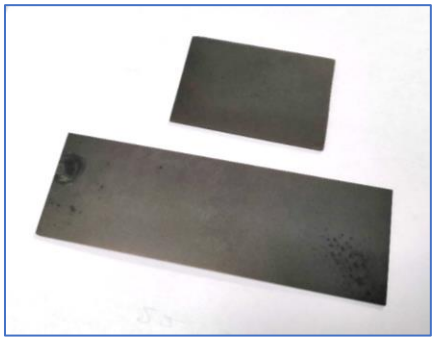

Figure 4.4. BiI_3 thin film as-deposited by ultrasonic spray deposition on glass substrates.

Initially, ethanol was used as a solvent for BiI_3 precursor solution as it has a low boiling point of 78 ℃ and an extremely low concentration solution was sufficient for the thin film deposition in ultrasonic spray. The spray-deposited BiI_3 thin films are displayed in **Figure 4.4**. However, ethanol can't be used to prepare precursor solutions of higher concentrations due to limitations of the dissolution of CsI and BiI_3.

4.3.1. Structure

X-ray diffraction (XRD)

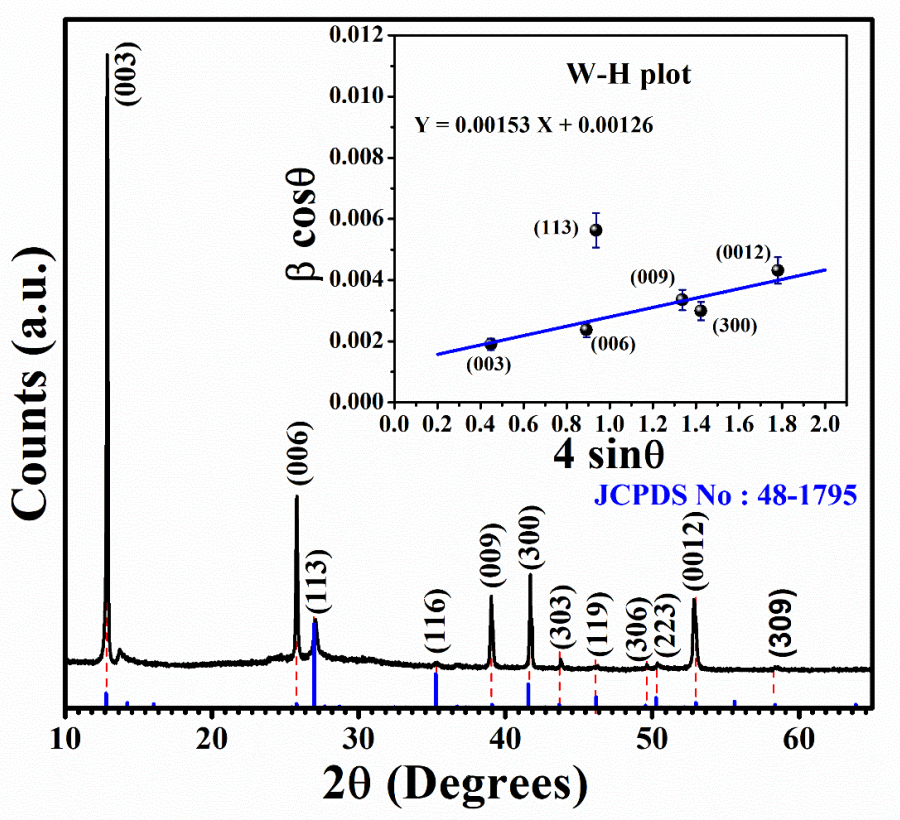

Figure 4.5. XRD pattern of the spray-deposited BiI_3 thin film. (inset) Williamson-Hall plot.

With the proper indexing, Figure 4.5 shows the X-ray diffraction patterns of BiI_3 thin film. The peaks in the diffraction patterns closely match with the JCPDS card 48-1795 of R-3 rhombohedral BiI_3 in the trigonal crystal system. The preferential orientation in the polycrystalline thin film, in contrast to the bulk BiI_3, is in the (003) direction. The other significant peaks noted correspond to (006), (113), (009), (300) and (0012) planes along with weak peaks from (116), (303), (119), (306), (223) and (309) planes [203,204]. Despite

the presence of BiOI impurity peaks in the precursor powder of the synthesized BiI_3, phase-pure BiI_3 thin film is revealed by the diffraction patterns. The BiOI phase present in the BiI_3 precursor powder has been effectively suppressed by the rapid nucleation followed by recrystallization of BiI_3 at a relatively high temperature (150 °C) during the deposition process.

The average crystallite size (D) was determined using the Scherrer equation (2.3) [188]. Additionally, accurate calculations of crystallite size and stress were made from the Williamson-Hall (W-H) plot using the equation (2.4) [189]. The broad (113) peak leads to a small R-square value (0.522) of the linear fit in the W-H plot, as seen in the inset of Figure 4.5, from which the crystallite size was calculated to be 110 nm as opposed to the 46 nm obtained from the Scherrer equation. This noticeable difference in average crystallite size values points to the presence of structural strain in BiI_3 thin films. The size of these crystallites, as determined by the W-H plot, may be comparable to the size of the large particles seen in the SEM images.

The texture coefficient indicates the preferential orientation of crystallite growth in the thin film which can be calculated using equation (2.5). The structural characteristics of the spray-coated BiI_3 thin film are given in **Table 4-1**. The Scherrer equation and W-H plot yielded crystallite sizes of 46 and 110 nm, respectively.

Table 4-1. The structural properties from the X-ray diffraction analysis.

Diffracted planes	2θ (°)	FWHM (°)	Texture coefficient (TC_{hkl})	Crystallite size (nm)	Average crystallite size (nm)	Crystallite size (W-H plot) (nm)	Lattice strain ($\times 10^{-3}$)
(003)	12.87	0.1094	0.34	73.06			
(006)	25.78	0.1393	0.33	58.51			
(113)	27.07	0.3315	0.01	24.64	46	110	1.53
(009)	39.05	0.2037	0.18	41.38			
(300)	41.70	0.1831	0.03	46.42			
(0012)	52.88	0.2761	0.12	32.14			
(003)	12.87	0.1094	0.34	73.06			

4.3.2. Morphology

Scanning electron microscopy (SEM)

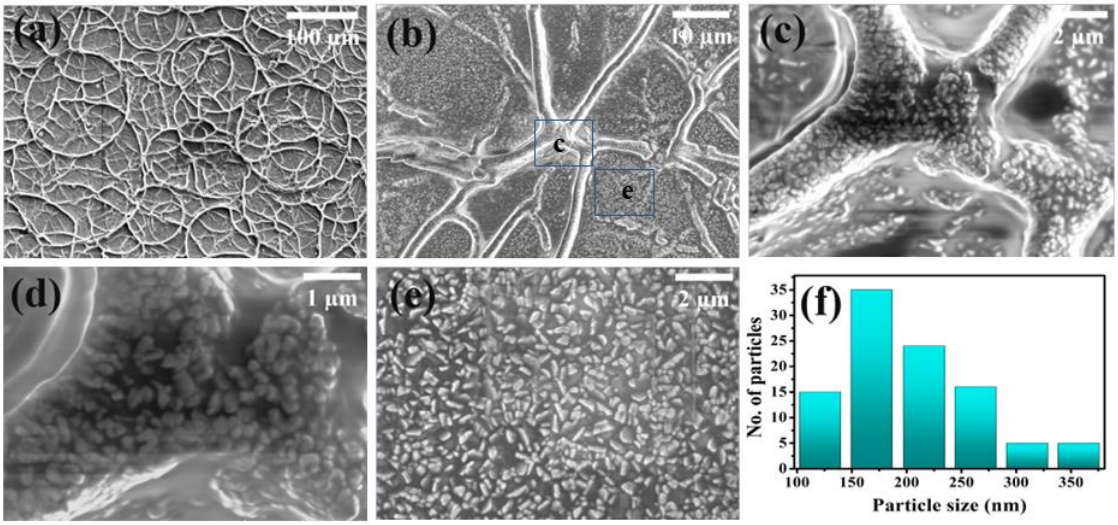

Figure 4.6. (a-e) Morphology of spray-deposited bismuth iodide thin films at different magnifications. (f) A measurement of the particle size distribution for 100 particles..

The scanning electron micrographs of the spray-deposited BiI_3 thin film at various magnifications are shown in Figure 4.6. An extensive branching network formed by the agglomeration of large particles with a dendrite-like appearance is visible in the images. As far as we know, BiI_3 thin films rarely exhibit these kinds of interesting morphologies. The in-situ crystallization at 150 ℃ and agglomeration of crystallites during the deposition might have resulted in such morphology.

4.3.3. Chemical states

X-ray photoelectron spectroscopy (XPS)

Figure 4.7 shows the survey spectra of the BiI_3 thin film with Al K_α radiation at room temperature in the full binding energy scale, highlighting the significant photoemission peaks identified from the sample surface corresponding to Bi, I, C, and O.

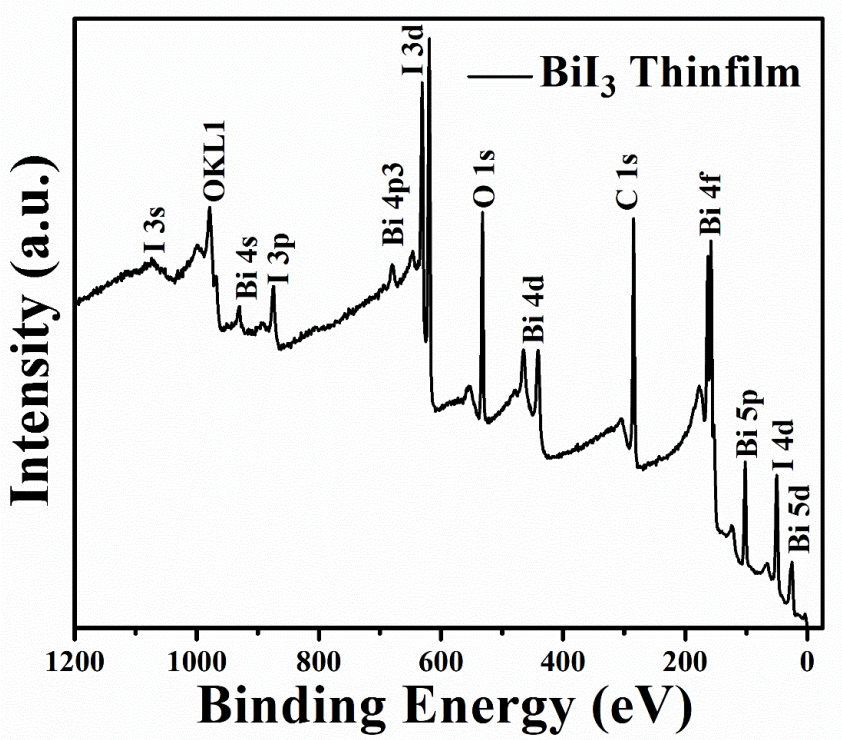

Figure 4.7. The XPS survey spectrum of ultrasonic spray deposited BiI_3 thin film.

High-resolution core-level scans were carried out in the designated energy ranges to examine the pertinent peaks of Bi 4f, I 3d, C 1s, and O 1s. The resulting spectra were then deconvoluted while taking into account the intensity ratios, FWHM, and spin-orbit splitting. The C 1s peak at 284.6 eV was used for the binding energy correction and the O 1s peak at 532.19 eV is from the adsorbed oxygen spiecies. The high-resolution Bi 4f scan in Figure 4.8a shows doublet peaks associated with $4f_{7/2}$ and $4f_{5/2}$ with a spin-orbit splitting of 5.3 eV. Further, the deconvolution of the spectrum reveals three doublet peaks c orresponding to different chemical states of Bi. The peaks at 164 and 158.66 eV indicate the 3+ state of Bi species in BiI_3, whereas the peaks at 162.3 and 157 eV are due to the elemental Bi (Bi^0) induced during the Ar-ion etching [201,205]. Besides, it is reported that long exposure to X-ray radiation can lead to more Bi^0 species in the sample [206]. Further, the peaks at 157.97 and 163.29 eV may be a consequence of ambient exposure forming bismuth oxide. However, the XRD pattern did not show the presence of oxide.

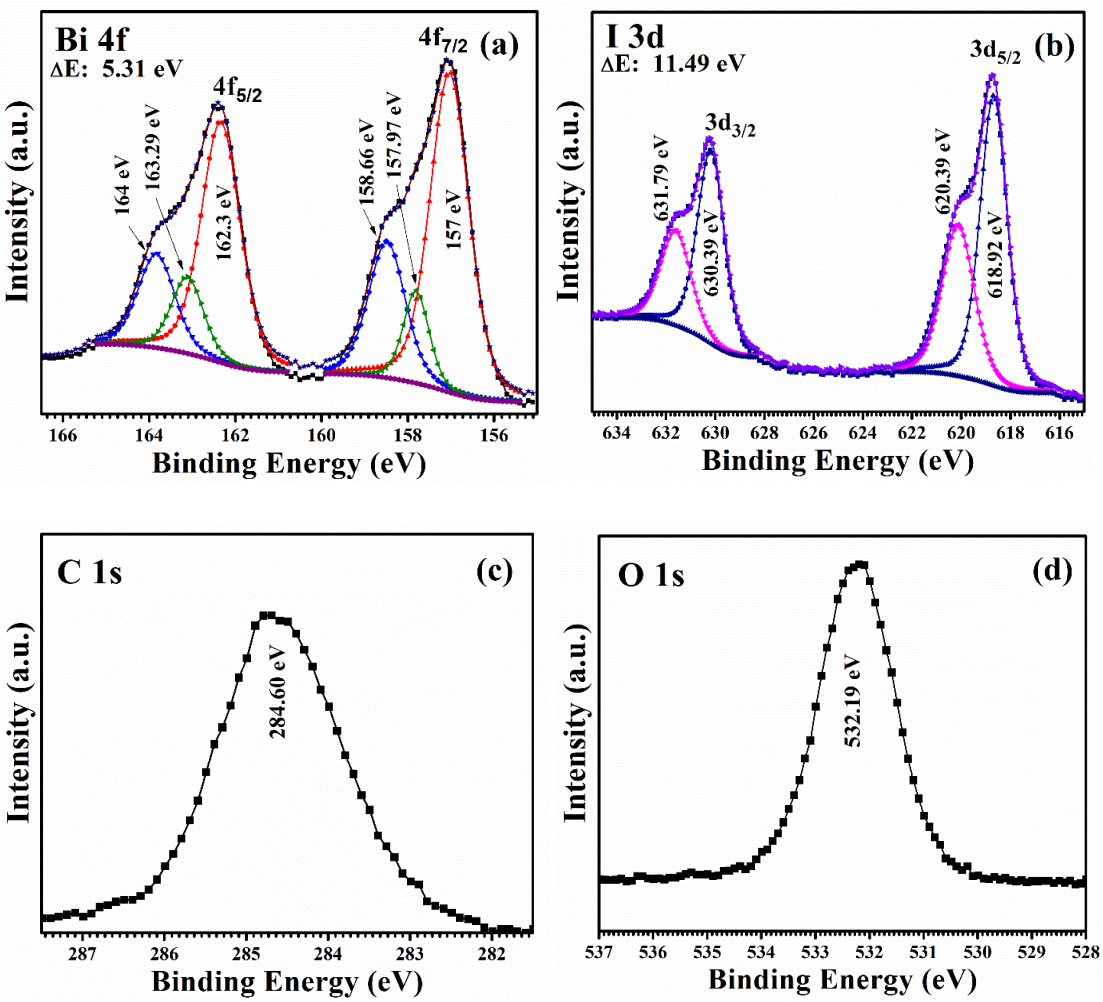

Figure 4.8. High-resolution core-level spectra of (a) Bi 4f, (b) I 3d, (c) C 1s and (d) O 1s states in BiI_3 thin film.

The peaks in Figure 4.8b corresponding to I $3d_{5/2}$ and $3d_{3/2}$ were detected with a spin-orbit separation of 11.49 eV. The peaks at 618.92 and 630.39 eV can be attributed to I^- in BiI_3 thin film [205]. The peaks at 631.79 and 620.39 eV can be ascribed to I in I_2 [201].

4.3.4. Optical properties

UV-Vis-NIR Spectroscopy

The UV-Vis-NIR absorbance spectrum of BiI_3 thin film is shown in Figure 4.9 which exhibits an absorption edge near ~822 nm. The absorption spectrum indicates the strong absorbing characteristics of the spray-deposited BiI_3 thin film.

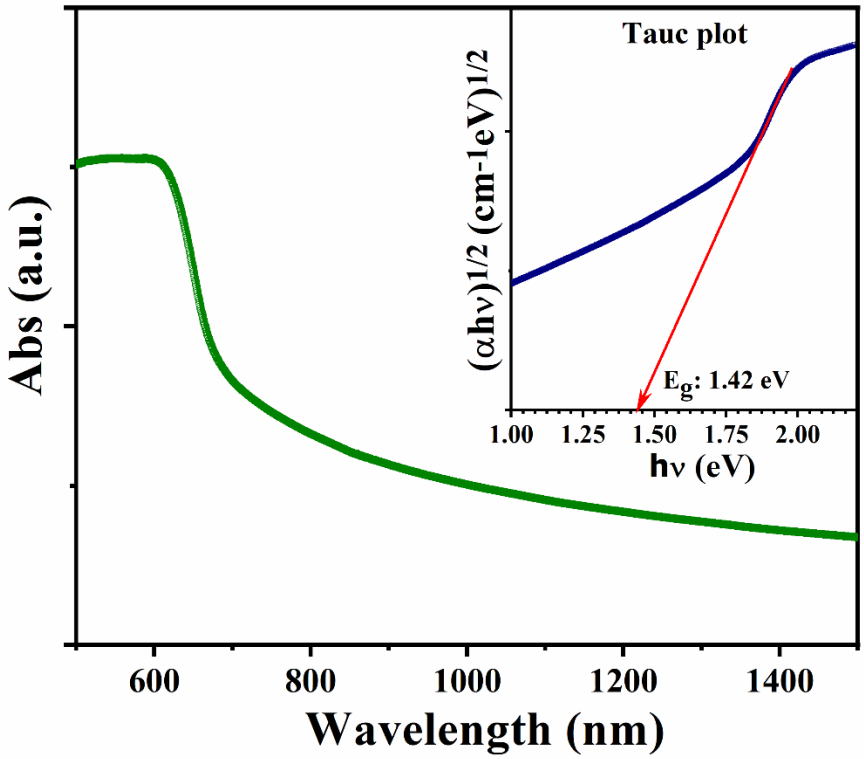

Figure 4.9. The absorption spectrum of BiI_3 thin film. (Inset) Tauc plot showing the calculated indirect bandgap.

The thickness of the thin film was measured to be around ~1 μm using a stylus profilometer. The absorption coefficient (α) was estimated from the formula (2.8) and the optical bandgap (E_g) was calculated from the Tauc relation in equation (2.7) .

An indirect allowed transition of 1.42 eV is revealed by the Tauc plot (inset of Figure 4.9), which is interestingly similar to the 1.44 eV predicted by the DFT calculations. This low indirect bandgap is due to the spin-orbit magnetic effects from heavy Bi and I elements in BiI_3 and it is very close to the optimum bandgap (1.40 eV) for maximum power conversion efficiency [207].

4.3.5. Photoresponse

The BiI_3 thin films have an extremely quick response time to light and are photoconductive. The measurements were conducted under the illumination of a 50 W halogen bulb and

LEDs with 1 V bias. The photocurrent response, in **Figure 4.10**, show a dark current of 6.1×10^{-13} A and an illumination current of 3.1×10^{-11} A.

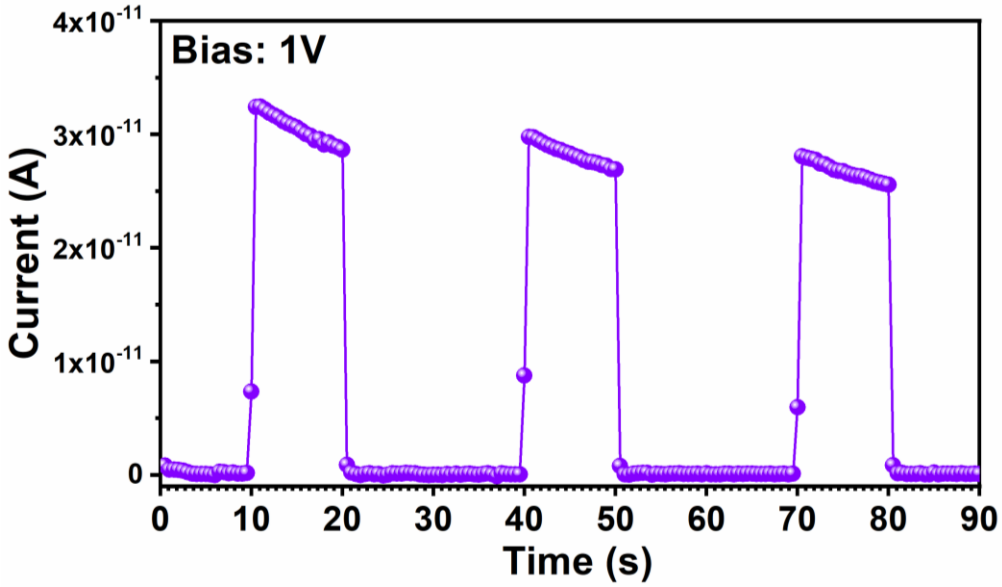

Figure 4.10. Photoresponse measurement under 50 W halogen lamp of BiI_3 thin film.

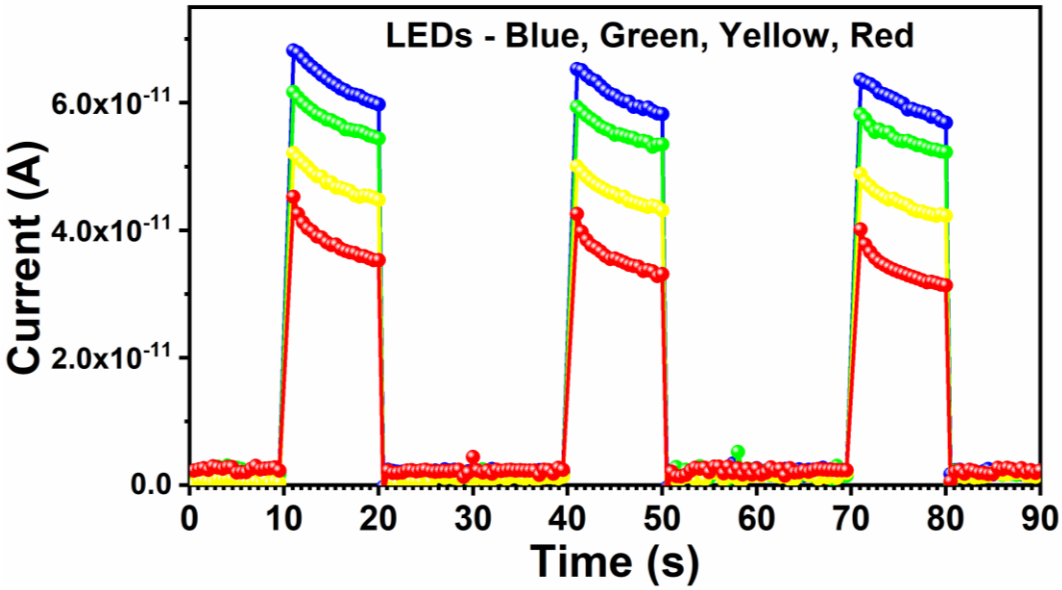

Figure 4.11. Photoresponse measurements under LEDs of BiI_3 film at 1V bias. The color of the curves represent the LED wavelength.

In addition, the response of the BiI_3 thin film to blue, green, yellow and red LEDs (50 W) are evaluated and the results are depicted in Figure 4.11. The sensitivity (S) of the BiI_3 thin

films under different illuminations is determined from the equation (2.10) and the obtained data is presented in Table 4-2 [208].

Table 4-2. The sensitivity of BiI_3 thin film to different illuminations under a bias of 1 V.

Sample	I_d (pA)	I_{ph}(pA)	Sensitivity (%)
Halogen lamp 1V	0.61	29.9	4890
Blue LED	2.24	61.1	2730
Green LED	2.24	55.0	2460
Yellow LED	2.24	45.3	2020
Red LED	2.24	36.0	1610

4.4. Effect of substrate temperature on BiI_3 thin films

Further, BiI_3 thin films were fabricated at various substrate temperatures and the as-deposited films are displayed in Figure 4.12**.**

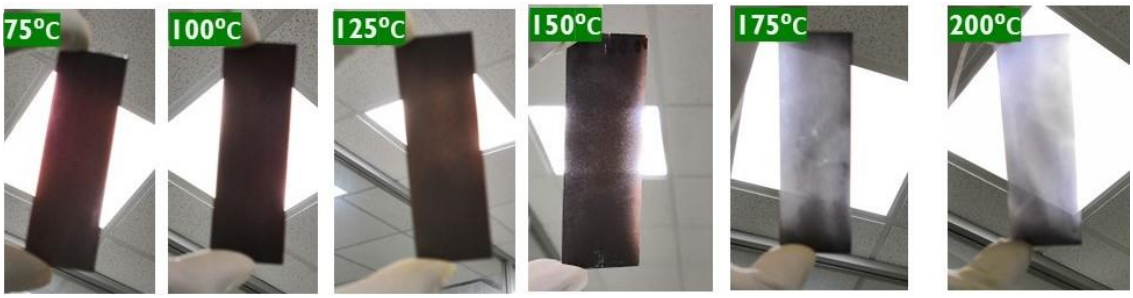

Figure 4.12. Ultrasonically spray deposited BiI_3 thin films at different substrate temperatures.

4.4.1. Structure

X-ray diffraction (XRD)

The X-ray diffraction patterns of the BiI_3 thin films deposited at different substrate temperatures from 75 to 200 ℃ are shown in Figure 4.13 which display the reflections of rhombohedral BiI_3 (ICDD no: 48-1795) structure [209]. The prominent reflections from BI75 sample correspond to (113) and (300) planes at 26.93 and 41.52°, respectively. It can be observed that while (113) and (300) are the only prominent peaks for films deposited below 150 ℃, higher temperatures favor a preferential growth along the (003) direction

perpendicular to the substrate surface. Besides, other peaks corresponding to (101), (012), (006), (116), (009), (119), (303), (223), (0012) and (226) were observed at 14.21, 16.03, 25.76, 35.24, 39.08, 46.18, 43.64, 50.22, 52.96 and 55.58°, respectively. However, above 125 ℃, small peaks corresponding to the (102) and (110) planes of the BiOI phase (ICDD no: 10-0445) were noted at 29.64 and 31.64° [210]. Higher substrate temperatures (150 ℃) resulted in non-uniform and powdery films as seen in Figure 4.12 due to the rapid evaporation of ethanol solvent.

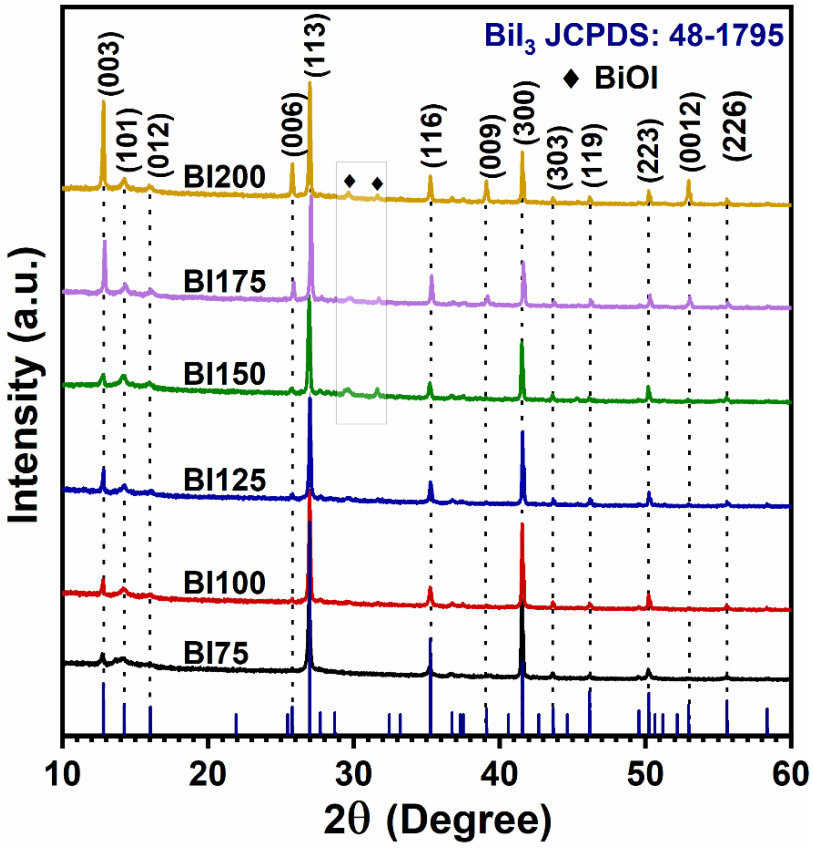

Figure 4.13. XRD profiles of BiI_3 thin films deposited at different substrate temperatures from 75 to 200 ℃.

Raman spectroscopy

The Raman spectra as depicted in Figure 4.14 supports the BiI_3 phase observed in the X-ray diffraction studies. The peaks at 84 and 106 cm^{-1} are associated with the E_g and A_g modes in BiI_3, respectively. The Raman peak around 159 cm^{-1} is explained to be the 2^{nd} order Raman line which is only observed in the bulk material [211]. On the other hand, the

peaks near 84 and 149 cm^{-1} could be the A_{1g} and E_g stretching modes of the Bi-I bond in BiOI [210,212].

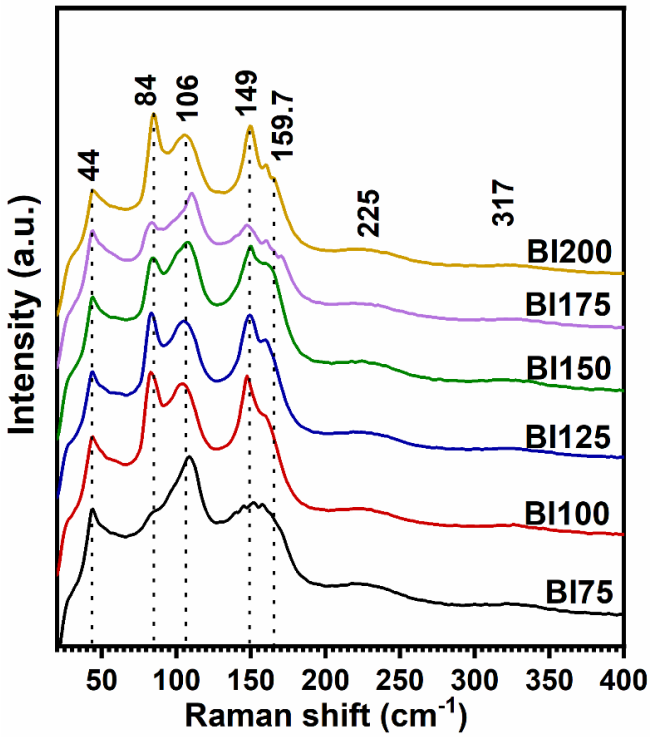

Figure 4.14. The Raman spectra of spray deposited BiI_3 thin films at different substrate temperatures.

4.4.2. Morphology

Scanning electron microscopy (SEM)

Scanning electron microscopy was used to probe the morphology of spray-deposited BiI_3 thin films and the images are depicted in Figure 4.15. The images (a-d) show large particles grown uniformly over the substrate surface when the temperature was between 75 and 150 °C. At higher temperatures, the faster solvent evaporation led to high agglomerations with poor coverage as can be seen in Figure 4.15e and f. This has resulted in non-uniform and powdery nature as seen from the physical appearance of the thin films in Figure 4.12. Most importantly, the thin films deposited at 125 and 150 °C display well-packed grains over the surface which can greatly improve the charge transport.

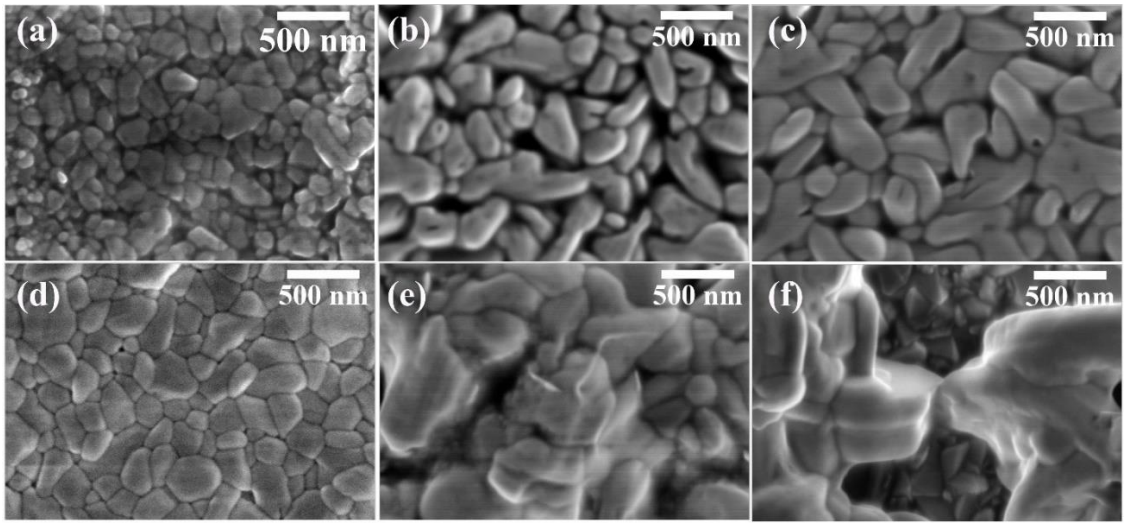

Figure 4.15. SEM images of (a) BI75 (b) BI100 (c) BI125 (d) BI150 (e) BI175 and (f) BI200 thin films.

4.4.3. Optical properties

UV-Vis-NIR Spectroscopy

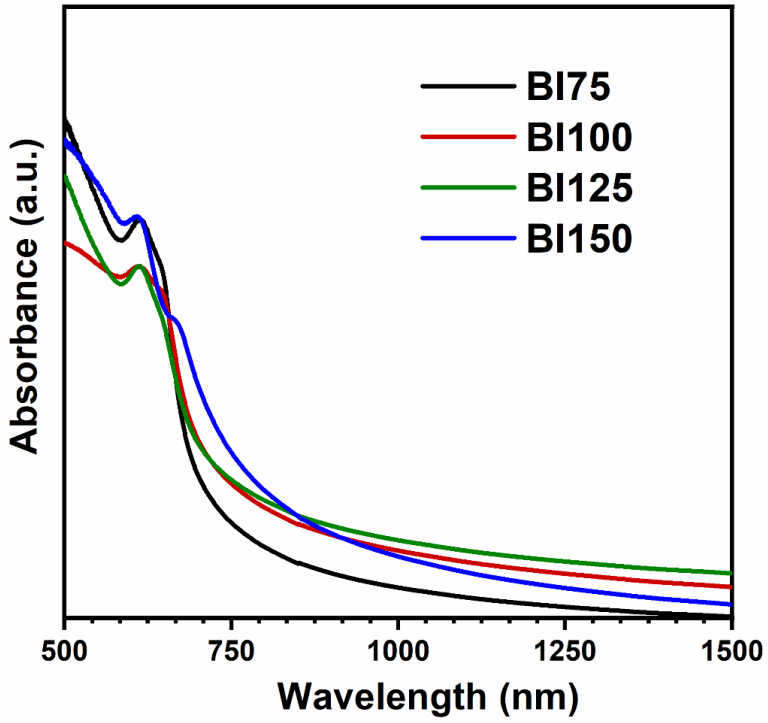

Figure 4.16. The absorption spectra of spray deposited BiI_3 thin films at different substrate temperatures.

The absorption, in Figure 4.16 slightly redshifts as the substrate temperature increases from 75 to 150 ℃. The absorption curves display a characteristic excitonic peak near 612 nm (2.02 eV) usually observed for BiI_3.The absorption coefficient (α) of the films with an average thickness (t) of 1 μm was calculated from the absorbance (A) data using the formula (2.8). Further, the direct and indirect band gaps were calculated using the Tauc relation (2.7) .The plots in Figure 4.17a,b estimate direct band gaps as well as indirect band gaps of BiI_3 thin films at different substrate temperatures.

Table 4-3. The band gap values of BiI_3 thin films deposited at different temperatures.

Sample	Direct band gap (eV)	Indirect band gap (eV)
BI75	1.77	1.46
BI100	1.73	1.35
BI125	1.72	1.30
BI150	1.60	0.98

It can be observed that the band gap value reduces with an increase in substrate temperature. This might be because of the improved charge transport through packed large grains and improved crystallinity at higher temperatures.

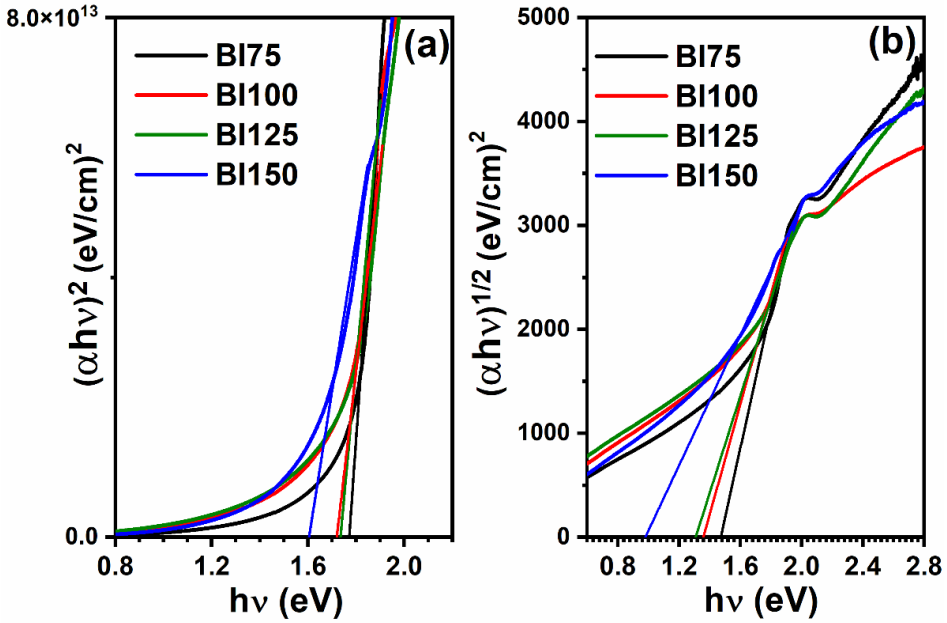

Figure 4.17. The (a) direct and (b) indirect bandgaps calculated for the BiI_3 thin films deposited at various substrate temperatures.

4.4.4. Photoresponse

The photoresponse measurements in Figure 4.18 show that all the films are responsive to light when illuminated under a 50 W halogen lamp. The comparatively better photo-to-dark current ratio, sensitivity ($S=I_{photo}/I_{dark}$), is observed for BI125 films. The BI125 thin film yielded a dark current (I_{dark}) of 12.2 nA and a light current (I_{light}) of 41.5 nA.

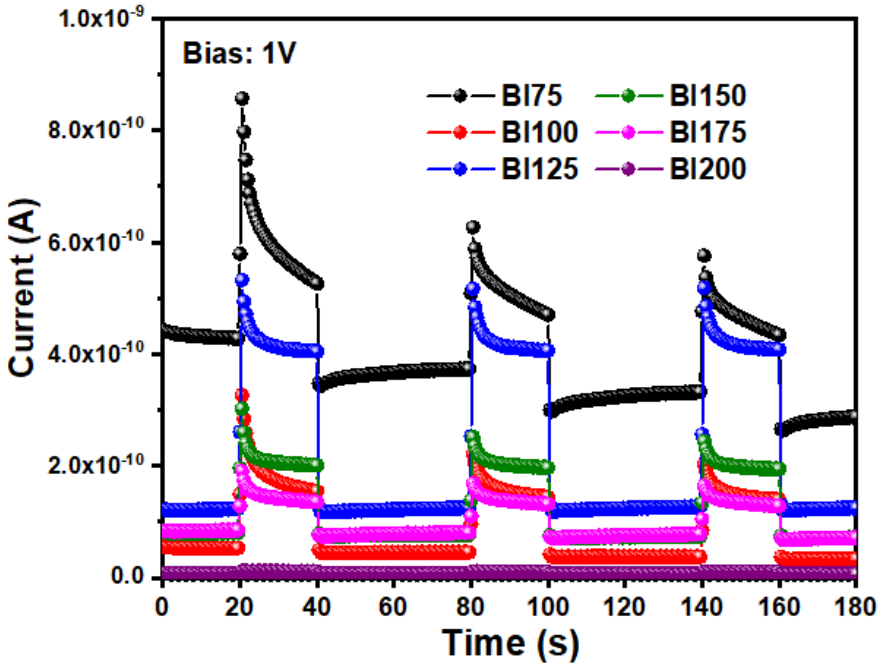

Figure 4.18. The photoresponse measurements of the BiI_3 thin films deposited at various substrate temperatures.

4.4.5. Thermal stability

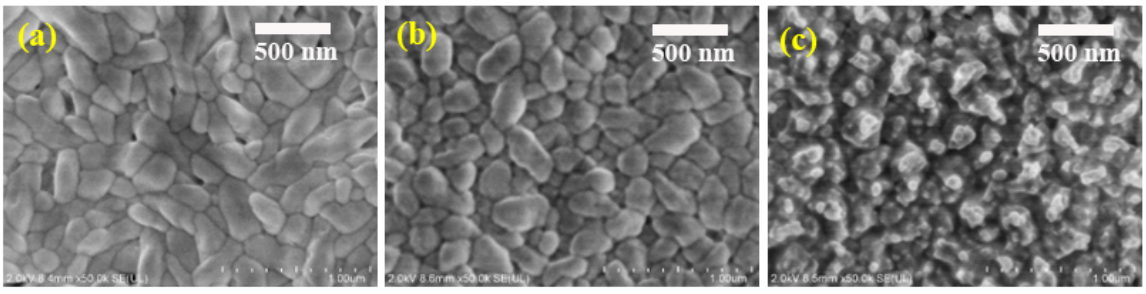

Figure 4.19. The SEM images of the RTP treated BI125 thin films at (a) 300, (b) 400 and (c) 500 ℃ for 20 s.

Rapid thermal processing of the BiI_3 thin films deposited at 125 ℃ was carried out at 300, 400 and 500 ℃ at a heating rate of 50 ℃/s for 20 s. The SEM images in **Figure 4.19** show

an improvement in the morphology with RTP at 300 and 400 ℃ as compared to the as-prepared samples. The grains are more closely packed and low pinholes were observed. However, at 500 ℃ the films underwent evaporation resulting in rougher surfaces with voids.

The photoresponse of the films after RTP is shown in **Figure 4.20**. The BiI_3 film thermally treated at 300 ℃ for 20 s demonstrates an enhanced photocurrent and low dark current. The dark current was effectively suppressed in these thin films to 9.45×10^{-13} A and the light current was 1.33×10^{-10} A, resulting in a sensitivity of 181 and an on/off ratio of 189.

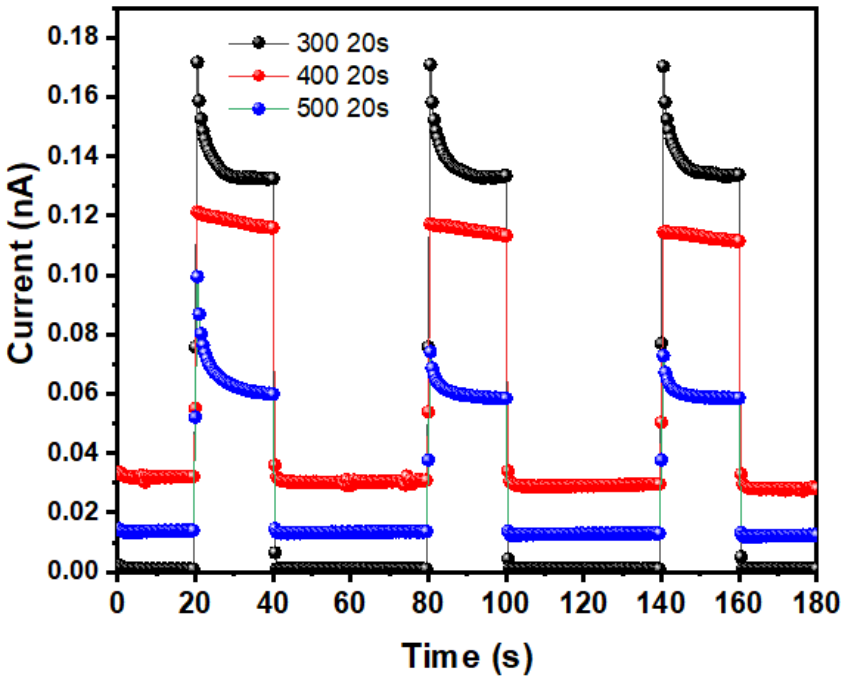

Figure 4.20. The photoresponse, at 1 V bias under 50 W halogen lamp, of the BiI_3 thin films after RTP treatments.

4.5. Conclusions

To initialize ultrasonic spray instrument parameters to obtain uniform thin films, BiI_3 powder was prepared and was used as a precursor for depositing its thin films. The obtained phase pure films had a dendritic-like morphology which is a consequence of droplet spreading in spray deposition. The BiI_3 thin films have an indirect band gap of around 1.42

eV which was well in agreement with the DFT results. Further, the films demonstrated excellent response to illumination from halogen lamp and LEDs at low bias voltages.

These exciting properties displayed by the spray-deposited BiI_3 thin film inspire further research and incorporation into optoelectronic devices. However, our interests were inclined towards exploring the material properties of $Cs_3Bi_2I_9$ and the uniform BiI_3 thin films realized here suggested the feasibility to obtain ternary films of $Cs_3Bi_2I_9$ by ultrasonic spray deposition as explained in the following chapter.

CHAPTER 5

SINGLE-STEP FABRICATION OF CESIUM BISMUTH IODIDE FILMS

The influence of important spray parameters is explored for obtaining $Cs_3Bi_2I_9$ thin films, using a precursor solution prepared with DMF. Further, a concentrated precursor solution is used to fabricate uniform thin films and a self-powered photodetector.

5.1. Introduction

This chapter broadly discusses the results observed in the initial optimization of $Cs_3Bi_2I_9$ thin films while using DMF as a solvent to prepare the precursor solution. Some of the crucial parameters of ultrasonic spray deposition, namely substrate temperature, precursor concentration, spray rate of solution and number (duration) of depositions, are varied and their influence on the thin film properties is analyzed. Further, using a concentrated precursor solution, careful and systematic examination of the structural, chemical, morphological, and optoelectronic characteristics of the $Cs_3Bi_2I_9$ films with increasing substrate temperature (150 to 400 °C) is conducted. Finally, we evaluate the applicability of these spray-deposited $Cs_3Bi_2I_9$ film in self-powered photodetection.

5.2. Effect of deposition parameters

5.2.1. Substrate temperature

The substrate temperature is one of the crucial parameters in spray deposition. Heating the substrate will not only help evaporate the solvent but also reduce the surface tension of the precursor solution, which reduces the contact angle between the precursor droplets and the

substrate surface, thus improving surface wetting and coverage. However, very high temperatures will evaporate the solvent rapidly before the droplets can spread and merge, resulting in non-uniform powdery surfaces. Besides, very low temperatures will delay the drying process causing shrinkage or dewetting that result in large area thickness deviations [213].

A photograph of the uniform and adherent $Cs_3Bi_2I_9$ thin films on glass substrates is displayed in **Figure 5.1.** At the lower temperatures, the coverage was comparatively poor, which may be attributed to the high surface tension of the DMF solvent resulting in a smaller contact angle with the substrate surface affecting the wetting and spreading.

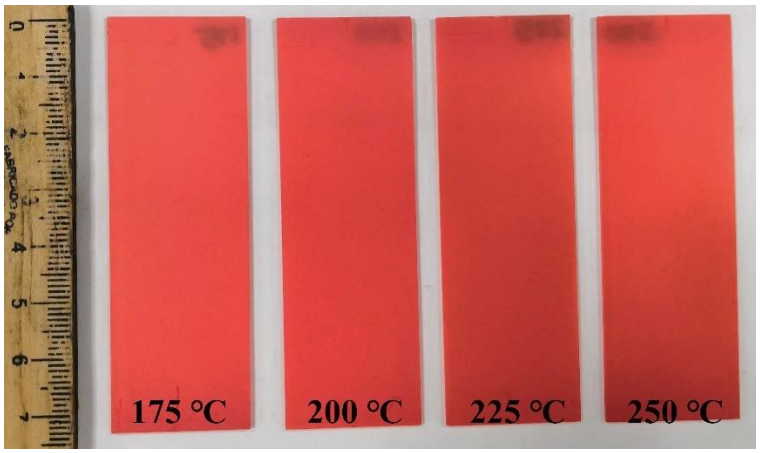

Figure 5.1. Ultrasonically spray deposited $Cs_3Bi_2I_9$ thin films at different substrate temperatures.

Structure

X-ray diffraction (XRD)

The X-ray diffraction patterns of the films deposited at different substrate temperatures are shown in **Figure 5.2**. All the peaks are well in match with the XRD diffraction database ICSD ref. code: 01-073-0707 corresponding to hexagonal structure ($P6_3/mmc$) of $Cs_3Bi_2I_9$ [14]. Noticeably, the thin film deposited at 175 °C is extremely oriented along {00*l*} direction marked by a very high-intensity peak at 25.2° corresponding to the (006) plane and the other peaks observed are (004), (0010) and (0012) at 16.8, 42.7 and 51.7°, respectively. The films showed a single crystalline nature at lower temperatures [14].

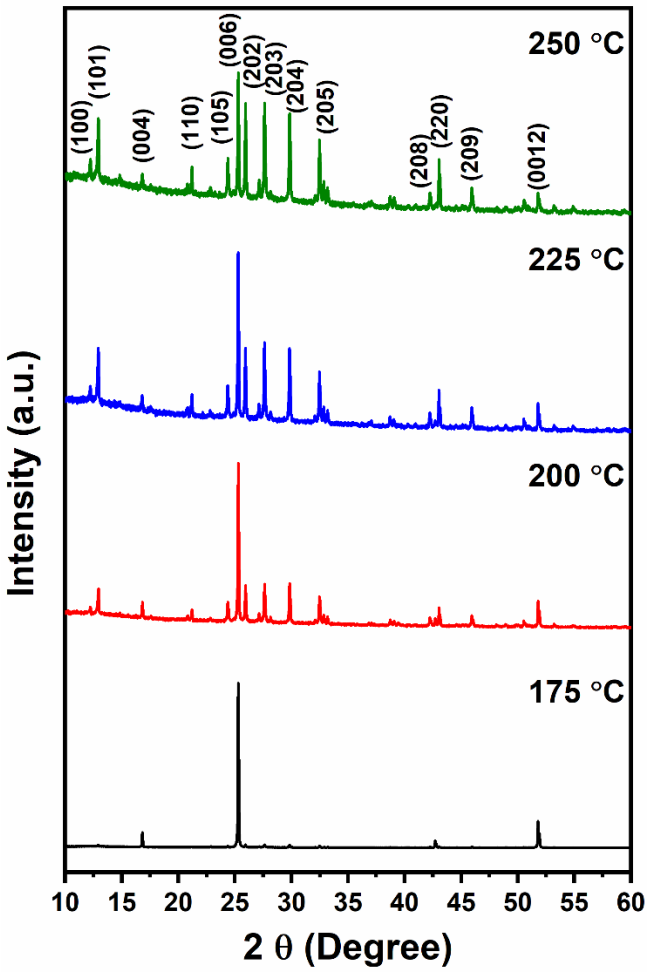

Figure 5.2. XRD patterns of the $Cs_3Bi_2I_9$ thin films deposited at different substrate temperatures.

However, higher substrate temperatures increased the polycrystalline nature of the films, marked by the considerable growth along the other planes such as (100), (101), (110), (105), (202), (203), (204), (205), (208), (220) and (209) at 12.2, 12.9, 21.2, 24.3, 25.9, 27.6, 29.8, 32.4, 42.2, 43 and 45.9°, respectively.

Raman Spectroscopy

The major Raman peaks are observed around 58, 103, 116 and 144 cm^{-1}, as seen in **Figure 5.3**, which are associated with the $Cs_3Bi_2I_9$ phase [214]. Sharp peaks at all temperatures show excellent crystallinity of the thin films.

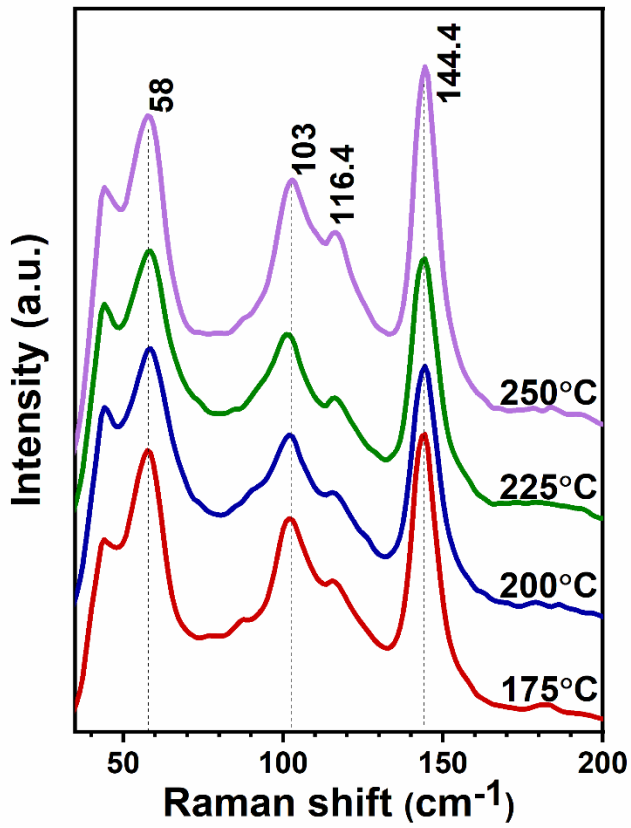

Figure 5.3. The Raman spectra of the $Cs_3Bi_2I_9$ thin films spray deposited at substrate temperatures of 175, 200, 225 and 250 ℃.

Morphology

Scanning Electron Microscopy (SEM)

The SEM images in **Figure 5.4** show bigger $Cs_3Bi_2I_9$ grains closely packed on the thin film surface. The particle size is reduced at higher temperatures complimenting the observations from X-ray diffraction studies. The prolonged drying time at the lower temperatures slowed the crystallization process leading to enhanced grain growth. On the other hand, the rapid crystallization and high evaporation rate of DMF solvent at 225 and 250 ℃ prevented the formation of large grains.

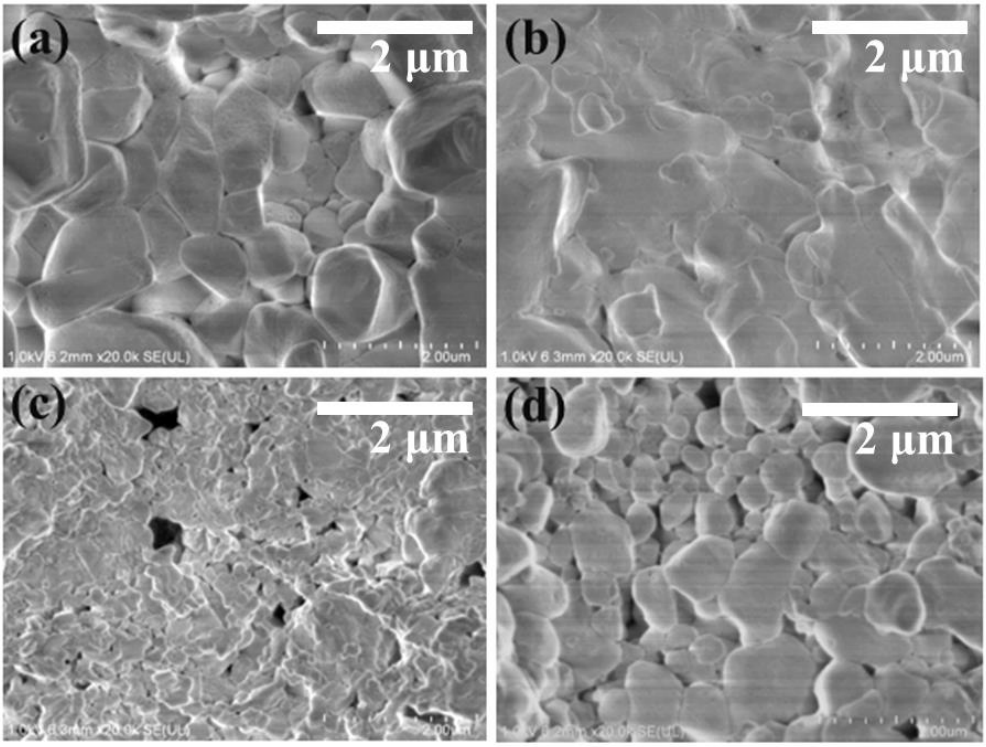

Figure 5.4. Scanning electron microscopy images (×20 k) of $Cs_3Bi_2I_9$ thin films at different substrate temperatures (a) 175, (b) 200, (c) 225 and (d) 250 ℃.

Chemical states

X-ray Photoelectron Spectroscopy (XPS)

Figure 5.5 shows the survey spectrum and core-level spectra of the $Cs_3Bi_2I_9$ thin film deposited at 200 ℃. The survey spectrum displays the characteristic peaks of Cs, Bi, I, O and C at the respective binding energy values. The C peak is due to the adventitious carbon due to the atmosphere exposure of thin film surface. In the high-resolution spectra, the doublet peaks of Cs 3d, Bi 4f and I 3d correspond to their +1, +3 and -1 states, respectively, as observed in $Cs_3Bi_2I_9$. The deconvoluted oxygen peaks can be attributed to the adsorbed atmospheric oxygen (532.48 eV) and bismuth oxide (530 eV) on the thin film surface.

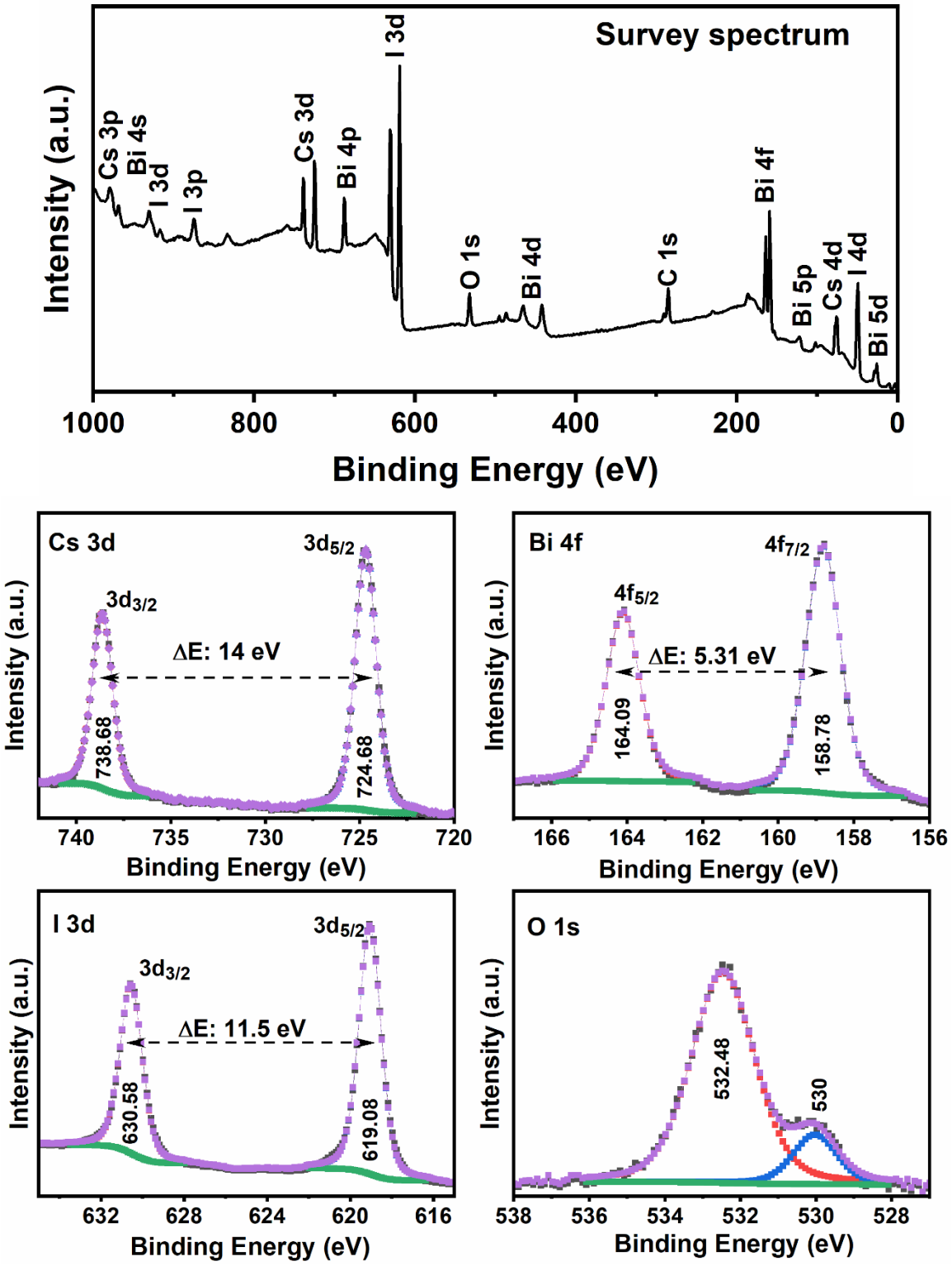

Figure 5.5. XPS survey spectrum and high-resolution core-level spectra of Cs 3d, Bi 4f, I 3d and O 1s of $Cs_3Bi_2I_9$ thin films deposited at 200 °C substrate temperature.

Optical properties

UV-Vis-NIR spectroscopy

The absorbance and transmittance, as well as the specular and diffused reflectance (DRS), are measured as shown in **Figure 5.6** to analyze the optical properties of $Cs_3Bi_2I_9$ thin films.

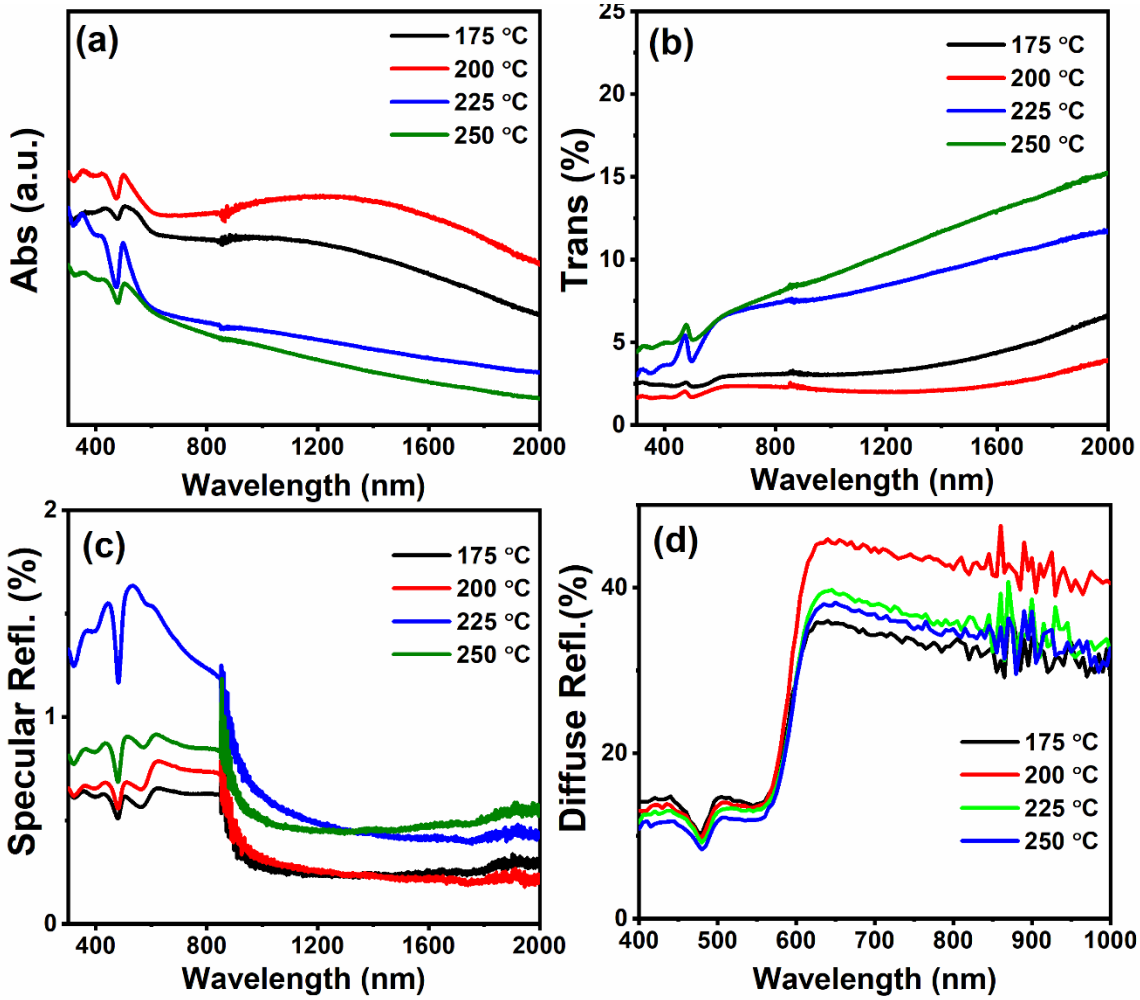

Figure 5.6. (a) Absorbance, (b) transmittance and (c) specular and (d) diffuse reflectance spectra of $Cs_3Bi_2I_9$ thin films deposited at different substrate temperatures.

Photoresponse

The transient photocurrent responses were measured under a 50 W halogen lamp at a 5 V bias. All the thin films are responsive to visible light illumination, as seen in Figure 5.7. Similar to previous reports, a low current in the 10 – 26 pA range is measured from the

thin film surface. The low photocurrent values significantly affect the sensitivity of the films. Besides, the thin films deposited at higher temperatures than 200 ℃ display a significant degradation in the presence of light and electric field.

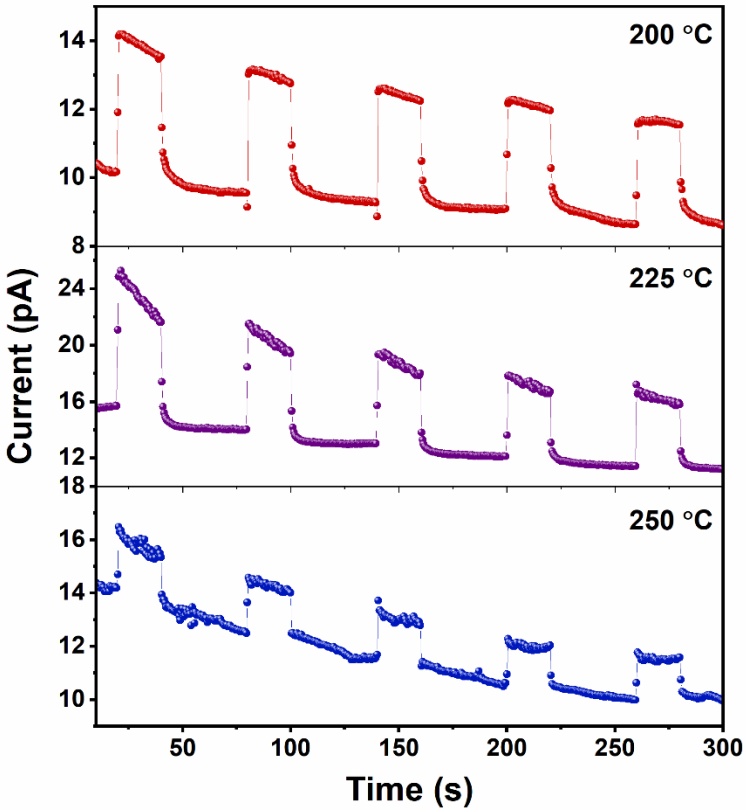

Figure 5.7. The photoresponse measurements of $Cs_3Bi_2I_9$ thin films deposited at 200, 225 and 250 ℃.

5.2.2. Concentration

The concentration of the precursor solution was further lowered keeping the substrate temperature at 200 ℃ and the CsI/BiI_3 ratio at 3/2. The obtained thin films are shown in **Figure 5.8**.

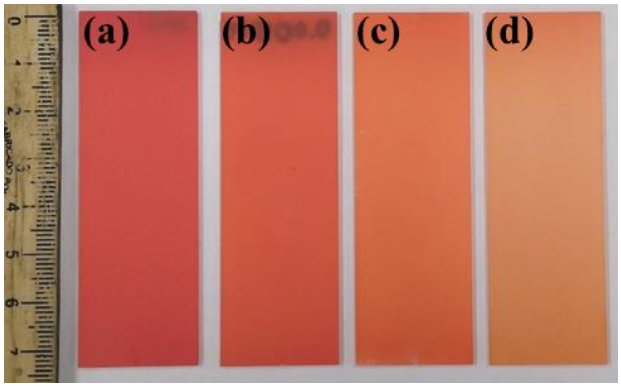

Figure 5.8. The thin films prepared from various BiI_3/CsI precursor concentrations (a) 0.01/0.015 (M) (b) 0.005/0.0075 (M/2) (c) 0.0025/0.00375 (M/4) (d) 0.00125/0.00187 (M/8) in Molar.

Structure

X-ray Diffraction (XRD) and Raman spectroscopy

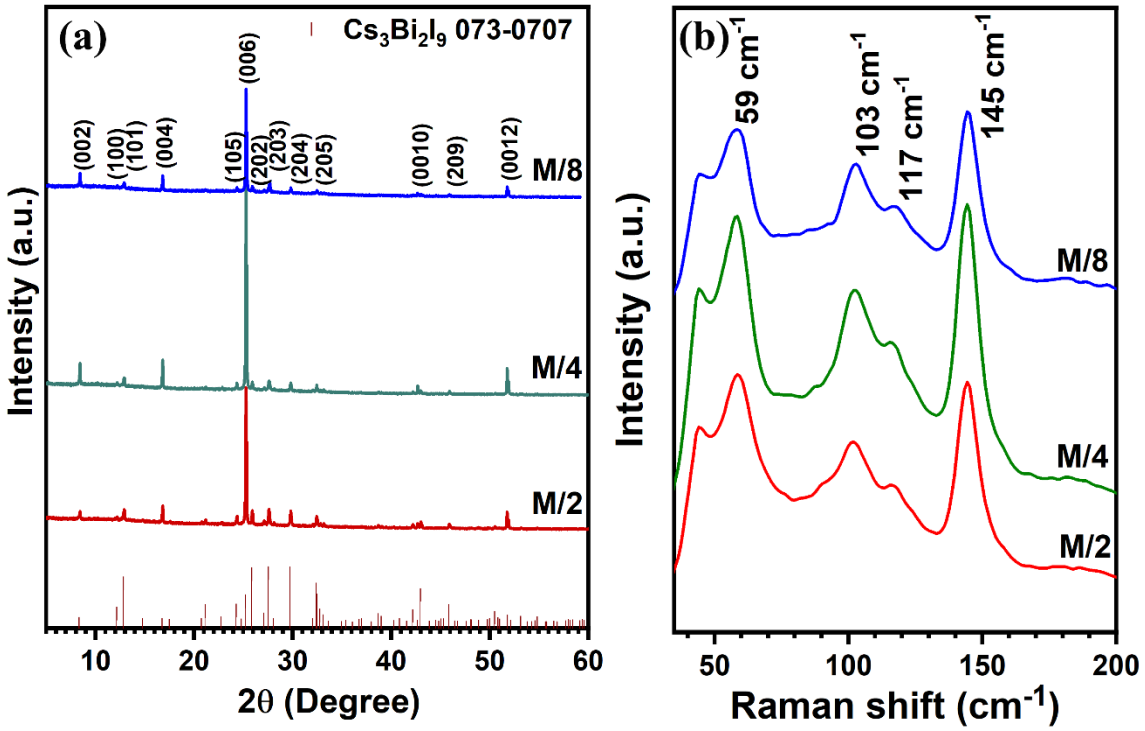

Figure 5.9. (a) XRD patterns and (b) Raman spectra of the spray deposited $Cs_3Bi_2I_9$ thin films with different concentrations.

The X-ray diffraction patterns in Figure 5.9a of the thin films are in match with the JCPDS card no. 01-073-0707 of hexagonal $Cs_3Bi_2I_9$ structure. The patterns show that as the concentration is lowered to 0.0025 M, the crystallites grow highly oriented in the (006)

direction with low-intensity peaks in other directions. However, at further low concentration of 0.00125 M the intensity of (006) plane is reduced. The Raman spectra in Figure 5.9b show characteristic peaks of $Cs_3Bi_2I_9$ at 59, 103, 117 and 145 cm^{-1}. The Raman spectra also supports the XRD patterns with sharp peaks noted in the case of 0.0025M thin films.

Morphology

Scanning Electron Microscopy (SEM)

The non-uniformity and agglomerated large particles are apparent in the morphological analysis using the SEM images in **Figure 5.10**. The film shows a highly powdery nature at lower concentrations with large voids.

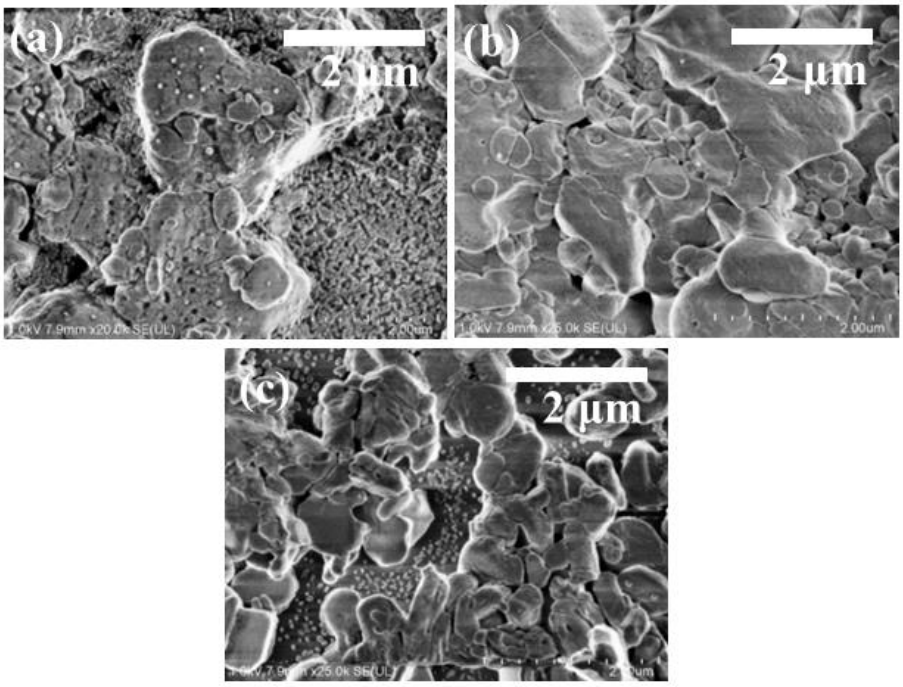

Figure 5.10. SEM images of the $Cs_3Bi_2I_9$ thin films with reduced precursor concentration (a) M/2, (b) M/4 and (c) M/8.

Chemical states

X-ray Photoelectron Spectroscopy (XPS)

The chemical states are identified with the high-resolution scans of Cs 3d, Bi 4f, I 3d and O 1s in the M/2 $Cs_3Bi_2I_9$ thin. The Cs 3d peaks were observed at 738.38 and 724.38 eV

with a spin-orbit separation of 14 eV which is associated with the +1 state of Cs in $Cs_3Bi_2I_9$. The Bi 4f peaks were observed at 164.15 and 158.84 eV which corresponds to the Bi^{3+} state. Additionally, the doublet at 162.19 and 156.88 eV are associated to the metallic bismuth which originates from the etching process during the analysis. Further, the I 3d spectrum shows peaks at 630.38 and 618.88 eV separated by 11.5 eV which is attributed to the -1 state of I in $Cs_3Bi_2I_9$. The O 1s spectrum reveals a peak at 530.18 eV after deconvolution, in addition to the adsorbed oxygen peak at 532.18 eV, which is due to the bismuth oxide in the thin film.

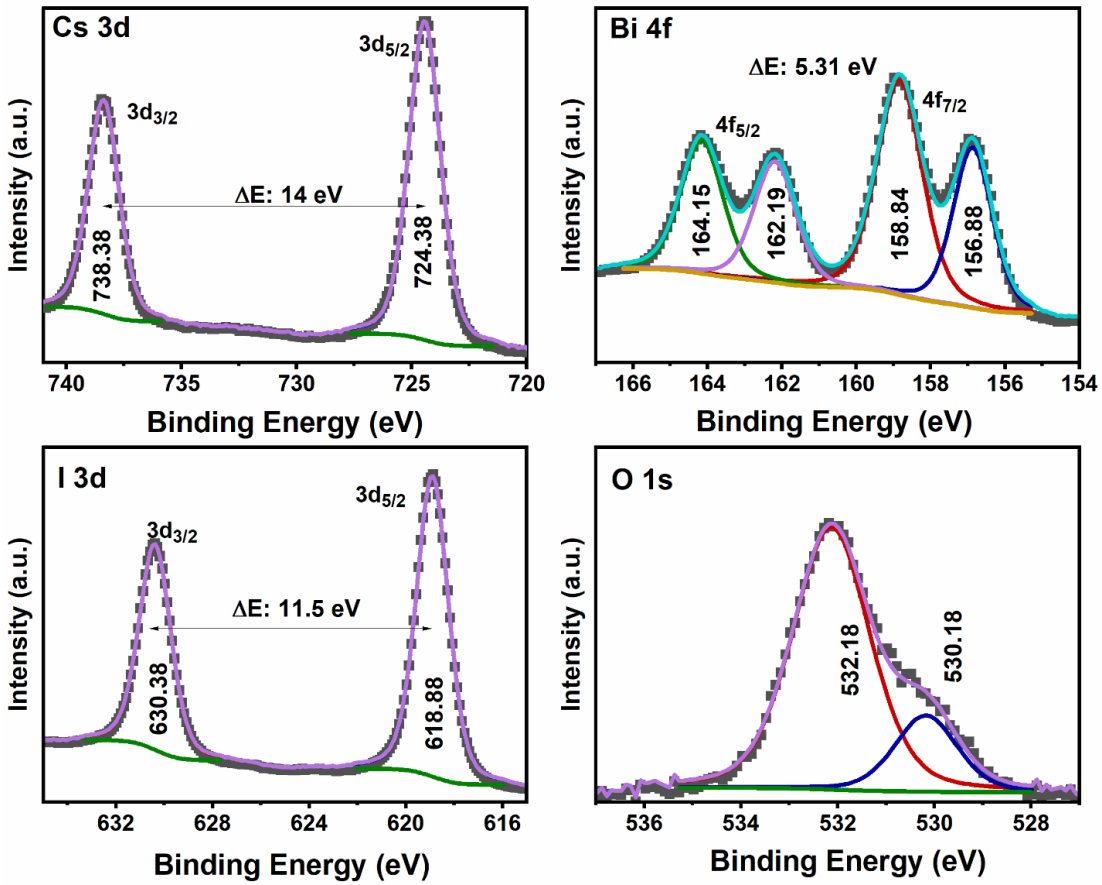

Figure 5.11. XPS core level spectra of M/2 $Cs_3Bi_2I_9$ thin film.

Optical properties

UV-Vis-NIR spectroscopy

The absorbance, transmittance and reflectance of the thin films are shown in **Figure 5.12**. The absorbance of the films does not show any sharp absorption, which may be due to the

powdery nature observed in SEM images. Moreover, the diffuse reflectance spectra reveal considerable scattering from the film surface.

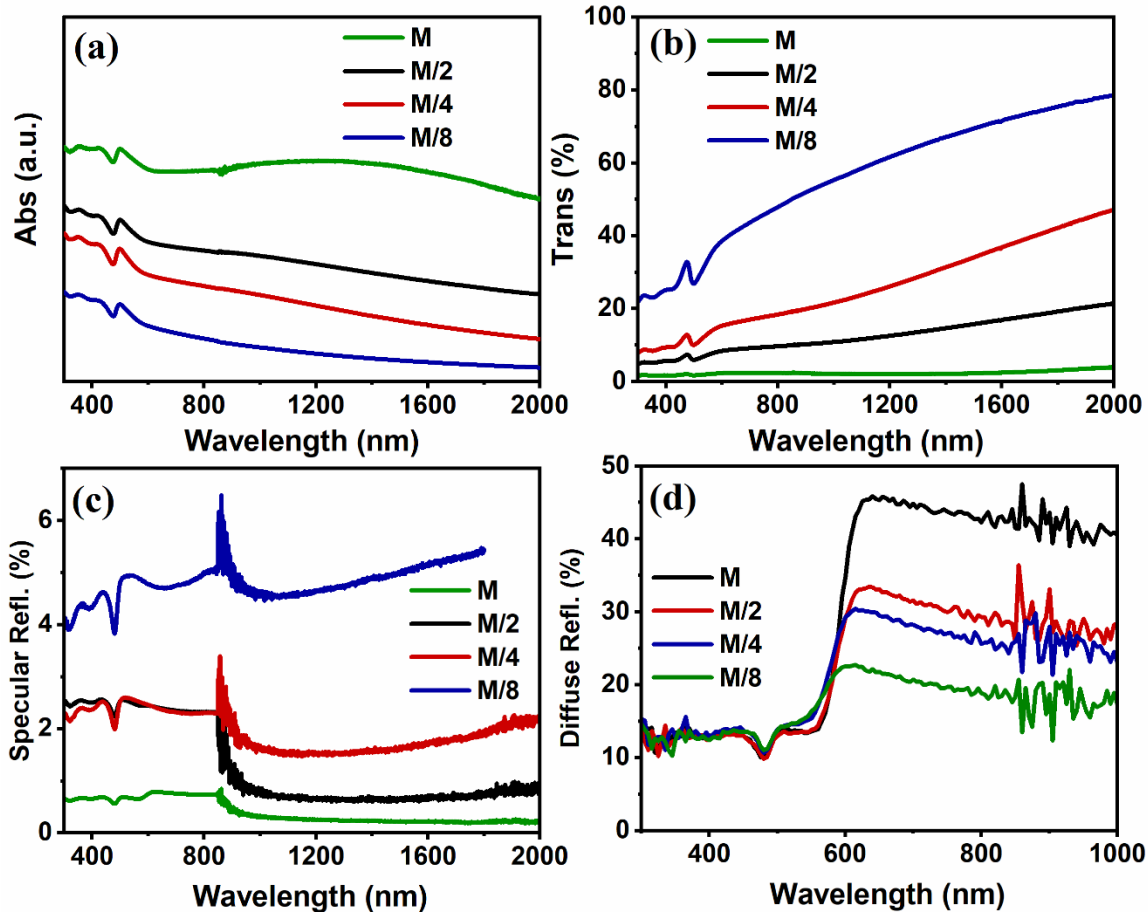

Figure 5.12. (a) Absorbance, (b) transmittance, (c) specular reflectance and (d) diffuse reflectance of $Cs_3Bi_2I_9$ thin films with different concentrations.

Photoresponse

The photoresponse of the films to a 50 W halogen lamp at 5 V bias is depicted in Figure 5.13. An increase in the dark current and the light current was observed in these thin films. The highest current was observed in the 0.00125M (BiI_3) film with a light current of ~90 pA and a dark current of ~70 pA. The sensitivity calculated are 0.30, 0.33 and 0.23 for 0.005M, 0.0025M and 0.00125M thin films, respectively.

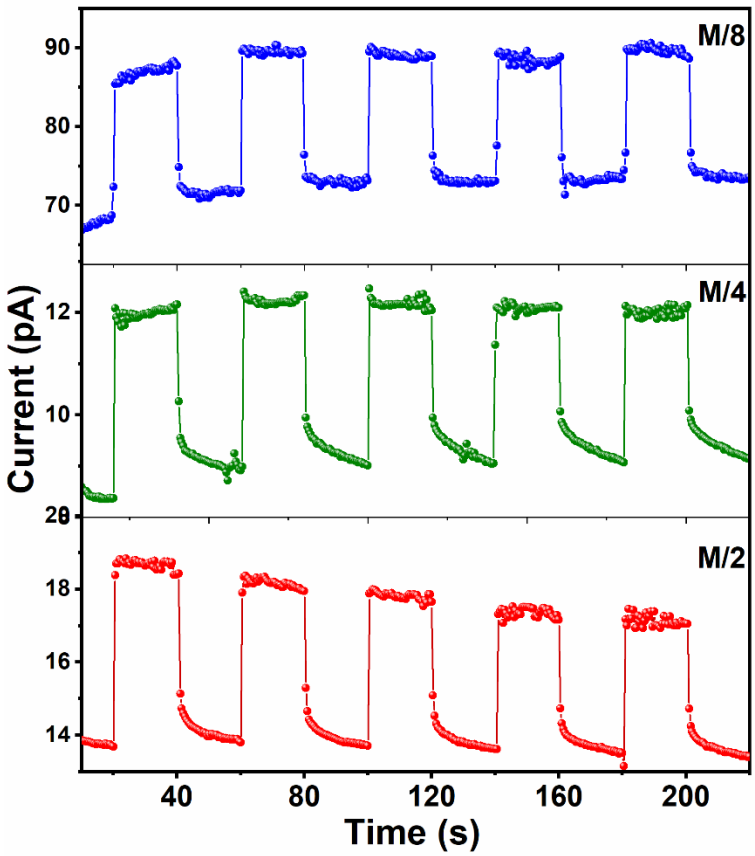

Figure 5.13. The photoresponse of the $Cs_3Bi_2I_9$ thin films spray-deposited with low concentration of precursor solution.

5.2.3. Spray rate

The precursor solution concentration was kept at 5 mM for BiI_3 and 7.5 mM for CsI which was sprayed at a substrate temperature of 200℃. In this study, thin films are deposited with different spray rates of 0.1 ml/min (SR0.1), 0.3 ml/min (SR0.3) and 0.9 ml/min (SR0.9) compared to the 0.6 ml/min used in the previous depositions and the as-deposited thin films are shown in **Figure 5.14**.

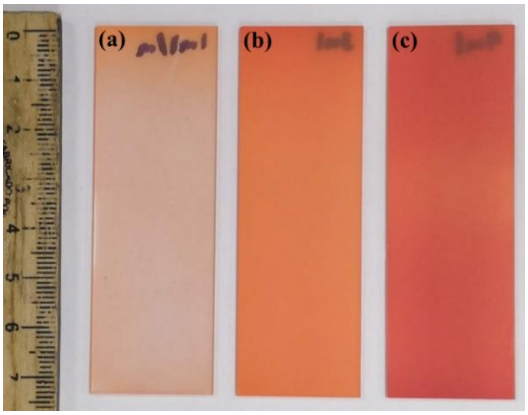

Figure 5.14. The $Cs_3Bi_2I_9$ thin films deposited by changing the spray rate of the precursor solution as (a) 0.1 ml/min, (b) 0.3 ml/min and (c) 0.9 ml/min.

Structure

X-ray Diffraction (XRD) and Raman spectroscopy

The XRD patterns in **Figure 5.15**a show that the films are preferentially oriented in the (006) direction. The SR0.3 thin film displays the highest (006) peak intensity which means the thin film at this spray rate has better growth along the (006) plane. Small peaks corresponding to other planes are also marked in the diffraction patterns.

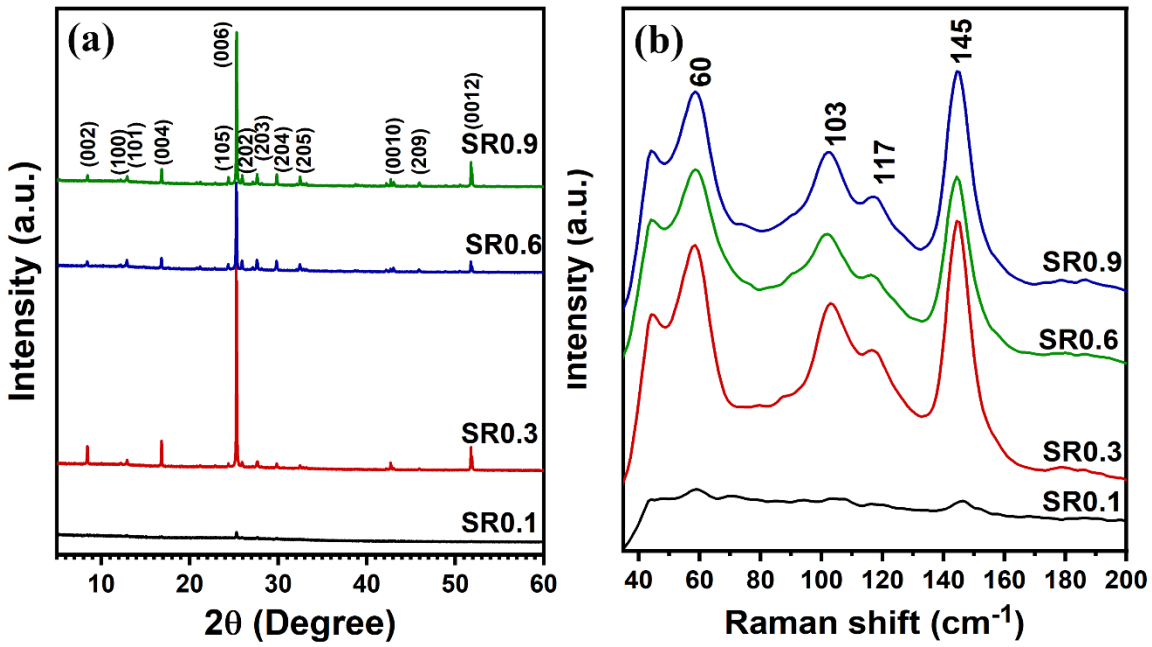

Figure 5.15. (a) XRD patterns and (b) Raman spectra of the $Cs_3Bi_2I_9$ thin films deposited at different spray rates.

The Raman spectra in **Figure 5.15**b also display the characteristic peaks corresponding to the $Cs_3Bi_2I_9$ phase. The peaks are observed at 60, 103, 117 and 145 cm^{-1}. Any indication of other impurity phases is absent in these structural analyses.

Morphology

Scanning Electron Microscopy (SEM)

The morphology of the thin films is not uniform and compact, which is evident in **Figure 5.16**. This suggests the powdery nature of the films. In addition to the low-concentration precursor solutions, the low spray rate leads to poor growth due to the absence of enough nucleation centers. **Figure 5.16**d shows a low-angle backscattered electron image of thin films deposited with 0.9 ml/min at low magnification. This clearly shows that the inefficient droplet spreading on the substrate surface leads to clusters of particles on the surface.

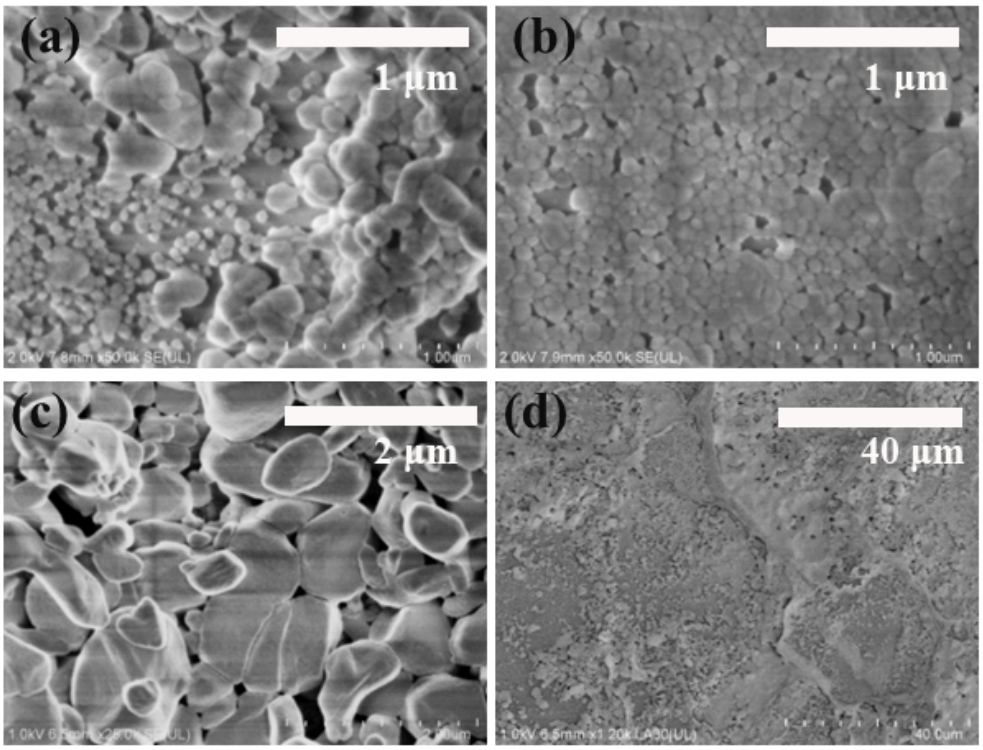

Figure 5.16. SEM images of $Cs_3Bi_2I_9$ thin films after varying the spray rate (a) 0.1 ml/min, (b) 0.3 m/min and (c) 0.9 ml/min. (d) LA-BSE image of 0.9 ml/min deposited $Cs_3Bi_2I_9$ thin film.

Chemical states

X-ray Photoelectron Spectroscopy (XPS)

The XPS high-resolution scans of core-levels of Cs, Bi, I and O after an Ar ion etching of the SR0.3 (0.3 ml/min) thin film are shown in **Figure 5.17**. The peaks in the Cs 3d scan at 724.38 and 738.38 eV are assigned to Cs $3d_{5/2}$ and $3d_{3/2}$, revealing the +1 state. In the Bi 4f scan, two doublets at 158.84 and 164.15 as well as at 156.88 and 162.19 eV are noted which are ascribed to the $4f_{72}$ and $4f_{5/2}$ peaks of Bi^{3+} and Bi^{0} states in the thin films. Further, the I 3d scan shows two peaks at 618.78 and 630.28 eV which corresponds to the $3d_{5/2}$ and $3d_{3/2}$ peaks suggesting the I^{-} state. The peak at 532.28 eV in O 1s scan is due to the atmospheric oxygen adsorbed to the thin film surface whereas the low intensity peak at 530.78 eV is from the oxygen bonded to Bi.

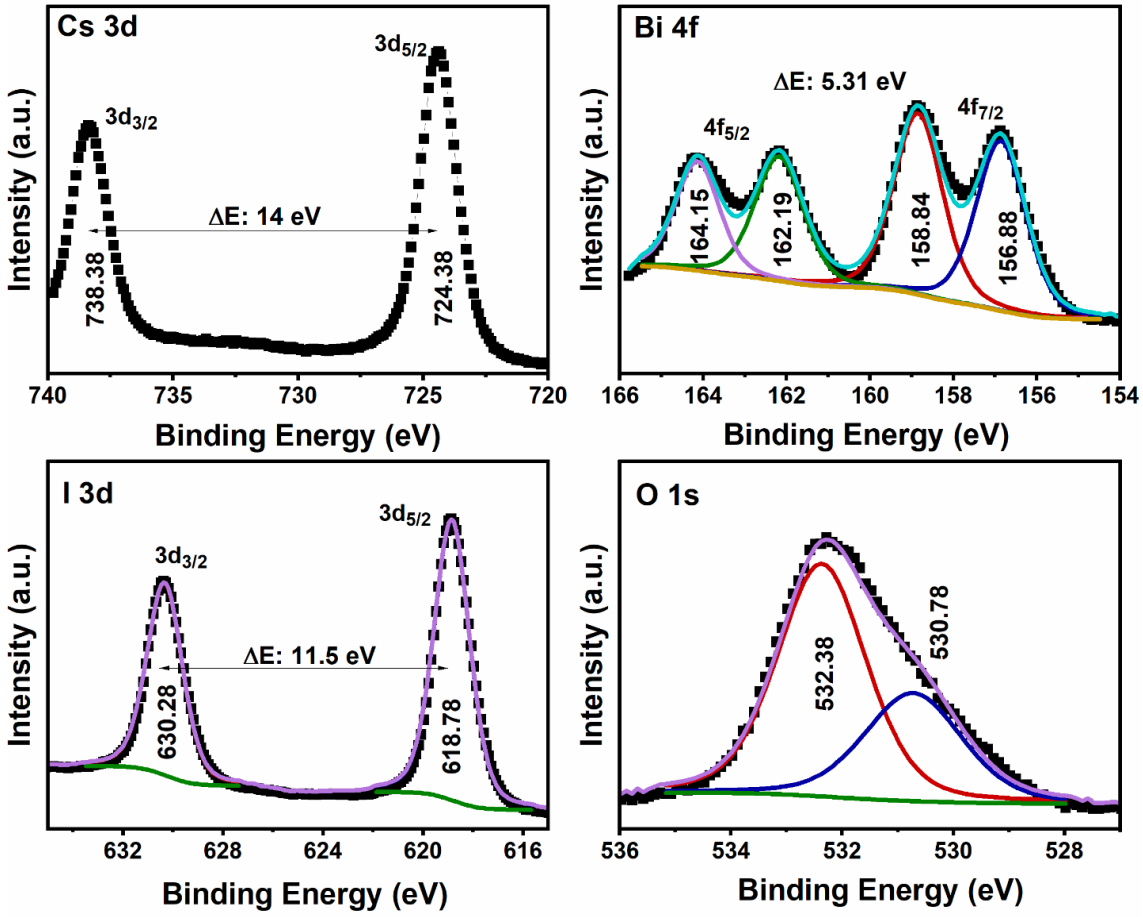

Figure 5.17. XPS core-level spectra of SR0.3 $Cs_3Bi_2I_9$ thin films deposited at a spray rate of 0.3 ml/min.

Optical properties

UV-Vis-NIR spectroscopy

The absorption, transmittance and reflectance of thin films fabricated with different spray rates are shown in **Figure 5.18**. The reflectance spectra and absence of sharp absorption in the absorption curves of the thin films again suggest their powdery nature, as evident in the SEM images and physical appearance.

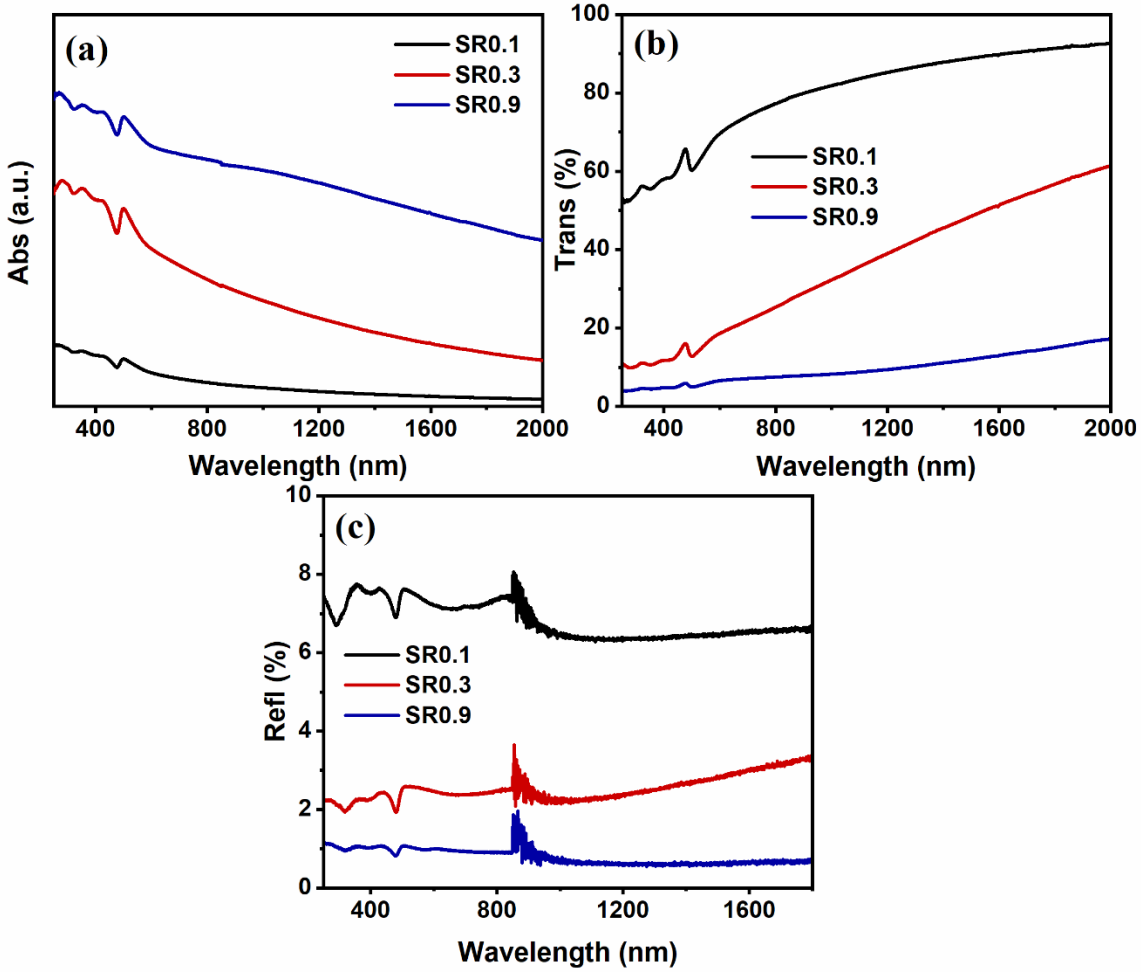

Figure 5.18. The (a) absorbance, (b) transmittance and (c) reflectance spectra of $Cs_3Bi_2I_9$ thin films with varying spray rates.

Photoresponse

The photocurrent response of the thin films at 5 V bias under the illumination of a 50 W halogen lamp is shown in **Figure 5.19**. At a very low spray rate of 0.1 ml/min (SR0.1) and a high spray rate of 0.9 ml/min (SR0.9), the response is not steady and shows a continuous degradation in the dark and light currents. However, the thin film fabricated with 0.3 ml/min (SR0.3) shows a better response in terms of stability and sensitivity.

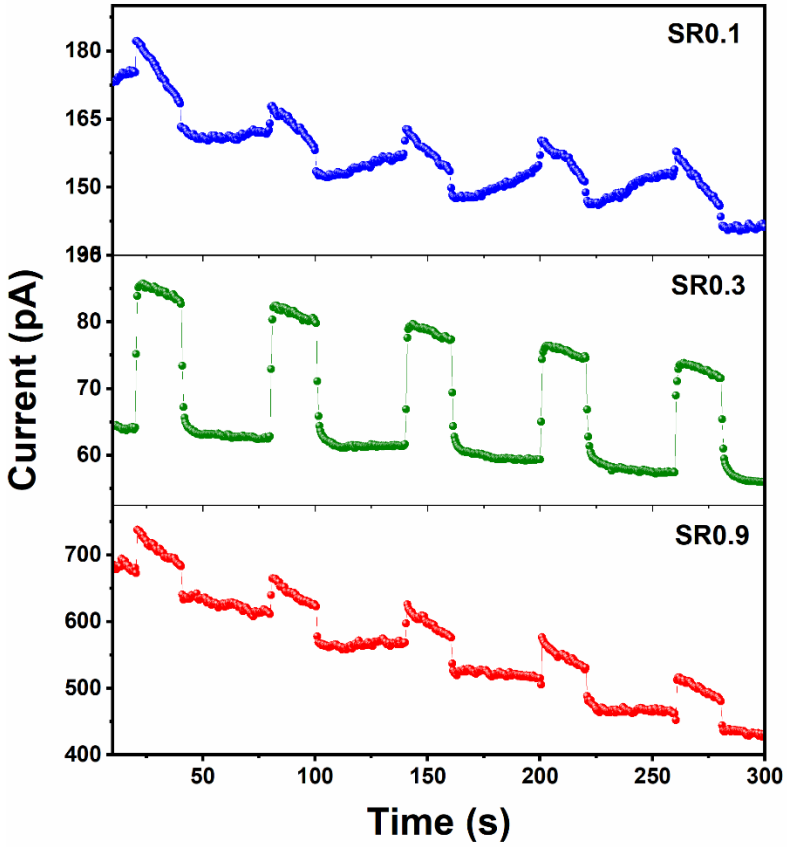

Figure 5.19. The photoresponse of the thin films with different spray rates of 0.1 ml/min (SR0.1), 0.3 ml/min (SR0.3) and 0.9 ml/min (SR0.9).

5.2.4. Number of depositions

The concentration of the precursor solution was maintained at 5 mM and 7.5 mM for BiI_3 and CsI, respectively, and substrate temperature was 200 °C. Based on the previous experiment, the spray rate was maintained at 0.3 ml/min and the number of spray depositions was increased from 20 to 40 (d40), 50 (d50) and 60 (d60) depositions to achieve better coverage and sufficient thickness.

Structure

X-ray Diffraction (XRD)

The X-ray diffraction patterns shown in **Figure 5.20** suggest that the crystallinity of the thin films is not significantly affected by the number of depositions up to 60. Like the previous experiments, the thin films are (006) oriented with the (006) peak at 25.20°. Peaks assigned to various other planes such as (002), (100), (101), (004), (105), (202), (203), (204), (205), (0010), (209) and (0012) are also marked in the diffraction patterns.

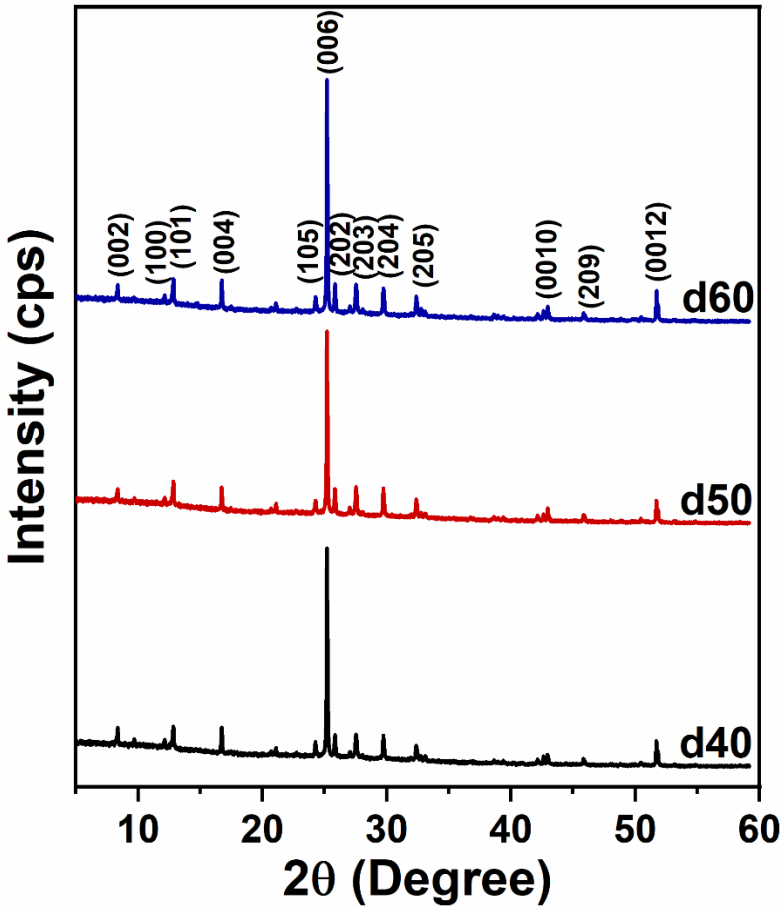

Figure 5.20. XRD patterns of the $Cs_3Bi_2I_9$ thin films with different deposition numbers such as 40 (d40), 50 (d50) and 60 (d60).

Morphology

Scanning Electron Microscopy (SEM)

The morphology of these thin films probed by SEM images is displayed in **Figure 5.21**, which shows that the films are covered with smaller particles but with better uniformity and coverage with more depositions. However, the low concentration of the precursor solution might lead to fewer nucleation sites upon spreading over the substrate. Besides, the high boiling point of DMF leads to the dissolution of thin films in subsequent depositions. The low solution concentration and the inefficient solvent evaporation lead to agglomerations when viewed over larger areas, as seen in a low-angle backscattered image of the d60 sample in Figure 5.21d.

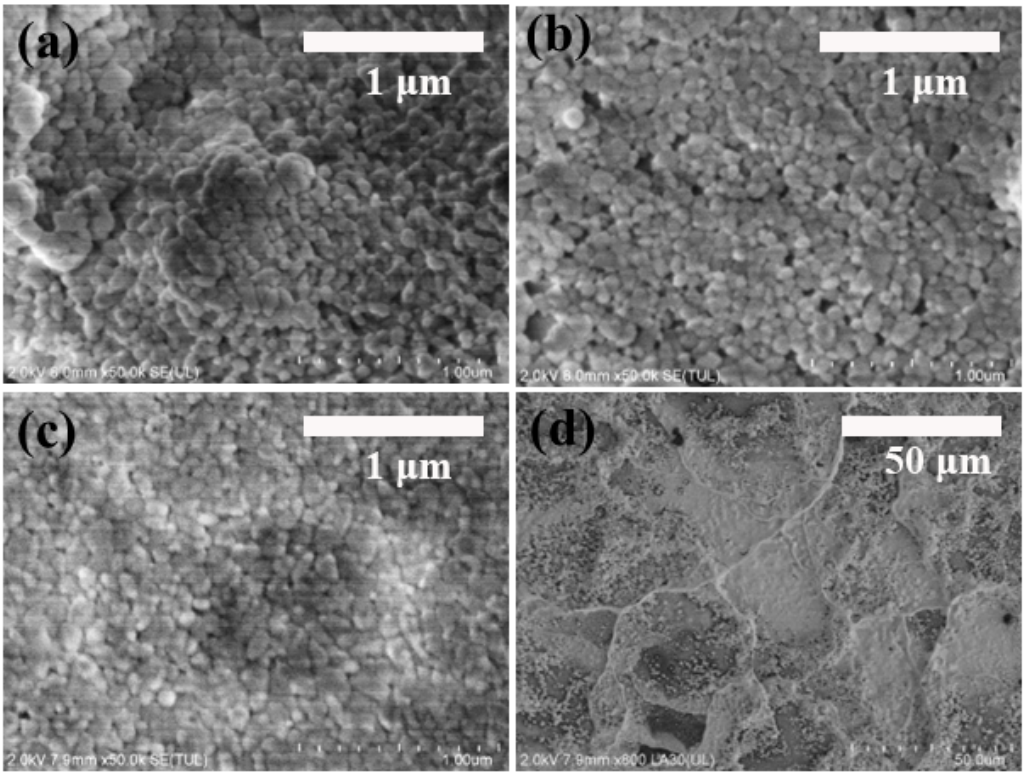

Figure 5.21. SEM images of the $Cs_3Bi_2I_9$ thin films with (a) 40 (b) 50 and (c) 60 depositions. (d) Low angle BSE image of the 60 times deposited $Cs_3Bi_2I_9$ thin film.

Chemical states

X-ray Photoelectron Spectroscopy (XPS)

The XPS high-resolution scans of core-levels of Cs, Bi, I and O after an Ar ion etching of the d60 thin film are depicted in **Figure 5.22**. The d60 thin film was deposited at 200 ℃

for 60 minutes and therefore is more prone to oxidation. The peaks in the Cs 3d scan at 724.58 and 738.58 eV are assigned to Cs $3d_{5/2}$ and $3d_{3/2}$, signifying the +1 state. In Bi 4f spectrum, the doublet at 158.94 and 164.25 are assigned to the $4f_{72}$ and $4f_{5/2}$ peaks of Bi^{3+} whereas the peaks at 156.93 and 162.23 eV correspond to Bi^{0} states in the thin films. The etching process to remove the film surface layer results in the generation of metallic bismuth. The I 3d scan shows two peaks at 619.03 and 630.53 eV, corresponding to the $3d_{5/2}$ and $3d_{3/2}$ peaks suggesting the I^{-} state. The deconvoluted O 1s spectrum displays two peaks at 532.46 and 530.68 eV which are attributed to the adsorbed atmospheric oxygen and oxygen from bismuth oxide, respectively.

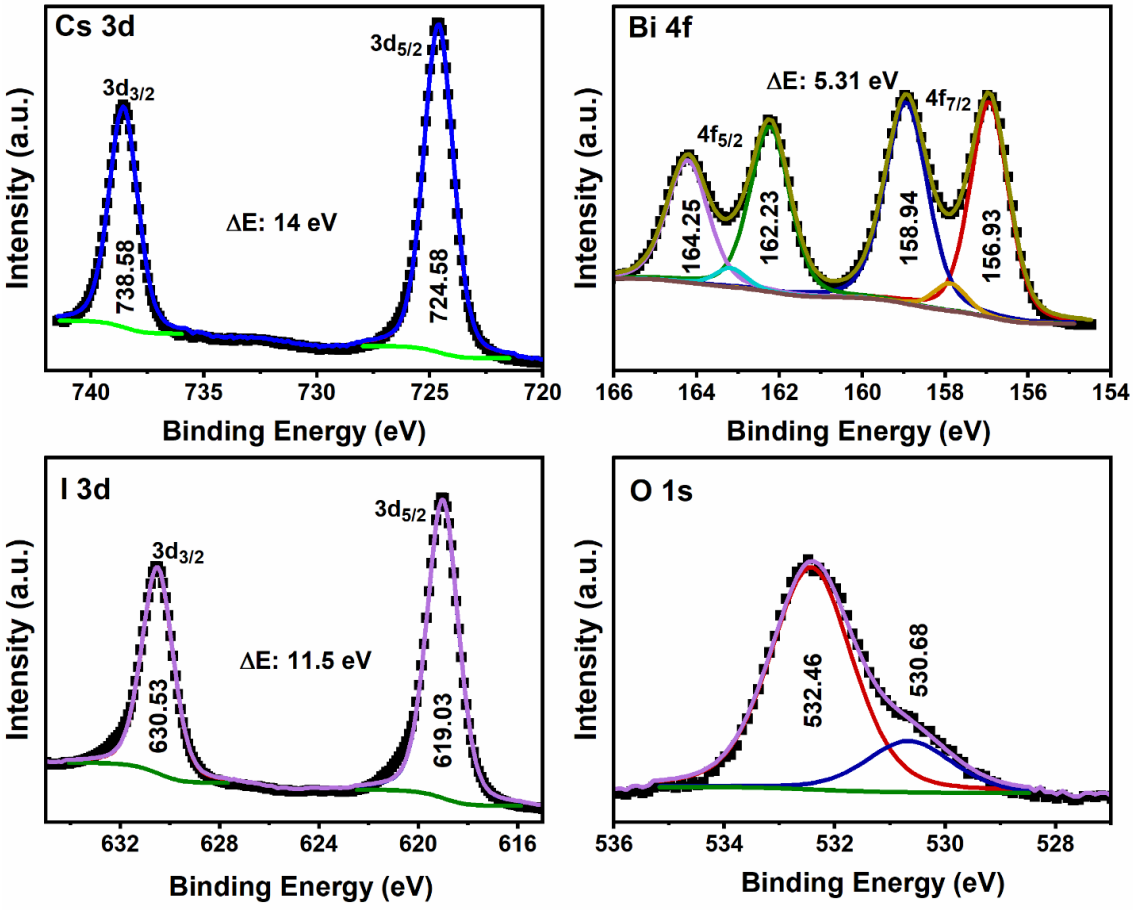

Figure 5.22. XPS high-resolution spectra of $Cs_3Bi_2I_9$ thin film (d60) after a single etching.

Optical properties

UV-Vis-NIR spectroscopy

The absorbance, transmittance and reflectance of the films are shown in **Figure 5.23**. Again, sharp absorption is absent in these films, which may suggest the powdery nature of the thin films.

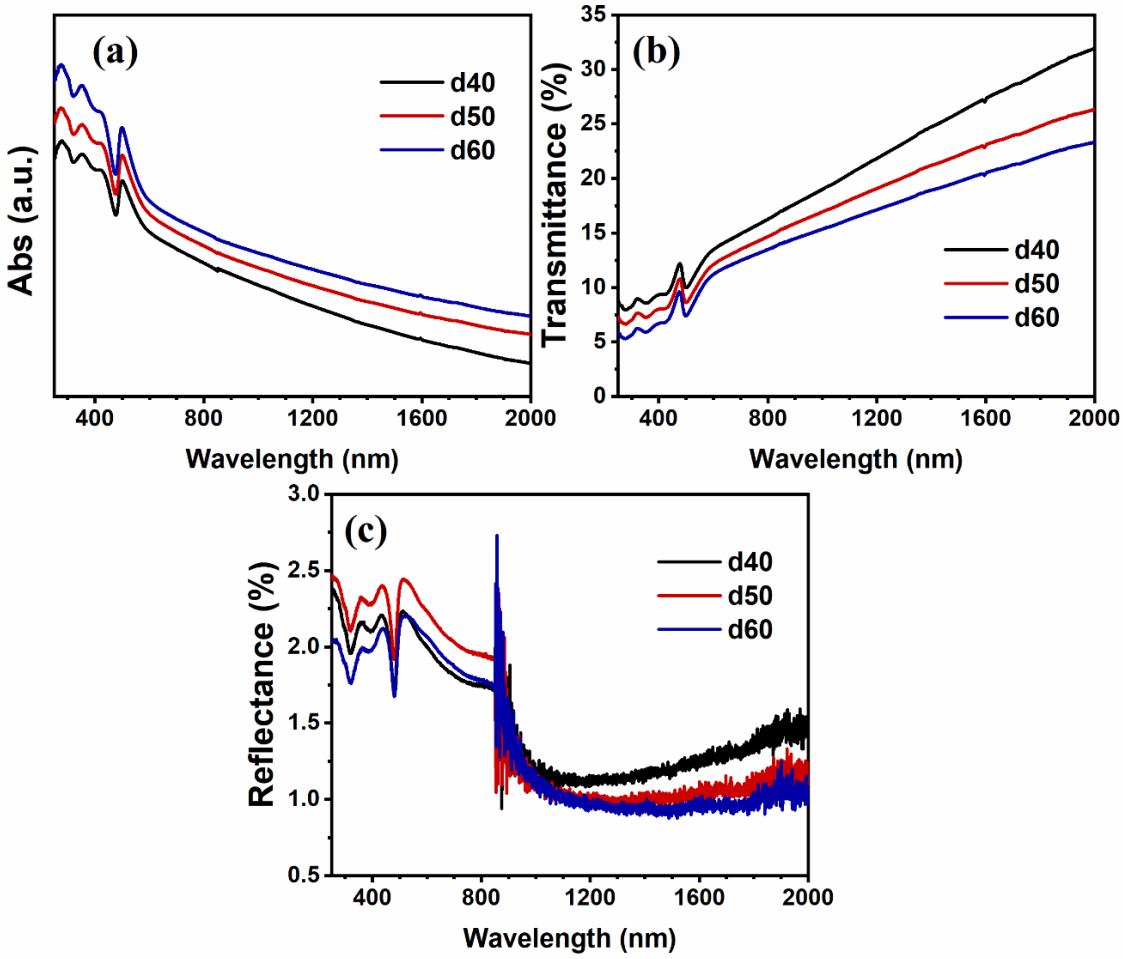

Figure 5.23. (a) Absorbance, (b) transmittance and (c) reflectance spectra of $Cs_3Bi_2I_9$ thin films with different deposition numbers.

Photoresponse

Figure 5.24 depicts the photoresponse of the thin films at 5 V bias under the illumination of a 50 W halogen lamp. The response curves demonstrate an increase in current with higher deposition numbers or higher thickness. The current under illumination increased

from ~60 to ~180 pA as the deposition was increased from 40 to 60 times. However, an increase in the dark current was also noted from ~47 to 130 pA.

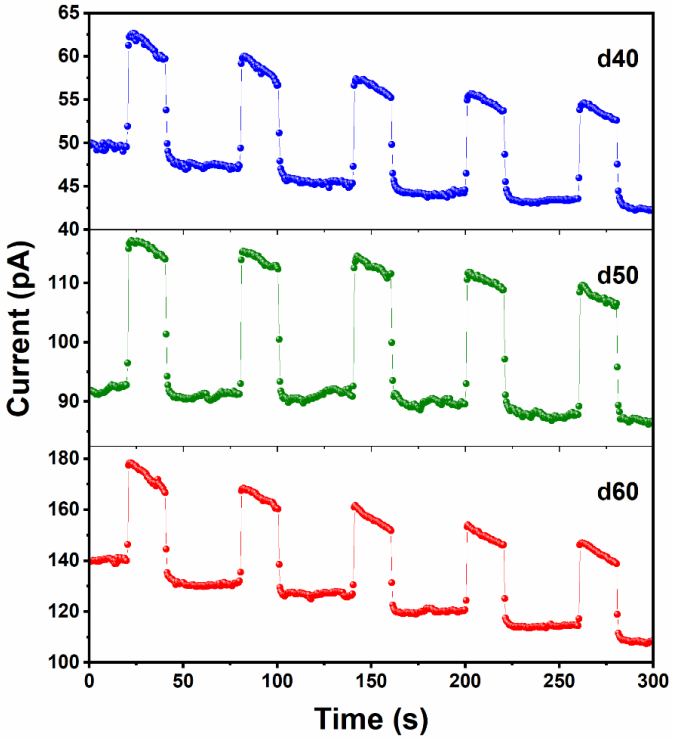

Figure 5.24. The photoresponse measurements of $Cs_3Bi_2I_9$ thin films with different number of depositions.

5.3. $Cs_3Bi_2I_9$ thin films from concentrated precursor solutions

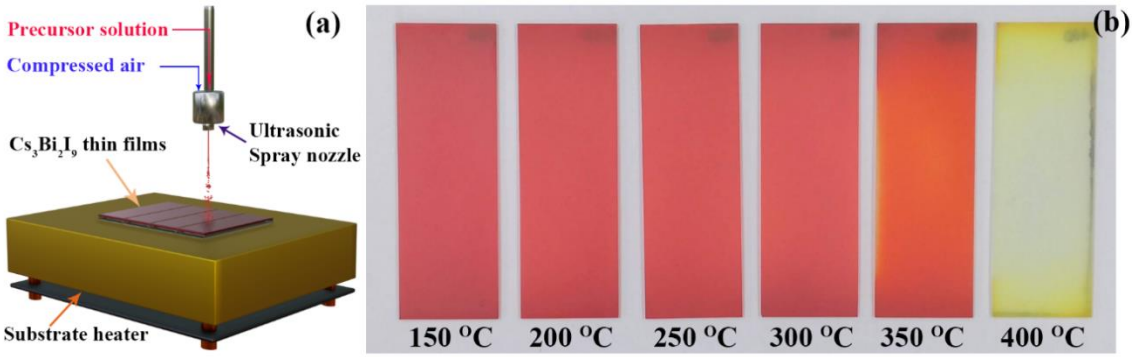

Figure 5.25. (a) The single-step ultrasonic spray deposition of $Cs_3Bi_2I_9$ thin films on a heated substrate. (b) The as deposited $Cs_3Bi_2I_9$ thin films at various substrate temperatures.

The $Cs_3Bi_2I_9$ thin films were deposited using a DMF-based precursor solution containing 0.1 M BiI_3 and 0.15 M CsI. **Figure 5.25**a shows the schematic representation of single-

step spray deposition of $Cs_3Bi_2I_9$ thin films and **Figure 5.25**b shows the spray-deposited films.

The substrate temperature is varied from 150 to 400 ℃ to analyze the thin film formation and *in situ* crystallization of the $Cs_3Bi_2I_9$ phase. Since the precursor solution is sprayed onto the heated substrates in ultrasonic spray deposition, the evaporation rate of the solvent is highly influential in the thin film formation. A balanced spray rate and solvent evaporation rate are required to avoid cracks, agglomerations and dewetting.

5.3.1. Structure

X-ray diffraction (XRD)

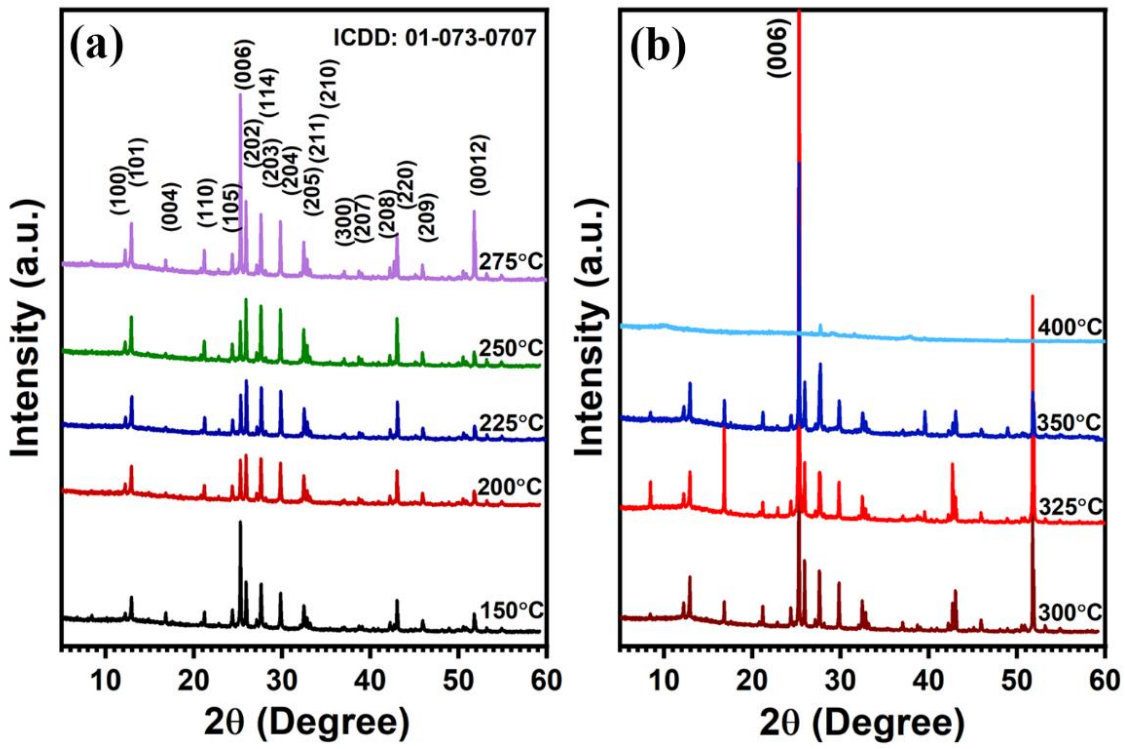

Figure 5.26. Diffraction patterns of the $Cs_3Bi_2I_9$ films deposited at various substrate temperatures (a) 150-275 ℃ and (b) 300-400 ℃.

Figure 5.26a & b show the X-ray diffraction (XRD) patterns of the $Cs_3Bi_2I_9$ thin films in agreement with the hexagonal $Cs_3Bi_2I_9$ phase (ICDD ref. no: 01-073-0707) with $P6_3/mmc$ (194) symmetry (Figure 5.27a**)** [88]. Here, the major peaks noted are (101), (110), (006), (202), (203), (204), (205), (220) and (0012) at 2θ values of 12.9°, 21.17°, 25.27°, 25.91°,

27.59°, 29.80°, 32.45°, 43.02° and 51.77°, respectively. In addition, low intensity peaks corresponding to (100), (004), (105), (114), (211), (210), (300), (207), (208) and (209) planes are also noted in all the diffractograms.

The XRD analysis up to 325 °C did not reveal any secondary phases corresponding to impurities. The XRD indicates phase-pure $Cs_3Bi_2I_9$ film growth on glass substrates by ultrasonic spray deposition in the temperature range of 150 – 325 ℃ with atmospheric conditions.

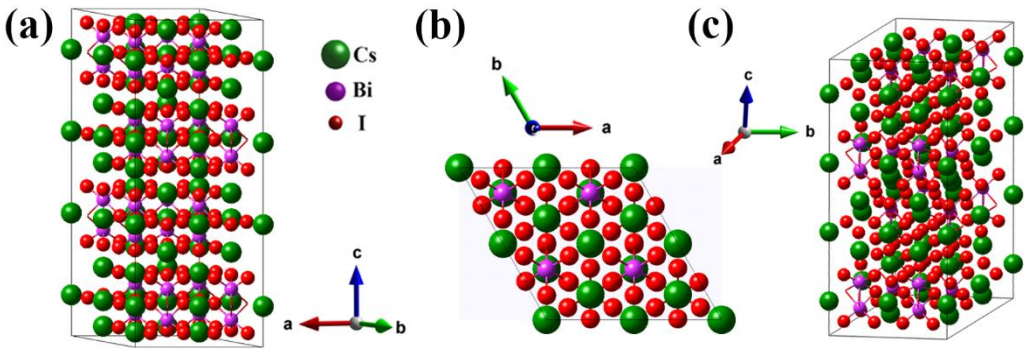

Figure 5.27. (a) The 2×2×2 supercell of $Cs_3Bi_2I_9$ structures build in MedeA software, Materials Design, Inc and it's (b) (006) and (c) (202) planes.

The film deposited at 150 ℃ shows (006) preferred orientation, while at 200 ℃ and 250 ℃, the relative intensity of the (006) peak is reduced to match the growth along (202) direction [102,107]. Again from 275 to 325 ℃, the preferred growth along the (006) plane perpendicular to the substrate surface is regained. The atomic structures of $Cs_3Bi_2I_9$ along the (006) and (202) planes are demonstrated in Figure 5.27b, c. The growth of $Cs_3Bi_2I_9$ films during the spray deposition can be understood based on the influence of four factors in direct control of substrate temperature, namely, (i) rate of crystallization, (ii) dissolution-recrystallization, (iii) solvent vapor annealing and (iv) thermal annealing between the depositions. Here, the low temperature delays solvent evaporation, slowing the crystallization of $Cs_3Bi_2I_9$, which favors a (006) preferred growth as seen in an earlier report of one-step spin-coated films where they were post-treated at low temperatures for slow crystallization to achieve large grain growth [73,102]. Further, the subsequent spray cycles at a low solvent evaporation rate can cause a dissolution-recrystallization process

that can favor the growth in other directions. For example, the spin-coated $Cs_3Bi_2I_9$ films after a dissolution-recrystallization process were (101) oriented [107]. The effects of solvent vapor annealing must be considered as the spray deposition process occurs in a closed chamber. In a previous report, the solvent-annealing of similar 0D-$(CH_3NH_3)_3Bi_2I_9$ film led to the onset of peaks corresponding to (10*l*) and (20*l*) planes, whereas a simple thermal-annealing resulted in more growth only along (00*l*) planes [215]. Furthermore, thermally annealed $Cs_3Bi_2I_9$ films up to 200 ℃ showed (006) oriented growth along with peaks corresponding to (20*l*) and (10*l*) peaks [96].

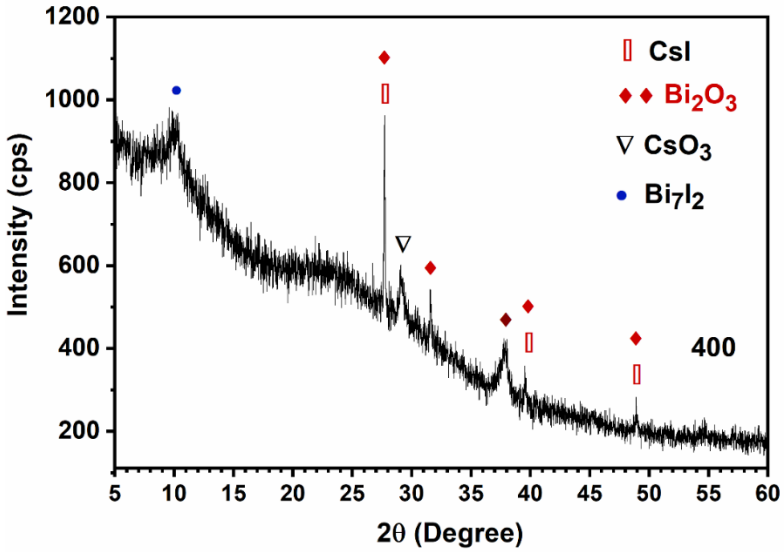

Figure 5.28. XRD profile of the thin film deposited at 400 ℃ substrate temperature.

Similar intensities are seen for the reflections corresponding to (006), (202), (203) and (204) planes in thin films fabricated at 200-250 ℃. In comparison to the film at 150 °C, the (006) oriented growth is significantly reduced at these moderate temperatures due to the increased crystallization rate. A combined effect of dissolution-recrystallization and solvent vapor annealing aids the growth of (101), (202), (203) and (204) planes observed in the XRD patterns. Higher deposition temperatures (275-325 ℃) expose the films to thermal annealing in between the depositions, in addition to the rapid crystallization, assisting the coalescence of crystallites and c-axis oriented growth [96,215]. However, the scattering intensities are reduced at 350 °C, indicating that the compound was evaporated during the deposition. Besides, minor peaks corresponding to CsI (00-006-0311) and Bi_2O_3

are observed in this XRD pattern suggesting the onset of $Cs_3Bi_2I_9$ decomposition at 350 ℃. Further at 400 ℃, the ternary film is completely decomposed with more evaporation showing only peaks corresponding to Bi_2O_3 (01-074-1374), CsO_3 (01-076-0327) and Bi_7I_2 (00-042-1293) phases as marked in Figure 5.28.

The average crystallite size (D) is estimated from the XRD profiles using the Scherrer equation (2.3) [216]. The lattice parameters are determined following a simple Rietveld refinement and the texture coefficients corresponding to (006) and (202) planes are calculated using the equation (2.5). The analysis of texture coefficients reveals that while the growth along the (006) plane is favored at high and low substrate temperatures; this preferential orientation is reduced at the intermediate temperatures (200 - 250 ℃) in spray deposition. The structural details are presented in Table 5-1.

Table 5-1. Structural parameters of pure $Cs_3Bi_2I_9$ films calculated from the XRD patterns.

Substrate temperature (℃)	Lattice parameters (Å)		Texture coefficient		Crystallite size (nm)
	a(=b)	c	TC_{006}	TC_{202}	
150	8.413	21.186	3.36	0.72	114
200	8.412	21.187	1.75	0.92	80
225	8.411	21.182	1.59	1.06	88
250	8.413	21.188	1.38	1.04	98
275	8.414	21.189	2.40	0.47	115
300	8.414	21.187	3.63	0.34	115
325	8.416	21.191	3.69	0.09	146

Raman spectroscopy

The Raman spectra of phase-pure thin films given in Figure 5.29 display major peaks near 65, 93 and 148 cm^{-1} and shoulders around 104 and 120 cm^{-1}. These peaks are associated with the various vibrational modes of $Cs_3Bi_2I_9$ [96,102,217]. Higher energy peaks result from the stretching of the terminal (~148 cm^{-1}) and bridging (~104 cm^{-1}) Bi-I bonds in the isolated $(Bi_2I_9)^{3-}$ anionic units, as seen in Figure 5.29, whereas the low-frequency spectra (~65 cm^{-1}) is described by their interactions with Cs^+ cations [92,94,217]. The peaks appear

slightly shifted to 63, 104 and 148 cm^{-1}, along with shoulders at 93 and 120 cm^{-1} in the case of films deposited at 350 °C.

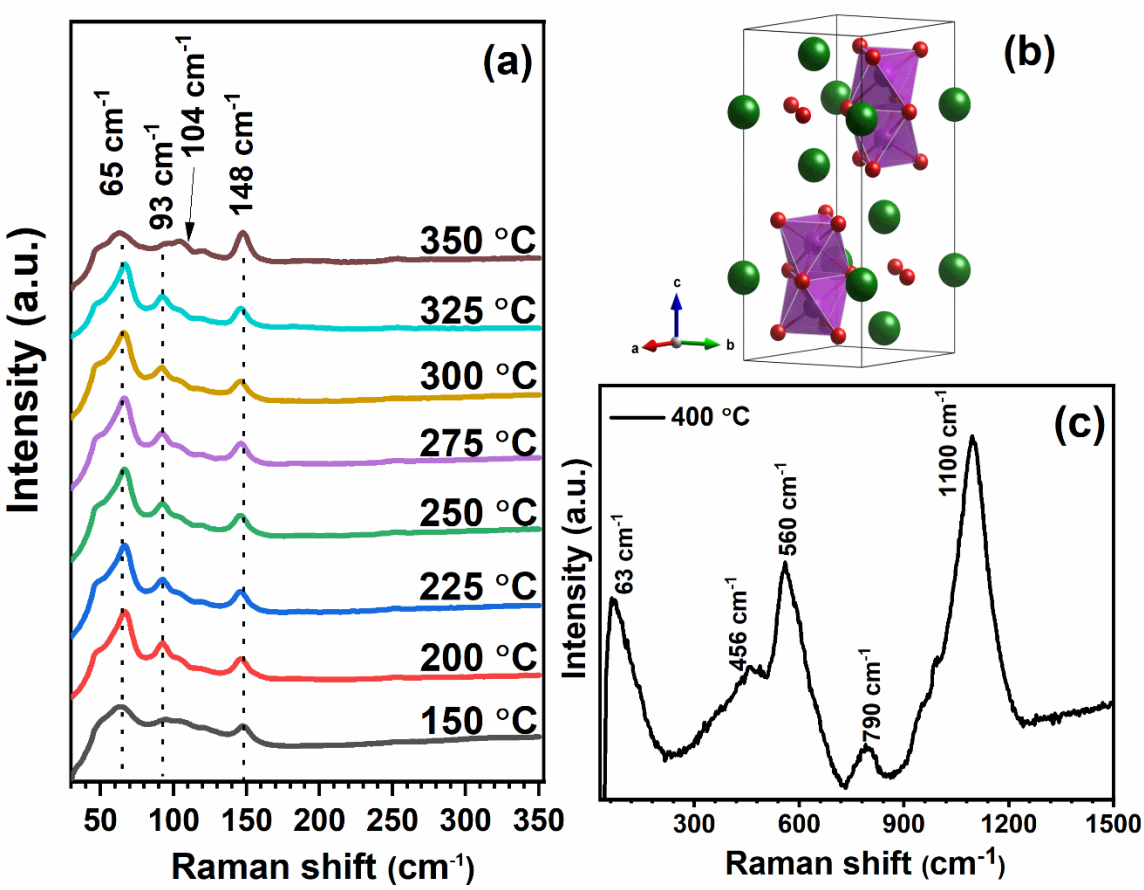

Figure 5.29. (a) The Raman spectra of $Cs_3Bi_2I_9$ films deposited at different substrate temperatures. (b) The $Cs_3Bi_2I_9$ structure with $[Bi_2I_9]^{3-}$ dimers. (c) The Raman spectrum of the $Cs_3Bi_2I_9$ film deposited at 400 °C.

Further, the transparent films formed at 400 °C show broad Raman peaks at different wavenumbers 63, 456, 560 and 1100 cm^{-1}, as seen in Figure 5.29b. These peaks are assigned to the α-Bi_2O_3, which has characteristic peaks around 62, 87, 129, 332, 456, 537, 1042 and 1414 cm^{-1}, which are concurrent with the XRD analysis [218]. The peaks between 120 and 150 cm^{-1} are associated with the displacement of Bi and O atoms, whereas the peaks between 100 and 200 cm^{-1} are attributed to the Bi-O vibrations in the BiO_6 octahedra. The higher energy peaks in the Raman spectrum of the bismuth oxide-rich film formed at 400 °C are caused by the symmetric stretching and Bi-O stretching vibrations [218].

5.3.2. Chemical composition and mapping

Energy Dispersive X-ray (EDX)

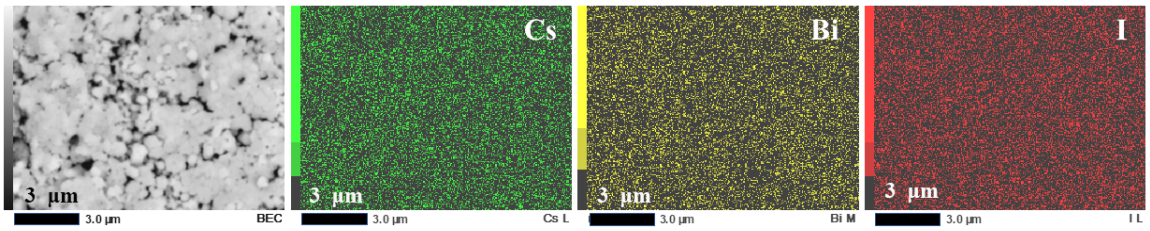

Figure 5.30. Distribution of Cs, Bi and I in the $Cs_3Bi_2I_9$ film deposited at 250 ℃ substrate temperature.

The elemental distribution images in Figure 5.30 obtained from the EDX analysis show that Cs, Bi and I are uniformly distributed throughout the spray-deposited films. Additionally, the elemental composition shown in Table 5-2 indicates that the films are iodine-rich and that the composition remains the same up to 300 ℃. However, at 350 ℃ substrate temperature, where the decomposition, evaporation, and oxidation of the compound are observed, a significant reduction in iodine content is noted.

Table 5-2. The elemental composition from EDX analysis (area of 2 μm^2) of spray-deposited films.

Substrate temperature (℃)	Cs/Bi (1.5)	I/Bi (4.5)	I/(Cs+Bi) (1.8)
150	1.3	8.9	4.1
200	1.2	8.8	3.9
250	1.2	9.3	3.9
300	1.3	9.4	4.2
350	1.3	7.6	3.3

Similar to the observations in the X-ray diffraction, Raman spectrum, and SEM image, the elemental composition also supports the presence of bismuth oxide (Bi_2O_3) and CsI in the 350 ℃ films in addition to the $Cs_3Bi_2I_9$ phase. Spray deposition at 400 ℃ causes the $Cs_3Bi_2I_9$ solution to rapidly decompose at the substrate surface, with significant I and Cs evaporation resulting in Bi_2O_3 and CsO_3, as well as a negligible amount of metal iodides.

5.3.3. Morphology

Scanning Electron Microscopy (SEM)

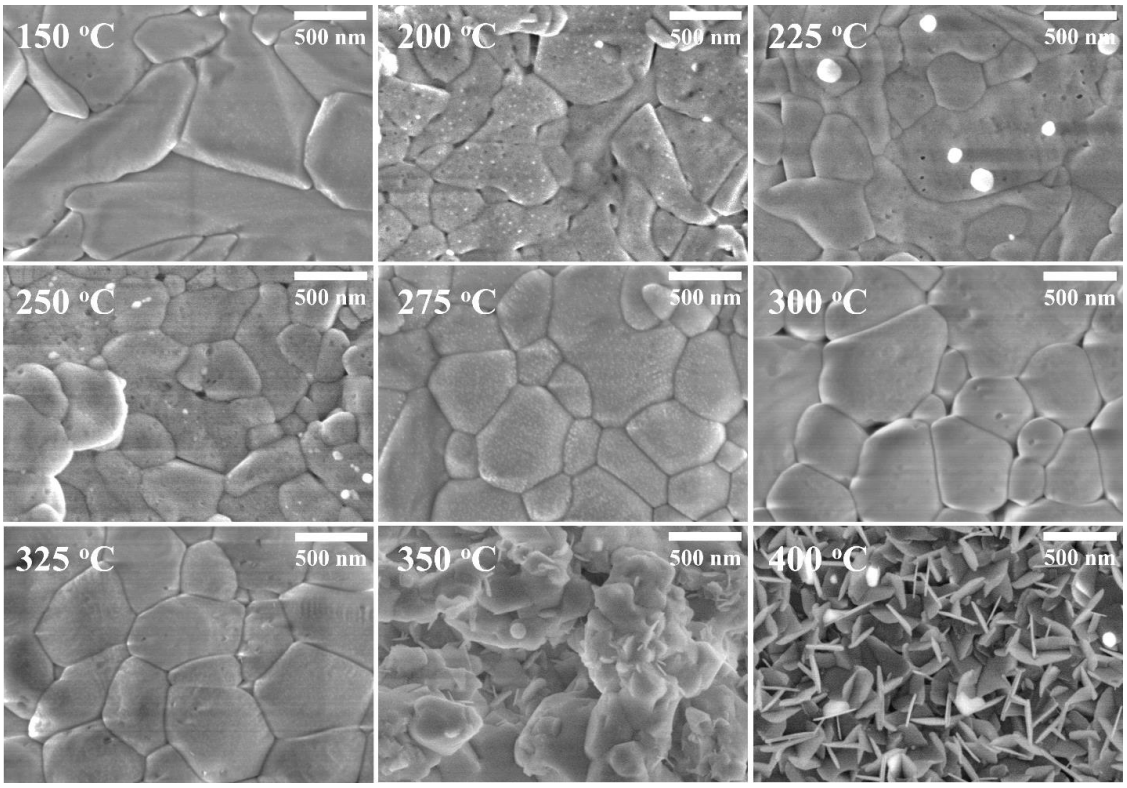

Figure 5.31. The scanning electron micrographs of spray deposited $Cs_3Bi_2I_9$ films at different substrate temperatures.

The SEM images in Figure 5.31 demonstrate that similar to organic lead halide perovskites, the spray-deposited $Cs_3Bi_2I_9$ films have compact morphology and large grains [219,220]. In the films deposited at temperatures below 250 °C, the average particle size ranges from 150 to 800 nm. In the films formed at 150 °C, long particles were seen with lengths up to 1.7 μm. However, from 250 °C onward, well-packed particles (300 - 900 nm) with a more circular shape are seen. This could be the result of more controlled crystallization with a faster solvent evaporation rate and dissolution-recrystallization in the ambient DMF solvent vapor [96]. This differs from our earlier report on two-step spray-deposited $Cs_3Bi_2I_9$ films with flake-like morphologies [217]. However, spray-coated Cs containing lead halide perovskite [221] and thin films made of $(CH_3NH_3)_3Bi_2I_9$ [82,83] were found to have such large and compact polygonal particle morphologies. Furthermore, the cross-

sectional SEM images in Figure 5.32 show that ultrasonic spray deposition can easily grow grains as a single layer perpendicular to the substrate, even for a thickness of 1800 nm. This can significantly reduce grain boundaries in the direction of carrier transport across device junctions [82].

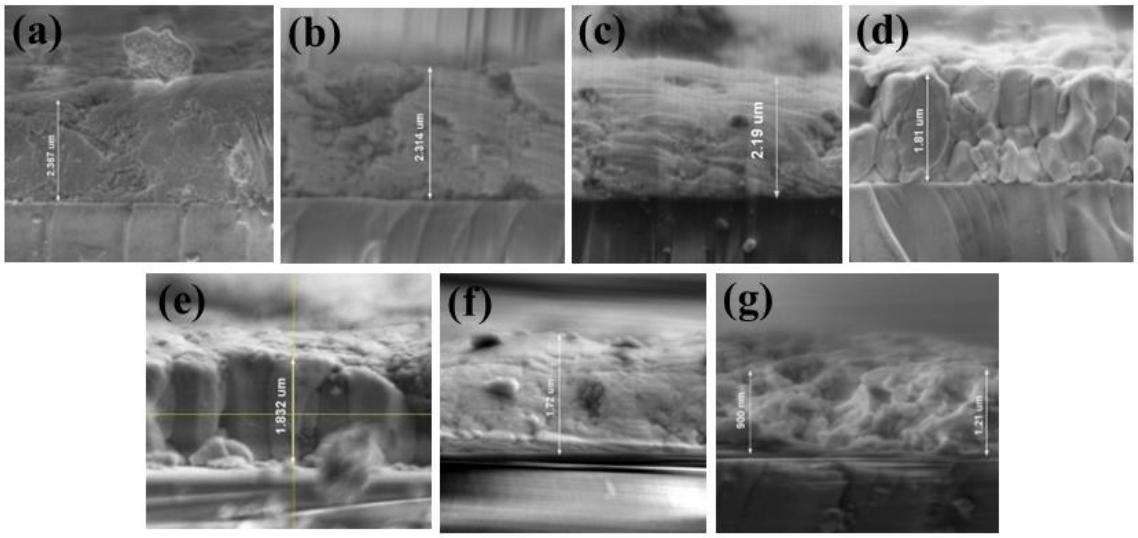

Figure 5.32. Cross sectional SEM images of spray cast $Cs_3Bi_2I_9$ films at various substrate temperatures (a) 150 (b) 200 (c) 250 (d) 275 (e) 300 (f) 325 and (g) 350 ℃.

At 350 °C, void regions and a change in morphology from large particles to very thin flakes with a width of 108 nm and a thickness of 12 nm are also noticeable, indicating the beginning of evaporation of the film. The thickness is reduced to as low as 900 nm due to the significant evaporation at 350 ℃. Further at 400 ℃, the morphology completely transforms into flakes (size ~227 nm, thickness ~ 30 nm). As seen from the XRD and Raman analysis, the formation of such flakes can be attributed to the formation of Bi_2O_3 following the breakdown and oxidation of $Cs_3Bi_2I_9$ [222].

5.3.4. Chemical states

X-ray photoelectron spectroscopy (XPS)

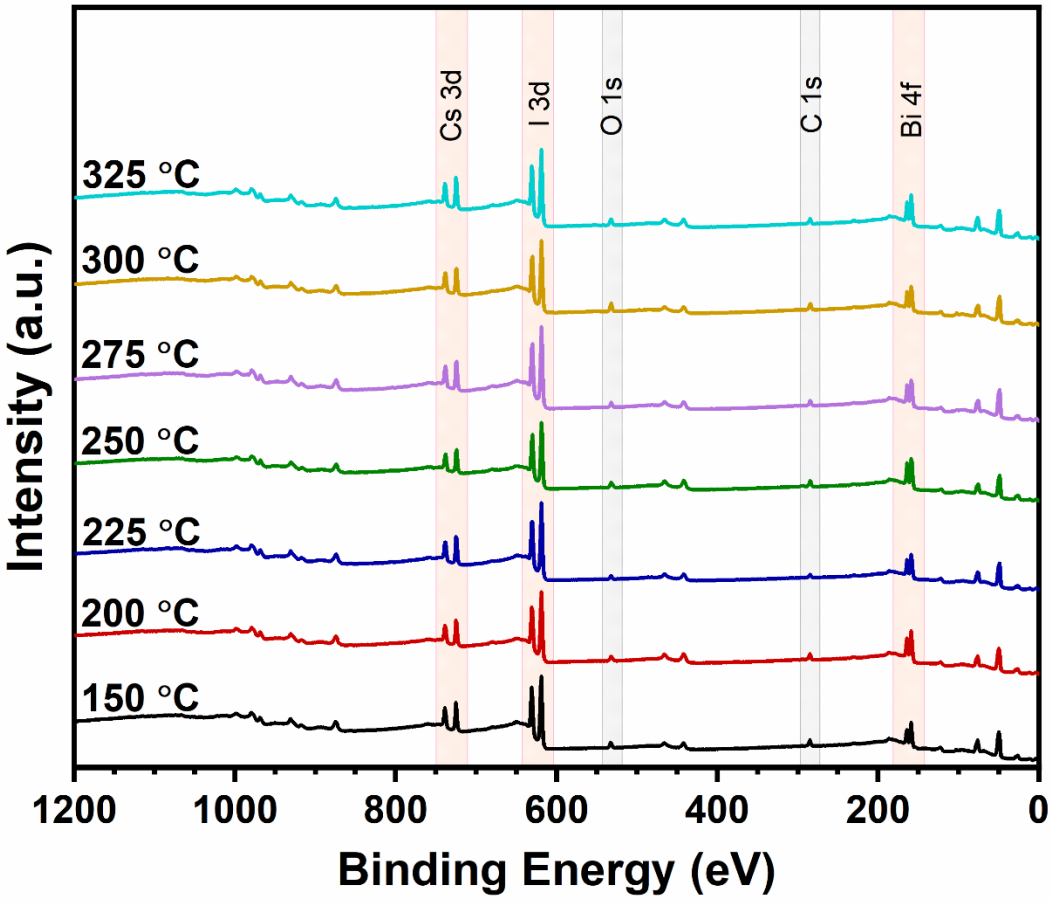

Figure 5.33. Survey spectrum of spray deposited $Cs_3Bi_2I_9$ films at different substrate temperatures.

Spray-deposited $Cs_3Bi_2I_9$ films are further examined using X-ray photoelectron spectroscopy (XPS). Characteristic signals from Cs, Bi, I, O and C are recognized from the survey scan patterns in Figure 5.33. The chemical states of the elements are identified from the core-level spectra, obtained by the high-resolution scan of the film surface, as displayed in Figure 5.34. At lower temperatures, Cs $3d_{5/2}$ and $3d_{3/2}$ peaks associated with the +1 state are noted at 724.58 and 738.58 eV with a spin-orbit splitting of 14 eV [130]. The Bi $4f_{7/2}$ and $4f_{5/2}$ peaks are found at 158.76 and 164.07 eV with a separation of 5.31 eV, specifying the Bi^{3+} state in $Cs_3Bi_2I_9$ [223]. The intense peaks observed at 618.98 and 630.48 eV at a

spin-orbit separation of 11.5 eV are ascribed to the $3d_{5/2}$ and $3d_{3/2}$ peaks of iodine (I^-) [130,201,217,223].

Interestingly, $Cs_3Bi_2I_9$ films via this large-area deposition in normal atmospheric conditions are stable up to 300 °C substrate temperatures as other metallic species or their oxides were not observed in the XPS studies. Generally, the metallic species observed in metal halide perovskites are associated with iodine deficiency, dissociation of precursors or improper crystallization [224]. Therefore, the iodine-rich films may be suppressing the generation of any metallic bismuth in our spray deposition route.

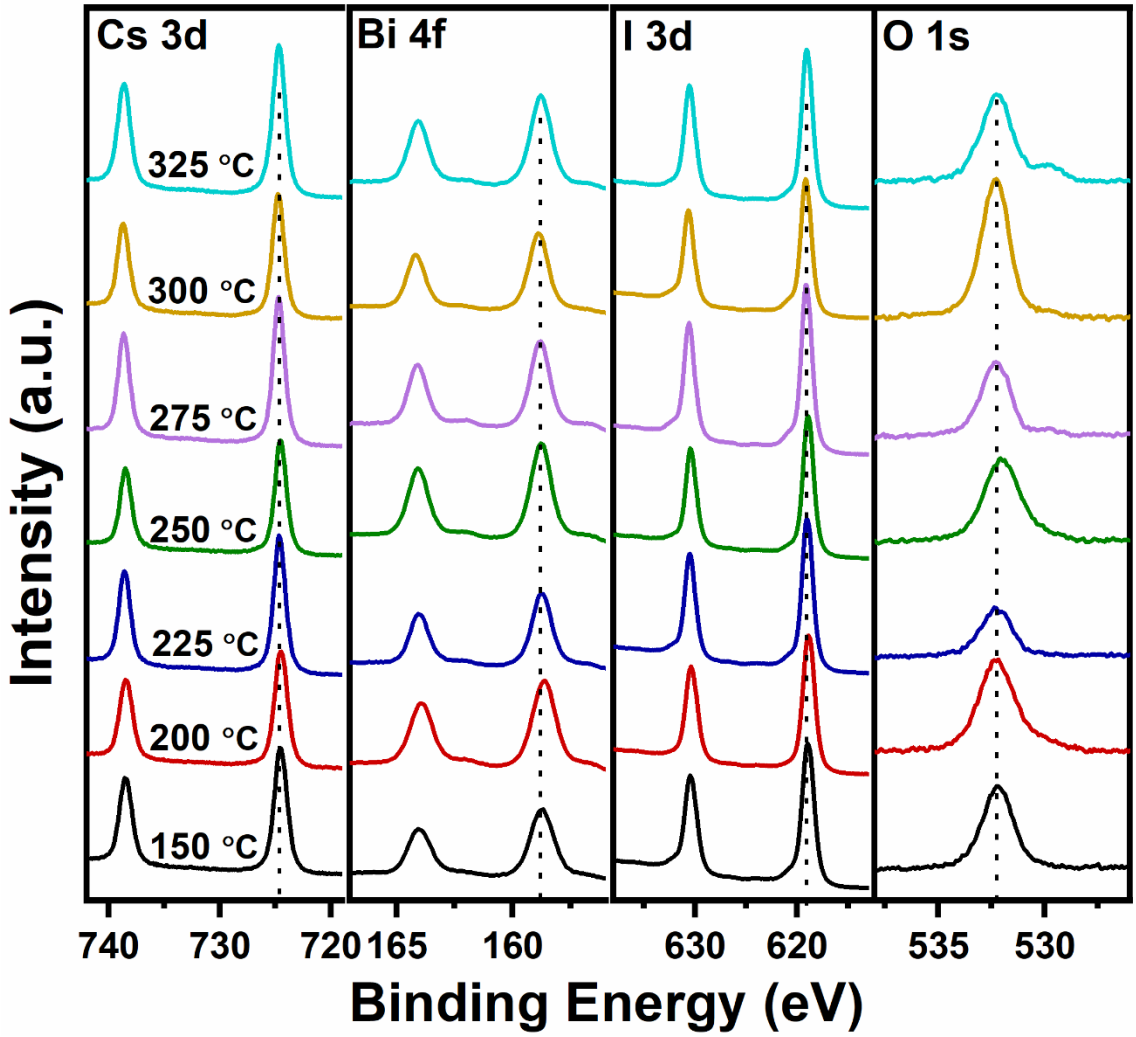

Figure 5.34. High-resolution core level scan of Cs, Bi, I and O in $Cs_3Bi_2I_9$ films spray deposited at different substrate temperatures.

However, the cesium and iodine photoelectron peak intensities are substantially reduced in the films deposited at 350 and 400 ℃ substrate temperatures indicating degradation and evaporation. In these films, the Cs 3d peaks are shifted to 724.77 and 738.69 eV suggesting the formation of CsI [217]. Besides, the intensity of Bi 4f doublet peaks associated with the Bi^{3+} state is significantly increased and their positions are seen at 158.88 and 164.18 eV, indicating changes in the local chemical environment in the ternary $Cs_3Bi_2I_9$ [225,226]. In addition to the absorbed oxygen peak at 532.08 eV, another O 1s peak at 529.53 eV is observed from 325 ℃ which indicates the formation of Bi-O bonds as a result of the oxidation of Bi in the sprayed precursor solution while Cs and I evaporate [225–227]. The binding energy values of Bi 4f and O 1s peaks are in accordance with the literature on the Bi_2O_3 phase and are also consistent with our XRD and EDX analysis [225–227].

Usually, at higher temperatures, $Cs_3Bi_2I_9$ degrade to BiI_3 and CsI and later, the former evaporates leaving only CsI behind on the substrate. However, during the spray deposition at higher temperatures, the precursor solution is continuously sprayed onto the substrate surface and the evaporation and oxidation result in more bismuth oxide on the suface along with CsI [217].

5.3.5. Optical properties

UV-Vis-NIR Spectroscopy

Figure 5.35a shows the absorption spectra of $Cs_3Bi_2I_9$ films exhibiting an absorption onset near 620 nm. The sharp absorption from 620 nm into the visible range can be observed in the films deposited at 250, 275 and 300 ℃.

The optical absorption coefficient (α) is determined according to the relation (2.8) to be 4.5×10^4 cm^{-1}. The band gap is estimated from Figure 5.35b following the Tauc relation (2.7) for direct band gap to plot hν vs. $(\alpha h\nu)^2$ and extrapolating the linear part to the x-axis where $(\alpha h\nu)^2 = 0$ [228]. The calculated direct band gap is around 2.1 eV. However, for 200 and 225 ℃ films, the values are reduced to ~1.8 eV. The band gap around 2 eV with a reasonable absorption coefficient is suitable for tandem solar cells and UV-Vis photodetectors [99].

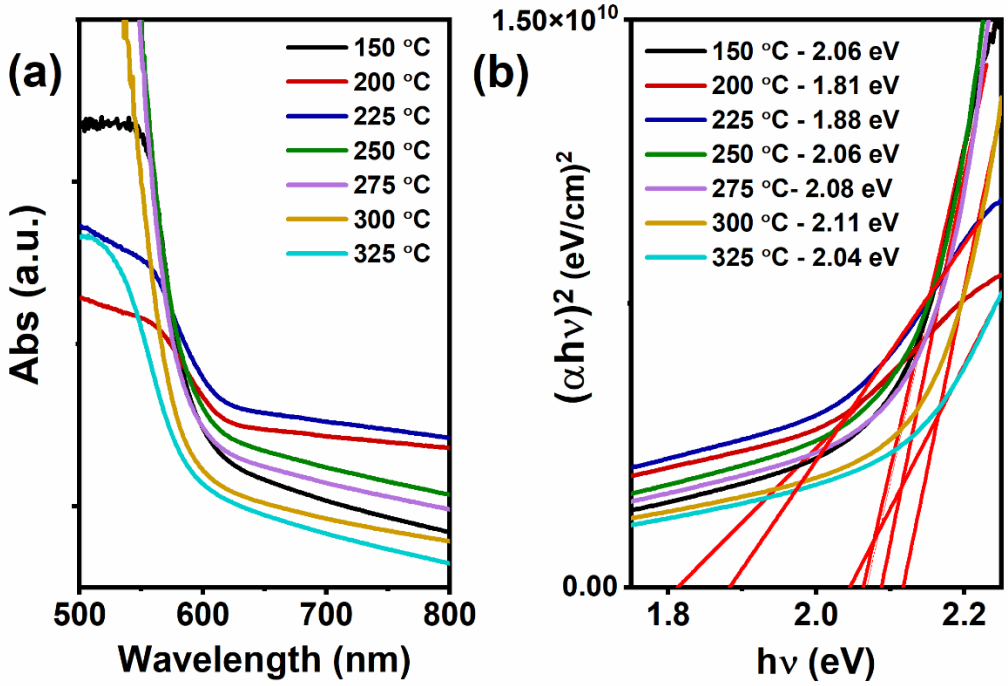

Figure 5.35. The (a) absorption spectra of $Cs_3Bi_2I_9$ films at different substrate temperature. (b) The direct band gaps of the films calculated form the absorption data.

Here, Bi^{3+} also adopts a stable $d^{10}s^2p^0$ electronic configuration just like Pb^{2+}. This provides wide bandwidth for the valence band due to the overlapping bands [229]. As determined by our DFT calculation [217], the band gap observed in $Cs_3Bi_2I_9$ is the energy difference between the covalent Bi 6s and I 5p in the valence band maximum (VBM) and Bi 6p at the conduction band minimum (CBM) [229]. In this case, the electronic structure of the compound is not significantly influenced by the Cs^+ cations. Instead, they fill the spaces between the face-shared metal halide octahedra, giving the compound its layered structure. The face-sharing octahedra produce a higher charge density around the Bi atoms in $Cs_3Bi_2I_9$ compared to the binary BiI_3 (E_g~1.67 eV) with edge-shared octahedra. Besides, the position of I 5p occupied states in the VBM of $Cs_3Bi_2I_9$ promote better hybridization with Bi $6s^2$ lone pair states resulting in the significant absorption of the compound [217,229].

5.3.6. Thermal stability

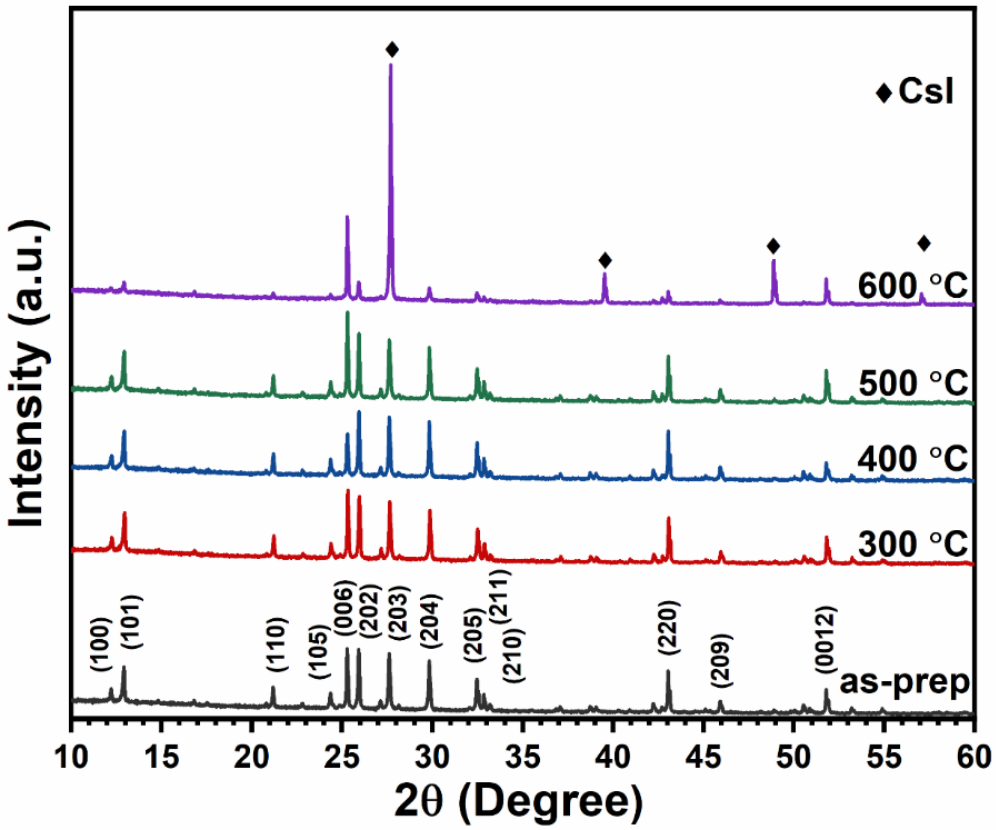

Figure 5.36. XRD patterns of RTP treated $Cs_3Bi_2I_9$ (250 ℃) films for 1 min.

To evaluate the structural and morphological changes as well as the stability of spray-deposited $Cs_3Bi_2I_9$ film, rapid thermal processing (RTP) was done at temperatures up to 600 ℃ for 1 min in low vacuum conditions (8-12 mbar). The corresponding diffractograms in Figure 5.36 demonstrate that the films are stable up to 500 ℃ but decompose to BiI_3 and CsI at 600 ℃. Compared to the 300 ℃ film, the intensity of the (006) peak reduces at 400 ℃ but again orients preferentially along the (006) plane at 500 ℃. Further, the morphological changes of $Cs_3Bi_2I_9$ films caused by rapid thermal processing can be seen in Figure 5.37.

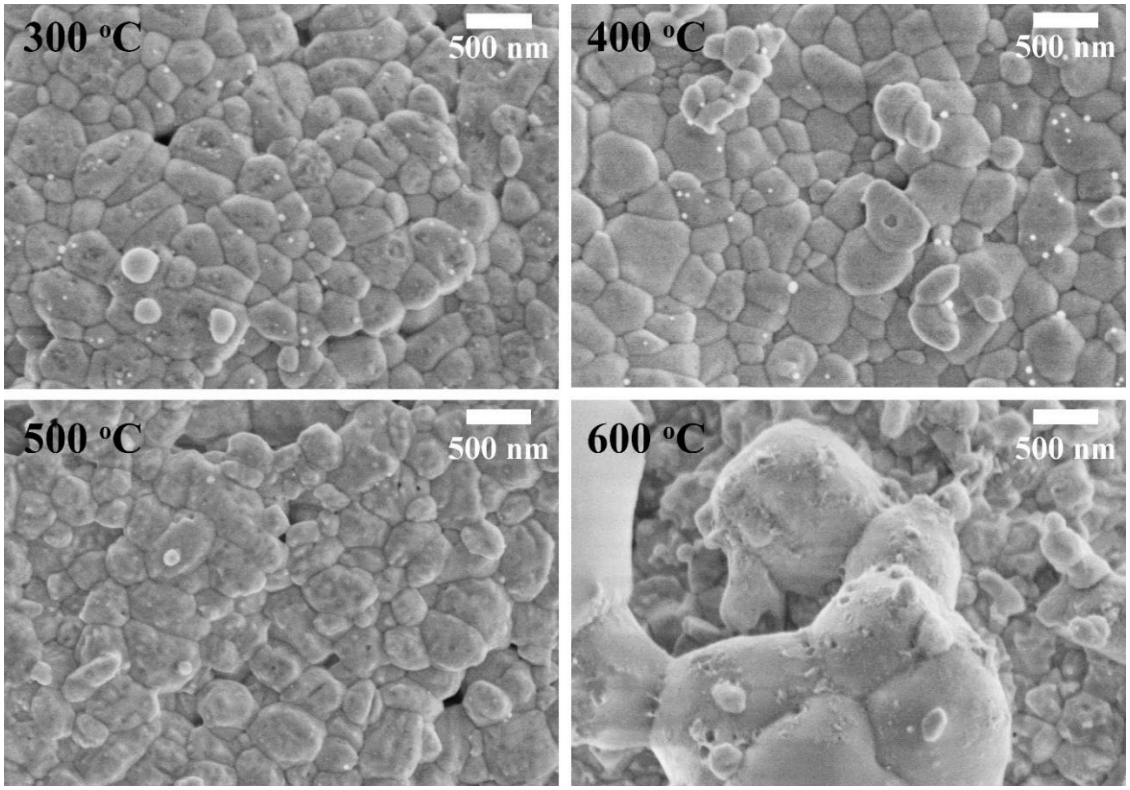

Figure 5.37. The SEM images of rapid thermal processed $Cs_3Bi_2I_9$ (250 ℃) films at different temperatures for 1 min.

According to the X-ray diffraction and SEM results, the films are stable up to 500 °C but rapidly degrade at 600 °C, forming large CsI particles up to 1 μm on the surface. The compact surface is composed of particles in the 300-500 nm range as measured from the SEM images of films treated at 300, 400 and 500 ℃.

5.3.7. Photoresponse

Photoresponse of the $Cs_3Bi_2I_9$ films are measured using Ag contacts on the film surface at 5 V bias using a 50 W halogen lamp illumination (Illuminance ~ 34029.66 lx). A stable photoresponse with a current in the nano ampere range is noted in Figure 5.38 for the films deposited at substrate temperatures of 200 to 275 ℃. The films obtained at 250 °C demonstrated stable sensitivity with a better photocurrent up to 1.4 nA despite low switching ratio in horizontal measurements.

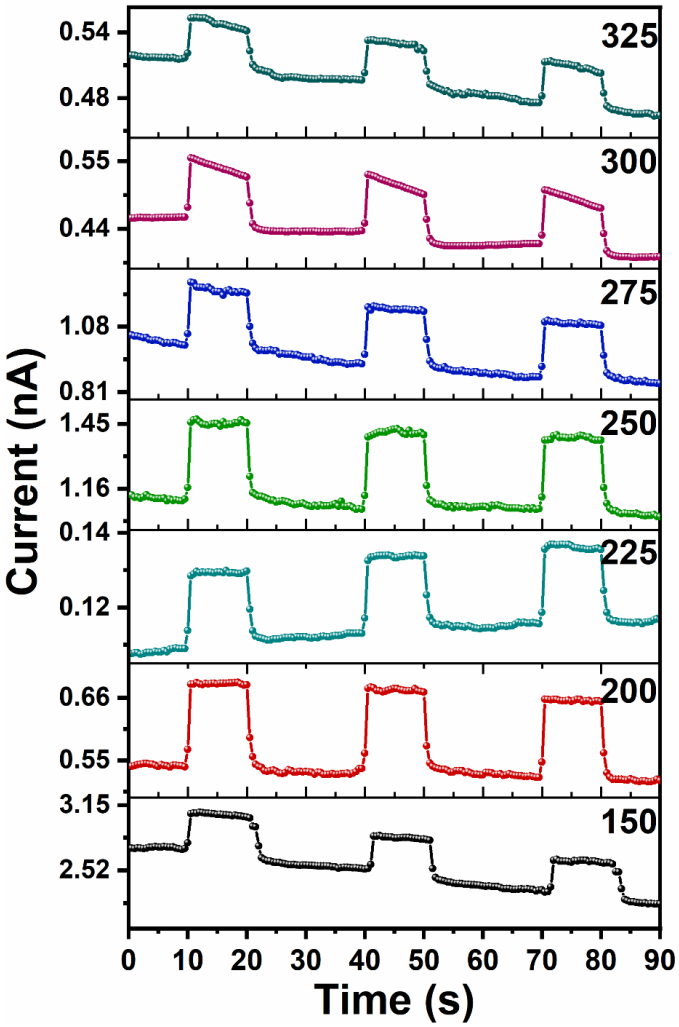

Figure 5.38. Photoresponse under 50 W halogen lamb at 5 V bias measured from horizontal Ag/$Cs_3Bi_2I_9$/Ag devices.

5.3.8. Self-powered photodetector

The absorption spectra of $Cs_3Bi_2I_9$ films indicate that they are suitable for short visible range photodetection, particularly in the blue region. Therefore, Ag/FTO/$Cs_3Bi_2I_9$/C-Ag photodetector was fabricated by depositing 250 ℃ $Cs_3Bi_2I_9$ film on the FTO-coated glass substrate. Figure 5.39a shows an exponential decay of the photocurrent from the initial cycle under an AM1.5 illumination. After 400 s, the photocurrent then stabilizes around 80 nA. The photodetection performance of the structure in the absence of any bias voltage points $Cs_3Bi_2I_9$ layers to self-powered device applications. Low dark current (~10^{-10} A) and relatively high photocurrent (~10^{-8} A) unveil the excellent self-powered photodetection

behavior of the FTO/$Cs_3Bi_2I_9$ junction. The strong FTO/$Cs_3Bi_2I_9$ Schottky junction, as seen in the inset of Figure 5.39a, forms the depletion region with a built-in electric field that separates and drives the photocarriers out of the semiconductor-electrode interface which is then collected as photocurrent. The spray-dposited device exhibits comparatively high photocurrent and, as a result, a high switching ratio. The self-powered positive photocurrent observed suggests that the holes are injected into the source terminal and electrons in the opposite direction.

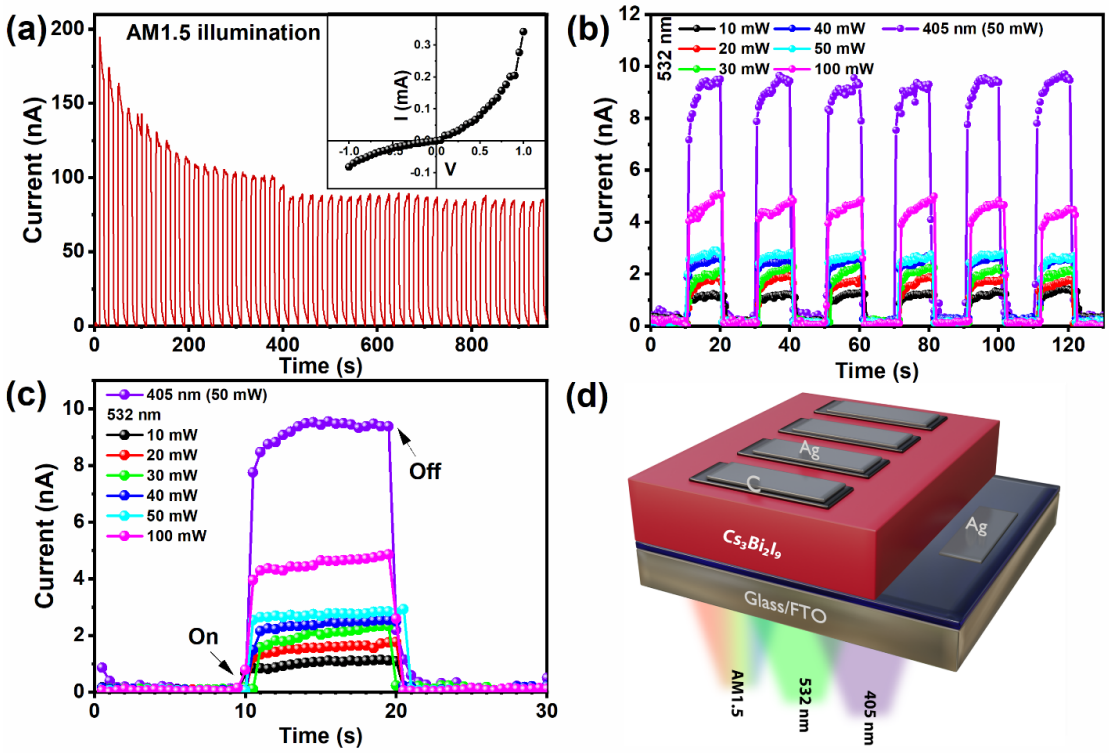

Figure 5.39. Self-powered photodetection in Ag/FTO/$Cs_3Bi_2I_9$/C-Ag photodetector under (a) AM1.5 illumination (b), (c) 532 nm laser illumination at various powers and 405 nm laser at 50 mW. (d) Schematic of the Ag/FTO/$Cs_3Bi_2I_9$/C-Ag photodetector structure.

Further, the photodetector was illuminated using 532 nm (10 - 100 mW) and 405 nm (50 mW) short-wavelength laser sources at 0 V bias and the responses are shown in Figure 5.39. The sensitivity, responsivity and detectivity are calculated at various light powers at 0 V to evaluate the heterojunction photodetector performance. The sensitivity (S) or signal-to-noise ratio (SNR), which is the photosensing performance of the photodetector, is estimated from the dark current (I_{dark}) and photocurrent ($I_{ph} = I_{light} - I_{dark}$) using the equation

(2.10). The responsivity (R) of the photodetector with an effective illumination area (A) of ~0.25 cm^2 is obtained using the equation (2.11). Further, its detectivity (D) is determined using the relation (2.12).

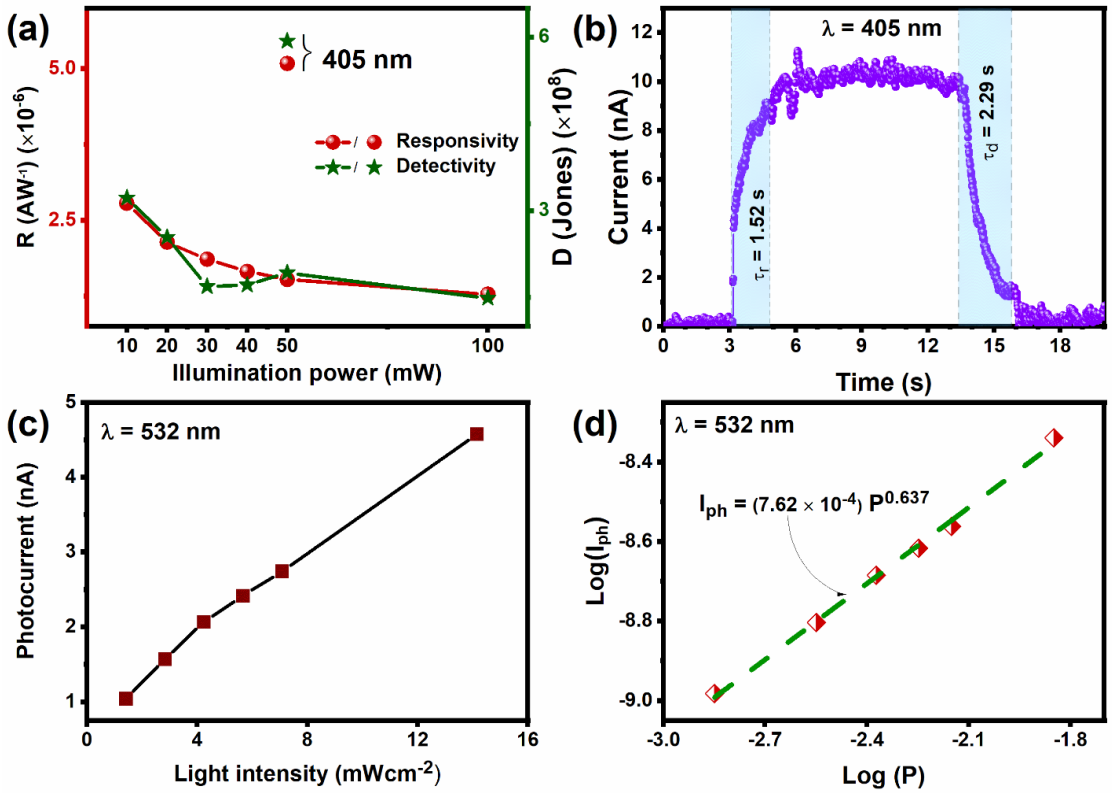

Figure 5.40. (a) The responsivity and detectivity of the FTO/$Cs_3Bi_2I_9$ photodetector. (b) The rise time and decay time calculated for the response to 405 nm illumination. (c) The linear dependence of photocurrent on light intensity and (d) the corresponding fitting of power law for 532 nm illumination.

As elucidated in Figure 5.40c, the photocurrent (I_{ph}) rises almost linearly with the power density (P) from 1.5 to 4 nA under 532 nm laser illumination and the power law ($I_{ph} = A.P^{\gamma}$) can best define the dependence, where A is a scaling constant and γ is an exponent to the light intensity [193,230]. A fitting to the power law, as shown in Figure 5.40d (dashed-line), obtain γ equal to 0.64 (between 0.5 and 1), which suggests the higher probability of electron-hole recombination and charge carrier scattering in the kinetics of photocurrent saturation [230]. The dark current detected is in the range of 48 - 94 pA. Although the absorption starts around 620 nm, the photodetector's limited performance to

532 nm illumination can be attributed to the strong excitonic behavior of $Cs_3Bi_2I_9$ above 470 nm, which is clear from earlier studies [106]. The high exciton binding energy traps the photogenerated carriers in the bioctahedral units instead of being collected at the contacts reducing the photocurrent [106]. Further, the photocurrent up on 405 nm laser illumination of 7.08 $mWcm^{-2}$ at 0 V was 9 - 10 nA giving the highest sensitivity of 157. Correspondingly, a photoresponsivity of 0.0051 mA/W and a detectivity of 5.93×10^8 Jones were determined for this self-powered photodetector based on the $Cs_3Bi_2I_9$ film. The self-powered photodetector by spray deposition has detectivity values that are comparable to those of the spin-coated $Cs_3Bi_2I_9$ polycrystalline thin-film photodetectors that were previously reported [14]. Figure 5.40b is used to calculate the response's rise time and decay time, which are determined to be 1.52 s and 2.29 s, respectively.

The 263 folds higher defect density and ~10^4 folds lower carrier mobility of the polycrystalline thin films compared to the $Cs_3Bi_2I_9$ SCs can be accounted for their limited performance [14]. The limitations imposed by the polycrystalline nature of $Cs_3Bi_2I_9$ thin films can be overcome in several ways. It is possible to enhance the transport properties by using different substrates with better lattice matching, such as the Si (111) plane. Heterostructures with 2D materials, such as graphene or MoS_2, that have excellent transport properties can also improve the photogenerated carrier collection, increasing the sensitivity of the device. In addition, using complexing agents to limit the reaction of the constituents of the precursor solution is a promising route to reduce the surface roughness and uniformity in sprayed perovskite thin films to improve the interfaces with contacts and electron transport layer.

5.4. Conclusions

The influence of various spray parameters on the properties of $Cs_3Bi_2I_9$ thin films were analyzed to understand and optimize the conditions to fabricate uniform thin films with better optoelectronic properties. All these initial experiments and analyses on the deposition parameters suggest that higher nucleation centers are needed to grow $Cs_3Bi_2I_9$ thin films while taking care of solvent evaporation. However, there are limitations to the high spray rates we can use at moderate temperatures while using a high boiling point

solvent. High spray rates may also lead to large droplets resulting in agglomerated regions. Therefore, a suitable method is to considerably increase the precursor concentration while maintaining the low spray rate for efficient solvent evaporation. The optimum spray parameters for obtaining good quality $Cs_3Bi_2I_9$ film are 200 ℃ substrate temperature, 0.3 ml/min spray rate and 10 depositions of 0.1 M/0.15 M BiI_3/CsI solution.

We synthesized high-quality $Cs_3Bi_2I_9$ films of distinctive morphology and texture for the first time via a single-step ultrasonic spray technique. Finally, incorporated the $Cs_3Bi_2I_9$ film into a self-powered photodetector with the configuration of Ag/FTO/$Cs_3Bi_2I_9$/C-Ag. The structural, morphological, chemical and optoelectronic analysis reveals that (006) texture-tuned $Cs_3Bi_2I_9$ films with large grains can be readily fabricated in atmospheric conditions using large-area ultrasonic spray deposition at substrate temperatures from 150 to 300 ℃. Moreover, the photoresponsive films have direct band gaps around ~2.00 eV with absorption coefficients in the order of ~10^4 cm^{-1} in the short wavelength region of the visible spectrum. Interestingly, the Ag/FTO/$Cs_3Bi_2I_9$/C-Ag photodetector demonstrated self-powered photodetection with sensitivity, responsivity and detectivity of 157, 0.0051 mA/W and 5.93×10^8 Jones, respectively, under a laser of 405 nm at 7.08 $mWcm^{-2}$. Rapid thermal processing of the film revealed that the films were stable up to 500 °C, making them an excellent choice for practical electronic operations.

To find a replacement for DMF in the ultrasonic spray deposition process of $Cs_3Bi_2I_9$ thin films, we explore ethanol-based precursor solutions of BiI_3 and CsI as discussed in the next chapter.

CHAPTER 6

TWO-STEP DEPOSITION OF CESIUM BISMUTH IODIDE THIN FILMS

This chapter presents our investigations to replace the DMF solvent with less toxic ethanol to fabricate $Cs_3Bi_2I_9$ thin film by ultrasonic spray deposition. Considering the limitations in solubility, we follow a two-step spray deposition.

6.1. Introduction

The research work in this chapter explains how sequential spray deposition of BiI_3 and CsI in ethanol-based precursor solutions results in the *in situ* formation of cesium bismuth iodide thin films. In order to obtain pure $Cs_3Bi_2I_9$ films, layer configuration and precursor molarity are varied to fabricate different thin film samples. They were investigated in detail using characterization techniques to probe their structure, morphology, optical and electronic properties as well as computational calculations. The optimized $Cs_3Bi_2I_9$ film formed heterojunctions with electron transport layers such as ZnO and CdS, which are analyzed to investigate on their potential for photovoltaics or photodetection.

6.2. Layer configuration and deposition numbers

6.2.1. Structure and morphology

Spray-deposited BiI_3 and CsI precursor layers

The XRD patterns of the precursor layers, BiI_3 and CsI, under the same conditions for obtaining the ternary $Cs_3Bi_2I_9$ films are shown in Figure 6.1 for comparison. BiI_3 has a rhombohedral crystal structure (ICDD ref. no: 00-048-1795, space group: R-3) with lattice

parameters a = 7.519 Å and c = 20.721 Å. The major diffraction peaks are observed at 12.79°, 14.23°, 26.96°, 35.24° and 41.55°, which are related to the (003), (101), (113), (116) and (300) planes, respectively. Besides, weak peaks corresponding to (012), (303), (119) and (223) planes are noted at 16.05°, 43.65°, 46.18° and 50.23°. On the other hand, the diffraction pattern of CsI shows an intense peak at 27.67° which is from the (110) plane, while minor peaks are observed at 31.41° and 48.78° from (200) and (211) planes, respectively. The pattern matches well with the cubic phase (ICDD ref. no: 00-006-0311, space group: Pm3m, a = 4.568 Å) of CsI.

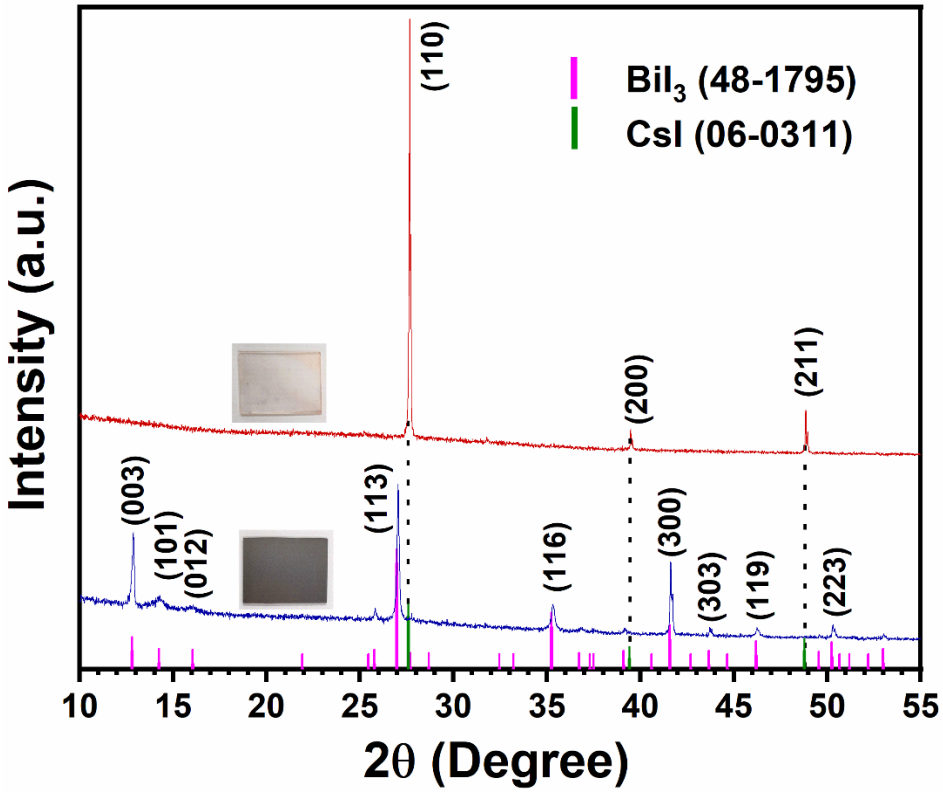

Figure 6.1. XRD patterns of BiI_3 and CsI precursor layers deposited by ultrasonic spray. Digital images of the precursor layers. (2×2.5 cm) are shown in the inset.

Spraying BiI_3 (0.01 M) solution on CsI (0.003 M) layer

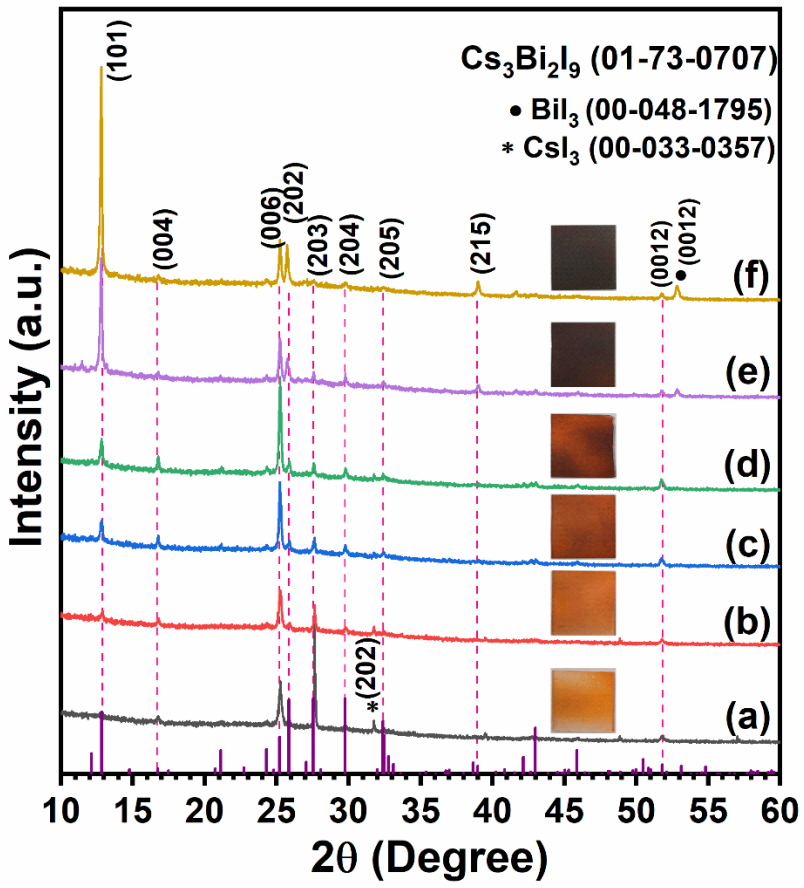

Figure 6.2. The XRD patterns of CsI/BiI_3 layer configuration with varying BiI_3 deposition numbers, (a) CB1 (b) CB2 (c) CB3 (d) CB4 (e) CB6 and (f) CB8.

Initially, a 0.01 M BiI_3 solution was reacted with a spray-deposited CsI layer (0.003 M) to investigate the crystallization of the ternary $Cs_3Bi_2I_9$. Here, the XRD profiles of the thin films obtained with the increasing number of BiI_3 depositions are analyzed, as seen in Figure 6.2. The deposition number was increased from 1 to 8 until the BiI_3 completely reacted with the underlying CsI. The films were labeled as CB1, CB2, CB3, CB4, CB6 and CB8. The XRD pattern of CB1 film indicates the emergence of a peak at 25.2° that corresponds to the (006) plane of $Cs_3Bi_2I_9$. The new peak confirms the formation of the $Cs_3Bi_2I_9$ phase as BiI_3 solution is sprayed on top of the CsI layer kept at 125 °C. The intensity of the (006) peak increases with more BiI_3 sprays (CB4) until four depositions, while the intensity of the CsI peak at 27.65° falls, which suggests more reaction and better

crystallinity of $Cs_3Bi_2I_9$. Further BiI_3 depositions lead to the peak shift from 12.84° (reflection from (101) plane of $Cs_3Bi_2I_9$) to 12.79° (reflection from (003) plane of BiI_3) with an abrupt increase in intensity revealing left-over BiI_3 in the CB6 and CB8 samples. The presence of excess BiI_3 is also evident from the shift in peak position from 25.86°, (202) plane of $Cs_3Bi_2I_9$, to 25.72°, (006) plane of BiI_3.

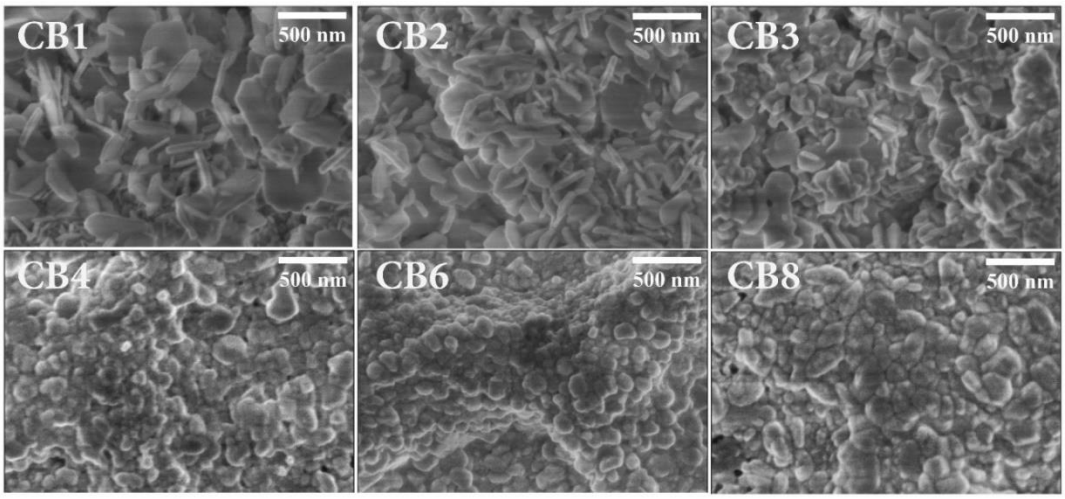

Figure 6.3. SEM images of CsI/BiI_3 thin films with 1, 2, 3, 4, 6 and 8 sprays of BiI_3 solution (0.01 M) over CsI layer (10 sprays of 0.003 M CsI solution).

The SEM images in **Figure 6.3** demonstrate the formation of $Cs_3Bi_2I_9$ nanosheets with BiI_3 deposition over CsI layer. However, with more depositions, the dissolution recrystallization of these nanosheets results in large and compact particles on the film surface.

Spraying CsI (0.009 M) solution on BiI_3 (0.01 M) layer

Additionally, the phase formation by spraying CsI solution over the BiI_3 layer was also analyzed. Here, a higher molarity (0.009 M) CsI solution was used to ensure a fast and efficient reaction with the underlying spray-deposited BiI_3 layer. Again, the number of CsI depositions was varied as 5, 10 and 15, and the XRD patterns of the samples compared to the $Cs_3Bi_2I_9$ phase (JCPDS card no: 01-73-0707) are shown in Figure 6.4.

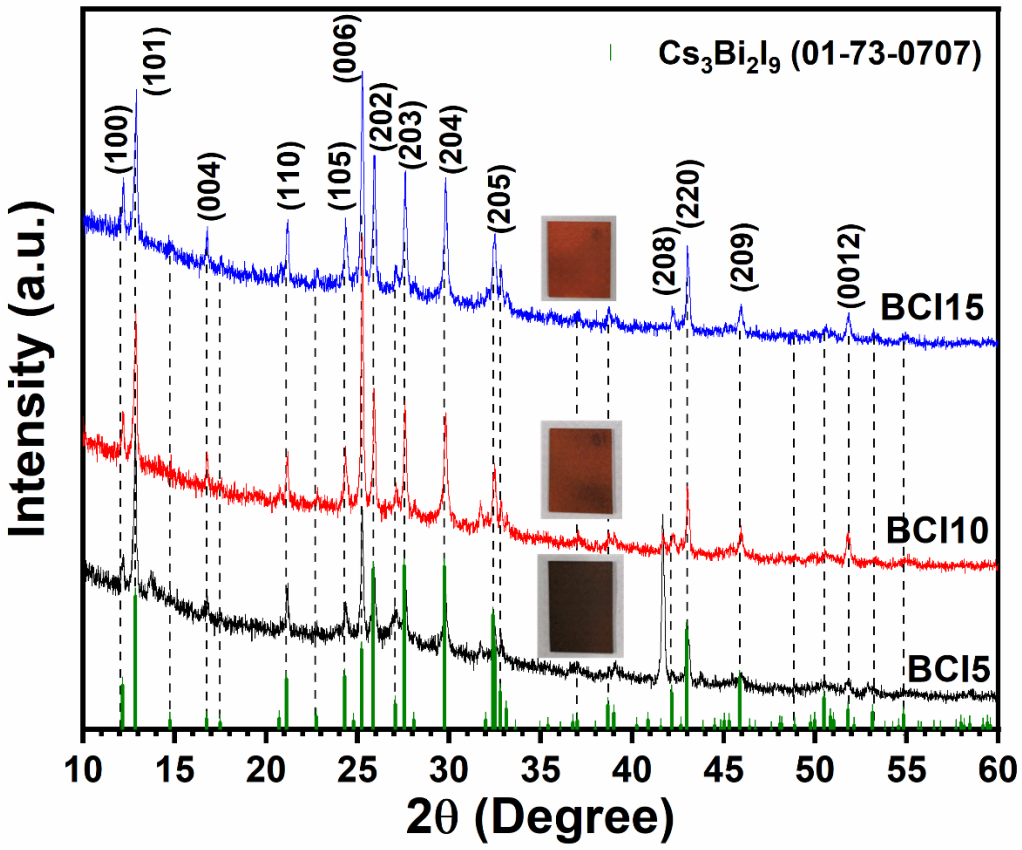

Figure 6.4. The XRD patterns of BiI_3/CsI thin films with different CsI deposition numbers.

The film with ten CsI depositions has a pure phase, while the film with five CsI depositions shows the presence of unreacted BiI_3. The films have a preferential orientation along the (006) direction.

The structure analysis of the films formed with different number of CsI depositions onto BiI_3 and vice-versa reveal the spontaneous reaction between CsI and BiI_3 irrespective of the layer configuration. However, spraying CsI on top of sprayed BiI_3 film showed fast crystallization to obtain pure $Cs_3Bi_2I_9$ phase, since the (110) oriented CsI with d_{100} of 3.23 Å was effectively intercalated to the (113) and (003) oriented layered BiI_3 structure with d_{113} of 3.3 Å and d_{003} of 6.91 Å during the spray process. Therefore, we concluded that better quality $Cs_3Bi_2I_9$ thin films can be obtained by 10 times spraying CsI solution over the BiI_3 thin films.

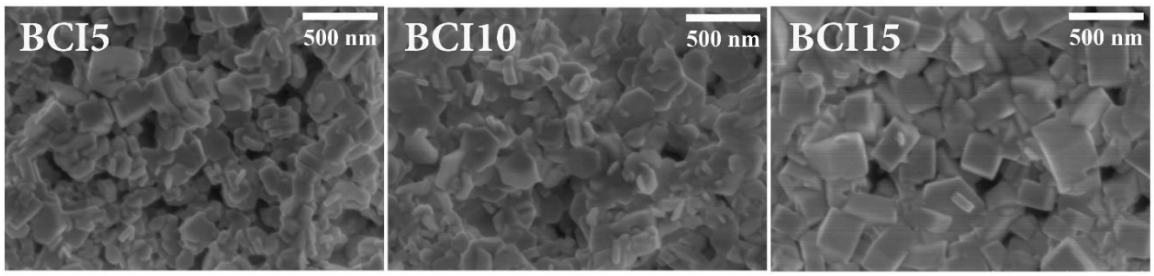

Figure 6.5. SEM images of BiI_3/CsI thin films with 5, 10 and 15 layers of CsI (0.009 M) deposited over BiI_3 layer (0.01 M).

Figure 6.5 displays the SEM images of the thin films fabricated by spraying CsI over BiI_3 layer. The larger number of CsI depositions results in bigger grains as compared to the small hexagonal grains observed at low deposition numbers.

6.3. Influence of CsI precursor concentration on the thin film properties

Furthermore, we varied the concentration of CsI precursor solution keeping the BiI_3/CsI configuration with ten depositions for each layer fabrication.

Table 6-1. Sample names with respect to the CsI precursor concentration.

CsI precursor concentration	0.003 M	0.009 M	0.015 M	0.021 M
Sample name	M003	M009	M015	M021

6.3.1. Structure

X-ray diffraction (XRD)

Figure 6.6 displays the diffraction patterns of the films formed by spraying CsI solutions of various molarities onto the sprayed BiI_3 films. The diffraction patterns unveil the *in situ* formation of $Cs_3Bi_2I_9$ phase during the spraying of CsI precursor solution over the BiI_3 layer.

Strong reflections of the $Cs_3Bi_2I_9$ phase are noted in the M009, M015 and M021 films and no other peaks corresponding to CsI or BiI_3 are observed. For these films, the major diffraction peaks located at 12.1, 12.8, 21.1, 25.2, 25.8, 27.6, 29.7, 32.3 and 42.9° are ascribed to (100), (101), (110), (006), (202), (203), (204), (205) and (220) planes of hexagonal $Cs_3Bi_2I_9$ phase closely in match with the ICDD ref. no. 01-73-0707 (a=b=8.412 Å, c= 21.182 Å, space group: $P6_3/mmc$ (194)) as depicted in Figure 6.6 [88,93,98]. The

growth of this 0D ternary phase is an outcome of the integration of Cs and I atoms into the layered 2D crystal structure of BiI_3. Even though the Cs atoms are not electronically bonded to the Bi or I atoms in the ternary crystal structure, the edge-sharing BiI_6 octahedra in BiI_3 restructure to face-sharing 0D $(Bi_2I_9)^{3-}$ anionic units resulting in the new $Cs_3Bi_2I_9$ phase [72].

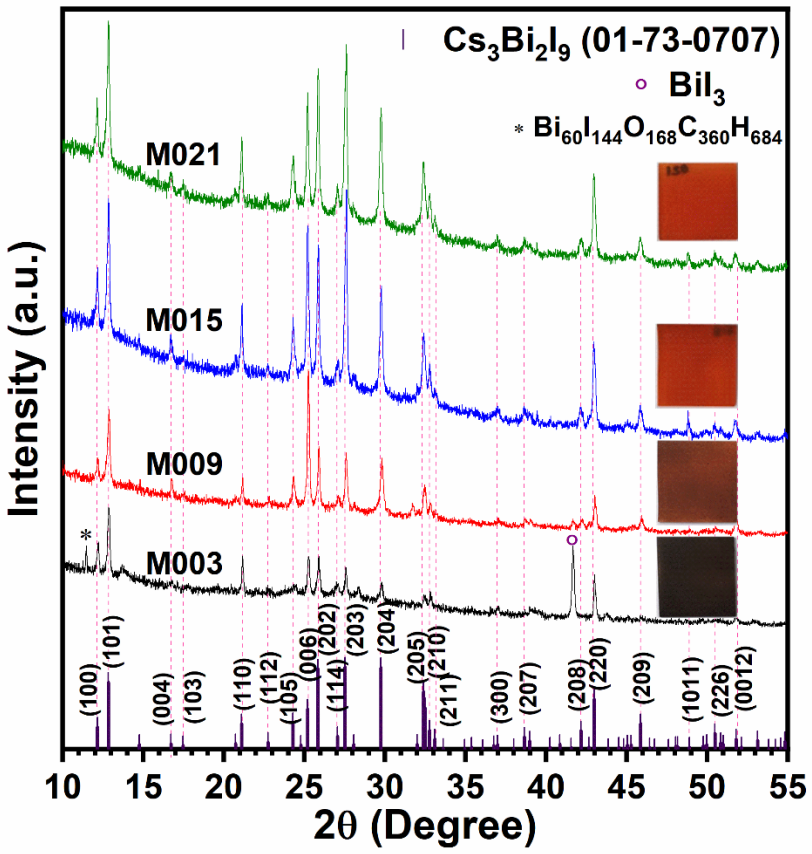

Figure 6.6. (a) The XRD profiles of BiI_3/CsI thin films with different molarity of CsI solutions and (Inset) Photographs of 2.5×2.5 cm-sized thin films.

Besides, the peak at 41.57° in M003 film, matching the (300) plane of the BiI_3 phase, suggests the presence of unreacted BiI_3 in the film along with the $Cs_3Bi_2I_9$ phase [231]. On the other hand, this may also indicate the formation of a BiI_3-rich $CsBi_3I_{10}$ phase with comparable growth directions as that of BiI_3 [93,125,136,198]. The improved intensity of $Cs_3Bi_2I_9$ peaks with CsI concentration signifies the effective diffusion and complete reaction with the BiI_3 on glass substrates. Noticeably, the preferential orientation changes

from (006) in M009 to (203) in M021 with increasing CsI concentration which may indicate that the more CsI present during the reaction can result in polycrystalline films [103,113,135]. In a previous report, spin-coated $Cs_3Bi_2I_9$ thin films heated at 125 ℃ for 30 min showed intense peaks corresponding to (202), (203), (204) and (205) planes [198]. By a similar method at a relatively low temperature of 80 ℃, the growth was in the {00*l*} directions with (006) preferential orientation [102]. Moreover, single crystalline films with (006) orientation were formed at 70 ℃ and polycrystalline films at 150 ℃ in which prominent reflections from crystal planes such as (101), (202), (203), etc. were also observed [14].

Table 6-2. Structural parameters of the spray-deposited $Cs_3Bi_2I_9$ thin films.

Sample	Lattice parameters		Crystallite size (nm)	Microstrain ($\times10^{-3}$)
	a=b (Å)	c (Å)		
M009	8.40	21.143	67.6	3.08
M015	8.41	21.179	58.5	3.39
M021	8.42	21.185	59	3.43

The lattice parameters estimated using equation (2.6) for hexagonal structure are close to the standard values (a=b=8.4116 Å and c= 21.1820 Å) as given in Table 6-2 [190]. The Williamson-Hall (W-H) plot is used to determine the microstrain (ε) contribution to peak broadening (β_ε) and to calculate the crystallite size following the linear equation (2.4) [232],

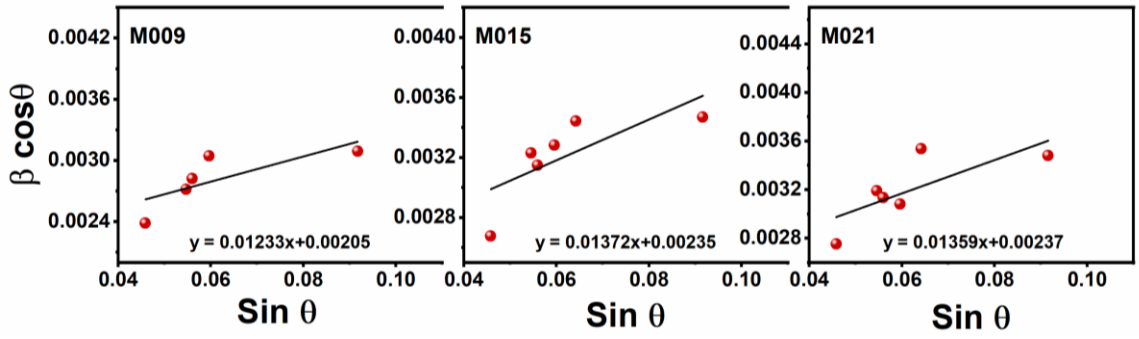

Figure 6.7. Williamson-Hall plots of the $Cs_3Bi_2I_9$ thin films.

W-H plots in Figure 6.7 indicate the presence of microstrain in the structure and the calculated crystallite size values are 67.6, 58.5 and 59 nm, respectively, for M009, M015 and M021 samples containing mainly $Cs_3Bi_2I_9$ phase.

Raman spectroscopy

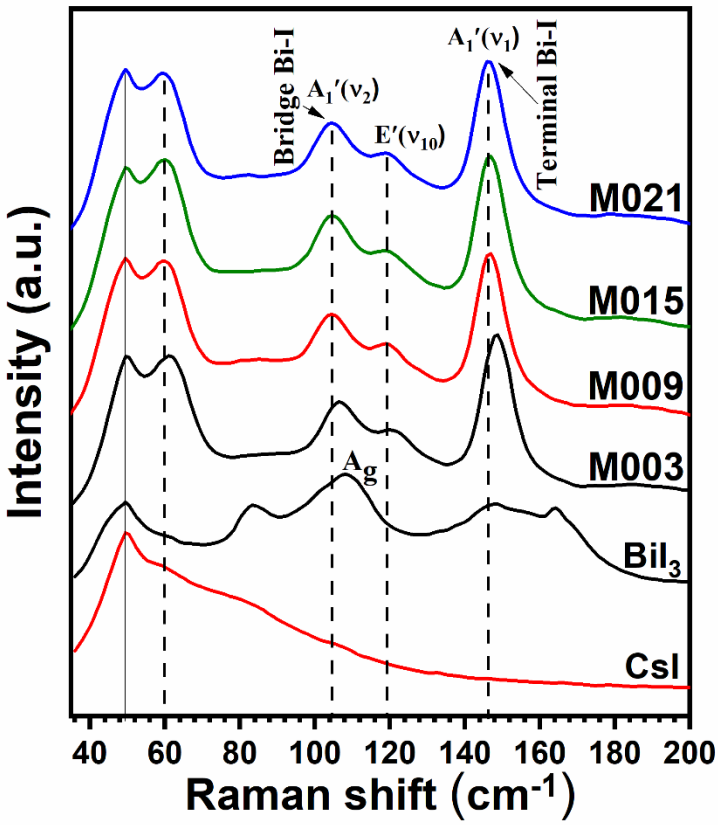

Figure 6.8. Raman spectra of the spray-deposited BiI_3 and CsI precursor layers as well as $Cs_3Bi_2I_9$ thin films.

Raman spectra of the spray-deposited BiI_3/CsI films with different CsI precursor concentrations are displayed in Figure 6.8. The characteristic peaks observed near 60, 104, 119 and 146 cm^{-1} correspond to the ternary $Cs_3Bi_2I_9$ phase. Raman peaks with similar values were reported for $Cs_3Bi_2I_9$ and $CsBi_3I_{10}$ phases [96,214]. No characteristic Raman peak of the CsI precursor layer is observed apart from the peak around 49 cm^{-1}, which is due to the glass substrate. The BiI_3 layer shows Raman peaks around 83, 109, 147 and 164 cm^{-1}, in which the broad and intense peak at 109 cm^{-1} is associated to the characteristic A_g mode of BiI_3 [117].

The high polarizability and strong exciton-phonon interactions inferred from the strong Raman scattering depend on the extent of defects and spatial interactions in the isolated $Bi_2I_9^{3-}$ units of the $Cs_3Bi_2I_9$ structure [92,214]. While their interactions with the bridging Cs^+ make up the low-frequency spectrum, the principal modes originate from the strongly bound anionic units. The major vibrational modes of $Bi_2I_9^{3-}$ originate from the terminal and bridging Bi-I stretching modes. The three bridging I atoms are bonded by two Bi atoms; therefore, the corresponding Bi-I stretching is weaker compared to the stretching modes of the Bi bonded to three terminal I atoms. Since the force constant of the terminal Bi-I bonds is higher, the peak associated with their stretching modes is observed at higher energies. Each type of these bonds exhibit one symmetric (A_1') and two antisymmetric (E'' and E') stretches associated and thus, there are six Raman active Bi-I stretching modes in $Cs_3Bi_2I_9$. Among these modes, symmetrical stretching results in more intensity peaks due to the relatively higher degeneracy than the antisymmetric modes [92]. Therefore, the peak observed near 146 cm^{-1} is attributed to the symmetric stretching of the terminal Bi-I bonds [$A_1'(v_1)$] in the $Bi_2I_9^{3-}$ bioctahedra, whereas the antisymmetric mode [$E'(v_{10})$] emerges at 119 cm^{-1}. On the other hand, the symmetric stretch associated with bridge Bi-I $A_1'(v_2)$ appears near 104 cm^{-1} [92,94].

On the other hand, various bending modes and ionic interactions with Cs^+ constitute the lower energy peaks seen in the Raman spectra [233]. The strong peaks in this range are due to the 0D molecular $Bi_2I_9^{3-}$ ions which are unrestricted for twist and rotation as the Cs^+ cations do not directionally bind them. Thus, these bending modes are as likely as the high energy stretching modes explaining the high intensity of the corresponding peak near 60 cm^{-1} [92].

6.3.2. Morphology

Scanning Electron Microscopy (SEM)

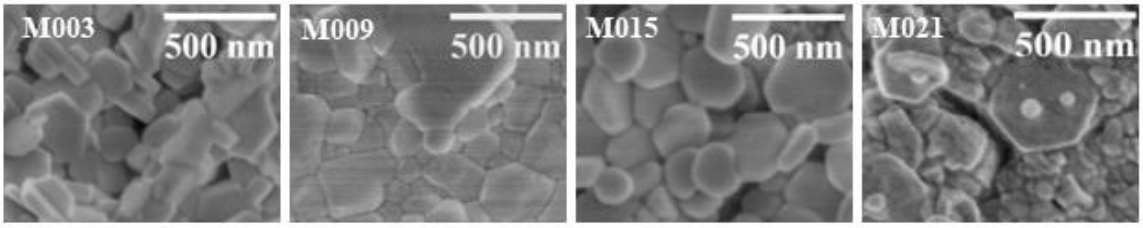

Figure 6.9. Scanning electron microscopy images of $Cs_3Bi_2I_9$ films with various CsI precursor concentrations.

The SEM images in **Figure 6.9** display the morphology of $Cs_3Bi_2I_9$ thin films with varying CsI precursor concentrations. The film shows that the surfaces are composed of compact grains or hexagonal-shaped nanosheets of ~280 nm average size [187]. However, for M021, when the CsI concentration was higher, more agglomerations are observed with smaller CsI particles.

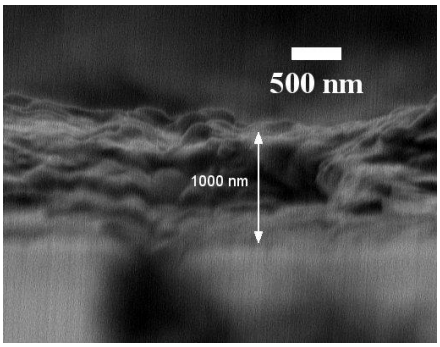

Figure 6.10. Cross sectional SEM image showing the thickness of the optimized M015 $Cs_3Bi_2I_9$ film.

The thickness of the optimized M015 film was measured to be ~1 μm from the cross-sectional SEM image in Figure 6.10. In general, the flake-like morphology may be mainly due to the layered nature of Bi_2I_9 bioctahedra [93]. Such nanosheet morphology was also observed in the case of spin-coated $Cs_3Bi_2I_9$ thin films which performed well in solar cells [96,107]. Khadka et al used antisolvent and solvent annealing to modify the nanosheets to a more compact morphology [96], whereas Bai et al. used a dissolution and

recrystallization route to reduce the nanosheet thickness to obtain a more uniform surface [107].

6.3.3. Chemical state and composition

X-ray photoelectron spectroscopy (XPS)

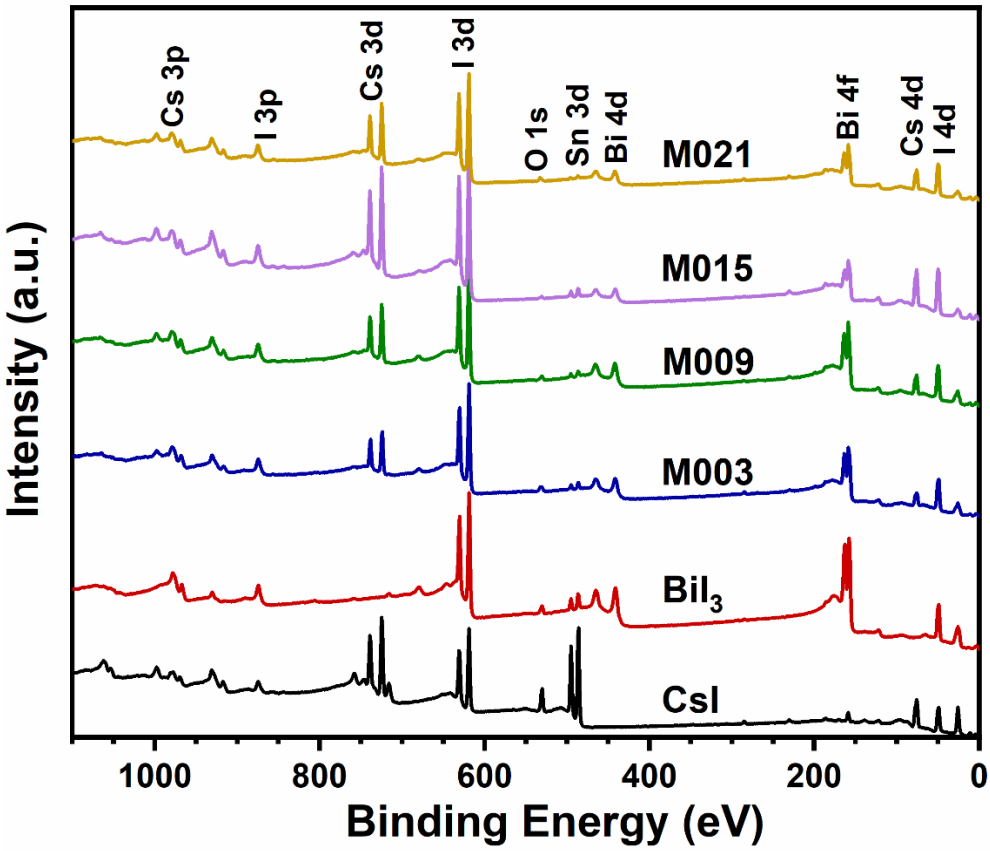

Figure 6.11. The survey spectra of precursor layers and the reacted films.

Survey scans of the precursors and the ternary films after a soft Ar^+ ion etch are compared in Figure 6.11. Further, the XPS high-resolution core-level scans, as illustrated in Figure 6.12, are used to identify the elemental states and chemical composition of the ternary films. In the survey patterns, elements of Cs, Bi and I along with the O and C species are detected as noted. The additionally observed Sn 3d peaks are originated from the FTO substrate.

Figure 6.12a represents the high-resolution core-level spectra of Cs 3d, Bi 4f and I 3d in the $Cs_3Bi_2I_9$ films in comparison with that of the pure CsI and BiI_3 films. With reference to the binary precursors, the binding energies of all elements shift to lower values in the $Cs_3Bi_2I_9$. The intensity of Cs increases with the higher molarity of CsI precursor solution but reduces again in M021. The peaks were deconvoluted using the Gaussian-Lorentzian sum function and the background was determined by a Shirley type function as shown in Figure 6.12b.

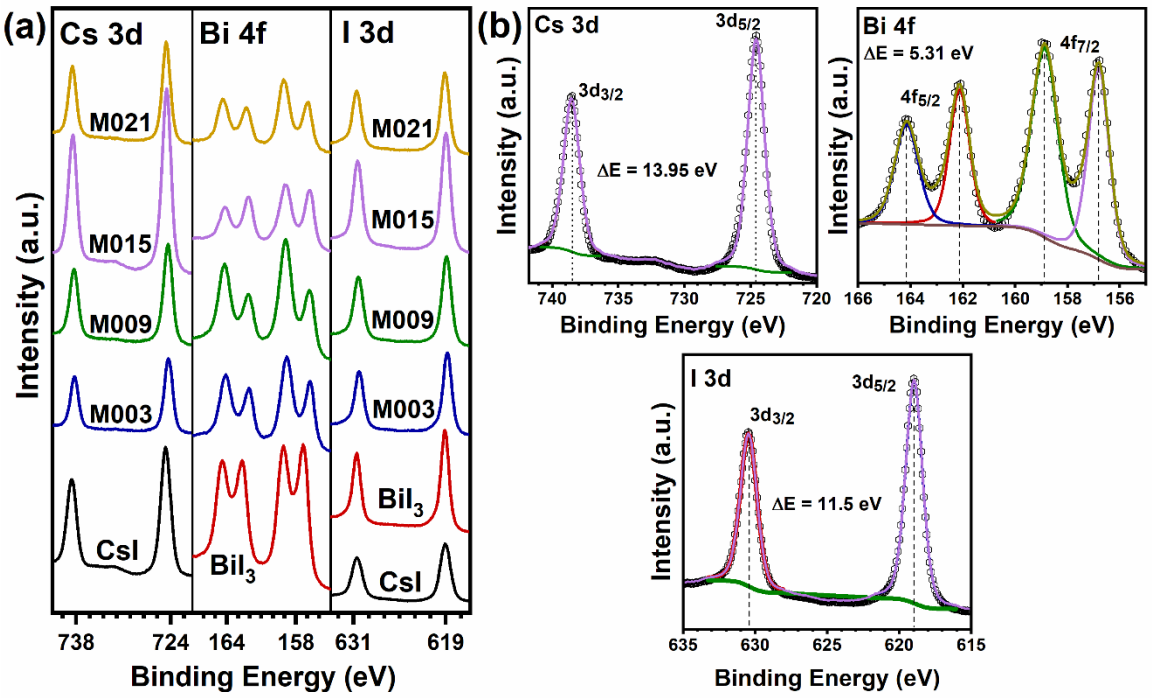

Figure 6.12. (a) XPS high-resolution core-level spectra of Cs, Bi and I in the precursor layers (CsI and BiI_3) as well as the reacted ternary films obtained with different CsI molarity (b) The deconvoluted spectra of M015 film after a soft Ar^+ ion etching.

Figure 6.13a, b depict the high-resolution XPS scans of the CsI and BiI_3 precursor layers. In pure CsI, Cs $3d_{5/2}$ and $3d_{3/2}$ peaks are at 724.78 and 738.74 eV with a spin-orbit splitting of 13.94 eV corresponding to the Cs^+ state. However, for the ternary M015 film in Figure 6.12b, these peaks shift to lower binding energy (BE) of 724.59 and 738.54 eV, indicating a change in its chemical environment. The reduced BE is due to the presence of higher valence anionic units $(Bi_2I_9)^{3-}$ which are not directly bonded to each other in 0D-$Cs_3Bi_2I_9$.

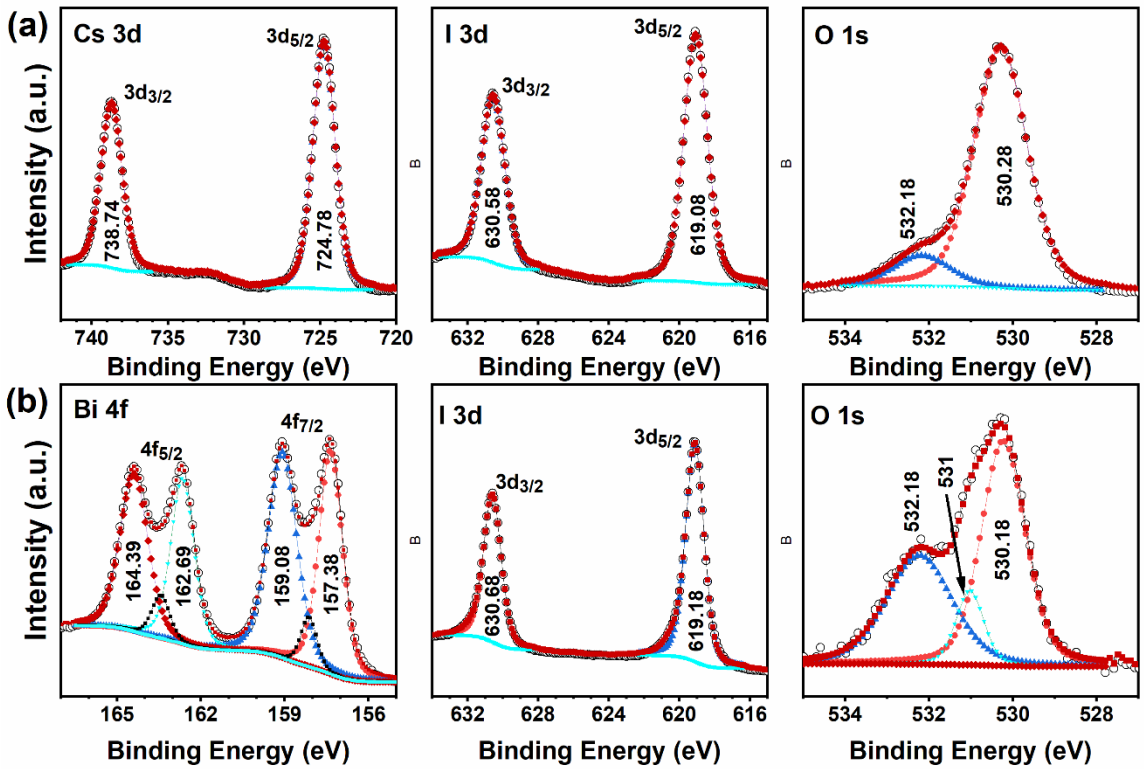

Figure 6.13. High resolution core-level spectra of various elements in the sprayed (a) CsI and (b) BiI_3 precursor layers obtained after a soft argon ion etch.

The Bi 4f core-level spectrum of the BiI_3 precursor layer in Figure 6.13b displays three doublet pairs. Among them, one at 159.08 and 164.38 eV with a separation of 5.3 eV is of Bi $4f_{7/2}$ and $4f_{5/2}$ corresponding to the 3+ state in BiI_3. The second doublet peaks noted at 157.38 and 162.69 eV are ascribed to Bi^0 state [72,157]. The origin of metallic bismuth is a result of the reduction of Bi^{3+} during the argon ion etching, similar to the Pb^0 state in organic lead halide perovskites [201,234]. The small peaks at 158.18 and 163.48 eV are ascribed to the Bi $4f_{7/2}$ and $4f_{5/2}$ levels in BiOI phase in the BiI_3 thin films. However, any noticeable peaks of such impurities are not present in the XRD patterns. In the M015 $Cs_3Bi_2I_9$ films (Figure 6.12b), the major peaks of Bi shift to lower binding energies by ~0.2 eV compared to that of the precursor BiI_3 layer. Similarly, metallic bismuth is also evident in all the ternary films primarily due to the Ar ion etching before the scans.

The iodine 3d spectra in Figure 6.13 show peaks at 619.08 and 630.58 eV for pure CsI films and at 619.18 and 630.68 eV for the BiI_3 layer correlating with that of I^- states [201].

In the $Cs_3Bi_2I_9$ films, I peaks were moved to the lower binding energy by ~0.1 – 0.2 eV as compared to the binary precursor films as seen in Figure 6.12b. These lower binding energy shifts, as compared to the binary precursor films may be due to the molecular salt structure of $Cs_3Bi_2I_9$, where the isolated $(Bi_2I_9)^{3-}$ anionic units are not directly bound by the Cs^+ cations.

The intense peaks oberved at 530.28 eV and 530.18 eV in the O 1s spectra of CsI and BiI_3 layers, in **Figure 6.13**, are due to the presence of cesium oxide and bismuth oxide, respectively. The additional peak noted at 531 eV for BiI_3 layer is associated to the BiOI phase. Besides, both the layers display a peak at 532.18 eV which corresponds to the adsorbed oxygen.

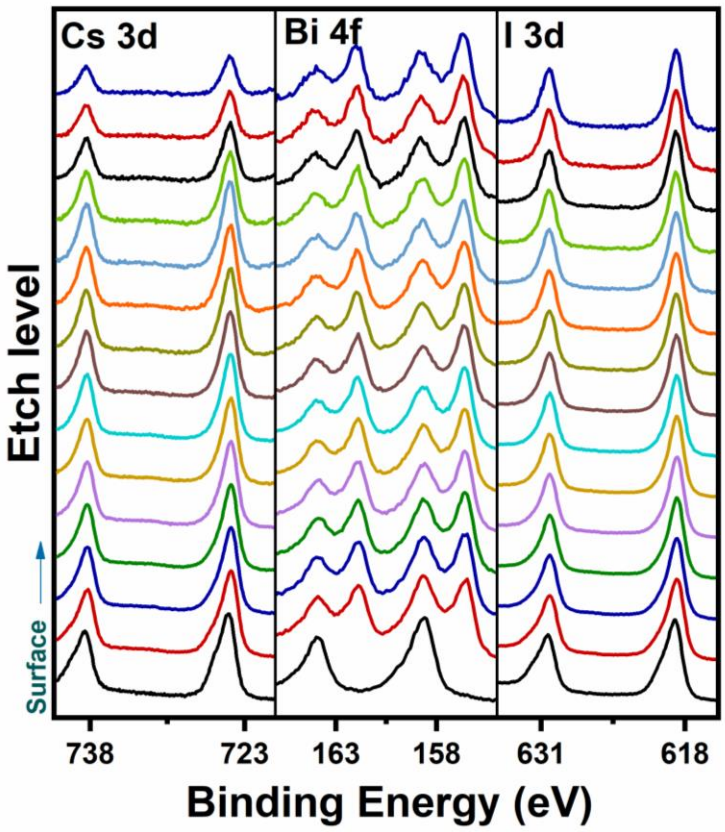

Figure 6.14. The depth profile of M015 thin film deposited on FTO coated glass substrate shows the presence of all elements throughout the film thickness.

The presence of Sn in the survey spectra suggests the detection of photoelectrons from the FTO substrates. A depth profile of the M015 film on FTO coated glass substrate is depicted

in Figure 6.14, which shows the presence of Cs, Bi and I throughout the depth of the film. This confirms the diffusion of Bi from the lower layer into the surface suggesting a complete reaction with CsI deposited as the top layer. Similarly, Cs was also detected in the lower levels of this depth profile.

The core-level spectra of each element were used to estimate the composition of each film and is listed in Table 6-3. The films show a higher Cs/Bi ratio and low I/Bi ratio as compared to the 1.5 and 4.5, respectively, of the $Cs_3Bi_2I_9$ composition. As expected, the Cs and I concentration increases with higher CsI molarities, however, it reduces again for M021 films.

Table 6-3. Elemental composition of the precursor layers and the ternary thin films quantified from the XPS high-resolution core-level spectra.

Sample	Atomic percentage (%)			Cs/Bi	I/Bi
	Cs	Bi	I		
BiI_3		27.3	72.7		2.7
CsI	51.9		48.1		
M003	23.1	20.1	56.8	1.2	2.8
M009	26.8	20.6	52.7	1.3	2.5
M015	35.7	13.8	50.5	2.6	4.7
M021	29.8	14.4	55.8	2.1	3.9

6.3.4. Optical properties

UV-Vis-NIR spectroscopy

The absorption spectra of $Cs_3Bi_2I_9$ films in Figure 6.15 feature an excitonic absorption peak at 500 nm (~2.48 eV) and the commencement of absorption is observed near 600 nm (~2.1 eV) in the case of M009, M015 and M021 films. On the other hand, the BiI_3-rich M003 film shows an extended absorption with absorption edges near 960 nm (~1.3 eV) and 780 nm (~1.6 eV), which may be due to the BiI_3 and $CsBi_3I_{10}$ phases present in the sample [198]. The peak at 500 nm implies the strong excitonic characteristics of the $Cs_3Bi_2I_9$ at room temperature, which is due to the zero-dimensional $(Bi_2I_9)^{3-}$ anionic units [94,231]. The strong excitonic peak reported at 2.5 eV reveals the high excitonic binding energy that

can deteriorate the charge carrier mobility and photocarrier collection resulting in high recombination rates [14,106]. Furthermore, the exponential absorption tail noted in these samples may be due to the high defect density and intrinsic structural disorders causing sub-bandgap transitions in the polycrystalline films [14,231]. Such a distinct absorption tail is typical for polycrystalline $Cs_3Bi_2I_9$ thin films (E_g ~ 2.12 eV), but their single crystalline thin films exhibited sharp absorption [14].

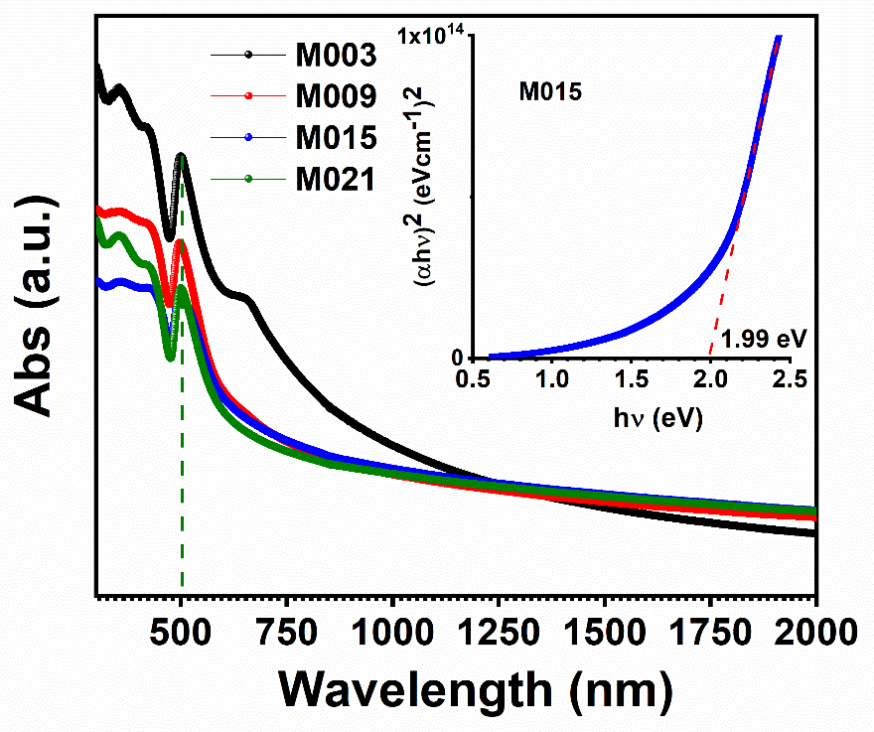

Figure 6.15. Absorption spectra of the spray-deposited BiI_3/CsI thin films with different concentrations of CsI. Tauc plot for the direct band gap estimation of M015 film is shown in the inset.

The absorption coefficient (α) was calculated using equation (2.8) and the optical band gap (E_g) was estimated using the Tauc equation (2.7) . The band gap analysis from the Tauc plot revealed that the M015 film has a direct band gap of ~1.99 eV, as illustrated in the inset of Figure 6.15. The 0D-$Cs_3Bi_2I_9$ has an indirect band gap in the range of 1.9 - 2.2 eV as per the previous reports [96–98,100]. Although the band gap of $Cs_3Bi_2I_9$ in our DFT calculations showed fundamental transitions of an indirect nature, the value is in good agreement with the experimental band gap calculated from the absorption data. Besides,

the less dispersed band structure also raises the prospect of closer-energy direct transitions. Both direct and indirect band gaps were reported for perovskite-derived $Cs_3Bi_2I_9$. Single crystals of $Cs_3Bi_2I_9$ were reported to have a direct band gap of 1.96 eV [113]. Lehner et al. reported an indirect band gap of 1.9 eV and 2.32 eV by experimental and DFT calculations, respectively [98]. Spin-coated $Cs_3Bi_2I_9$ thin films heated at 100 °C demonstrated an indirect band gap of ~2.1 eV with an absorption coefficient of ~10^4 cm^{-1} [231]. DFT calculations by Hong et al. indicated a band gap of 2.12 eV that could be lowered by Ga or In doping. Moreover, the calculations including dual cations predicted a change in the nature of the band gap from indirect to direct [199].

6.3.5. Photoresponse

As seen in Figure 6.16a, the M015 film demonstrated the best response among the pure $Cs_3Bi_2I_9$ thin films when illuminated by a 50 W halogen lamp. No appreciable response is recorded in the case of other samples with more localized agglomerations and voids, as observed in their morphology. Besides, poor interface with electrical contacts due to the powdery M021 films hindered the charge collection. The films are highly resistive in the order of ~$10^{10} – 10^{12}$ Ωcm, which may not be favorable for photovoltaic applications [103]. On the other hand, such resistive films are suitable for detecting hard radiations like gamma rays and X-rays [92]. Even though $Cs_3Bi_2I_9$ has a band gap of around 2 eV and a reasonable absorption coefficient, the strong electron-phonon interactions cause small polarons that lead to self-trapped excitons [92]. Moreover, the material's structural disorders and sub-band-gap states impede the charge transport lowering the carrier mobility [135]. These localized structural defects may be the reason for the low photocurrent density observed in $Cs_3Bi_2I_9$ [99].

The M015 film under 10 V bias was illuminated using a 532 nm laser source at 40 W and the response was measured as in Figure 6.16c. The sensitivity (S) of the film to the illumination is calculated using equation (2.10) and the responsivity (R) is determined by the relation (2.11). The illumination light density P_λ is 28.2 Wcm^{-2} and the effective area (A) is 0.25 cm^2. Detectivity (D) of the film is calculated from the formula (2.12) [209]. The photosensitivity, responsivity and detectivity are calculated to be 58%, 7.29×10^{-8}

mAW^{-1} and 2.17×10^3 Jones, respectively for the photodetector. The low photocurrent and sensitivity are the result of the strong excitonic behavior in $Cs_3Bi_2I_9$, which leads to the recombination of photogenerated carriers trapped by the $(Bi_2I_9)^{3-}$ dimers. This inefficiency in the separation of photogenerated carriers is mainly a reason for such low photocurrent in the material. Apart from that, the high probability of electron-hole recombination at the interfaces results in a large dark current [106].

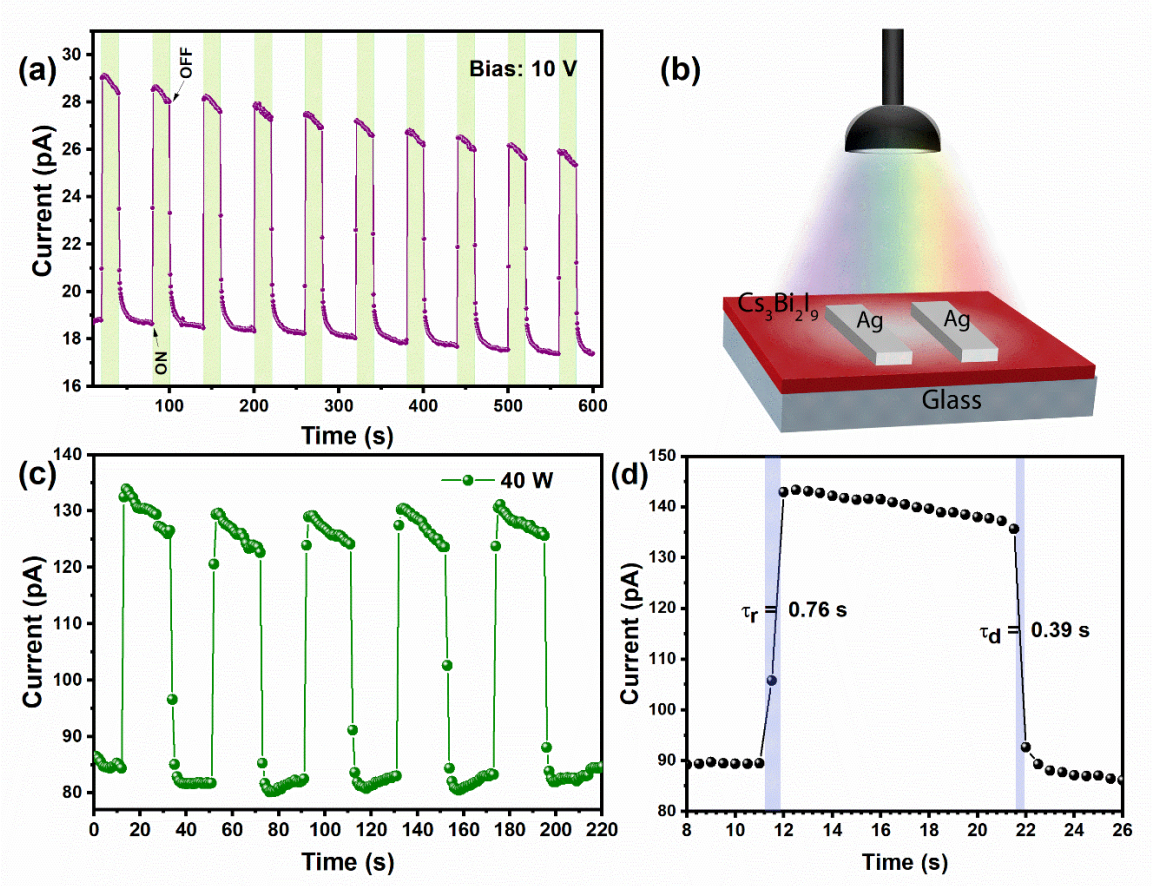

Figure 6.16. (a) The photoresponse of $Cs_3Bi_2I_9$ (M015) thin film under 50 W halogen lamp. (b) Photoresponse measurements. (c) Photocurrent response of M015 film to the 532 nm laser (40 W) illumination under 10 V bias. (d) Rise and decay time determined for the response.

Moreover, the decay-rise times were estimated as shown in Figure 6.16d and obtained a decay time (τ_d) of 0.39 s and a rise time (τ_r) of 0.76 s. This short decay time as compared to the rise time is due to the fast saturation of photogenerated carriers followed by the onset of recombination which results in the observed decrease in photocurrent during the illumination. The rapid recombination of the photogenerated carriers led to this faster decay

process in the $Cs_3Bi_2I_9$ film when the illumination source was switched off [235]. Earlier, reports of {00*l*} oriented $Cs_3Bi_2I_9$ nanoplates-based photodetector showed detectivity up to 10^{10} Jones and responsivity of 33.1 mAW^{-1} [103]. Likewise, a single crystalline $Cs_3Bi_2I_9$ thin film photodetector displayed an enhanced ON/OFF ratio as high as 11000. The responsivity and detectivity of these photodetectors were 1.9 – 7.2 mAW^{-1} and 2.7×10^{10} – 1×10^{11} Jones [14]. Recently, $Al_2O_3/Cs_3Bi_2I_9$ photodetectors showed the highest responsivity of 100 mAW^{-1} and an ON/OFF ratio of 3.85×10^3 [106].

6.3.6. Thermal stability

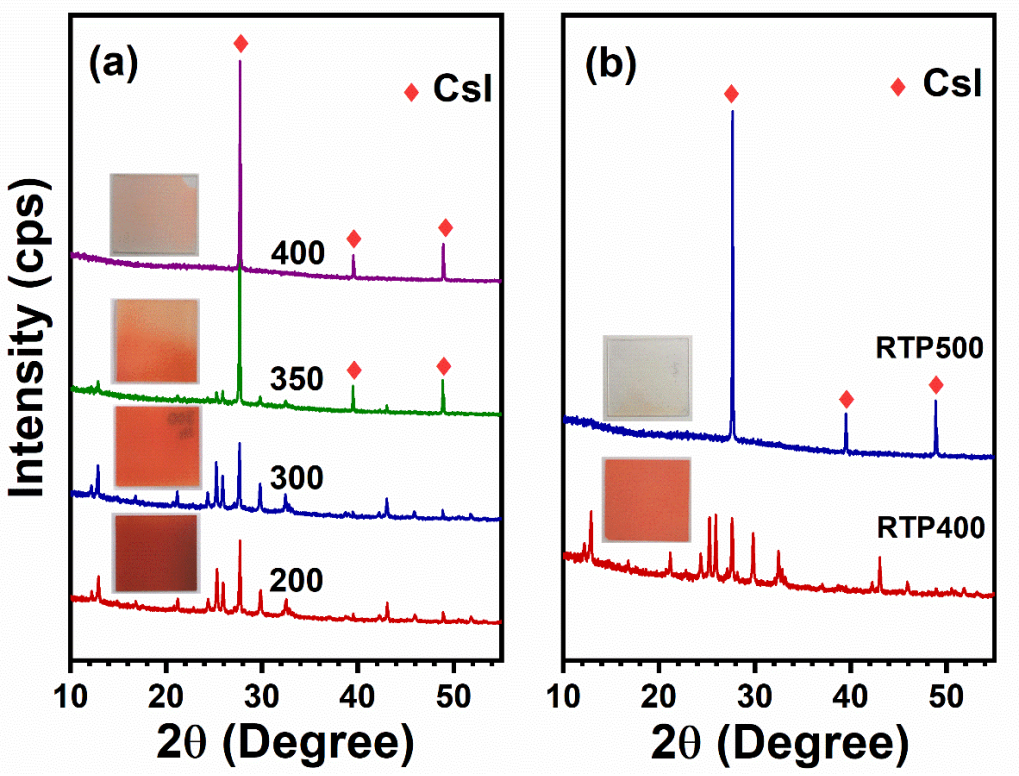

Figure 6.17. The XRD patterns of the M015 $Cs_3Bi_2I_9$ films (a) annealed for 1 h in vacuum at 200 °C, 300 °C, 350 °C and 400 °C as well as (b) Rapid thermal processed for 3 min at 400 °C and 500 °C. (Inset) Photographs of annealed samples of size 2.5×2.5 cm.

The spray-deposited $Cs_3Bi_2I_9$ thin films are subjected to a low vacuum annealing and a rapid thermal process to analyze the thermal stability. The XRD patterns of the thermally treated thin films are shown in Figure 6.17. The $Cs_3Bi_2I_9$ thin films showed phase stability up to 300 °C during a 1-hour low vacuum annealing process. However, higher temperatures caused its decomposition, as evidenced by the appearance of large CsI particles on the

substrate with the evaporation of BiI_3. In contrast, the phase degraded after 400 °C in the 3-min RTP treatment. At lower temperatures, the RTP improved the growth along (101), (006) and (202) directions, marked by the increased intensity of corresponding peaks.

Figure 6.18 shows the surface morphology of the thermally treated M015 thin film. Large voids and spherical particles in SEM imply that $Cs_3Bi_2I_9$ decomposition and BiI_3 evaporation start at 350 ℃ in typical low vacuum annealing and close to 500 ℃ in RTP.

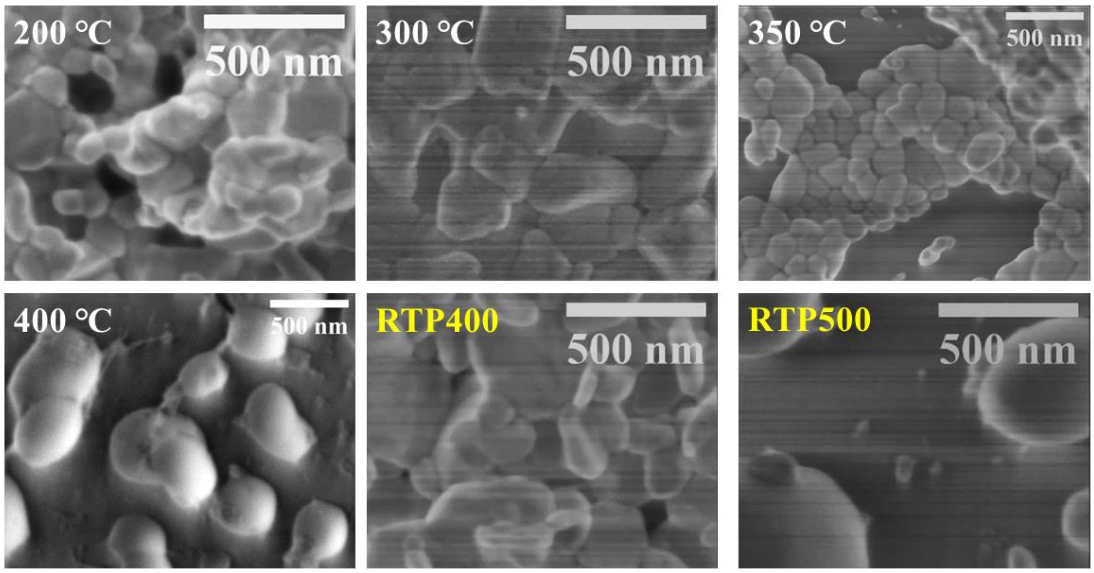

Figure 6.18. The scanning electron microscopy images of the films annealed for 1 h at 200, 300, 350 and 400 ℃ and rapid thermal processed for 3 min at 400 ℃ (RTP400) and 500 ℃ (RTP500).

The thermal decomposition of the $Cs_3Bi_2I_9$ after 400 ℃ is as follows [136],

$$Cs_3Bi_2I_9(s) \rightarrow 3CsI\ (s) + 2\ BiI_3\ (g)$$

$Cs_3Bi_2I_9$ polycrystalline thin films are formed by the *in situ* crystallization when the sprayed CsI precursor solution is diffused and reacted with the spray-deposited BiI_3 thin film. These perovskite-derivative thin films show compact morphology decorated with hexagonal sheets like the spin-coated $Cs_3Bi_2I_9$ films [96,107]. In contrast to earlier reports, the direct band gap in this instance results in high absorption coefficients for the material [96–98]. However, their optoelectronic applications suffer from the strong excitonic character and long absorption tail. The performance of $Cs_3Bi_2I_9$ in solar cells is constrained by the low

photocurrent density and ineffective carrier extraction caused by their wide band gap and morphological flaws. Various strategies have been proposed to overcome these limitations in optoelectronic devices. The large band gap of $Cs_3Bi_2I_9$ can be tuned by doping trivalent cations like Ga or In [97] and Ru [100]. With the help of various techniques, such as double perovskite structures [23,50,147], dual anion engineering [156], dual cations, and passivation of defects by excess Bi_3 [97,99], structural flaws and self-trapped excitons from strong electron–phonon interactions can be reduced. Additionally, to achieve high photocurrent density while suppressing the dark current, it is necessary to address the significant energy level mismatch, a lack of suitable hole transport layers, and ohmic contacts.

6.3.7. Heterojunctions

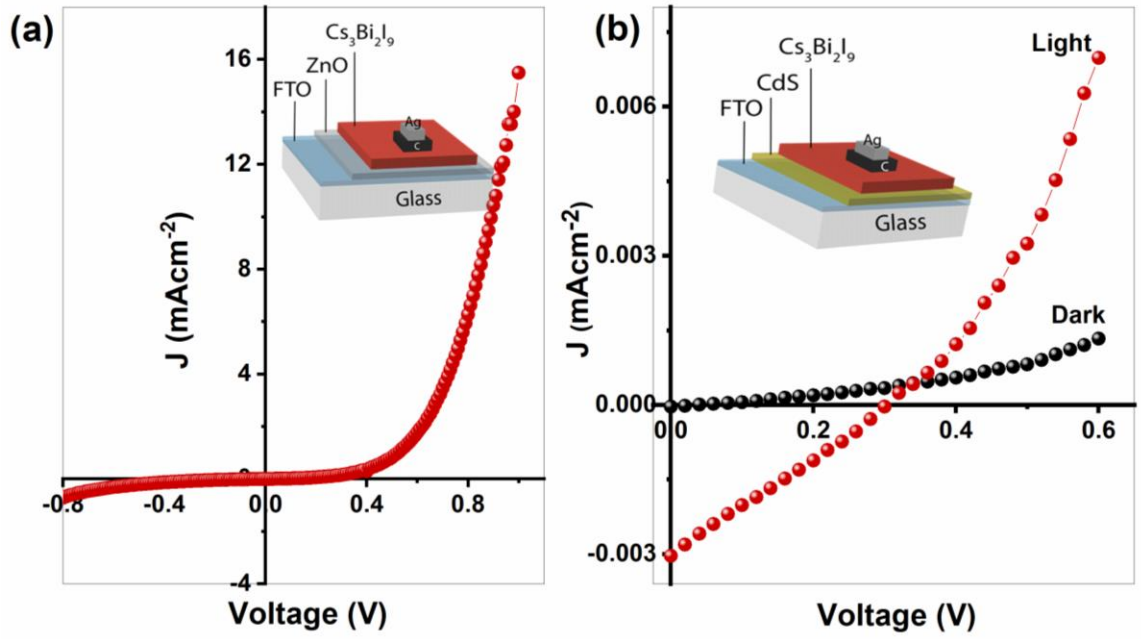

Figure 6.19. J-V characteristics of (a) glass/FTO/ZnO/$Cs_3Bi_2I_9$/C-Ag and (b) glass/FTO/CdS/$Cs_3Bi_2I_9$/C-Ag structures.

The pure $Cs_3Bi_2I_9$ thin film (M015) obtained by spraying 0.015 M CsI precursor solution over the BiI_3 thin film as described in 2.4.3 is used for the fabrication of heterojunction devices. J-Vcharacteristics of glass/FTO/ZnO/$Cs_3Bi_2I_9$/C-Ag and glass/FTO/CdS/$Cs_3Bi_2I_9$/C-Ag heterojunctions and their schematic illustrations are shown

in Figure 6.19. Figure 6.19a shows a good rectification behavior at the fully-sprayed ZnO/$Cs_3Bi_2I_9$ junction. However, in this instance, under illumination, no photovoltaic performance was observed. The ZnO/$Cs_3Bi_2I_9$ junction has a turn-on voltage of approximately 0.56 V and a maximum forward-to-reverse current ratio of 7.5 at 0.7 V.

The J-V characteristics of glass/FTO/CdS/$Cs_3Bi_2I_9$/C-Ag under dark and illumination conditions are depicted in Figure 6.19b. The curves demonstrate the heterojunction's photovoltaic performance yielding a 300 mV open-circuit voltage (V_{oc}) and a 0.003 $mAcm^{-2}$ short-circuit current density (J_{sc}).

The ideal diode equation (2.9) can be used to estimate the ideality factor (n) of this p-n junction [192]. The ideality factor estimated from the ln I vs. V curve in Figure 6.20 is 1.75, which faintly varies from the ideal case (n=1) as defined by the diffusion model.

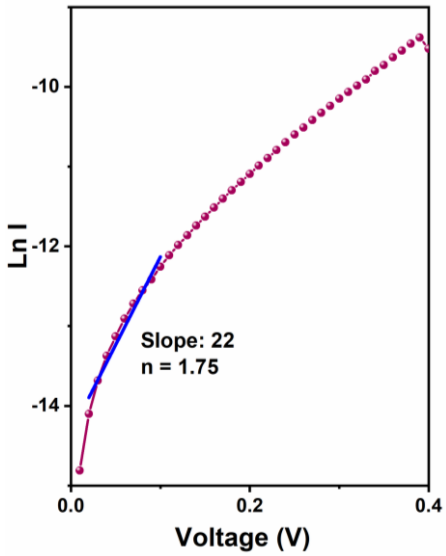

Figure 6.20. ln I vs V curve for the glass/FTO/n-ZnO/p-$Cs_3Bi_2I_9$/C/Ag structure.

In addition to the lack of HTL, the significant energy level mismatch between $Cs_3Bi_2I_9$ and ZnO may be the reason for the absence of a photovoltaic effect with no V_{oc}. However, other factors such as interface irregularities during the spray deposition, morphology-related interfacial properties, non-radiative defects or structural disorders in $Cs_3Bi_2I_9$, which decline the mobility of carriers, are accountable for this poor photovoltaic performance with ZnO and low current density with CdS [99,214]. Moreover, the performance of

$Cs_3Bi_2I_9$ as a photovoltaic device is also constrained by charge carrier localization and anisotropic charge transfer [99].

6.4. Conclusions

By sequentially depositing BiI_3 and CsI layers by ultrasonic spray deposition of ethanol-based precursor solutions, the 0D perovskite-derivative $Cs_3Bi_2I_9$ thin films are fabricated. Spraying 0.015 M CsI solution ten times was the best method for the complete *in situ* crystalization and conversion of BiI_3 films (~800 nm) to $Cs_3Bi_2I_9$ films. The technique may be used to scale up the deposition of perovskite thin films according to detailed investigations of structure, morphology, composition, and optical characteristics. A direct bandgap of ~1.99 eV was obtained, which implies their possible applications in photovoltaic devices with improvements in the transport and collection of photogenerated carriers. Furthermore, the photoresponse demonstrated by the optimized film (M015) indicates their possible applications in photodetectors. Most importantly, the J-V characteristics of n-ZnO/p-$Cs_3Bi_2I_9$ and n-CdS/p-$Cs_3Bi_2I_9$ heterojunctions endorse their application in solar cells.

Further, we utilize the limited solubility of BiI_3 and CsI in acetone for the deposition of $Cs_3Bi_2I_9$ thin films. Then we incorporate Bi_2S_3 nanorods to achieve $Cs_3Bi_2I_9$:Bi_2S_3 composite thin films in the final discussion of this thesis.

CHAPTER 7

BISMUTH SULFIDE NANORODS INCORPORATED CESIUM BISMUTH IODIDE THIN FILMS

Acetone is used as a solvent for the ultrasonic spray deposition of Bi_2S_3 and $Cs_3Bi_2I_9$ thin films. Further, solution engineering of the $Cs_3Bi_2I_9$ precursor solution with thioacetamide, Bi_2S_3 nanorods are grown in the bulk of the $Cs_3Bi_2I_9$ thin films. The $Cs_3Bi_2I_9$: Bi_2S_3 composite thin films demonstrate exciting self-powered detection in the broad spectral range.

7.1. Introduction

This chapter describes our investigations on the cesium bismuth iodide thin films deposited using acetone solvent. In addition, our attempts to incorporate sulfur into the structure by introducing thioacetamide into the precursor solution have considerably improved the film quality, especially, due to the in-situ growth of bismuth sulfide nanorods in the grain boundaries. We study these composite films in detail by analyzing its structural, morphological, elemental, optical and electrical characterizations. In addition, we also realize pure bismuth sulfide thin films by the same method to compare the properties.

7.2. Ultrasonically sprayed bismuth sulfide thin film

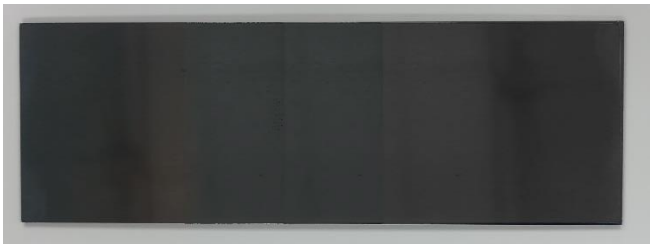

Figure 7.1. Spray-deposited Bi_2S_3 thin film.

The Bi_2S_3 thin film obtained by ultrasonic spray deposition is displayed in **Figure 7.1**.

7.2.1. Structure

X-ray diffraction (XRD) and Raman spectroscopy

The X-ray diffraction pattern in Figure 7.2a of the spray-deposited thin film is in match with the standard reference pattern of Bi_2S_3 (bismuthinite) (ICDD: 00-043-1471) of orthorhombic crystal structure (space group: Pbnm, 62). The highly amorphous nature of the thin film can be noted from the low intensity peaks in the diffraction pattern. Further, assigning planes to the diffraction peaks suggests that the Bi_2S_3 thin film of nanorod morphology is (130) oriented with the corresponding peak at 25.06°. The other peaks from (200), (120), (220), (101), (211) and (240) crystalline planes are noted at 15.80°, 17.75°, 22.48°, 23.80°, 28.74° and 35.71° [236–239].

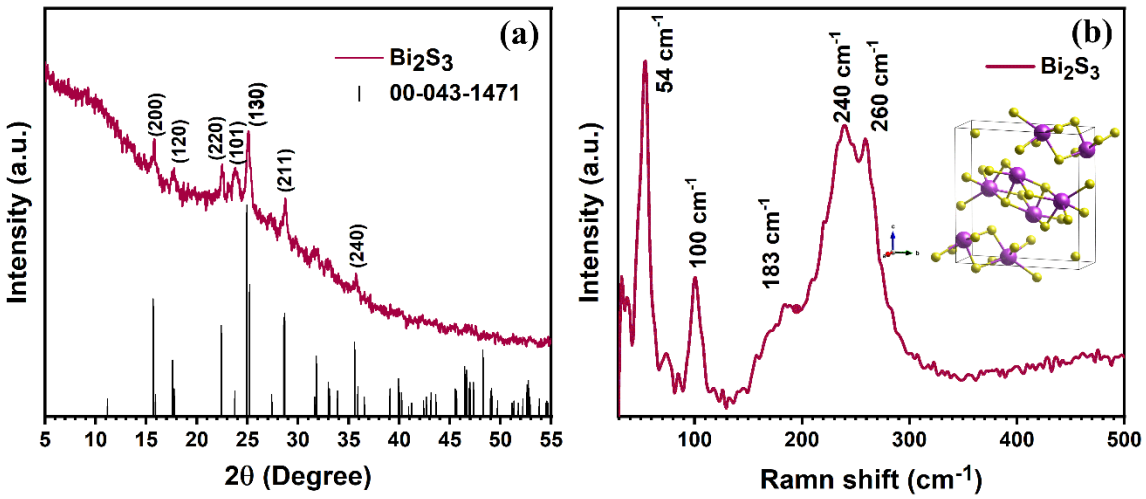

Figure 7.2. The (a) XRD pattern and (b) Raman spectrum of Bi_2S_3 thin film deposited by ultrasonic spray. (inset) Unit cell of Bi_2S_3.

Figure 7.2b displays the Raman spectrum of Bi_2S_3 thin film with characteristic peaks at 54, 100 cm^{-1} and a broad peak from 150 to 200 cm^{-1}. Moreover, intense and broad Raman peaks observed at 240 and 260 cm^{-1} are related to the A_g and B_{1g} vibrations of Bi_2S_3 [237,240].

7.2.2. Morphology

Scanning Electron Microscopy (SEM)

Figure 7.3. The nanorod morphology of spray-deposited Bi_2S_3 thin film.

The typical morphology of the Bi_2S_3 thin films fabricated by ultrasonic spray deposition is displayed in **Figure 7.3**. The thin films are composed of nearly vertical nanorods with an average diameter of 70 nm whereas the length varies from 700 nm to 1µm. The densely grown nanorods are uniform throughout the thin film surface without any aggregations or voids. The growth of Bi_2S_3 in the nanorod form is promoted due to the inherent chain-like structure of Bi-S [236].

7.2.3. Chemical state

X-ray photoelectron spectroscopy (XPS)

Figure 7.4 shows the survey spectrum of elemental states in Bi_2S_3 thin film fabricated by ultrasonic spray deposition. The spectrum obtained after a single Ar etching confirms the absence of any elements other than the anticipated Bi and S.

The XPS high resolution core-level spectrum of Bi 4f in Bi_2S_3 thin film is shown in **Figure 7.5**. The spectrum is deconvoluted to identify the S 2p peaks since the S 2p states are also oberved in the same binding energy range as that of Bi 4f. The intense peaks at 158.28 and 163.58 eV are assigned to the Bi $4f_{7/2}$ and $4f_{5/2}$ peaks of the Bi^{3+} state in Bi_2S_3 [241]. Similarly, the peaks observed at 157.08 and 162.38 eV are due to the metallic bismuth (Bi^0) species resulting from the etching process.

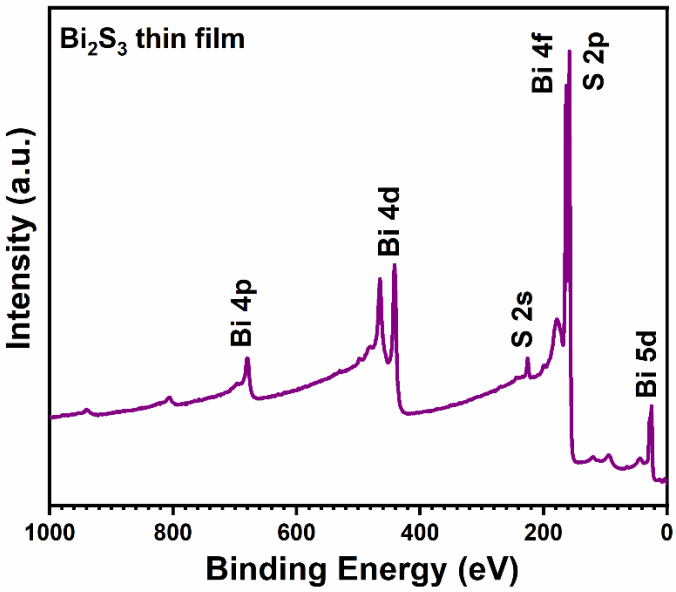

Figure 7.4. The XPS survey spectrum of Bi_2S_3 thin film.

The shaded peaks at 161.08 and 162.18 eV in **Figure 7.5** obtained after the deconvolution of the Bi 4f spectrum is ascribed to the S $2p_{3/2}$ and $2p_{1/2}$ peaks, respectively. These peaks correspond to the S^{2-} state in Bi_2S_3 [236].

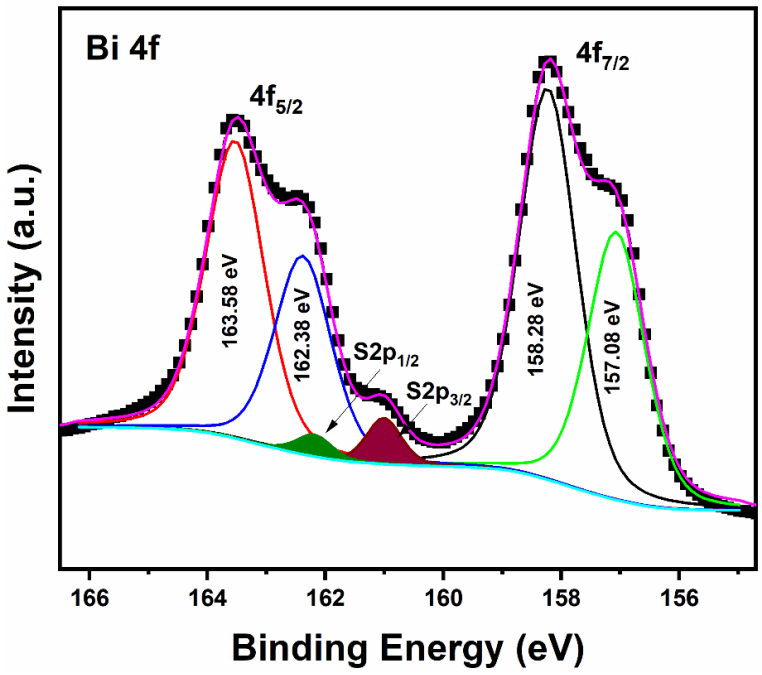

Figure 7.5. The Bi 4f high resolution scan after etching the surface of Bi_2S_3 thin film.

7.2.4. Optical properties

UV-Vis-NIR Spectroscopy

The absorption spectrum of the Bi_2S_3 thin film is displayed in **Figure 7.6** which shows the onset of absorption near 850 nm. The inset shows the transmittance spectrum of the films.

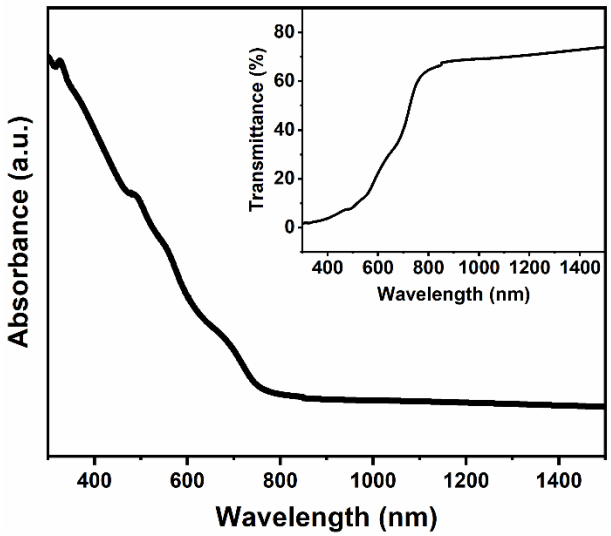

Figure 7.6. The absorption spectrum of the spray-deposited Bi_2S_3 thin films.

7.2.5. Photoresponse

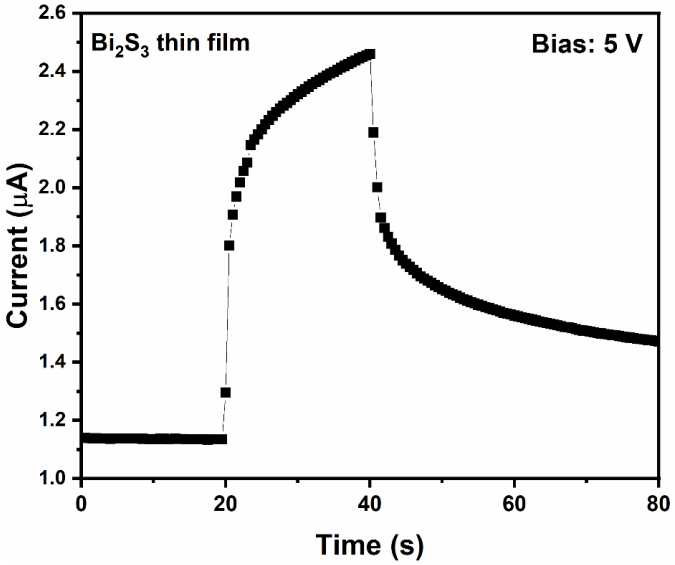

Figure 7.7. Photoresponse of the Bi_2S_3 thin film under 50 W halogen lamp.

The photoresponse of the Bi_2S_3 thin film at 5 V bias under the illumination by a 50 W halogen lamp is shown in **Figure 7.7**. The curve shows current in the microampere range with a dark current of 1.14 μA and a light current of ~2.38 μA.

7.3. $Cs_3Bi_2I_9$:Bi_2S_3 composite films

The pure and bismuth sulfide integrated thin films fabricated by ultrasonic spray deposition are displayed in **Figure 7.8**. Thioacetamide added to the $Cs_3Bi_2I_9$ precursor solution was varied as 0.005, 0.01, 0.03 and 0.05 M for Bi_2S_3 nanorod growth.

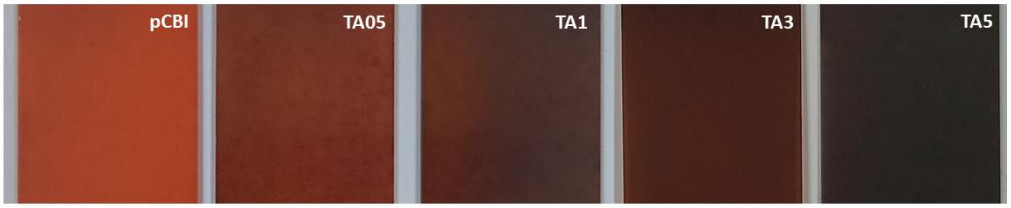

Figure 7.8. The pure $Cs_3Bi_2I_9$ (pCBI) and $Cs_3Bi_2I_9$:Bi_2S_3 (TA) composite films with different thioacetamide concentration.(thin film area 2.5 cm × 2.5 cm).

7.3.1. Structure

X-ray diffraction (XRD) and Raman spectroscopy

The powder X-ray diffraction patterns in Figure 7.9a of the thin films feature only peaks of hexagonal $Cs_3Bi_2I_9$ ($P6_3/mmc$), similar to the pure $Cs_3Bi_2I_9$ (pCBI) thin films matching with the ICDD file 01-073-0707. Noticeably, the polycrystalline nature increases in the TA3 and TA5 thin films as different from the (006) oriented growth in pCBI, TA05 and TA1 thin films deposited with lower thioacetamide (TA) concentration. The texture coefficients corresponding to the (006) and (101) planes have been calculated [242]. The TC_{006} increases from 2.68 for pCBI to 3.87 for TA1 and then decreases to 2.65 and 2.49 for TA3 and TA5, respectively. At the same time, TC_{101} increases from 0.19 to 0.84 with thioacetamide concentration. The (006) oriented crystallization of $Cs_3Bi_2I_9$ is favored with an increase in TA concentration up to 0.01 M. However, higher TA concentrations seem to limit this (006) growth resulting in polycrystalline thin films. On the other hand, a continuous improvement in the intensity of the (101) peak with TA concentration suggests that the presence of TA enhances the crystallization of $Cs_3Bi_2I_9$ along the (101) direction.

Further, even with the highest TA concentration (TA5), any peak corresponding to the Bi_2S_3 is not observed. This may be due to the poor crystallinity of Bi_2S_3 thin films with very low intensity peaks as observed in the diffraction pattern displayed in **Figure 7.2**a and therefore is not obvious in the XRD patterns of the composite thin films in Figure 7.9a.

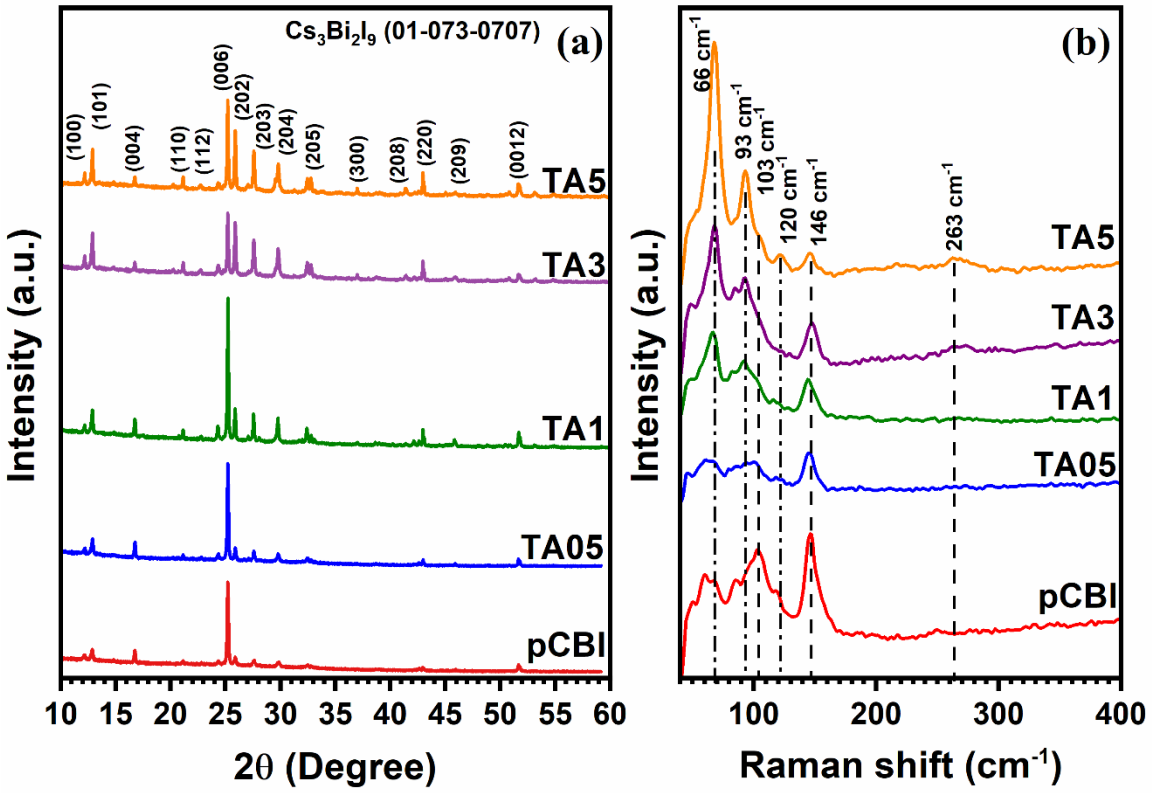

Figure 7.9. (a) The X-ray diffraction patterns and (b) Raman spectra of the pure $Cs_3Bi_2I_9$ and $Cs_3Bi_2I_9$:Bi_2S_3 composite thin films.

The peaks around 66, 103 and 146 cm^{-1} in the Raman spectra of the thin films in **Figure 7.9**b are related to the $Cs_3Bi_2I_9$ phase [217]. The low-frequency Raman line close to 66 cm^{-1} is ascribed to the vibrations of $[Bi_2I_9]^{3-}$ bioctahedral units with A_1^+ symmetry. The $[BiI_6]^{3-}$ vibrations inside this bioctahedra result in the peak near 103 cm^{-1}. The highest intensity peak in pCBI at 146 cm^{-1} is associated with the vibrational modes of Bi-I bonds [214]. However, the Raman spectra of the composite thin films display an additional peak at 263 cm^{-1} compared to pCBI arising from the B_{1g} vibrations in Bi_2S_3 which was seen in **Figure 7.2**b [240]. The reduced intensity of Raman peak at 146 cm^{-1} in the composite thin films

as compared to pCBI may suggest interactions between the vibrational modes of Bi-I with Bi-S bonds of Bi_2S_3. Besides,the increase in the intensity of Raman peak at 66 and 93 cm^{-1} in the composite thin films may be due to the contribution from Bi_2S_3 which have a characteristic peak around 54 cm^{-1} and 100 cm^{-1}.

7.3.2. Morphology

Scanning Electron Microscopy (SEM)

Figure 7.10 presents the morphology of pCBI and composite thin films, revealing the vertically aligned Bi_2S_3 nanorods *in situ* grown in the bulk of the $Cs_3Bi_2I_9$ layer through the spray deposition. These nanorod structures in the composite thin films can be compared to the typical morphology of the spray-deposited Bi_2S_3 thin film, which is also depicted in **Figure 7.10**.

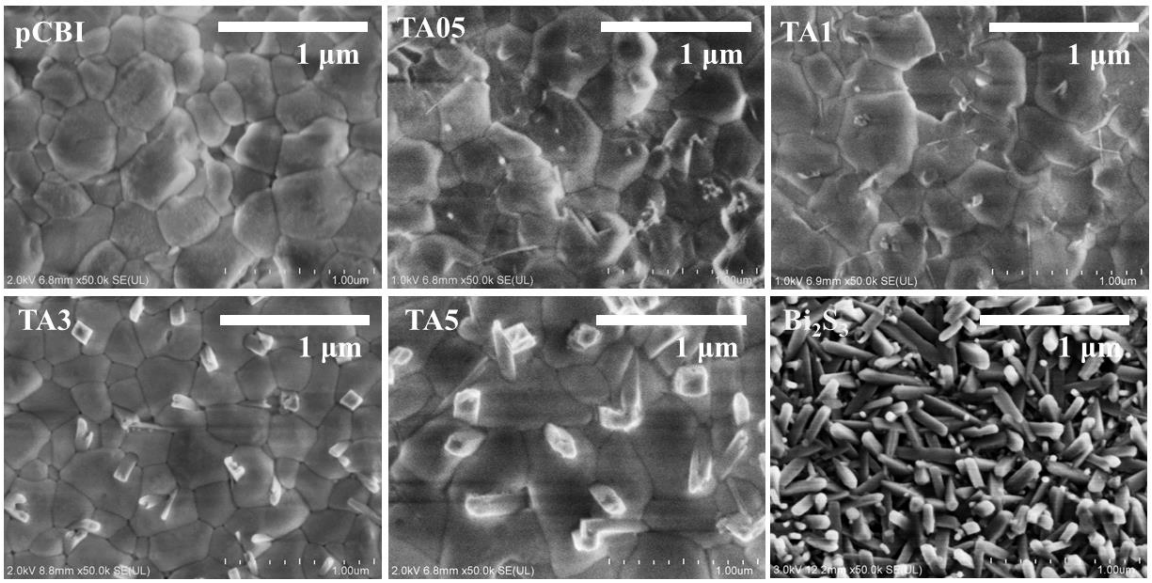

Figure 7.10. The SEM images of pure $Cs_3Bi_2I_9$, $Cs_3Bi_2I_9$: Bi_2S_3 composite and Bi_2S_3 thin films by ultrasonic spray deposition.

In the composite films, the growth of the Bi_2S_3 nanorods is noticed mainly in the grain boundaries of $Cs_3Bi_2I_9$. These nanorods appear denser and larger with increased thioacetamide (TA) concentration in the precursor solution. In the TA5 composite film deposited with the highest TA concentration, long nanorods protruding from the surface of $Cs_3Bi_2I_9$ can be observed.

Moreover, the low magnification images given in **Figure 7.11** reveal aggregations on the pCBI thin film surface due to the ineffective droplet spreading and evaporation followed by a very rapid crystallization. On the other hand, the TA3 composite film morphology presents better uniformity and a smooth surface, proving that the presence of thioacetamide enhances the thin film formation. Here, thioacetamide may act as a complexing agent in the precursor solution, thereby introducing an additional pyrolysis step in the growth mechanism of $Cs_3Bi_2I_9$ involving the parallel growth of Bi_2S_3 nanorods.

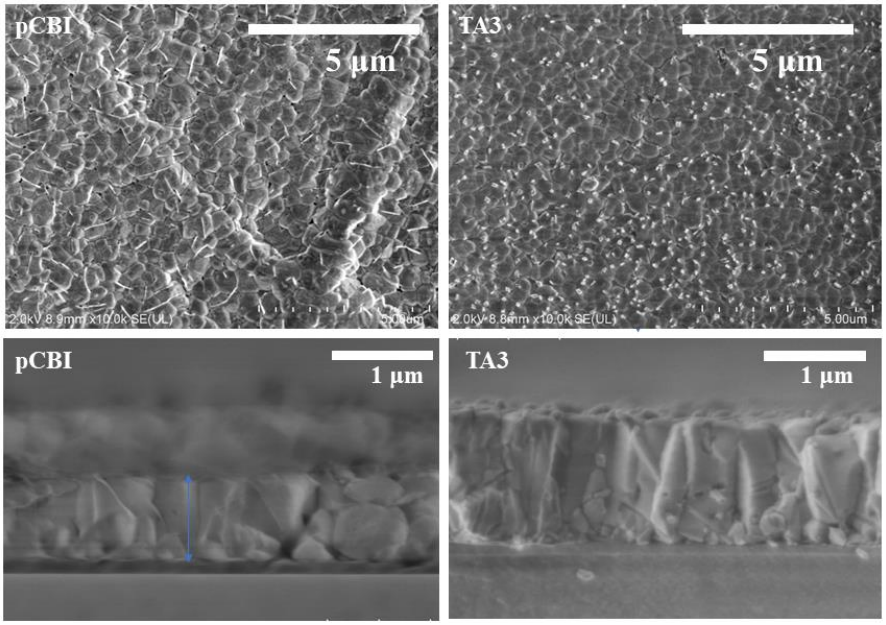

Figure 7.11. (Above) The low magnification SEM images of pure $Cs_3Bi_2I_9$ (pCBI) and $Cs_3Bi_2I_9$:Bi_2S_3 (TA3) thin films. (Below) The cross-sectional SEM image of pCBI and TA3 thin films on glass substrate.

The cross-sectional images of pCBI and TA3 film in **Figure 7.11** display enhanced droplet spreading during the composite thin film formation, explained by the noticeable aggregations in pure $Cs_3Bi_2I_9$ thin film. The thickness of the pCBI and TA3 composite film was measured to be 760 nm and 1060 nm, respectively, from the cross-sectional images. The concurrent growth of Bi_2S_3 nanorods may offer more nucleation centers for the $Cs_3Bi_2I_9$ crystallization resulting in highly uniform thin films of longer grains perpendicular to the substrate surface, as seen in **Figure 7.12**.

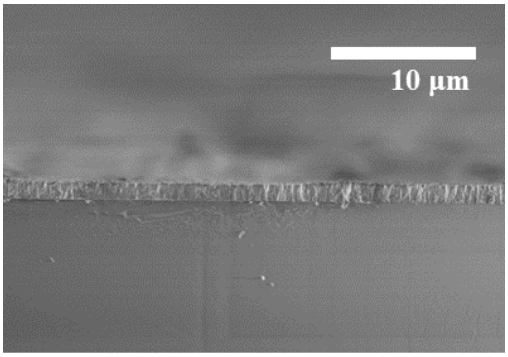

Figure 7.12. Low magnification cross-sectional image of TA3 composite thin film.

7.3.3. Chemical states

X-ray photoelectron spectroscopy (XPS)

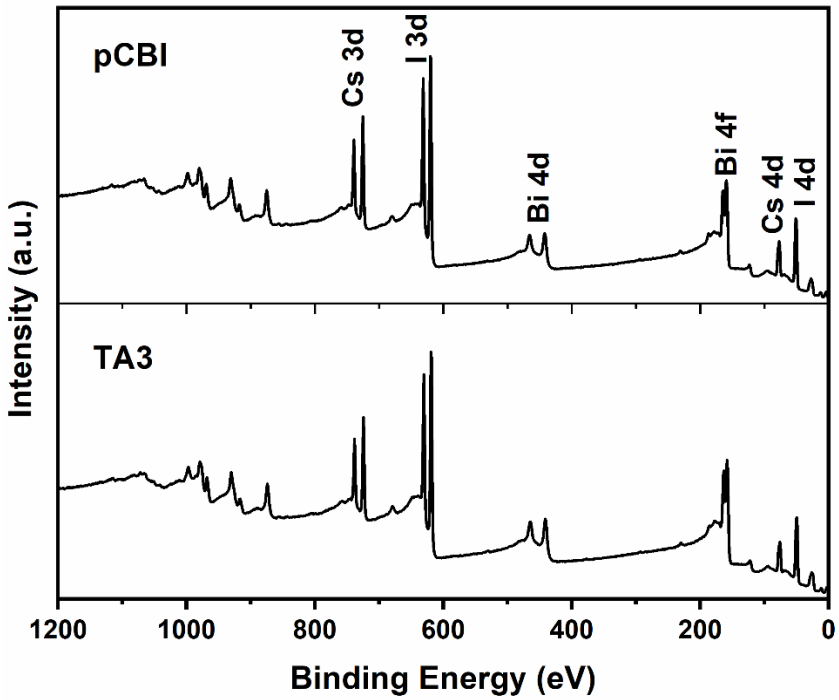

Figure 7.13. The XPS survey spectrum of pCBI and TA3 thin films.

The XPS spectra obtained after a soft Ar ion etching were used to identify and compare the elemental distribution and chemical states of pure $Cs_3Bi_2I_9$ and TA3 thin films. Though a flood gun is used in the measurements for charge compensation, the spectra were calibrated using the adventitious carbon (C 1s) peak at 284.6 eV [243]. The background of the high-

resolution spectra was determined based on a Shirly-type function which was used for fitting the curves using the Gaussian-Lorentzian sum function.

The survey spectra of pCBI and TA3 thin films in **Figure 7.13** show the presence of Cs, Bi and I in both films. Any significant shift in binding energy or additional peaks corresponding to other elements is not observed in the survey spectra. The Bi 4f high-resolution scan of pCBI thin film in **Figure 7.14** shows Bi $4f_{7/2}$ and $4f_{5/2}$ peaks near 159.18 and 164.48 eV, respectively, separated by 5.3 eV which are associated with the Bi^{3+} oxidized state in $Cs_3Bi_2I_9$ whereas it is 159.10 and 164.40 eV in TA3 composite film [223]. Besides, the 4f doublet near 157.2 and 162.5 eV in both the thin films is attributed to the atomic bismuth state (Bi^0) which generally originates from the etching process to remove the surface contaminants [134,217]. Additionally, the S 2p peak deconvoluted in the Bi 4f scan of TA3 composite thin film at 161.04 eV is attributed to the S^{2-} state in Bi_2S_3 [236]. The S 2p peak can be compared with the high-resolution scan of Bi_2S_3 thin film in **Figure 7.5**.

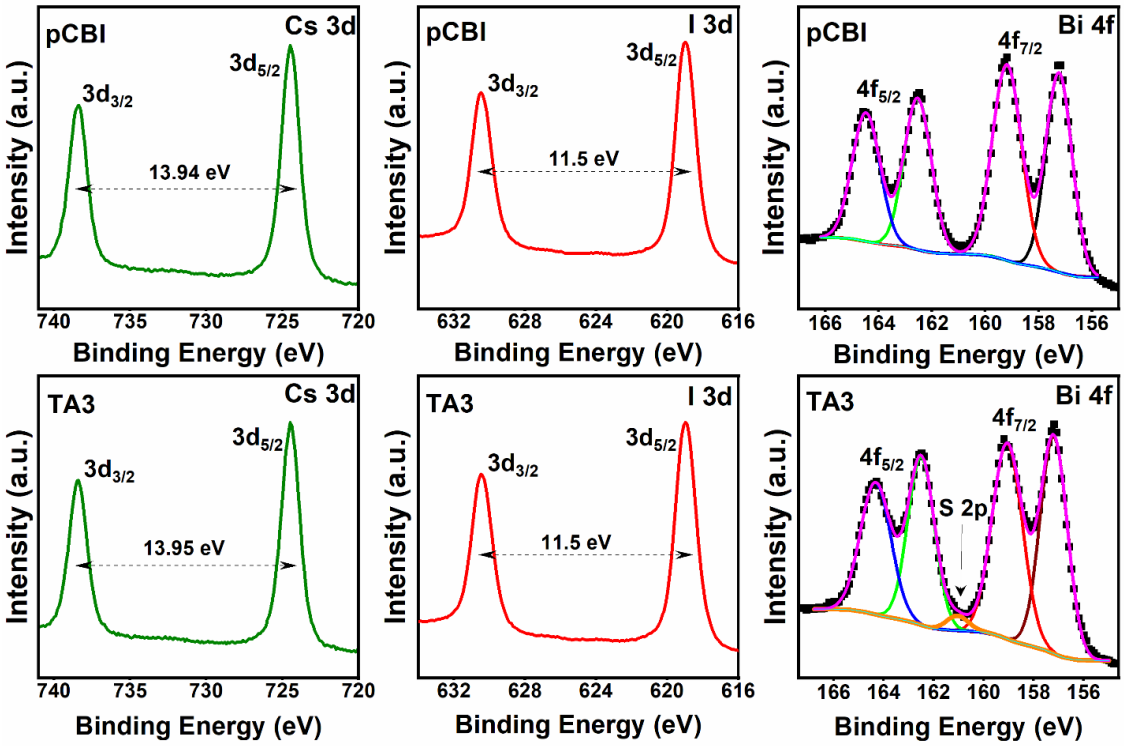

Figure 7.14. High-resolution Cs 3d, I 3d and Bi 4f scans of pCBI and TA3 thin film.

Further, the Cs and I core-level high-resolution scans of pCBI and TA3 thin films can be found in **Figure 7.14**. The Cs $3d_{5/2}$ and $3d_{3/2}$ peaks are noted at 724.44 and 738.38 eV in the pCBI thin film whereas for the TA3 composite film the respective peaks are observed at 724.48 and 738.43 eV [134]. The I 3d core-level spectrum comprises of $3d_{5/2}$ and $3d_{3/2}$ peaks located at 618.93 and 630.43 eV for pCBI thin film and at 618.98 and 630.48 eV for TA3 composite film [132,134]. The similar binding energy values of the elements in the two films suggest that the presence of nanorods does not change the chemical environment of the $Cs_3Bi_2I_9$ phase. This confirms that the Bi_2S_3 and $Cs_3Bi_2I_9$ are phase-separated and there are negligible interactions between them.

Furthermore, the depth profile analysis of the TA3 thin film in **Figure 7.15** reveals the elemental distribution from the surface to the TA3/glass substrate interface.

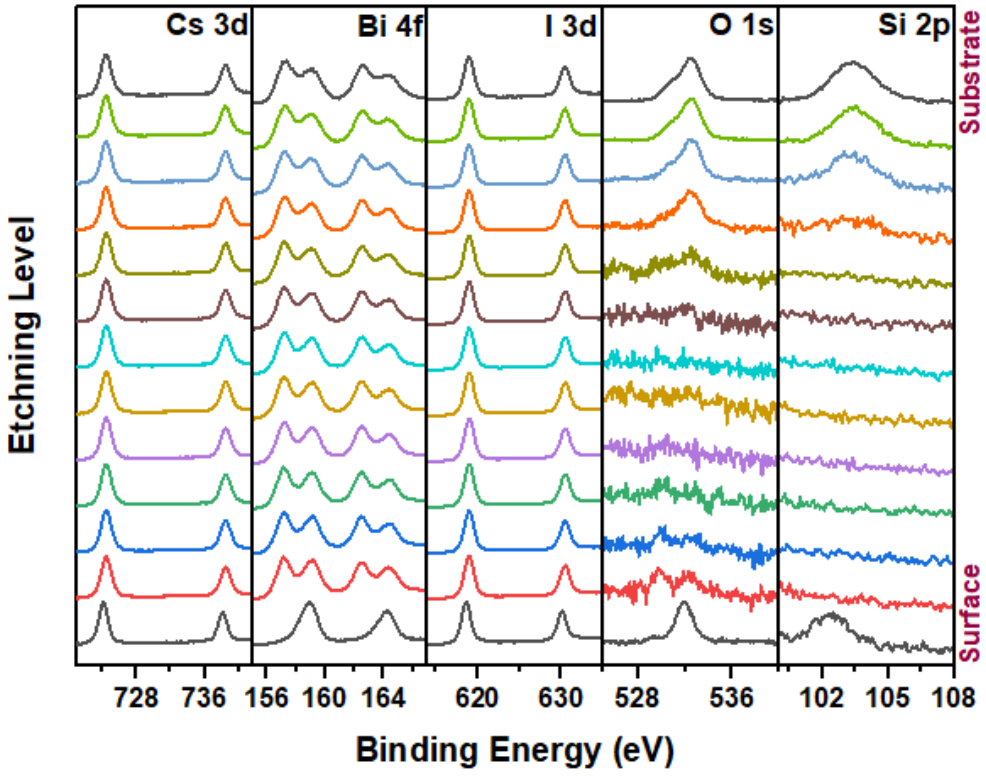

Figure 7.15. The XPS depth profile of TA3 composite thin film on glass substrate.

7.3.4. Optical properties

UV-Vis-NIR Spectroscopy

The absorption spectra of composite thin films in **Figure 7.16**a show a small shoulder around 850 nm in addition to the onset of absorption around 620 nm, as evident in its inset. The main absorption in the spectrum below 600 nm is caused by the $Cs_3Bi_2I_9$, which has a band gap of around 2.2 eV [127]. The direct band gaps calculated for pCBI, TA05, TA1, TA3 and TA5 thin films using the Tauc plots in **Figure 7.16**b are 2.15, 2.21, 2.24, 2.22 and 2.18 eV, respectively. The shoulder in the absorption curves of composite thin films around 900 nm results from the Bi_2S_3 thin film, which has a band gap close to 1.37 eV [240,244].

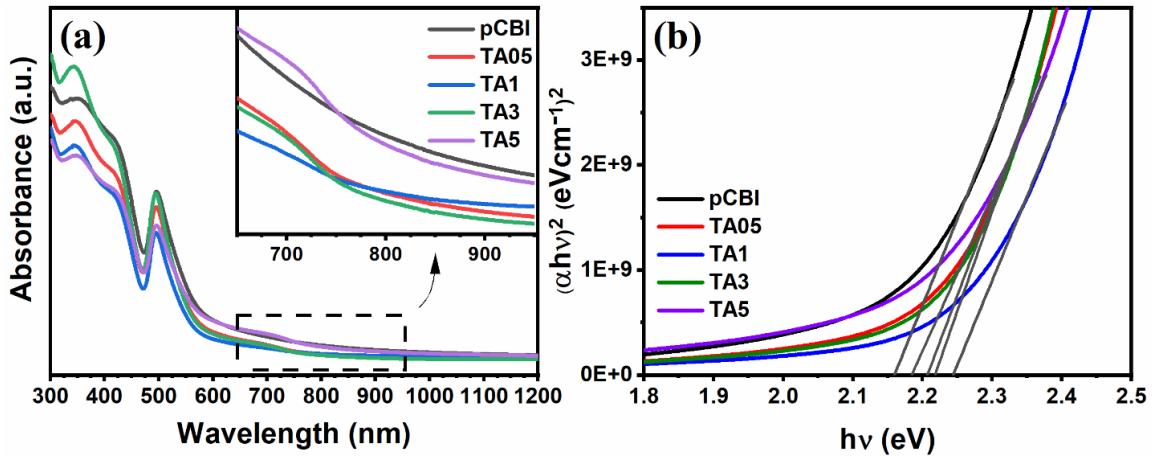

Figure 7.16. The (a) absorbance spectra and (b) calculated direct band gaps of the pCBI and composite thin films.

Similar optical band gap values imply that in situ growth of Bi_2S_3 nanorods has little to no impact on the optical characteristics of the $Cs_3Bi_2I_9$ phase. The growth mechanism or rate of crystallization of $Cs_3Bi_2I_9$, however, may be impacted by variations in TA concentration, which could result in minute changes in absorption.

7.3.5. Photoresponse

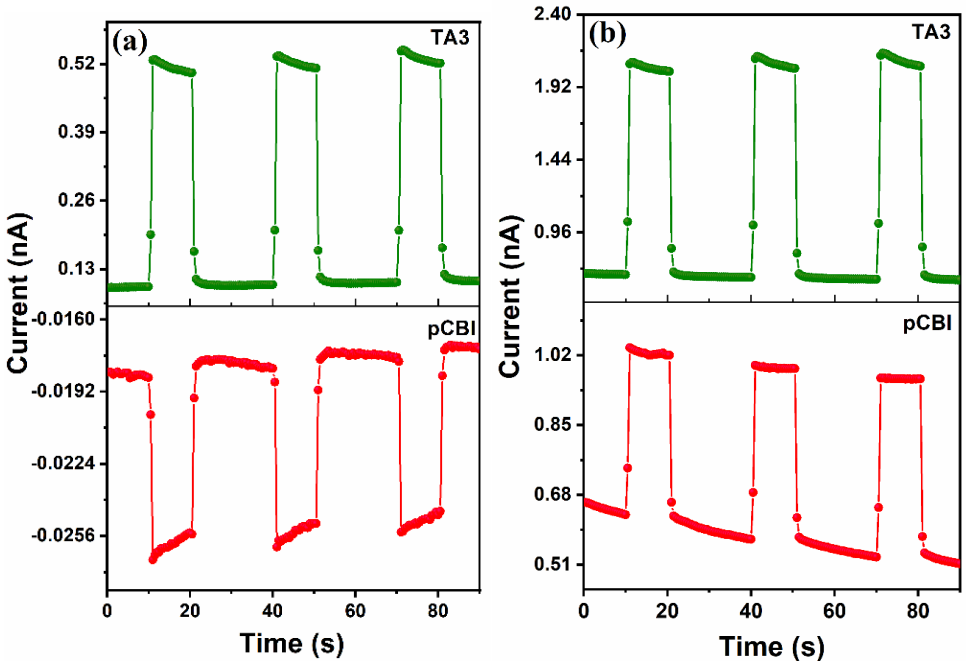

Figure 7.17. Photoresponse of the pCBI and TA3 composite thin films under 50 W halogen lamp at (a) 0 V and (b) 1V bias.

The photoresponse of the pCBI and TA3 thin films under 1 V and 0 V bias conditions is shown in **Figure 7.17**. In comparison to pure $Cs_3Bi_2I_9$ at 1 V bias, the TA3 thin film maintains a low dark current of 0.68 nA while delivering photocurrent up to 1.35 nA with a sensitivity of 198 %. Furthermore, the figure shows that in $Cs_3Bi_2I_9$:Bi_2S_3 composite films, a negative photoresponse changed to a positive behavior under zero bias.

7.3.6. Thermal stability

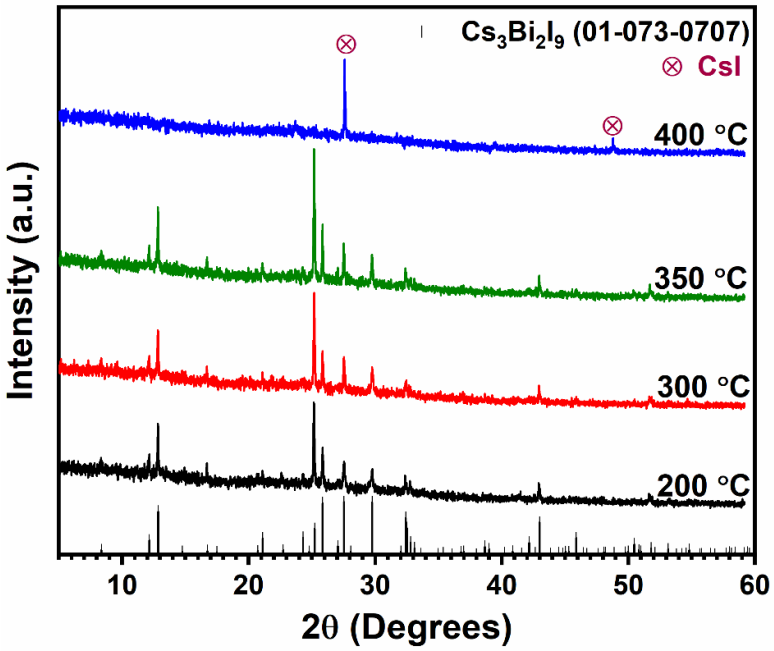

Figure 7.18. The XRD patterns of thermally treated TA3 thin films at various temperatures.

The TA3 composite thin film was annealed for 30 minutes in a low vacuum furnace at 200, 300, 350 and 400 ℃ to examine its thermal stability and morphological changes. The annealing temperature improves the (006) growth in the TA3 thin films, as seen in Figure 7.18. The thin film, however, significantly decomposes at 400 ℃, with only CsI peaks visible in the XRD patterns.

However, the Raman spectra in Figure 7.19 demonstrate a rise in the intensity of the 265 cm^{-1} peak associated with the Bi_2S_3 phase. This may indicate a relative increase in the Bi_2S_3 nanorods compared to $Cs_3Bi_2I_9$ in the composite thin film. SEM images in Figure 7.20 support this observation in which the thin film treated at 400 ℃ shows Bi_2S_3 nanorods and CsI particles due to the decomposition of $Cs_3Bi_2I_9$.

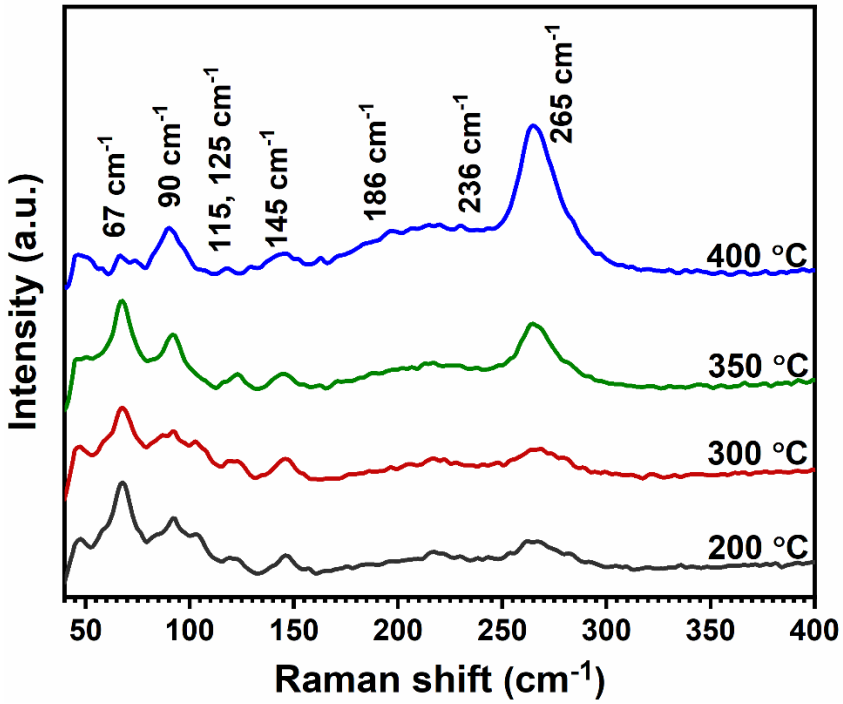

Figure 7.19. Raman spectra of thermally treated TA3 thin films at various temperatures.

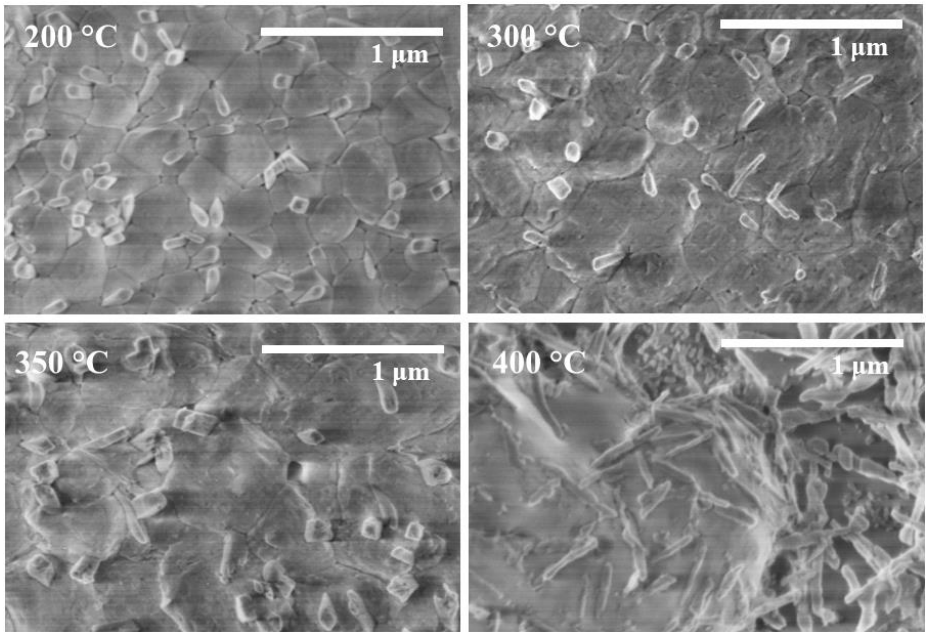

Figure 7.20. The SEM images of the TA3 composite films with different annealing temperatures.

7.3.7. Self-powered photodetector

Compared to the control device using pure $Cs_3Bi_2I_9$ thin film in heterojunction photodetectors, the spray-deposited $Cs_3Bi_2I_9$:Bi_2S_3 composite layer showed excellent self-powered detection properties. The transient current measurements under AM1.5 illumination are used to evaluate the performance of the two devices. The FTO/CdS/$Cs_3Bi_2I_9$/C-Ag photodetector, illustrated in the Figure 7.21a, shows a continuous fall in the on/off ratio with a notable light-induced photocurrent degradation as seen in Figure 7.21b. The photocurrent reduced from 0.39 μA to 0.27 μA while the dark current increased from 6.7 nA to 11 nA in 10 min due to the light-induced effects, which is much more apparent in the degrading nature of the current during illumination.

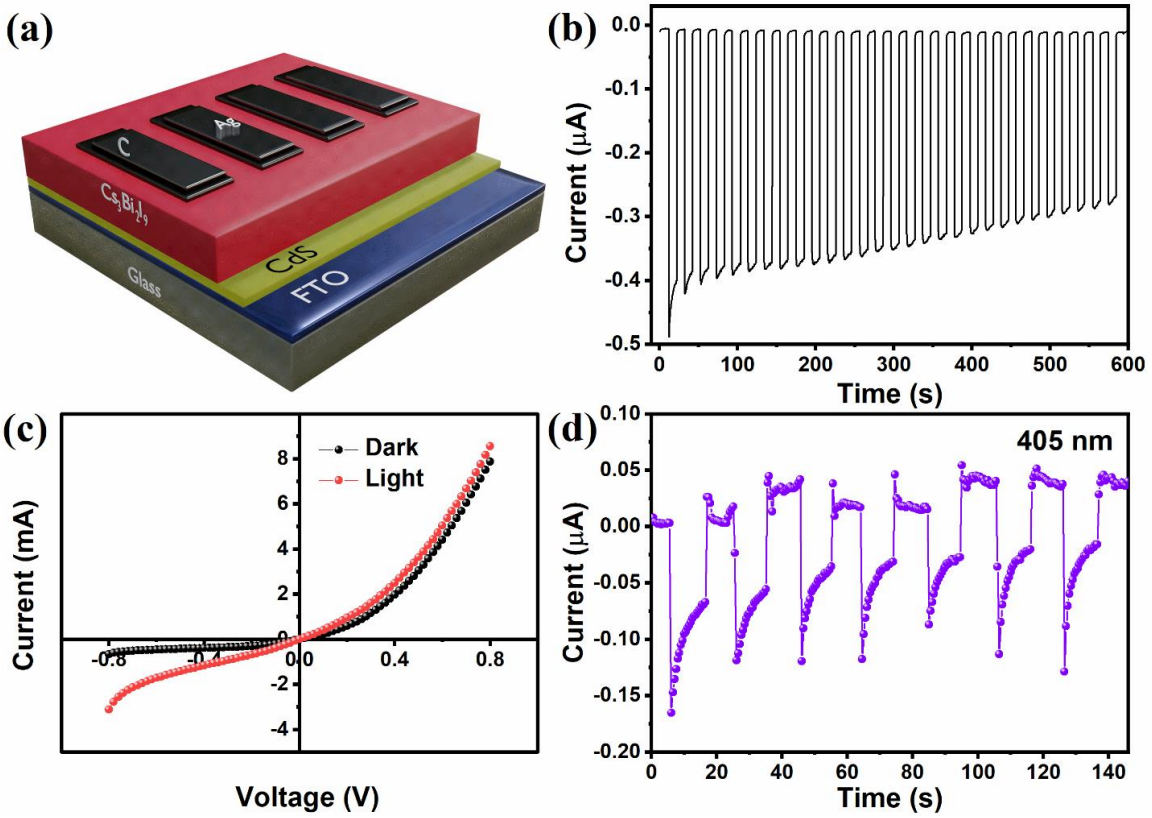

Figure 7.21. (a) Schematic of the FTO/CdS/pCBI/C-Ag device, (b)The response of the junction at 0 V bias under AM 1.5 illumination and its (c) IV characteristics and (d) Response of the heterostructure to 405 nm (50 mW) laser illumination.

The I-V characteristics of the heterojunction, displayed in Figure 7.21c, also suggest the enhanced Schottky nature of the junction under illumination. This may suggest that there is faster recombination of the photogenerated carriers in $Cs_3Bi_2I_9$ thin film, which may be a consequence of the aforementioned light-induced halide ion migrations leading to a higher density of trap states. Besides, the unstable response of the device to 405 nm illumination under zero bias is depicted in Figure 7.21d.

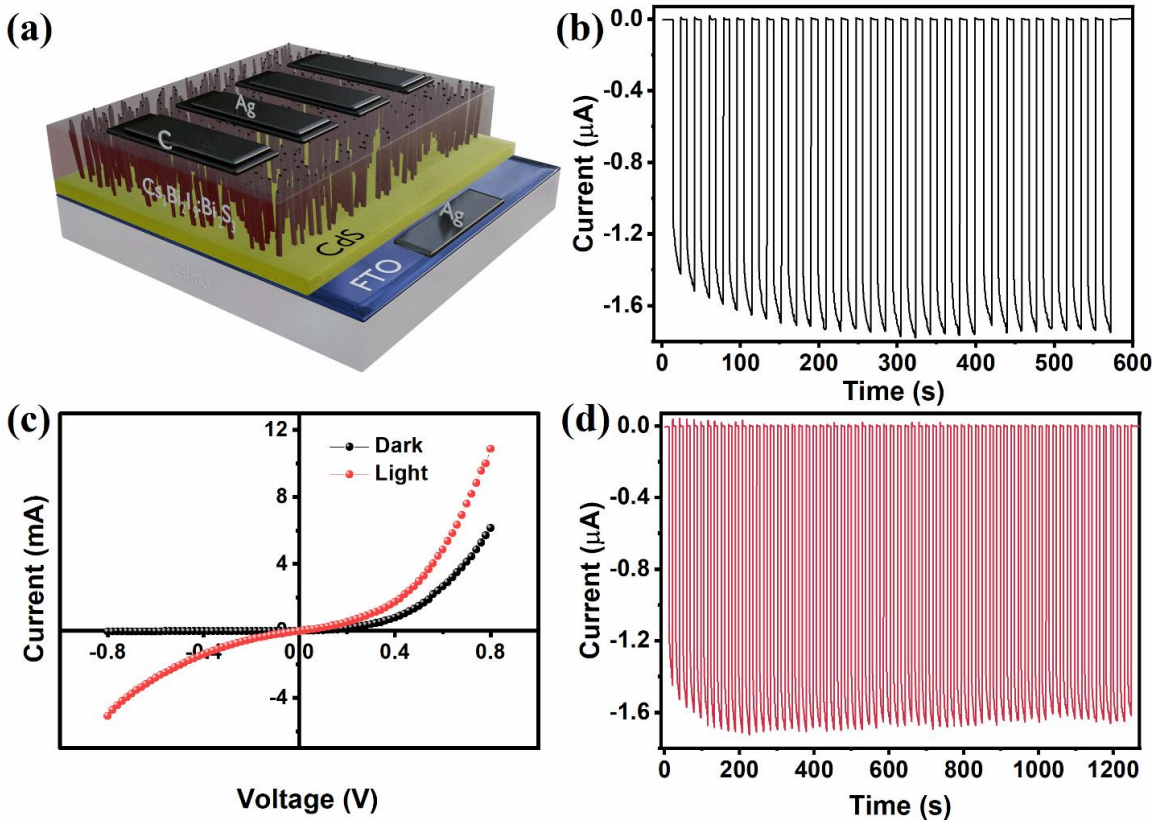

Figure 7.22. (a) An illustration of FTO/CdS/TA3/C-Ag device. (b)The response of the device under AM 1.5 illumination at 0 V bias. (c) The IV characteristics of the heterojunction device. (d) The repeatability and stability of the response under AM 1.5 illumination.

Interestingly, our *in situ* grown $Cs_3Bi_2I_9$:Bi_2S_3 composite thin film performs better in the photodetector structure illustrated in Figure 7.22a. Figure 7.22b demonstrates a more stabilized photocurrent about four times (~1.8 μA) as that of the pure $Cs_3Bi_2I_9$-based device measured under the AM1.5 illumination. In the composite device, the conducting Bi_2S_3 nanorods collect the photogenerated carriers before going through recombination in the

bulk of the $Cs_3Bi_2I_9$ and transfer to the electrodes. More importantly, we observed an initial increase in photocurrent that is stabilized after 200 s without experiencing any light-induced degradation. Figure 7.22d shows that this stable dark and photocurrent cycle is continued over 20 mins of continuous measurements.

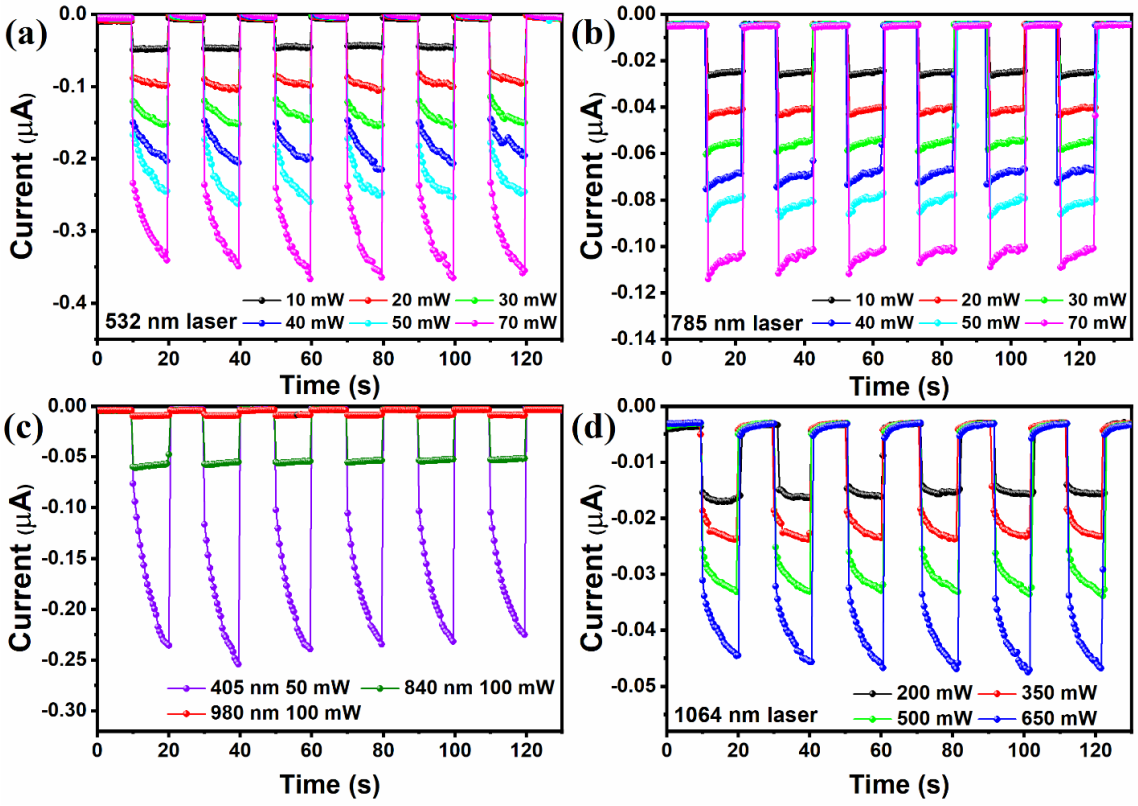

Figure 7.23. The response of FTO/CdS/TA3/C-Ag heterstructure to various laser illuminations of (a) 532 nm (b) 785 nm (c) 405, 840 and 980 nm as well as (d) 1064 nm laser.

Further, the performance of the composite thin film was assessed using light sources of 405, 532, 785, 840, 980 and 1064 nm wavelengths in self-driven mode. While all other illuminations were power-adjustable, the 840 and 980 illuminations were each of 100 mW power and the 405 nm illumination was of 50 mW power. Intriguingly, the photodetector demonstrated appreciable self-driven response under all illuminations, as seen in Figure 7.23, indicating broad detection capabilities of the TA3 composite film.

The photodetector produced maximum photocurrent up to ~0.25 μA under 405 and 532 nm illumination of 50 mW. Figure 7.24a & b shows the dependence of photocurrent (I_{ph}) on

illumination power density (P), which was evaluated using the power law ($I_{ph} \propto P^{\theta}$). The log ($I_{ph}$) vs. log (P) plots using the power law are displayed in Figure 7.24c,d, which estimates the θ values of 0.95, 0.82 and 0.85 for 532, 785 and 1064 nm lasers, respectively [106]. The values of θ less than but closer to 1 indicate less recombination in the $Cs_3Bi_2I_9$:Bi_2S_3 composite thin film [31].

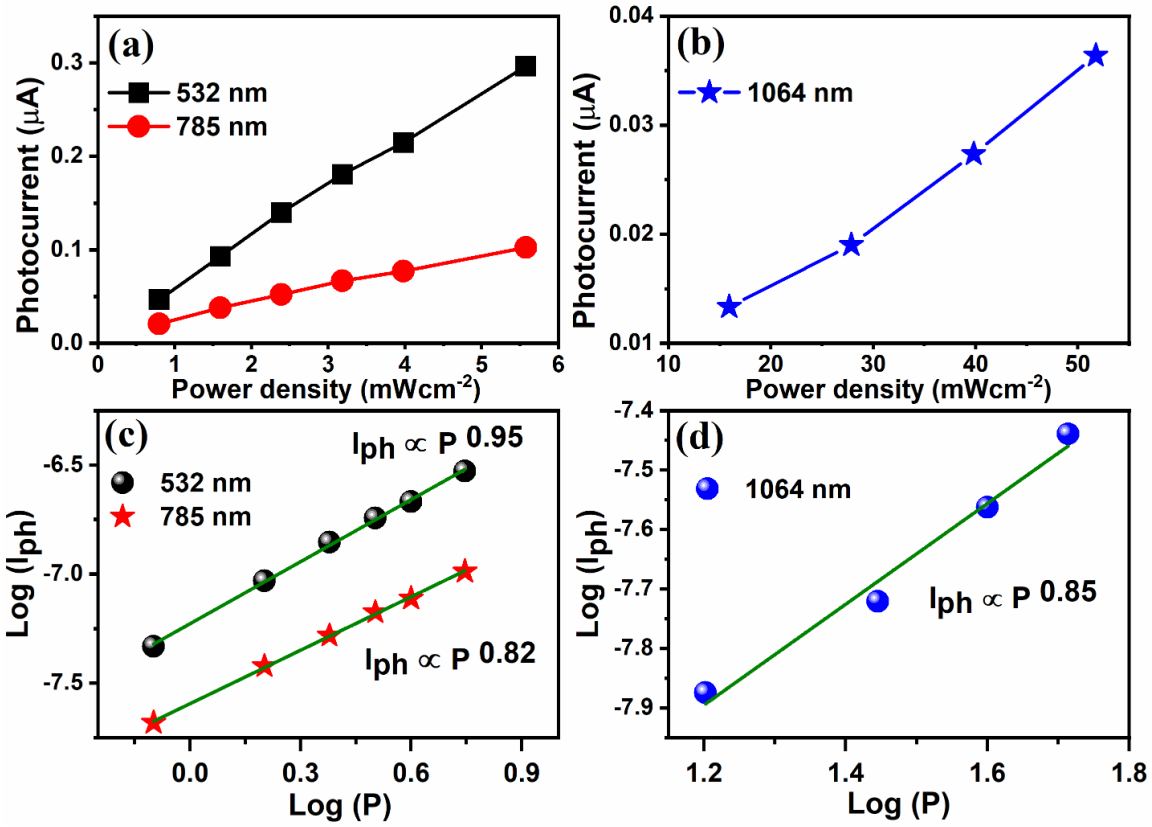

Figure 7.24. The photocurrent vs power density curves for (a) 532 nm and 785 nm as well as (b) 1064 nm illumination. Power law fitting for the (c) 532, 785 and (d) 1064 nm laser irradiations.

The responsivity and detectivity were calculated using the equations (2.11) and (2.12). Figure 7.25 compare the detectivity and responsivity of TA3 devices for all the illuminations from 405 – 1064 nm. The TA3 device demonstrated the best self-powered detection performance under the 532 nm (790 μWcm^{-2}) source with a detectivity of 8.18 × 10^9 Jones and responsivity of 0.59 mAW^{-1}. The detectivity ranged from ~5.1 × 10^9 to 6.6 × 10^7 Jones over the broad spectral range of 405 - 1064 nm.

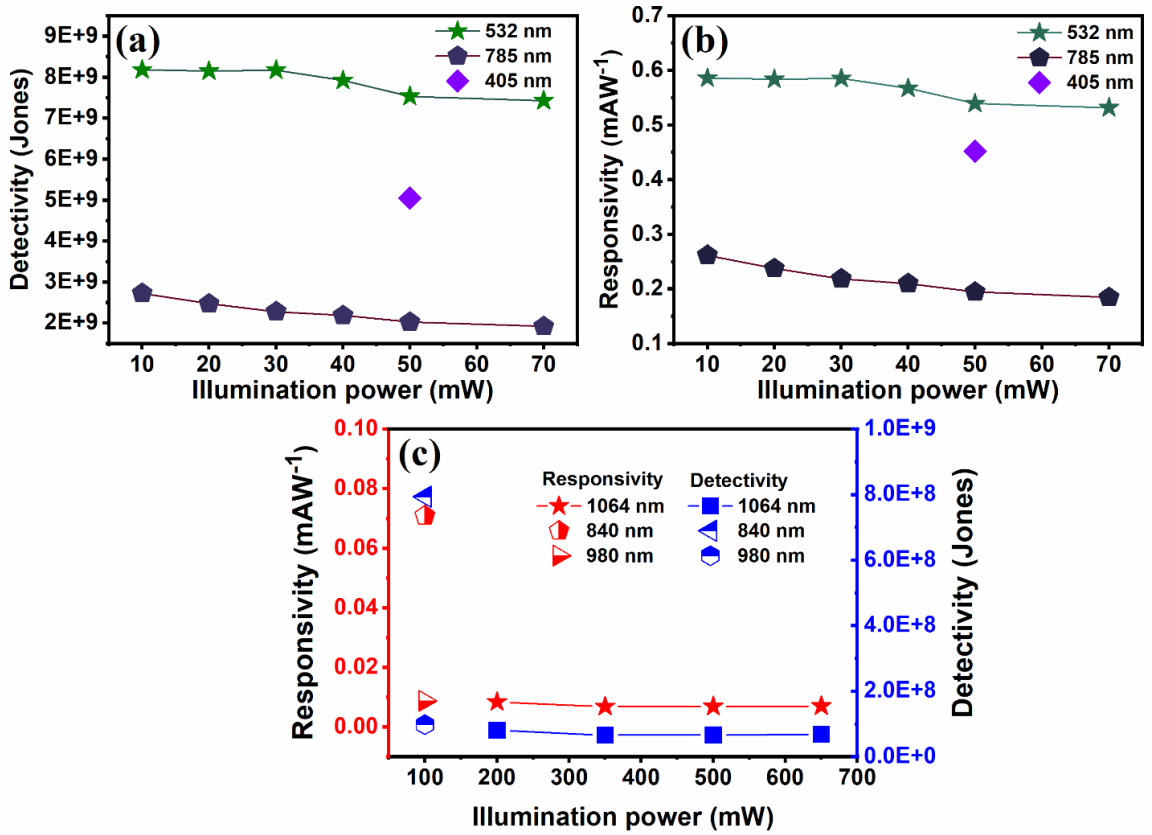

Figure 7.25. The detection performance of FTO/CdS/TA3/C-Ag to various illuminations. (a) Detectivity to 532, 785 and 405 nm (b) Responsivity to 532, 785 and 405 nm laser illuminations (c) Responsivity and detectivity to 840, 980 and 1064 nm.

Previously, spin-coated $Cs_3Bi_2I_9$ in self-powered photodetectors demonstrated response in the 450-950 nm range with detectivities up to ~10^{10} – 10^{12} Jones [104]. Here, the spray-cast device with $Cs_3Bi_2I_9$:Bi_2S_3 shows broader detection from the 405 – 1064 nm wavelength range. Most importantly, the photocurrent is improved to the micro-ampere range without any complicated structure compared to the detectors reported earlier [105,111]. Moreover, this novel method for growing nanostructures in the perovskite thin film in a single-step ultrasonic spray deposition holds significant potential to improve charge extraction and performance in various optoelectronic devices.

7.4. Conclusions

The ultrasonic spray deposition technique is efficient in the in-situ growth of Bi_2S_3 nanorods in perovskite-inspired $Cs_3Bi_2I_9$ thin films, which can be adopted for other

perovskite material/transport layer combinations with common metal cations and similar reaction dynamics. Here, the conducting Bi_2S_3 nanorods were successful in collecting the photogenerated carriers from the bulk of the $Cs_3Bi_2I_9$, thus suppressing the carrier recombination process as well as light and electric field induced degradation of the photocurrent. The FTO/CdS/TA3/C-Ag device based on these composite film exhibits outstanding photostability and repeatability for extended operations. The photodetector showed broad detection characteristics in the 405 – 1064 nm range with the best detectivity of 8.18×10^9 Jones and responsivity of 0.59 mAW^{-1} under 532 nm laser illumination. This performance shows the potential of scalable ultrasonic spray deposition technique in designing optoelectronic devices based on lead-free perovskites and perovskite-inspired materials.

CHAPTER 8

CONCLUSIONS

This chapter concisely describes the conclusions and contributions of the present work to the scientific knowledge.

This thesis presents the ultrasonic spray deposition and systematic characterization of the lead-free $Cs_3Bi_2I_9$ thin films fabricated. Through these investigations we draw a deep insight into the structure-property relations in all-inorganic lead-free perovskite $Cs_3Bi_2I_9$, both theoretically and experimentally. Based on our hypothesis, we fabricated $Cs_3Bi_2I_9$ thin films by ultrasonic spray deposition technique to provide scientific data on their potential for optoelectronic devices. In addition, we have investigated the possibilities of using environment-friendly solvents like ethanol and acetone instead of the generally used dimethyl formamide (DMF) or dimethyl sulfoxide (DMSO) solvents for the deposition of halide compounds.

In sumary:

VASP based Density Functional Theory

- The density functional theory calculations explains the contributions of each element in the compound to the electronic properties of BiI_3 and $Cs_3Bi_2I_9$.
- The electronic band structure calculations yield a band gap of 1.44 eV and 1.99 eV for BiI_3 and $Cs_3Bi_2I_9$, respectively.
- The density of states calculations show the contribution of I p states in the CBM of both BiI_3 and $Cs_3Bi_2I_9$, which points to possible engineering routes in the halide ions that can alter the electronic properties.

- Most importantly, the calculations give us enough information to understand the experimental properties by correlating with the theoretical calculations for further investigation.

Ultrasonic spray deposition (USD) of all-inorganic lead-free $Cs_3Bi_2I_9$

- Optimization of deposition parameters of a USD system for the formation of good quality thin films.
- Single-step spray deposition of $Cs_3Bi_2I_9$ thin films using dimethyl formamide (DMF) as a solvent.
- A systematic study on the growth of $Cs_3Bi_2I_9$ thin film by varying the substrate temperature from 150 to 400 °C.
- Analysis of the structure, morphology, chemical state and photophysical properties of the spray-deposited films.
- Formation of phase-pure $Cs_3Bi_2I_9$ thin films with optical band gap of around 2 eV.
- Spray-deposited $Cs_3Bi_2I_9$ thin films with compact morphology composed of large polygonal grains (300-900 nm) of vertical growth up to 1800 nm.
- (Ag/$Cs_3Bi_2I_9$/Ag) photoconductor using the $Cs_3Bi_2I_9$ films deposited at 250 °C demonstrated illumination current up to 1.4 nA under a 50 W halogen lamp illumination.
- Rapid thermal processing for 1 min indicates the thermal stability of the thin films up to 500 °C.
- Glass/FTO/$Cs_3Bi_2I_9$/C-Ag photodiode with self-powered photodetection properties under the 405 nm (50 mW) illumination yielding a detectivity of 5.93×10^8 Jones and a responsivity of 0.0051 mAW^{-1}.
- A two-step synthesis of $Cs_3Bi_2I_9$ thin film based on ethanol, a more benign solvent by sequential spraying of CsI on BiI_3 thin film.
- A systematic analysis of the thin films formed by varying the CsI solution concentration (0.003-0.021 M) and the number of depositions (5, 10 and 15).
- Phase-pure $Cs_3Bi_2I_9$ films of ~1000 nm thickness by spraying a 0.015 M CsI solution (7 ml in 10 times deposition) over the spray-deposited BiI_3 thin film.

- The $Cs_3Bi_2I_9$ thin films composed of hexagonal-shaped nanosheets or flakes (~280 nm), a distinct morphology in comparison with that of the films formed by the single-step deposition, with similar band gap.
- Fabrication of photovoltaic device Glass/FTO/CdS/$Cs_3Bi_2I_9$/C-Ag giving 300 mV open-circuit voltage (V_{oc}) and a 0.003 $mAcm^{-2}$ short-circuit current density (J_{sc}).
- The glass/FTO/ZnO/$Cs_3Bi_2I_9$/C-Ag heterojunction with a turn-on voltage of approximately 0.56 V and a maximum forward-to-reverse current ratio of 7.5 at 0.7 V. The junction yielded an ideality factor of 1.75.
- Bi_2S_3 thin films composed of vertically aligned nanorods by ultrasonic spray deposition.
- *in situ* growth of Bi_2S_3 nanorods in the $Cs_3Bi_2I_9$ films by solution engineering of $Cs_3Bi_2I_9$ precursor with different concentrations of thioacetamide (0.005, 0.01, 0.03 and 0.05 M).
- The simultaneous growth of nanorods in the bulk affecting the crystallinity of $Cs_3Bi_2I_9$ thin films to form polycrystalline nanocomposite thin films with enhanced columnar growth (~1060 nm).
- The calculated optical band gap was around 2.2 eV.
- A better illumination current of 2.40 nA from the composite thin films compared to the 1.02 nA of pure $Cs_3Bi_2I_9$ thin film under a 50 W halogen lamp.
- The composite thin films had thermal stability up to 350 ℃.
- Good photostability of the composite films in contrary to the degrading photocurrent of pure $Cs_3Bi_2I_9$ thin film.
- The photodetector of Glass/FTO/$Cs_3Bi_2I_9$:Bi_2S_3/C-Ag structure yielding a detectivity of 8.18×10^9 Jones and a responsivity of 0.59 mAW^{-1}.

Therefore, ultrasonic spray deposition is viable for better growth when considering deposition over a large area. This is particularly important because this is a possibility for using non-toxic solvents such as ethanol or acetone, which have solubility limitations but lower boiling points than the usually used DMF or DMSO. Besides, the precursor

preparation also allows solvent mixtures since low concentrations can be used here in ultrasonic spray deposition as different from the spin coating.

Potential for device applications

Table 8-1. The performance parameters of various $Cs_3Bi_2I_9$ based photodetectors.

Device structure	Deposition method		R (AW^{-1})	D* (Jones) ($\times10^{10}$)	On/off ratio	τ_r/τ_d (ms)	Ref.
ITO/$Cs_3Bi_2I_9$/ITO (450 nm, 10 V)	Spin coating	nanocrystals	33.1×10^{-3}	~1	~40	10.2/37.2	[103]
FTO/$Cs_3Bi_2I_9$/Ag (white light: 450-950 nm, 0V)	Spin coating	Micro crystals	0.59×10^{-6}	1.2	1.4×10^{4}	62.74 /90.25	[104]
ITO/PEDOT:PSS/$Cs_3Bi_2I_{9-x}Br_x$/C60/BCP/Ag (410 nm, 0 V)	Spin coating	Thin film	15×10^{-3}	46	4.1×10^{4}	40.7/27.1	[105]
ITO/$Cs_3Bi_2I_9$/Au (white light, -2 V)	Space limited method	SC thin film	7.2×10^{-3}	10	1.1×10^{4}	247/230 $\times10^{-3}$	[14]
ITO/$Cs_3Bi_2I_9$/Au (white light, -2 V)	Spin coating	PC thin film	7×10^{-3}	0.72	23-24	582/ 385.5×10^{-3}	[14]
FTO/Al_2O_3/$Cs_3Bi_2I_9$/Au (405 nm, 0V)	Spin coating	PC Thin film	100 $\times10^{-3}$	--	3.85×10^{3} (1.7 mW)	--	[106]
graphene/$Cs_3Bi_2I_9$ (325 nm, -5 V)	Space limited method	Single crystal	13.8×10^{-3}	52.4	--	13.2/15.5	[110]
MoS_2/$Cs_3Bi_2I_9$ (325 nm, -5 V)			1.42	1150	--	11.6/14.9	
Ag/Si/$Cs_3Bi_2I_9$/Au (450 nm, 3 V)	Space limited method	Single crystalline film	--	39	3×10^{3}	0.0015/0.422	[245]
Au/$Cs_3Bi_2I_9$/Au (343 nm, 1 V)		Single crystal	3.15×10^{-3}	0.087			[246]
ITO/SnO_2/$Cs_3Bi_2I_9$-SC/PTAA/Au/ITO (405 nm, 0 V)	SACM	Single crystal	52.06×10^{-3}	100	5.7×10^{3}	--	[111]
Au/$Cs_3Bi_2I_9$/Au (405 nm)	Spin coating	nanocrystals	14.67 $\times10^{-3}$	14.2	--	--	[109]
p-Si/$Cs_3Bi_2I_9$/Graphene (650 nm, -2 V)	Spin coating	nanocrystals	23.6	1750	--	$31/34\times10^{-3}$	

The spray-cast $Cs_3Bi_2I_9$ thin films were suitable for photodetection applications in the 400-500 nm range. Especially the material has very good detectivity and responsivity to blue light; therefore, $Cs_3Bi_2I_9$ can be a potential material for devices to detect the radiations harmful to human eyes. The performance of the reported photodetectors fabricated using other methods, in Table 8-1, can be compared with the spray-deposited devices fabricated in this work shown in Table 8-2.

The hole transport-free photovoltaic devices, which we are particularly interested in, did not demonstrate significant performance. However, their photovoltaic behavior suggests they may be more suitable for tandem solar cells, considering the band gap.

Table 8-2. Heterojunction photodetectors made from spray-deposited $Cs_3Bi_2I_9$ thin films in this work.

Device structure	R (AW^{-1})	D^* (Jones)	On/off ratio	τ_r/τ_d
FTO/$Cs_3Bi_2I_9$/C-Ag (405 nm, 50 mW, bias: 0 V)	5.1×10^{-6}	5.93×10^{8}	~10^2	1.52/2.29 s
FTO/CdS/$Cs_3Bi_2I_9$:Bi_2S_3/C-Ag (532 nm, 10 mW, bias: 0 V)	0.59×10^{-3}	8.18×10^{9}	~68	0.28/0.31 s

In general, the investigations and findings in this study contribute to the deep understanding of perovskite-inspired $Cs_3Bi_2I_9$ thin films, especially their structure and photophysical properties, as well as their optoelectronic performance. Furthermore, this research will inspire to explore the potential of ultrasonic spray deposition in the fabrication of lead-free and stable perovskites with non-toxic solvents. Moreover, the real-time growth of nanostructures during the deposition of structurally stable lead-free halide thin films opens the door to exploring composite thin films to overcome the current limitations of lead-free perovskites.

REFERENCES

[1] A. Kojima, K. Teshima, Y. Shirai, T. Miyasaka, Organometal halide perovskites as visible-light sensitizers for photovoltaic cells, J. Am. Chem. Soc. 131 (2009) 6050–6051. doi:10.1021/ja809598r.

[2] Best Research-Cell Efficiencies, National Renewable Energy Laboratory, (n.d.). https://www.nrel.gov/pv/assets/pdfs/best-research-cell-efficiencies.20200311.pdf (accessed March 26, 2020).

[3] E. Lamanna, F. Matteocci, E. Calabrò, L. Serenelli, E. Salza, L. Martini, F. Menchini, M. Izzi, A. Agresti, S. Pescetelli, S. Bellani, A.E. Del Río Castillo, F. Bonaccorso, M. Tucci, A. Di Carlo, Mechanically Stacked, Two-Terminal Graphene-Based Perovskite/Silicon Tandem Solar Cell with Efficiency over 26%, Joule. (2020). doi:10.1016/j.joule.2020.01.015.

[4] T. Duong, H. Pham, T.C. Kho, P. Phang, K.C. Fong, D. Yan, Y. Yin, J. Peng, M.A. Mahmud, S. Gharibzadeh, B.A. Nejand, I.M. Hossain, M.R. Khan, N. Mozaffari, Y.L. Wu, H. Shen, J. Zheng, H. Mai, W. Liang, C. Samundsett, M. Stocks, K. McIntosh, G.G. Andersson, U. Lemmer, B.S. Richards, U.W. Paetzold, A. Ho-Ballie, Y. Liu, D. Macdonald, A. Blakers, J. Wong-Leung, T. White, K. Weber, K. Catchpole, High Efficiency Perovskite-Silicon Tandem Solar Cells: Effect of Surface Coating versus Bulk Incorporation of 2D Perovskite, Adv. Energy Mater. 10 (2020) 1903553. doi:10.1002/aenm.201903553.

[5] J.P. Mailoa, C.D. Bailie, E.C. Johlin, E.T. Hoke, A.J. Akey, W.H. Nguyen, M.D. McGehee, T. Buonassisi, A 2-terminal perovskite/silicon multijunction solar cell enabled by a silicon tunnel junction, Appl. Phys. Lett. 106 (2015) 121105. doi:10.1063/1.4914179.

[6] H. Lai, J. Luo, Y. Zwirner, S. Olthof, A. Wieczorek, F. Ye, Q. Jeangros, X. Yin, F. Akhundova, T. Ma, R. He, R.K. Kothandaraman, X. Chin, E. Gilshtein, A. Müller, C. Wang, J. Thiesbrummel, S. Siol, J.M. Prieto, T. Unold, M. Stolterfoht, C. Chen, A.N. Tiwari, D. Zhao, F. Fu, High-Performance Flexible All-Perovskite Tandem Solar Cells with Reduced V OC -Deficit in Wide-Bandgap Subcell, Adv. Energy Mater. (2022) 2202438. doi:10.1002/aenm.202202438.

[7] M. Worku, Y. Tian, C. Zhou, H. Lin, M. Chaaban, L. Xu, Q. He, D. Beery, Y. Zhou, X. Lin, Y. Su, Y. Xin, B. Ma, Hollow Metal Halide Perovskite Nanocrystals with Efficient Blue Emissions, Sci. Adv. 6 (2020) eaaz5961. doi:10.26434/chemrxiv.9636824.v1.

[8] C. Wang, Y. Wang, X. Su, V.G. Hadjiev, S. Dai, Z. Qin, H.A. Calderon Benavides, Y. Ni, Q. Li, J. Jian, M.K. Alam, H. Wang, F.C. Robles Hernandez, Y. Yao, S. Chen, Q. Yu, G. Feng, Z. Wang, J. Bao, Extrinsic Green Photoluminescence from the Edges of 2D Cesium Lead Halides, Adv. Mater. 31 (2019) 1902492. doi:10.1002/adma.201902492.

[9] J. Luo, X. Wang, S. Li, J. Liu, Y. Guo, G. Niu, L. Yao, Y. Fu, L. Gao, Q. Dong, C. Zhao, M. Leng, F. Ma, W. Liang, L. Wang, S. Jin, J. Han, L. Zhang, J. Etheridge, J. Wang, Y. Yan, E.H. Sargent, J. Tang, Efficient and stable emission of warm-white light from lead-free halide double perovskites, Nature. 563 (2018) 541–545. doi:10.1038/s41586-018-0691-0.

[10] Y. Liu, J. Cui, K. Du, H. Tian, Z. He, Q. Zhou, Z. Yang, Y. Deng, D. Chen, X. Zuo, Y. Ren, L. Wang, H. Zhu, B. Zhao, D. Di, J. Wang, R.H. Friend, Y. Jin, Efficient blue light-emitting diodes based on quantum-confined bromide perovskite nanostructures, Nat. Photonics. 13 (2019) 760–764. doi:10.1038/s41566-019-0505-4.

[11] P. Han, X. Zhang, X. Mao, B. Yang, S. Yang, Z. Feng, D. Wei, W. Deng, T. Pullerits, K. Han, Size effect of lead-free halide double perovskite on luminescence property, Sci. China Chem. 62 (2019) 1405–1413. doi:10.1007/s11426-019-9520-1.

[12] A. Zhizhchenko, S. Syubaev, A. Berestennikov, A. V. Yulin, A. Porfirev, A. Pushkarev, I. Shishkin, K. Golokhvast, A.A. Bogdanov, A.A. Zakhidov, A.A. Kuchmizhak, Y.S. Kivshar, S. V. Makarov, Single-Mode Lasing from Imprinted Halide-Perovskite Microdisks, ACS Nano. 13 (2019) 4140–4147. doi:10.1021/acsnano.8b08948.

[13] P. Brenner, O. Bar-On, M. Jakoby, I. Allegro, B.S. Richards, U.W. Paetzold, I.A. Howard, J. Scheuer, U. Lemmer, Continuous wave amplified spontaneous emission in phase-stable lead halide perovskites, Nat. Commun. 10 (2019) 1–7. doi:10.1038/s41467-019-08929-0.

[14] W. Li, X. Wang, J. Liao, Y. Jiang, D. Kuang, Enhanced On–Off Ratio Photodetectors Based on Lead-Free Cs 3 Bi 2 I 9 Single Crystal Thin Films, Adv. Funct. Mater. 1 (2020) 1909701. doi:10.1002/adfm.201909701.

[15] T. Liu, X. Zhao, J. Li, Z. Liu, F. Liscio, S. Milita, B.C. Schroeder, O. Fenwick, Enhanced control of self-doping in halide perovskites for improved thermoelectric performance, Nat. Commun. 10 (2019) 1–9. doi:10.1038/s41467-019-13773-3.

[16] J. Tong, Z. Song, D.H. Kim, X. Chen, C. Chen, A.F. Palmstrom, P.F. Ndione, M.O. Reese, S.P. Dunfield, O.G. Reid, J. Liu, F. Zhang, S.P. Harvey, Z. Li, S.T. Christensen, G. Teeter, D. Zhao, M.M. Al-Jassim, M.F.A.M. Van Hest, M.C. Beard, S.E. Shaheen, J.J. Berry, Y. Yan, K. Zhu, Carrier lifetimes of >1 ms in Sn-Pb perovskites enable efficient all-perovskite tandem solar cells, Science (80-.). 364 (2019) 475–479. doi:10.1126/science.aav7911.

[17] Z. Yi, N.H. Ladi, X. Shai, H. Li, Y. Shen, M. Wang, Will organic–inorganic hybrid halide lead perovskites be eliminated from optoelectronic applications?, Nanoscale Adv. 1 (2019) 1276–1289. doi:10.1039/C8NA00416A.

[18] J.M. Richter, M. Abdi-Jalebi, A. Sadhanala, M. Tabachnyk, J.P.H. Rivett, L.M.

Pazos-Outón, K.C. Gödel, M. Price, F. Deschler, R.H. Friend, Enhancing photoluminescence yields in lead halide perovskites by photon recycling and light out-coupling, Nat. Commun. 2016 71. 7 (2016) 1–8. doi:10.1038/ncomms13941.

[19] J. Gong, M. Yang, D. Rebollar, J. Rucinski, Z. Liveris, K. Zhu, T. Xu, Divalent anionic doping in perovskite solar cells for enhanced chemical stability, Adv. Mater. 30 (2018) 6–11. doi:10.1002/adma.201800973.

[20] X. Meng, Z. Cai, Y. Zhang, X. Hu, Z. Xing, Z. Huang, Z. Huang, Y. Cui, T. Hu, M. Su, X. Liao, L. Zhang, F. Wang, Y. Song, Y. Chen, Bio-inspired vertebral design for scalable and flexible perovskite solar cells, Nat. Commun. 11 (2020) 1–10. doi:10.1038/s41467-020-16831-3.

[21] A. Furasova, P. Voroshilov, M. Baranov, P. Tonkaev, A. Nikolaeva, K. Voronin, L. Vesce, S. Makarov, A. Di Carlo, Mie-resonant mesoporous electron transport layer for highly efficient perovskite solar cells, Nano Energy. 89 (2021) 106484. doi:10.1016/j.nanoen.2021.106484.

[22] M. Long, T. Zhang, Y. Chai, C.F. Ng, T.C.W. Mak, J. Xu, K. Yan, Nonstoichiometric acid-base reaction as reliable synthetic route to highly stable CH 3 NH 3 PbI 3 perovskite film, Nat. Commun. 7 (2016) 1–11. doi:10.1038/ncomms13503.

[23] M.R. Filip, S. Hillman, A.A. Haghighirad, H.J. Snaith, F. Giustino, Band Gaps of the Lead-Free Halide Double Perovskites Cs2BiAgCl6 and Cs2BiAgBr6 from Theory and Experiment, J. Phys. Chem. Lett. 7 (2016) 2579–2585. doi:10.1021/acs.jpclett.6b01041.

[24] W. Wei, Y. Zhang, Q. Xu, H. Wei, Y. Fang, Q. Wang, Y. Deng, T. Li, A. Gruverman, L. Cao, J. Huang, Monolithic integration of hybrid perovskite single crystals with heterogenous substrate for highly sensitive X-ray imaging, Nat. Photonics 2017 115. 11 (2017) 315–321. doi:10.1038/nphoton.2017.43.

[25] X. Wang, J. Li, Y. Chen, J. Ran, Y. Yuan, B. Yang, Spray-Coating Thick Films of All-Inorganic Halide Perovskites for Filterless Narrowband Photodetectors, ACS Appl. Mater. Interfaces. 14 (2022) 24583–24591. doi:10.1021/acsami.2c03585.

[26] K. Amratisha, W. Tuchinda, P. Ruankham, A. Naikaew, Graded multilayer triple cation perovskites for high speed and detectivity self - powered photodetector via scalable spray coating process, Sci. Rep. 12 (2022) 1–12. doi:10.1038/s41598-022-14774-x.

[27] G.R. Adams, V.O. Eze, M.A.S. Shohag, R. Simpson, H. Parker, O.I. Okoli, Fabrication of rapid response self-powered photodetector using solution-processed triple cation lead-halide perovskite, Eng. Res. Express. 2 (2020) 015043. doi:10.1088/2631-8695/ab7b38.

[28] C. Li, C. Han, Y. Zhang, Z. Zang, M. Wang, X. Tang, J. Du, Enhanced photoresponse of self-powered perovskite photodetector based on ZnO

nanoparticles decorated CsPbBr3 films, Sol. Energy Mater. Sol. Cells. 172 (2017) 341–346. doi:10.1016/j.solmat.2017.08.014.

[29] H. Lu, W. Tian, F. Cao, Y. Ma, B. Gu, L. Li, A Self-Powered and Stable All-Perovskite Photodetector-Solar Cell Nanosystem, Adv. Funct. Mater. 26 (2016) 1296–1302. doi:10.1002/adfm.201504477.

[30] H. Zhou, J. Zeng, Z. Song, C.R. Grice, C. Chen, Z. Song, D. Zhao, H. Wang, Y. Yan, Self-Powered All-Inorganic Perovskite Microcrystal Photodetectors with High Detectivity, J. Phys. Chem. Lett. 9 (2018) 2043–2048. doi:10.1021/acs.jpclett.8b00700.

[31] F. Cao, L. Meng, M. Wang, W. Tian, L. Li, Gradient Energy Band Driven High-Performance Self-Powered Perovskite/CdS Photodetector, Adv. Mater. 31 (2019) 1806725. doi:10.1002/adma.201806725.

[32] H. Zhou, J. Mei, M. Xue, Z. Song, H. Wang, High-stability, self-powered perovskite photodetector based on a CH3NH3PbI3/GaN heterojunction with C60 as an electron transport layer, J. Phys. Chem. C. 121 (2017) 21541–21545. doi:10.1021/acs.jpcc.7b07536.

[33] H. Wei, Y. Fang, P. Mulligan, W. Chuirazzi, H.H. Fang, C. Wang, B.R. Ecker, Y. Gao, M.A. Loi, L. Cao, J. Huang, Sensitive X-ray detectors made of methylammonium lead tribromide perovskite single crystals, Nat. Photonics. 10 (2016) 333–339. doi:10.1038/nphoton.2016.41.

[34] R. Zhuang, X. Wang, W. Ma, Y. Wu, X. Chen, L. Tang, H. Zhu, J. Liu, L. Wu, W. Zhou, X. Liu, Y. Yang, Highly sensitive X-ray detector made of layered perovskite-like (NH4)3Bi2I9 single crystal with anisotropic response, Nat. Photonics. 13 (2019) 602–608. doi:10.1038/s41566-019-0466-7.

[35] H. Min, D.Y. Lee, J. Kim, G. Kim, K.S. Lee, J. Kim, M.J. Paik, Y.K. Kim, K.S. Kim, M.G. Kim, T.J. Shin, S. Il Seok, Perovskite solar cells with atomically coherent interlayers on SnO2 electrodes, Nature. 598 (2021) 444–450. doi:10.1038/s41586-021-03964-8.

[36] Z. Chen, B. Turedi, A.Y. Alsalloum, C. Yang, X. Zheng, I. Gereige, A. AlSaggaf, O.F. Mohammed, O.M. Bakr, Single-Crystal MAPbI 3 Perovskite Solar Cells Exceeding 21% Power Conversion Efficiency, ACS Energy Lett. 4 (2019) 1258–1259. doi:10.1021/acsenergylett.9b00847.

[37] A.Y. Alsalloum, B. Turedi, X. Zheng, S. Mitra, A.A. Zhumekenov, K.J. Lee, P. Maity, I. Gereige, A. AlSaggaf, I.S. Roqan, O.F. Mohammed, O.M. Bakr, Low-Temperature Crystallization Enables 21.9% Efficient Single-Crystal MAPbI 3 Inverted Perovskite Solar Cells, ACS Energy Lett. 5 (2020) 657–662. doi:10.1021/acsenergylett.9b02787.

[38] A. Krishna, H. Zhang, Z. Zhou, T. Gallet, M. Dankl, O. Ouellette, F.T. Eickemeyer, F. Fu, S. Sanchez, M. Mensi, S.M. Zakeeruddin, U. Rothlisberger,

G.N. Manjunatha Reddy, A. Redinger, M. Grätzel, A. Hagfeldt, Nanoscale interfacial engineering enables highly stable and efficient perovskite photovoltaics, Energy Environ. Sci. (2021). doi:10.1039/D1EE02454J.

[39] J. Li, H. Wang, X.Y. Chin, H.A. Dewi, K. Vergeer, T.W. Goh, J.W.M. Lim, J.H. Lew, K.P. Loh, C. Soci, T.C. Sum, H.J. Bolink, N. Mathews, S. Mhaisalkar, A. Bruno, Highly Efficient Thermally Co-evaporated Perovskite Solar Cells and Mini-modules, Joule. 4 (2020) 1035–1053. doi:10.1016/j.joule.2020.03.005.

[40] K. Yoshikawa, H. Kawasaki, W. Yoshida, T. Irie, K. Konishi, K. Nakano, T. Uto, D. Adachi, M. Kanematsu, H. Uzu, K. Yamamoto, Silicon heterojunction solar cell with interdigitated back contacts for a photoconversion efficiency over 26%, Nat. Energy. 2 (2017) 17032. doi:10.1038/nenergy.2017.32.

[41] New world records: perovskite-on-silicon-tandem solar cells, EPFL News. (2022). https://www.csem.ch/press/new-world-records-perovskite-on-silicon-tandem-solar?pid=172296 (accessed October 12, 2022).

[42] Y. Nishigaki, T. Nagai, M. Nishiwaki, T. Aizawa, M. Kozawa, K. Hanzawa, Y. Kato, H. Sai, H. Hiramatsu, H. Hosono, H. Fujiwara, Extraordinary Strong Band-Edge Absorption in Distorted Chalcogenide Perovskites, Sol. RRL. (2020) 1900555. doi:10.1002/solr.201900555.

[43] F. Hermerschmidt, F. Mathies, V.R.F. Schröder, C. Rehermann, N.Z. Morales, E.L. Unger, E.J.W. List-Kratochvil, Finally, inkjet-printed metal halide perovskite LEDs – utilizing seed crystal templating of salty PEDOT:PSS, Mater. Horizons. (2020). doi:10.1039/D0MH00512F.

[44] C. Cho, B. Zhao, G.D. Tainter, J.Y. Lee, R.H. Friend, D. Di, F. Deschler, N.C. Greenham, The role of photon recycling in perovskite light-emitting diodes, Nat. Commun. 11 (2020) 1–8. doi:10.1038/s41467-020-14401-1.

[45] H. Zhu, Y. Fu, F. Meng, X. Wu, Z. Gong, Q. Ding, M. V. Gustafsson, M.T. Trinh, S. Jin, X.Y. Zhu, Lead halide perovskite nanowire lasers with low lasing thresholds and high quality factors, Nat. Mater. 14 (2015) 636–642. doi:10.1038/nmat4271.

[46] R.A. John, N. Yantara, Y.F. Ng, G. Narasimman, E. Mosconi, D. Meggiolaro, M.R. Kulkarni, P.K. Gopalakrishnan, C.A. Nguyen, F. De Angelis, S.G. Mhaisalkar, A. Basu, N. Mathews, Ionotronic Halide Perovskite Drift-Diffusive Synapses for Low-Power Neuromorphic Computation, Adv. Mater. 30 (2018) 1805454. doi:10.1002/ADMA.201805454.

[47] IEC, IEC 61215-1:2016 | IEC Webstore | rural electrification, solar power, solar panel, photovoltaic, PV, smart city, LVDC, (2016). https://webstore.iec.ch/publication/24312 (accessed May 30, 2020).

[48] D.B. Straus, S. Guo, A.M. Abeykoon, R.J. Cava, Understanding the Instability of the Halide Perovskite CsPbI 3 through Temperature-Dependent Structural

Analysis, Adv. Mater. (2020) 2001069. doi:10.1002/adma.202001069.

[49] Z. Chen, G. Brocks, S. Tao, P.A. Bobbert, Unified theory for light-induced halide segregation in mixed halide perovskites, Nat. Commun. 12 (2021) 2687. doi:10.1038/s41467-021-23008-z.

[50] G. Volonakis, M.R. Filip, A.A. Haghighirad, N. Sakai, B. Wenger, H.J. Snaith, F. Giustino, Lead-Free Halide Double Perovskites via Heterovalent Substitution of Noble Metals, J. Phys. Chem. Lett. 7 (2016) 1254–1259. doi:10.1021/acs.jpclett.6b00376.

[51] K. Wang, Z. Jin, L. Liang, H. Bian, D. Bai, H. Wang, J. Zhang, Q. Wang, S. Liu, All-inorganic cesium lead iodide perovskite solar cells with stabilized efficiency beyond 15%, Nat. Commun. 9 (2018) 4544. doi:10.1038/s41467-018-06915-6.

[52] Z. Xiong, W. Hu, Y. She, Q. Lin, L. Hu, X. Tang, K. Sun, Air-Stable Lead-Free Perovskite Thin Film Based on CsBi3I10 and Its Application in Resistive Switching Devices, ACS Appl. Mater. Interfaces. 11 (2019) 30037–30044. doi:10.1021/acsami.9b09080.

[53] D. Kang, N. Park, On the Current–Voltage Hysteresis in Perovskite Solar Cells: Dependence on Perovskite Composition and Methods to Remove Hysteresis, Adv. Mater. 31 (2019) 1805214. doi:10.1002/adma.201805214.

[54] L. Shi, M.P. Bucknall, T.L. Young, M. Zhang, L. Hu, J. Bing, D.S. Lee, J. Kim, T. Wu, N. Takamure, D.R. McKenzie, S. Huang, M.A. Green, A.W.Y. Ho-Baillie, Gas chromatography–mass spectrometry analyses of encapsulated stable perovskite solar cells, Science (80-.). (2020) eaba2412. doi:10.1126/science.aba2412.

[55] H. Chen, J. Lin, J. Kang, Q. Kong, D. Lu, J. Kang, M. Lai, L.N. Quan, Z. Lin, J. Jin, L. Wang, M.F. Toney, P. Yang, Structural and spectral dynamics of single-crystalline Ruddlesden-Popper phase halide perovskite blue light-emitting diodes, Sci. Adv. 6 (2020) eaay4045. doi:10.1126/sciadv.aay4045.

[56] X. Gong, L. Guan, Q. Li, Y. Li, T. Zhang, H. Pan, Q. Sun, Y. Shen, C. Grätzel, S.M. Zakeeruddin, M. Grätzel, M. Wang, Black phosphorus quantum dots in inorganic perovskite thin films for efficient photovoltaic application, Sci. Adv. 6 (2020) eaay5661. doi:10.1126/sciadv.aay5661.

[57] P. Liu, W. Wang, S. Liu, H. Yang, Z. Shao, Fundamental Understanding of Photocurrent Hysteresis in Perovskite Solar Cells, Adv. Energy Mater. 9 (2019) 1803017. doi:10.1002/aenm.201803017.

[58] Y. Wang, M.I. Dar, L.K. Ono, T. Zhang, M. Kan, Y. Li, L. Zhang, X. Wang, Y. Yang, X. Gao, Y. Qi, M. Grätzel, Y. Zhao, Thermodynamically stabilized β-CsPbI 3 –based perovskite solar cells with efficiencies >18%, Science (80-.). 365 (2019) 591–595. doi:10.1126/science.aav8680.

[59] S.S. Mali, J. V. Patil, J.A. Steele, C.K. Hong, Ambient processed and stable all-inorganic lead halide perovskite solar cells with efficiencies nearing 20% using a spray coated Zn1−xCsxO electron transport layer, Nano Energy. 90 (2021) 106597. doi:10.1016/j.nanoen.2021.106597.

[60] B. Abdollahi Nejand, D.B. Ritzer, H. Hu, F. Schackmar, S. Moghadamzadeh, T. Feeney, R. Singh, F. Laufer, R. Schmager, R. Azmi, M. Kaiser, T. Abzieher, S. Gharibzadeh, E. Ahlswede, U. Lemmer, B.S. Richards, U.W. Paetzold, Scalable two-terminal all-perovskite tandem solar modules with a 19.1% efficiency, Nat. Energy. (2022) 1–11. doi:10.1038/s41560-022-01059-w.

[61] B. Ericson, H. Hu, E. Nash, G. Ferraro, J. Sinitsky, M.P. Taylor, Blood lead levels in low-income and middle-income countries: a systematic review, Lancet Planet. Heal. 5 (2021) e145–e153. doi:10.1016/S2542-5196(20)30278-3/ATTACHMENT/FC7ADD9E-DE70-4876-9DBD-7EA139076090/MMC3.PDF.

[62] X. Zhang, D. Barceló, R.J. Clougherty, B. Gao, H. Harms, B. Tefsen, M. Vithanage, H. Wang, Z. Wang, M. Wells, "Potentially Toxic Element"─Something that Means Everything Means Nothing, Environ. Sci. Technol. (2022). doi:10.1021/ACS.EST.2C03056.

[63] J. Ling, P.K.K. Kizhakkedath, T.M. Watson, I. Mora-Seró, L. Schmidt-Mende, T.M. Brown, R. Jose, A Perspective on the Commercial Viability of Perovskite Solar Cells, Sol. RRL. (2021) 2100401. doi:10.1002/solr.202100401.

[64] X. Liu, T. Wu, J.Y. Chen, X. Meng, X. He, T. Noda, H. Chen, X. Yang, H. Segawa, Y. Wang, L. Han, Templated growth of FASnI3 crystals for efficient tin perovskite solar cells, Energy Environ. Sci. 13 (2020) 2896–2902. doi:10.1039/D0EE01845G.

[65] H. Ban, T. Nakajima, Z. Liu, H. Yu, Q. Sun, L. Dai, Y. Shen, X.L. Zhang, J. Zhu, P. Chen, M. Wang, Over 8% efficient CsSnI3-based mesoporous perovskite solar cells enabled by two-step thermal annealing and surface cationic coordination dual treatment, J. Mater. Chem. A. 10 (2022) 3642–3649. doi:10.1039/D1TA09811J.

[66] N.K. Noel, S.D. Stranks, A. Abate, C. Wehrenfennig, S. Guarnera, A.A. Haghighirad, A. Sadhanala, G.E. Eperon, S.K. Pathak, M.B. Johnston, A. Petrozza, L.M. Herz, H.J. Snaith, Lead-free organic-inorganic tin halide perovskites for photovoltaic applications, Energy Environ. Sci. 7 (2014) 3061–3068. doi:10.1039/c4ee01076k.

[67] M. Li, W. Zuo, Y.-G. Yang, M.H. Aldamasy, Q. Wang, S.H.T. Cruz, S.-L. Feng, M. Saliba, Z.-K. Wang, A. Abate, Tin Halide Perovskite Films Made of Highly Oriented 2D Crystals Enable More Efficient and Stable Lead-free Perovskite Solar Cells, ACS Energy Lett. (2020) 1923–1929. doi:10.1021/acsenergylett.0c00782.

[68] S.M. Jain, T. Edvinsson, J.R. Durrant, Green fabrication of stable lead-free bismuth based perovskite solar cells using a non-toxic solvent, Commun. Chem. 2

(2019) 1–7. doi:10.1038/s42004-019-0195-3.

[69] M. Roknuzzaman, K. (Ken) Ostrikov, K. Chandula Wasalathilake, C. Yan, H. Wang, T. Tesfamichael, Insight into lead-free organic-inorganic hybrid perovskites for photovoltaics and optoelectronics: A first-principles study, Org. Electron. Physics, Mater. Appl. 59 (2018) 99–106. doi:10.1016/j.orgel.2018.04.051.

[70] T. Krishnamoorthy, H. Ding, C. Yan, W.L. Leong, T. Baikie, Z. Zhang, M. Sherburne, S. Li, M. Asta, N. Mathews, S.G. Mhaisalkar, Lead-free germanium iodide perovskite materials for photovoltaic applications, J. Mater. Chem. A. 3 (2015) 23829–23832. doi:10.1039/c5ta05741h.

[71] W. Guo, Y. Zhu, M. Zhang, J. Du, Y. Cen, S. Liu, Y. He, H. Zhong, X. Wang, J. Shi, The Dion–Jacobson perovskite CsSbCl 4 : a promising Pb-free solar-cell absorber with optimal bandgap ∼1.4 eV, strong optical absorption ∼10 5 cm −1 , and large power-conversion efficiency above 20%, J. Mater. Chem. A. (2021). doi:10.1039/D1TA02969J.

[72] M.B. Johansson, B. Philippe, A. Banerjee, D. Phuyal, S. Mukherjee, S. Chakraborty, M. Cameau, H. Zhu, R. Ahuja, G. Boschloo, H. Rensmo, E.M.J. Johansson, Cesium Bismuth Iodide Solar Cells from Systematic Molar Ratio Variation of CsI and BiI3, Inorg. Chem. 58 (2019) 12040–12052. doi:10.1021/acs.inorgchem.9b01233.

[73] B.-W. Park, B. Philippe, X. Zhang, H. Rensmo, G. Boschloo, E.M.J. Johansson, Bismuth Based Hybrid Perovskites A 3 Bi 2 I 9 (A: Methylammonium or Cesium) for Solar Cell Application, Adv. Mater. 27 (2015) 6806–6813. doi:10.1002/adma.201501978.

[74] S. Öz, J.-C. Hebig, E. Jung, T. Singh, A. Lepcha, S. Olthof, F. Jan, Y. Gao, R. German, P.H.M. van Loosdrecht, K. Meerholz, T. Kirchartz, S. Mathur, Zero-dimensional (CH3NH3)3Bi2I9 perovskite for optoelectronic applications, Sol. Energy Mater. Sol. Cells. 158 (2016) 195–201. doi:10.1016/j.solmat.2016.01.035.

[75] M. Abulikemu, S. Ould-Chikh, X. Miao, E. Alarousu, B. Murali, G.O. Ngongang Ndjawa, J. Barbé, A. El Labban, A. Amassian, S. Del Gobbo, Optoelectronic and photovoltaic properties of the air-stable organohalide semiconductor (CH 3 NH 3) 3 Bi 2 I 9, J. Mater. Chem. A. 4 (2016) 12504–12515. doi:10.1039/C6TA04657F.

[76] M. Lyu, J.H. Yun, M. Cai, Y. Jiao, P. V. Bernhardt, M. Zhang, Q. Wang, A. Du, H. Wang, G. Liu, L. Wang, Organic–inorganic bismuth (III)-based material: A lead-free, air-stable and solution-processable light-absorber beyond organolead perovskites, Nano Res. 9 (2016) 692–702. doi:10.1007/s12274-015-0948-y.

[77] X. Zhang, G. Wu, Z. Gu, B. Guo, W. Liu, S. Yang, T. Ye, C. Chen, W. Tu, H. Chen, Active-layer evolution and efficiency improvement of (CH3NH33Bi2I9-based solar cell on TiO2-deposited ITO substrate, Nano Res. 9 (2016) 2921–2930. doi:10.1007/s12274-016-1177-8.

[78] S.S. Mali, H. Kim, D.-H. Kim, C. Kook Hong, Anti-Solvent Assisted Crystallization Processed Methylammonium Bismuth Iodide Cuboids towards Highly Stable Lead-Free Perovskite Solar Cells, ChemistrySelect. 2 (2017) 1578–1585. doi:10.1002/slct.201700025.

[79] M. Kong, H. Hu, L. Wan, M. Chen, Y. Gan, J. Wang, F. Chen, B. Dong, D. Eder, S. Wang, Nontoxic (CH 3 NH 3) 3 Bi 2 I 9 perovskite solar cells free of hole conductors with an alternative architectural design and a solution-processable approach, RSC Adv. 7 (2017) 35549–35557. doi:10.1039/C7RA04924B.

[80] T. Okano, Y. Suzuki, Gas-assisted coating of Bi-based (CH3NH3)3Bi2I9 active layer in perovskite solar cells, Mater. Lett. 191 (2017) 77–79. doi:10.1016/j.matlet.2017.01.047.

[81] A. Kulkarni, T. Singh, M. Ikegami, T. Miyasaka, Photovoltaic enhancement of bismuth halide hybrid perovskite by N-methyl pyrrolidone-assisted morphology conversion, RSC Adv. 7 (2017) 9456–9460. doi:10.1039/c6ra28190g.

[82] Z. Zhang, X. Li, X. Xia, Z. Wang, Z. Huang, B. Lei, Y. Gao, High-Quality (CH3NH3)3Bi2I9 Film-Based Solar Cells: Pushing Efficiency up to 1.64%, J. Phys. Chem. Lett. 8 (2017) 4300–4307. doi:10.1021/acs.jpclett.7b01952.

[83] J. Huang, Z. Gu, X. Zhang, G. Wu, H. Chen, Lead-free (CH3NH3)3Bi2I9 perovskite solar cells with fluorinated PDI films as organic electron transport layer, J. Alloys Compd. 767 (2018) 870–876. doi:10.1016/j.jallcom.2018.07.185.

[84] S.M. Jain, D. Phuyal, M.L. Davies, M. Li, B. Philippe, C. De Castro, Z. Qiu, J. Kim, T. Watson, W.C. Tsoi, O. Karis, H. Rensmo, G. Boschloo, T. Edvinsson, J.R. Durrant, An effective approach of vapour assisted morphological tailoring for reducing metal defect sites in lead-free, (CH3NH3)3Bi2I9 bismuth-based perovskite solar cells for improved performance and long-term stability, Nano Energy. 49 (2018) 614–624. doi:10.1016/j.nanoen.2018.05.003.

[85] N.C. Miller, M. Bernechea, Research Update: Bismuth based materials for photovoltaics, APL Mater. 6 (2018). doi:10.1063/1.5026541.

[86] I. Grinberg, D.V. West, M. Torres, G. Gou, D.M. Stein, L. Wu, G. Chen, E.M. Gallo, A.R. Akbashev, P.K. Davies, J.E. Spanier, A.M. Rappe, Perovskite oxides for visible-light-absorbing ferroelectric and photovoltaic materials, Nature. 503 (2013) 509–512. doi:10.1038/nature12622.

[87] R. Nechache, C. Harnagea, S. Li, L. Cardenas, W. Huang, J. Chakrabartty, F. Rosei, Bandgap tuning of multiferroic oxide solar cells, Nat. Photonics. 9 (2014) 61–67. doi:10.1038/nphoton.2014.255.

[88] O. Lindqvist, G. Johansson, F. Sandberg, T. Norin, The Crystal Structure of Cesium Bismuth Iodide, Cs3Bi2I9., Acta Chem. Scand. 22 (1968) 2943–2952. doi:10.3891/acta.chem.scand.22-2943.

[89] B. Chabot, E. Parthé, Cs 3 Sb 2 I 9 and Cs 3 Bi 2 I 9 with the hexagonal Cs 3 Cr 2 Cl 9 structure type, Acta Crystallogr. Sect. B Struct. Crystallogr. Cryst. Chem. 34 (1978) 645–648. doi:10.1107/S0567740878003684.

[90] A. V. Arakcheeva, G. Chapuis, M. Meyer, The LT phase of Cs3Bi2I9, Zeitschrift Für Krist. - Cryst. Mater. 216 (2001) 2644–2650. doi:10.1524/zkri.216.4.199.23261.

[91] Q. Sun, Y. Xu, H. Zhang, B. Xiao, X. Liu, J. Dong, Y. Cheng, B. Zhang, W. Jie, M.G. Kanatzidis, Optical and electronic anisotropies in perovskitoid crystals of Cs 3 Bi 2 I 9 studies of nuclear radiation detection, J. Mater. Chem. A. 6 (2018) 23388–23395. doi:10.1039/C8TA09525F.

[92] K.M. McCall, C.C. Stoumpos, S.S. Kostina, M.G. Kanatzidis, B.W. Wessels, Strong Electron–Phonon Coupling and Self-Trapped Excitons in the Defect Halide Perovskites A 3 M 2 I 9 (A = Cs, Rb; M = Bi, Sb), Chem. Mater. 29 (2017) 4129–4145. doi:10.1021/acs.chemmater.7b01184.

[93] M.B. Johansson, H. Zhu, E.M.J. Johansson, Extended Photo-Conversion Spectrum in Low-Toxic Bismuth Halide Perovskite Solar Cells, J. Phys. Chem. Lett. 7 (2016) 3467–3471. doi:10.1021/acs.jpclett.6b01452.

[94] J. Liang, Q. Fang, H. Wang, R. Xu, S. Jia, Y. Guan, Q. Ai, G. Gao, H. Guo, K. Shen, X. Wen, T. Terlier, G.P. Wiederrecht, X. Qian, H. Zhu, J. Lou, Perovskite-Derivative Valleytronics, Adv. Mater. 32 (2020) 2004111. doi:10.1002/adma.202004111.

[95] M. Pazoki, M.B. Johansson, H. Zhu, P. Broqvist, T. Edvinsson, G. Boschloo, E.M.J. Johansson, Bismuth Iodide Perovskite Materials for Solar Cell Applications: Electronic Structure, Optical Transitions, and Directional Charge Transport, J. Phys. Chem. C. 120 (2016) 29039–29046. doi:10.1021/acs.jpcc.6b11745.

[96] D.B. Khadka, Y. Shirai, M. Yanagida, K. Miyano, Tailoring the film morphology and interface band offset of caesium bismuth iodide-based Pb-free perovskite solar cells, J. Mater. Chem. C. 7 (2019) 8335–8343. doi:10.1039/c9tc02181g.

[97] K.-H.H. Hong, J. Kim, L. Debbichi, H. Kim, S.H. Im, Band Gap Engineering of Cs 3 Bi 2 I 9 Perovskites with Trivalent Atoms Using a Dual Metal Cation, J. Phys. Chem. C. 121 (2017) 969–974. doi:10.1021/acs.jpcc.6b12426.

[98] A.J. Lehner, D.H. Fabini, H.A. Evans, C.A. Hébert, S.R. Smock, J. Hu, H. Wang, J.W. Zwanziger, M.L. Chabinyc, R. Seshadri, Crystal and Electronic Structures of Complex Bismuth Iodides A3Bi2I9 (A = K, Rb, Cs) Related to Perovskite: Aiding the Rational Design of Photovoltaics, Chem. Mater. 27 (2015) 7137–7148. doi:10.1021/acs.chemmater.5b03147.

[99] B. Ghosh, B. Wu, H.K. Mulmudi, C. Guet, K. Weber, T.C. Sum, S. Mhaisalkar, N. Mathews, Limitations of Cs 3 Bi 2 I 9 as Lead-Free Photovoltaic Absorber

Materials, ACS Appl. Mater. Interfaces. 10 (2018) 35000–35007. doi:10.1021/acsami.7b14735.

[100] J. Gu, G. Yan, Y. Lian, Q. Mu, H. Jin, Z. Zhang, Z. Deng, Y. Peng, Bandgap engineering of a lead-free defect perovskite Cs 3 Bi 2 I 9 through trivalent doping of Ru 3+, RSC Adv. 8 (2018) 25802–25807. doi:10.1039/C8RA04422H.

[101] K. Seshan, Deposition Technologies and Applications: Introduction and Overview, in: Handb. Thin Film Depos. Tech. Princ. Methods, Equip. Appl. Second Ed., William Andrew Publishing, 2020: pp. 39–72. doi:10.1201/9781482269680-11.

[102] R. Waykar, A. Bhorde, S. Nair, S. Pandharkar, B. Gabhale, R. Aher, S. Rondiya, A. Waghmare, V. Doiphode, A. Punde, P. Vairale, M. Prasad, S. Jadkar, Environmentally stable lead-free cesium bismuth iodide (Cs3Bi2I9) perovskite: Synthesis to solar cell application, J. Phys. Chem. Solids. 146 (2020) 109608. doi:10.1016/j.jpcs.2020.109608.

[103] Z. Qi, X. Fu, T. Yang, D. Li, P. Fan, H. Li, F. Jiang, L. Li, Z. Luo, X. Zhuang, A. Pan, Highly stable lead-free Cs3Bi2I9 perovskite nanoplates for photodetection applications, Nano Res. 12 (2019) 1894–1899. doi:10.1007/s12274-019-2454-0.

[104] A.A. Hussain, Constructing Caesium-Based Lead-Free Perovskite Photodetector Enabling Self-Powered Operation with Extended Spectral Response, ACS Appl. Mater. Interfaces. 12 (2020) 46317–46329. doi:10.1021/acsami.0c14083.

[105] D. Liu, B.-B. Yu, M. Liao, Z. Jin, L. Zhou, X. Zhang, F. Wang, H. He, T. Gatti, Z. He, Self-Powered and Broadband Lead-Free Inorganic Perovskite Photodetector with High Stability, ACS Appl. Mater. Interfaces. 12 (2020) 30530–30537. doi:10.1021/acsami.0c05636.

[106] W. Li, Y. Liu, Y. Gao, Z. Ji, Y. Fu, C. Zhao, W. Mai, Tunneling-assisted highly sensitive and stable lead-free Cs3Bi2I9perovskite photodetectors for diffuse reflection imaging, J. Mater. Chem. C. 9 (2021) 1008–1013. doi:10.1039/d0tc04485g.

[107] F. Bai, Y. Hu, Y. Hu, T. Qiu, X. Miao, S. Zhang, Lead-free, air-stable ultrathin Cs3Bi2I9 perovskite nanosheets for solar cells, Sol. Energy Mater. Sol. Cells. 184 (2018) 15–21. doi:10.1016/j.solmat.2018.04.032.

[108] Y. Hu, S. Zhang, X. Miao, L. Su, F. Bai, T. Qiu, J. Liu, G. Yuan, Ultrathin Cs 3 Bi 2 I 9 Nanosheets as an Electronic Memory Material for Flexible Memristors, Adv. Mater. Interfaces. 4 (2017) 1700131. doi:10.1002/admi.201700131.

[109] J. Wang, Y. Li, L. Ma, G. Shen, Q. Yang, Air-Stabilized Lead-Free Hexagonal Cs3Bi2I9 Nanocrystals for Ultrahigh-Performance Optical Detection, Adv. Funct. Mater. 32 (2022) 2203072. doi:10.1002/adfm.202203072.

[110] P. Zhang, Y. Zhang, W. Wang, L. Gao, G. Li, S. Zhang, J. Lu, Y. Yu, J. Zhang, Multispectral photodetectors based on 2D material/Cs3Bi2I9 heterostructures with

high detectivity, Nanotechnology. 32 (2021) 415202. doi:10.1088/1361-6528/AC1130.

[111] K. Dong, H. Zhou, M. Xiao, P. Gui, Z. Gao, F. Yao, W. Shao, C. Liu, C. Tao, W. Ke, G. Fang, Semi-transparent, high-performance lead-free Cs3Bi2I9single crystal self-driven photodetector, Appl. Phys. Lett. 120 (2022) 191102. doi:10.1063/5.0090569.

[112] K.M. McCall, Z. Liu, G. Trimarchi, C.C. Stoumpos, W. Lin, Y. He, I. Hadar, M.G. Kanatzidis, B.W. Wessels, α-Particle Detection and Charge Transport Characteristics in the A 3 M 2 I 9 Defect Perovskites (A = Cs, Rb; M = Bi, Sb), ACS Photonics. 5 (2018) 3748–3762. doi:10.1021/acsphotonics.8b00813.

[113] Y. Zhang, Y. Liu, Z. Xu, H. Ye, Z. Yang, J. You, M. Liu, Y. He, M.G. Kanatzidis, S. (Frank) Liu, Nucleation-controlled growth of superior lead-free perovskite Cs3Bi2I9 single-crystals for high-performance X-ray detection, Nat. Commun. 11 (2020) 1–11. doi:10.1038/s41467-020-16034-w.

[114] Y. Liu, Z. Xu, Z. Yang, Y. Zhang, J. Cui, Y. He, H. Ye, K. Zhao, H. Sun, R. Lu, M. Liu, M.G. Kanatzidis, S. (Frank) Liu, Inch-Size 0D-Structured Lead-Free Perovskite Single Crystals for Highly Sensitive Stable X-Ray Imaging, Matter. 3 (2020) 180–196. doi:10.1016/j.matt.2020.04.017.

[115] S.O. Kasap, X-ray sensitivity of photoconductors: Application to stabilized a-Se, J. Phys. D. Appl. Phys. 33 (2000) 2853–2865. doi:10.1088/0022-3727/33/21/326.

[116] N. Daem, J. Dewalque, F. Lang, A. Maho, G. Spronck, C. Henrist, P. Colson, S.D. Stranks, R. Cloots, Spray-Coated Lead-Free Cs 2 AgBiBr 6 Double Perovskite Solar Cells with High Open-Circuit Voltage, Sol. RRL. (2021) 2100422. doi:10.1002/solr.202100422.

[117] Y. Wang, X. Shi, G. Wang, J. Tong, D. Pan, All-inorganic and lead-free BiI 3 thin film solar cells by iodization of BiSI thin films, J. Mater. Chem. C. 8 (2020) 14066–14074. doi:10.1039/D0TC03753B.

[118] A.J. Lehner, H. Wang, D.H. Fabini, C.D. Liman, C.-A. Hébert, E.E. Perry, M. Wang, G.C. Bazan, M.L. Chabinyc, R. Seshadri, Electronic structure and photovoltaic application of BiI 3, Appl. Phys. Lett. 107 (2015) 131109. doi:10.1063/1.4932129.

[119] U.H. Hamdeh, R.D. Nelson, B.J. Ryan, U. Bhattacharjee, J.W. Petrich, M.G. Panthani, Solution-Processed BiI 3 Thin Films for Photovoltaic Applications: Improved Carrier Collection via Solvent Annealing, Chem. Mater. 28 (2016) 6567–6574. doi:10.1021/acs.chemmater.6b02347.

[120] B. Yoo, D. Ding, J.M. Marin-Beloqui, L. Lanzetta, X. Bu, T. Rath, S.A. Haque, Improved Charge Separation and Photovoltaic Performance of BiI3 Absorber Layers by Use of an in Situ Formed BiSI Interlayer, ACS Appl. Energy Mater. 2 (2019) 7056–7061. doi:10.1021/acsaem.9b00838.

[121] W. Hu, X. He, Z. Fang, W. Lian, Y. Shang, X. Li, W. Zhou, M. Zhang, T. Chen, Y. Lu, L. Zhang, L. Ding, S. Yang, Bulk heterojunction gifts bismuth-based lead-free perovskite solar cells with record efficiency, Nano Energy. 68 (2020) 104362. doi:10.1016/j.nanoen.2019.104362.

[122] J.H. Heo, M.H. Lee, D.H. Song, C.E. Song, J.-J. Lee, K.-H. Hong, S.H. Im, Planar Type Trivalent Bismuth Based Pb-Free Perovskite Solar Cells, Nanosci. Nanotechnol. Lett. 10 (2018) 591–595. doi:10.1166/nnl.2018.2688.

[123] M.T. Islam, M.R. Jani, K.M. Shorowordi, Z. Hoque, A.M. Gokcek, V. Vattipally, S.S. Nishat, S. Ahmed, Numerical simulation studies of Cs3Bi2I9 perovskite solar device with optimal selection of electron and hole transport layers, Optik (Stuttg). 231 (2021) 166417. doi:10.1016/j.ijleo.2021.166417.

[124] J. Shin, M. Kim, S. Jung, C.S. Kim, J. Park, A. Song, K.B. Chung, S.H. Jin, J.H. Lee, M. Song, Enhanced efficiency in lead-free bismuth iodide with post treatment based on a hole-conductor-free perovskite solar cell, Nano Res. 11 (2018) 6283–6293. doi:10.1007/s12274-018-2151-4.

[125] H. Zhu, M.B. Johansson, E.M.J. Johansson, The Effect of Dopant-Free Hole-Transport Polymers on Charge Generation and Recombination in Cesium-Bismuth-Iodide Solar Cells, ChemSusChem. 11 (2018) 1114–1120. doi:10.1002/cssc.201702169.

[126] G.X. Liang, X.Y. Chen, Z.H. Chen, H. Bin Lan, Z.H. Zheng, P. Fan, X.Q. Tian, J.Y. Duan, Y.D. Wei, Z.H. Su, Inorganic and Pb-Free CsBi3I10 Thin Film for Photovoltaic Applications, J. Phys. Chem. C. 123 (2019) 27423–27428. doi:10.1021/acs.jpcc.9b09617.

[127] S.L. Hamukwaya, H. Hao, M.M. Mashingaidze, T. Zhong, S. Tang, J. Dong, J. Xing, H. Liu, Potassium Iodide-Modified Lead-Free Cs3Bi2I9 Perovskites for Enhanced High-Efficiency Solar Cells, Nanomaterials. 12 (2022) 3751. doi:10.3390/nano12213751.

[128] Y. Lou, M. Fang, J. Chen, Y. Zhao, Formation of highly luminescent cesium bismuth halide perovskite quantum dots tuned by anion exchange, Chem. Commun. (2018). doi:10.1039/c8cc01110a.

[129] B. Yang, J. Chen, F. Hong, X. Mao, K. Zheng, S. Yang, Y. Li, T. Pullerits, W. Deng, K. Han, Lead-Free, Air-Stable All-Inorganic Cesium Bismuth Halide Perovskite Nanocrystals, Angew. Chemie - Int. Ed. 56 (2017) 12471–12475. doi:10.1002/anie.201704739.

[130] B.-M. Bresolin, C. Günnemann, D.W. Bahnemann, M. Sillanpää, Pb-Free Cs3Bi2I9 Perovskite as a Visible-Light-Active Photocatalyst for Organic Pollutant Degradation, Nanomaterials. 10 (2020) 763. doi:10.3390/nano10040763.

[131] B.M. Bresolin, P. Sgarbossa, D.W. Bahnemann, M. Sillanpää, Cs3Bi2I9/g-C3N4 as a new binary photocatalyst for efficient visible-light photocatalytic processes,

Sep. Purif. Technol. 251 (2020) 117320. doi:10.1016/j.seppur.2020.117320.

[132] Z.-L. Liu, R.-R. Liu, Y.-F. Mu, Y.-X. Feng, G.-X. Dong, M. Zhang, T.-B. Lu, In Situ Construction of Lead-Free Perovskite Direct Z-Scheme Heterojunction Cs 3 Bi 2 I 9 /Bi 2 WO 6 for Efficient Photocatalysis of CO 2 Reduction, Sol. RRL. 5 (2021) 2000691. doi:10.1002/solr.202000691.

[133] K. Adams, J. Mallows, T. Li, D. Kampouris, J.H.J. Thijssen, N. Robertson, Cs 3 Bi 2 I 9 as high-performance electrode material achieving high capacitance and stability in an economical supercapacitor, J. Phys. Energy. 1 (2019) 034001. doi:10.1088/2515-7655/ab22d7.

[134] N. Tewari, S.B. Shivarudraiah, J.E. Halpert, Photorechargeable Lead-Free Perovskite Lithium-Ion Batteries Using Hexagonal Cs 3 Bi 2 I 9 Nanosheets, Nano Lett. 21 (2021) 5578–5585. doi:10.1021/acs.nanolett.1c01000.

[135] N.K. Tailor, S. Satapathi, Structural Disorder and Spin Dynamics Study in Millimeter-Sized All-Inorganic Lead-Free Cesium Bismuth Halide Perovskite Single Crystals, ACS Appl. Energy Mater. 3 (2020) 11732–11740. doi:10.1021/acsaem.0c01849.

[136] P. Sebastia-Luna, M.C. Gélvez-Rueda, C. Dreessen, M. Sessolo, F.C. Grozema, F. Palazon, H.J. Bolink, Potential and limitations of CsBi 3 I 10 as a photovoltaic material, J. Mater. Chem. A. 8 (2020) 15670–15674. doi:10.1039/D0TA02237C.

[137] N. Pai, J. Lu, T.R. Gengenbach, A. Seeber, A.S.R. Chesman, L. Jiang, D.C. Senevirathna, P.C. Andrews, U. Bach, Y. Cheng, A.N. Simonov, Silver Bismuth Sulfoiodide Solar Cells: Tuning Optoelectronic Properties by Sulfide Modification for Enhanced Photovoltaic Performance, Adv. Energy Mater. 9 (2019) 1803396. doi:10.1002/aenm.201803396.

[138] S.R. Rondiya, R.A. Jagt, J.L. MacManus-Driscoll, A. Walsh, R.L.Z. Hoye, Self-trapping in bismuth-based semiconductors: Opportunities and challenges from optoelectronic devices to quantum technologies, Appl. Phys. Lett. 119 (2021) 220501. doi:10.1063/5.0071763.

[139] L. Zhang, C. Liu, L. Wang, C. Liu, K. Wang, B. Zou, Pressure-Induced Emission Enhancement, Band-Gap Narrowing, and Metallization of Halide Perovskite Cs 3 Bi 2 I 9, Angew. Chemie - Int. Ed. 57 (2018) 11213–11217. doi:10.1002/anie.201804310.

[140] Z. Shuang, H. Zhou, D. Wu, X. Zhang, B. Xiao, G. Ma, J. Zhang, H. Wang, Low-temperature process for self-powered lead-free Cs2AgBiBr6 perovskite photodetector with high detectivity, Chem. Eng. J. 433 (2022) 134544. doi:10.1016/j.cej.2022.134544.

[141] W. Pan, H. Wu, J. Luo, Z. Deng, C. Ge, C. Chen, X. Jiang, W.-J. Yin, G. Niu, L. Zhu, L. Yin, Y. Zhou, Q. Xie, X. Ke, M. Sui, J. Tang, Cs2AgBiBr6 single-crystal X-ray detectors with a low detection limit, Nat. Photonics. 11 (2017) 726–732.

doi:10.1038/s41566-017-0012-4.

[142] E. Greul, M.L. Petrus, A. Binek, P. Docampo, T. Bein, Highly stable, phase pure Cs2AgBiBr6 double perovskite thin films for optoelectronic applications, J. Mater. Chem. A. 5 (2017). doi:10.1039/c7ta06816f.

[143] C. Wu, Q. Zhang, Y. Liu, W. Luo, X. Guo, Z. Huang, H. Ting, W. Sun, X. Zhong, S. Wei, S. Wang, Z. Chen, L. Xiao, The Dawn of Lead-Free Perovskite Solar Cell: Highly Stable Double Perovskite Cs2AgBiBr6 Film, Adv. Sci. 5 (2018) 1700759. doi:10.1002/advs.201700759.

[144] P. Fan, H.-X. Peng, Z.-H. Zheng, Z.-H. Chen, S.-J. Tan, X.-Y. Chen, Y.-D. Luo, Z.-H. Su, J.-T. Luo, G.-X. Liang, Single-Source Vapor-Deposited Cs2AgBiBr6 Thin Films for Lead-Free Perovskite Solar Cells, Nanomaterials. 9 (2019) 1760. doi:10.3390/nano9121760.

[145] B. Wang, N. Li, L. Yang, C. Dall'Agnese, A.K. Jena, S. Sasaki, T. Miyasaka, H. Tamiaki, X.-F. Wang, Chlorophyll Derivative-Sensitized TiO 2 Electron Transport Layer for Record Efficiency of Cs 2 AgBiBr 6 Double Perovskite Solar Cells, J. Am. Chem. Soc. 143 (2021) 2207–2211. doi:10.1021/jacs.0c12786.

[146] B. Wang, N. Li, L. Yang, C. Dall'Agnese, A.K. Jena, T. Miyasaka, X.-F. Wang, Organic Dye/Cs 2 AgBiBr 6 Double Perovskite Heterojunction Solar Cells, J. Am. Chem. Soc. (2021) jacs.1c07200. doi:10.1021/jacs.1c07200.

[147] H. Zhong, M. Yang, G. Tang, S. Yuan, Type-II Lateral Heterostructures of Monolayer Halide Double Perovskites for Optoelectronic Applications, ACS Energy Lett. (2020) 2275–2282. doi:10.1021/acsenergylett.0c01046.

[148] A. Mrotzek, D.-Y. Chung, N. Ghelani, T. Hogan, M.G. Kanatzidis, Structure and Thermoelectric Properties of the New Quaternary Bismuth Selenides A1−xM4−xBi11+xSe21 (A=K and Rb and Cs; M=Sn and Pb)—Members of the Grand Homologous Series Km(M6Se8)m(M5+nSe9+n), Chemistry (Easton). 7 (2001) 1915–1926. doi:10.1002/1521-3765(20010504)7:9<1915::AID-CHEM1915>3.0.CO;2-2.

[149] D.-Y. Chung, T.P. Hogan, M. Rocci-Lane, P. Brazis, J.R. Ireland, C.R. Kannewurf, M. Bastea, C. Uher, M.G. Kanatzidis, A New Thermoelectric Material: CsBi 4 Te 6, J. Am. Chem. Soc. 126 (2004) 6414–6428. doi:10.1021/ja039885f.

[150] M.G. Kanatzidis, T.J. McCarthy, T.A. Tanzer, L.-H. Chen, L. Iordanidis, T. Hogan, C.R. Kannewurf, C. Uher, B. Chen, Synthesis and Thermoelectric Properties of the New Ternary Bismuth Sulfides KBi 6.33 S 10 and K 2 Bi 8 S 13, Chem. Mater. 8 (1996) 1465–1474. doi:10.1021/cm9600182.

[151] J. Zhao, S.M. Islam, O.Y. Kontsevoi, G. Tan, C.C. Stoumpos, H. Chen, R.K. Li, M.G. Kanatzidis, The Two-Dimensional AxCdxBi4-xQ6 (A = K, Rb, Cs; Q = S, Se): Direct Bandgap Semiconductors and Ion-Exchange Materials, J. Am. Chem.

Soc. 139 (2017) 6978–6987. doi:10.1021/jacs.7b02243.

[152] J. Zhao, S.M. Islam, S. Hao, G. Tan, C.C. Stoumpos, C. Wolverton, H. Chen, Z. Luo, R. Li, M.G. Kanatzidis, Homologous Series of 2D Chalcogenides Cs-Ag-Bi-Q (Q = S, Se) with Ion-Exchange Properties, J. Am. Chem. Soc. 139 (2017) 12601–12609. doi:10.1021/jacs.7b06373.

[153] Y. Wang, S.R. Kavanagh, I. Burgués-Ceballos, A. Walsh, D. Scanlon, G. Konstantatos, Cation disorder engineering yields AgBiS2 nanocrystals with enhanced optical absorption for efficient ultrathin solar cells, Nat. Photonics 2022. (2022) 1–7. doi:10.1038/s41566-021-00950-4.

[154] R. Nie, A. Mehta, B. Park, H.-W. Kwon, J. Im, S. Il Seok, Mixed Sulfur and Iodide-Based Lead-Free Perovskite Solar Cells, J. Am. Chem. Soc. 140 (2018) 872–875. doi:10.1021/jacs.7b11332.

[155] J. Li, X. Liu, J. Xu, J. Chen, C. Zhao, M. Salma Maneno, B. Zhang, J. Yao, Fabrication of Sulfur-Incorporated Bismuth-Based Perovskite Solar Cells via a Vapor-Assisted Solution Process, Sol. RRL. 3 (2019) 1900218. doi:10.1002/solr.201900218.

[156] Y.Y. Sun, J. Shi, J. Lian, W. Gao, M.L. Agiorgousis, P. Zhang, S. Zhang, Discovering lead-free perovskite solar materials with a split-anion approach, Nanoscale. 8 (2016) 6284–6289. doi:10.1039/c5nr04310g.

[157] M. Vigneshwaran, T. Ohta, S. Iikubo, G. Kapil, T.S. Ripolles, Y. Ogomi, T. Ma, S.S. Pandey, Q. Shen, T. Toyoda, K. Yoshino, T. Minemoto, S. Hayase, Facile synthesis and characterization of sulfur doped low bandgap bismuth based perovskites by soluble precursor route, Chem. Mater. 28 (2016) 6436–6440. doi:10.1021/acs.chemmater.6b02315.

[158] H. Cai, X. Liang, X. Ye, J. Su, J. Guan, J. Yang, Y. Liu, X. Zhou, R. Han, J. Ni, J. Li, J. Zhang, High Efficiency over 20% of Perovskite Solar Cells by Spray Coating via a Simple Process, ACS Appl. Energy Mater. 3 (2020) 9696–9702. doi:10.1021/acsaem.0c01129.

[159] S. Kooij, A. Astefanei, G.L. Corthals, D. Bonn, Size distributions of droplets produced by ultrasonic nebulizers, Sci. Rep. 9 (2019) 6128. doi:10.1038/s41598-019-42599-8.

[160] M. Faraday, On the forms and states assumed by the fluids in contact with vibrating elastic surfaces, Philos. Trans. R. Soc. London A. 52 (1831) 319.

[161] R.W. Wood, A.L. Loomis, XXXVIII. The physical and biological effects of high-frequency sound-waves of great intensity, London, Edinburgh, Dublin Philos. Mag. J. Sci. 4 (1927) 417–436. doi:10.1080/14786440908564348.

[162] R.J. Lang, Ultrasonic Atomization of Liquids, J. Acoust. Soc. Am. 34 (1962) 6–8. doi:10.1121/1.1909020.

[163] K. Yasuda, Y. Bando, S. Yamaguchi, M. Nakamura, A. Oda, Y. Kawase, Analysis of concentration characteristics in ultrasonic atomization by droplet diameter distribution, Ultrason. Sonochem. 12 (2005) 37–41. doi:10.1016/j.ultsonch.2004.05.008.

[164] H. Chen, X. Ding, X. Pan, T. Hayat, A. Alsaedi, Y. Ding, S. Dai, Comprehensive studies of air-brush spray deposition used in fabricating high-efficiency CH3NH3PbI3 perovskite solar cells: Combining theories with practices, J. Power Sources. 402 (2018) 82–90. doi:10.1016/j.jpowsour.2018.07.097.

[165] D. Perednis, L.J. Gauckler, Thin film deposition using spray pyrolysis, J. Electroceramics. 14 (2005) 103–111. doi:10.1007/s10832-005-0870-x.

[166] J.H. Heo, M.H. Lee, M.H. Jang, S.H. Im, Highly efficient CH3NH3PbI3−xClx mixed halide perovskite solar cells prepared by re-dissolution and crystal grain growth via spray coating, J. Mater. Chem. A. 4 (2016) 17636–17642. doi:10.1039/c6ta06718b.

[167] E.J. Cassella, E.L.K. Spooner, T. Thornber, M.E. O'Kane, T.E. Catley, J.E. Bishop, J.A. Smith, O.S. Game, D.G. Lidzey, Gas-Assisted Spray Coating of Perovskite Solar Cells Incorporating Sprayed Self-Assembled Monolayers, Adv. Sci. 9 (2022) 2104848. doi:10.1002/advs.202104848.

[168] K. Amratisha, J. Ponchai, P. Kaewurai, P. Pansa-Ngat, K. Pinsuwan, P. Kumnorkaew, P. Ruankham, P. Kanjanaboos, Layer-by-layer spray coating of stacked perovskite absorber for perovskite solar cell with better performance and stability under humid environment, Opt. Mater. Express. 10 (2020) 1497–1508. doi:10.1364/ome.391546.

[169] T. Thornber, O.S. Game, E.J. Cassella, M.E. O'Kane, J.E. Bishop, T.J. Routledge, T.I. Alanazi, M. Togay, P.J.M. Isherwood, L.C. Infante-Ortega, D.B. Hammond, J.M. Walls, D.G. Lidzey, Nonplanar Spray-Coated Perovskite Solar Cells, ACS Appl. Mater. Interfaces. 14 (2022) 37587–37594. doi:10.1021/acsami.2c05085.

[170] J.E. Bishop, C.D. Read, J.A. Smith, T.J. Routledge, D.G. Lidzey, Fully Spray-Coated Triple-Cation Perovskite Solar Cells, Sci. Rep. 10 (2020) 6610. doi:10.1038/s41598-020-63674-5.

[171] A.T. Barrows, A.J. Pearson, C.K. Kwak, A.D.F. Dunbar, A.R. Buckley, D.G. Lidzey, Efficient planar heterojunction mixed-halide perovskite solar cells deposited via spray-deposition, Energy Environ. Sci. 7 (2014) 2944–2950. doi:10.1039/c4ee01546k.

[172] J.E. Bishop, D.K. Mohamad, M. Wong-Stringer, A. Smith, D.G. Lidzey, Spray-cast multilayer perovskite solar cells with an active-area of 1.5 cm2, Sci. Rep. 7 (2017) 1–11. doi:10.1038/s41598-017-08642-2.

[173] L.R. V. Buizza, A.D. Wright, G. Longo, H.C. Sansom, C.Q. Xia, M.J. Rosseinsky, M.B. Johnston, H.J. Snaith, L.M. Herz, Charge-Carrier Mobility and Localization

in Semiconducting Cu2AgBiI6 for Photovoltaic Applications, ACS Energy Lett. 6 (2021) 1729–1739. doi:10.1021/ACSENERGYLETT.1C00458.

[174] H.C. Sansom, G. Longo, A.D. Wright, L.R. V. Buizza, S. Mahesh, B. Wenger, M. Zanella, M. Abdi-Jalebi, M.J. Pitcher, M.S. Dyer, T.D. Manning, R.H. Friend, L.M. Herz, H.J. Snaith, J.B. Claridge, M.J. Rosseinsky, Highly Absorbing Lead-Free Semiconductor Cu 2 AgBiI 6 for Photovoltaic Applications from the Quaternary CuI–AgI–BiI 3 Phase Space, J. Am. Chem. Soc. 143 (2021) 3983–3992. doi:10.1021/jacs.1c00495.

[175] P. Hohenberg, W. Kohn, Inhomogeneous electron gas, Phys. Rev. 136 (1964) B864. doi:10.1103/PHYSREV.136.B864/FIGURE/1/THUMB.

[176] W. Kohn, L.J. Sham, Self-consistent equations including exchange and correlation effects, Phys. Rev. 140 (1965) A1133. doi:10.1103/PHYSREV.140.A1133/FIGURE/1/THUMB.

[177] G. Kresse, J. Furthmüller, Efficient iterative schemes for ab initio total-energy calculations using a plane-wave basis set, Phys. Rev. B - Condens. Matter Mater. Phys. 54 (1996) 11169–11186. doi:10.1103/PhysRevB.54.11169.

[178] G. Kresse, J. Furthmüller, Efficiency of ab-initio total energy calculations for metals and semiconductors using a plane-wave basis set, Comput. Mater. Sci. 6 (1996) 15–50. doi:10.1016/0927-0256(96)00008-0.

[179] MedeA® 3.0 software, Materials Design Inc., San Diego, CA, USA, (2018). https://www.materialsdesign.com/.

[180] J.P. Perdew, A. Ruzsinszky, G.I. Csonka, O.A. Vydrov, G.E. Scuseria, L.A. Constantin, X. Zhou, K. Burke, Restoring the Density-Gradient Expansion for Exchange in Solids and Surfaces, Phys. Rev. Lett. 100 (2008) 136406. doi:10.1103/PhysRevLett.100.136406.

[181] D. Joubert, From ultrasoft pseudopotentials to the projector augmented-wave method, Phys. Rev. B - Condens. Matter Mater. Phys. 59 (1999) 1758–1775. doi:10.1103/PhysRevB.59.1758.

[182] T. Mohammad, V. Kumar, V. Dutta, Electric field assisted spray coated lead free bismuth iodide perovskite thin film for solar cell application, Sol. Energy. 182 (2019) 72–79. doi:10.1016/j.solener.2019.02.034.

[183] S. Ulična, B. Dou, D.H. Kim, K. Zhu, J.M. Walls, J.W. Bowers, M.F.A.M. Van Hest, Scalable Deposition of High-Efficiency Perovskite Solar Cells by Spray-Coating, ACS Appl. Energy Mater. 1 (2018) 1853–1857. doi:10.1021/acsaem.8b00328.

[184] R.R. Chamberlin, J.E. Hill, Process for making conductive film, 3148084, 1964. https://www.google.si/patents/US3148084 (accessed November 21, 2019).

[185] R.R. Chamberlin, J.S. Skarman, Chemical Spray Deposition Process for Inorganic

Films, J. Electrochem. Soc. 113 (1966) 86. doi:10.1149/1.2423871.

[186] Ultrasonic Spray Pyrolysis, (n.d.). https://www.cysi.wang/Electrospinning/Ultrasonic-atomization-pyrolysis-spraying-system.html (accessed March 15, 2020).

[187] S. Devasia, A. A.Ramachandran, S. Shaji, D.A. Avellaneda, J.A. Aguilar Martinez, B. Krishnan, Bismuth triiodide: Ab-initio simulations to spray cast thin films for optoelectronic applications, Scientia. 15 (2019) 98–111. http://www.scientia.mercycollege.edu.in/pdf/scientia-15.pdf#page=99.

[188] SCHERRER, P., Nachr Ges Wiss Goettingen, Math. Phys. 2 (1918) 98–100.

[189] A. Monshi, M.R. Foroughi, M.R. Monshi, Modified Scherrer Equation to Estimate More Accurately Nano-Crystallite Size Using XRD, World J. Nano Sci. Eng. 02 (2012) 154–160. doi:10.4236/wjnse.2012.23020.

[190] R. Amiruddin, S. Devasia, D.K. Mohammedali, M.C. Santhosh Kumar, Investigation on P-N dual acceptor doped p-type ZnO thin films and subsequent growth of pencil-like nanowires, Semicond. Sci. Technol. 30 (2015) 035009. doi:10.1088/0268-1242/30/3/035009.

[191] G. Greczynski, L. Hultman, X-ray photoelectron spectroscopy: Towards reliable binding energy referencing, Prog. Mater. Sci. 107 (2020) 100591. doi:10.1016/j.pmatsci.2019.100591.

[192] S. Devasia, P. V. Athma, E.I. Anila, Controlling the zinc oxide unipolarity through dual acceptor doping for spray-cast homojunction diode, Mater. Lett. 238 (2019) 112–115. doi:10.1016/j.matlet.2018.11.157.

[193] S. Li, Z. Yan, Z. Liu, J. Chen, Y. Zhi, D. Guo, P. Li, Z. Wu, W. Tang, A self-powered solar-blind photodetector with large: V oc enhancing performance based on the PEDOT:PSS/Ga2O3 organic-inorganic hybrid heterojunction, J. Mater. Chem. C. 8 (2020) 1292–1300. doi:10.1039/c9tc06011a.

[194] D. Wang, G. Li, Advances in Photoelectric Detection Units for Imaging Based on Perovskite Materials, Laser Photon. Rev. 16 (2022) 2100713. doi:10.1002/LPOR.202100713.

[195] A.J. Lehner, H. Wang, D.H. Fabini, C.D. Liman, C.-A. Hébert, E.E. Perry, M. Wang, G.C. Bazan, M.L. Chabinyc, R. Seshadri, Electronic structure and photovoltaic application of BiI 3, Appl. Phys. Lett. 107 (2015) 131109. doi:10.1063/1.4932129.

[196] K. Hoang, S.D. Mahanti, J.R. Salvador, M.G. Kanatzidis, Atomic ordering and gap formation in Ag-Sb-based ternary chalcogenides, Phys. Rev. Lett. 99 (2007) 1–4. doi:10.1103/PhysRevLett.99.156403.

[197] R.E. Brandt, R.C. Kurchin, R.L.Z. Hoye, J.R. Poindexter, M.W.B. Wilson, S. Sulekar, F. Lenahan, P.X.T. Yen, V. Stevanović, J.C. Nino, M.G. Bawendi, T.

Buonassisi, Investigation of Bismuth Triiodide (BiI 3) for Photovoltaic Applications, J. Phys. Chem. Lett. 6 (2015) 4297–4302. doi:10.1021/acs.jpclett.5b02022.

[198] M.B. Johansson, H. Zhu, E.M.J. Johansson, Extended Photo-Conversion Spectrum in Low-Toxic Bismuth Halide Perovskite Solar Cells, J. Phys. Chem. Lett. 7 (2016) 3467–3471. doi:10.1021/acs.jpclett.6b01452.

[199] K.H. Hong, J. Kim, L. Debbichi, H. Kim, S.H. Im, Band gap engineering of Cs3Bi2I9 perovskites with trivalent atoms using a dual metal cation, J. Phys. Chem. C. 121 (2017) 969–974. doi:10.1021/acs.jpcc.6b12426.

[200] A.H. Slavney, T. Hu, A.M. Lindenberg, H.I. Karunadasa, A Bismuth-Halide Double Perovskite with Long Carrier Recombination Lifetime for Photovoltaic Applications, J. Am. Chem. Soc. 138 (2016) 2138–2141. doi:10.1021/jacs.5b13294.

[201] J.F. Moulder, W.F. Stickle, P.E. Sobol, K.D. Bomben, Handbook of X-ray photoelectron spectroscopy: a reference book of standard spectra for identification and interpretation of XPS data, 1992. doi:9780962702624.

[202] Y. Wang, K. Deng, L. Zhang, Visible Light Photocatalysis of BiOI and Its Photocatalytic Activity Enhancement by in Situ Ionic Liquid Modification, J. Phys. Chem. C. 115 (2011) 14300–14308. doi:10.1021/jp2042069.

[203] N.F. Coutinho, S. Cucatti, R.B. Merlo, J.M.C. Silva Filho, N.F.B. Villegas, F. Alvarez, A.F. Nogueira, F.C. Marques, The Thermomechanical Properties of Thermally Evaporated Bismuth Triiodide Thin Films, Sci. Rep. 9 (2019) 11785. doi:10.1038/s41598-019-48194-1.

[204] T.K. Chaudhuri, A.B. Patra, P.K. Basu, R.S. Saraswat, H.N. Acharya, Preparation of bismuth iodide thin films by a chemical method, Mater. Lett. 8 (1989) 361–363. doi:10.1016/0167-577X(89)90008-6.

[205] K.M. Boopathi, S. Raman, R. Mohanraman, F.-C. Chou, Y.-Y. Chen, C.-H. Lee, F.-C. Chang, C.-W. Chu, K. Moorthy Boopathi, S. Raman, R. Mohanraman, F.-C. Chou, Y.-Y. Chen, C.-H. Lee, F.-C. Chang, C.-W. Chu, Solution-processable bismuth iodide nanosheets as hole transport layers for organic solar cells, Sol. Energy Mater. Sol. Cells. 121 (2014) 35–41. doi:10.1016/j.solmat.2013.10.031.

[206] D.M. Fabian, S. Ardo, Hybrid organic–inorganic solar cells based on bismuth iodide and 1,6-hexanediammonium dication, J. Mater. Chem. A. 4 (2016) 6837–6841. doi:10.1039/C6TA00517A.

[207] W. Shockley, W.T. Read, Statistics of the Recombination of Holes and Electrons, Phys. Rev. 87 (1952) 835–842. doi:dx.doi.org/10.1103/PhysRev.87.835.

[208] B. Hemanth Kumar, S. Shaji, M.C. Santhosh Kumar, Fabrication of visible light photodetector using co-evaporated Indium Sulfide thin films, J. Mater. Sci. Mater.

Electron. 30 (2019) 17986–17998. doi:10.1007/s10854-019-02152-9.

[209] Q. Wei, Y. Wang, J. Yin, Y. Xia, Z. Liu, High-Performance Visible-Light Photodetectors built on 2D-Nanoplate-Assembled Large-Scale BiI3 Films, Adv. Electron. Mater. 5 (2019) 1900159. doi:10.1002/aelm.201900159.

[210] L. Shan, L. He, J. Suriyaprakash, L. Yang, Photoelectrochemical (PEC) water splitting of BiOI{001} nanosheets synthesized by a simple chemical transformation, J. Alloys Compd. 665 (2016) 158–164. doi:10.1016/j.jallcom.2016.01.008.

[211] Y. Yang, C. Wang, J. Hou, J. Dai, Raman scattering, far infrared spectrum of BiI3 nanocrystallites, Mater. Lett. 57 (2003) 2185–2188. doi:10.1016/S0167-577X(02)01171-0.

[212] H. Li, Z. Yang, J. Zhang, Y. Huang, H. Ji, Y. Tong, Indium doped BiOI nanosheets: Preparation, characterization and photocatalytic degradation activity, Appl. Surf. Sci. 423 (2017) 1188–1197. doi:10.1016/j.apsusc.2017.06.301.

[213] J.E. Bishop, T.J. Routledge, D.G. Lidzey, Advances in Spray-Cast Perovskite Solar Cells, J. Phys. Chem. Lett. 9 (2018) 1977–1984. doi:10.1021/acs.jpclett.8b00311.

[214] A. Nilă, M. Baibarac, A. Matea, R. Mitran, I. Baltog, Exciton-phonon interactions in the Cs 3 Bi 2 I 9 crystal structure revealed by Raman spectroscopic studies, Phys. Status Solidi. 254 (2017) 1552805. doi:10.1002/pssb.201552805.

[215] J.K. Wenderott, A. Raghav, M. Shtein, P.F. Green, S. Satapathi, Local Optoelectronic Characterization of Solvent-Annealed, Lead-Free, Bismuth-Based Perovskite Films, Langmuir. 34 (2018) 7647–7654. doi:10.1021/acs.langmuir.8b01003.

[216] U. Holzwarth, N. Gibson, The Scherrer equation versus the “Debye-Scherrer equation,” Nat. Nanotechnol. 2011 69. 6 (2011) 534–534. doi:10.1038/nnano.2011.145.

[217] S. Devasia, S. Shaji, D.A. Avellaneda, J.A.A. Martinez, B. Krishnan, In situ crystallization of 0D perovskite derivative Cs3Bi2I9 thin films via ultrasonic spray, J. Alloys Compd. 893 (2022) 162294. doi:10.1016/j.jallcom.2021.162294.

[218] M. Malligavathy, D. Pathinettam Padiyan, Role of pH in the hydrothermal synthesis of phase pure alpha Bi2O3 nanoparticles and its structural characterization, Int. Assoc. Adv. Mater. 2 (2021) 51–55. doi:10.5185/AMP.2017/112.

[219] Q. Cao, Y. Li, H. Zhang, J. Yang, J. Han, T. Xu, S. Wang, Z. Wang, B. Gao, J. Zhao, X. Li, X. Ma, S.M. Zakeeruddin, W.E.I. Sha, X. Li, M. Grätzel, Efficient and stable inverted perovskite solar cells with very high fill factors via incorporation of star-shaped polymer, Sci. Adv. 7 (2021) eabg0633.

doi:10.1126/sciadv.abg0633.

[220] T. Abzieher, T. Feeney, F. Schackmar, Y.J. Donie, I.M. Hossain, J.A. Schwenzer, T. Hellmann, T. Mayer, M. Powalla, U.W. Paetzold, From Groundwork to Efficient Solar Cells: On the Importance of the Substrate Material in Co-Evaporated Perovskite Solar Cells, Adv. Funct. Mater. (2021) 2104482. doi:10.1002/adfm.202104482.

[221] J.E. Bishop, J.A. Smith, C. Greenland, V. Kumar, N. Vaenas, O.S. Game, T.J. Routledge, M. Wong-Stringer, C. Rodenburg, D.G. Lidzey, High-Efficiency Spray-Coated Perovskite Solar Cells Utilizing Vacuum-Assisted Solution Processing, ACS Appl. Mater. Interfaces. 10 (2018) 39428–39434. doi:10.1021/acsami.8b14859.

[222] M. Gotić, S. Popović, S. Musić, Influence of synthesis procedure on the morphology of bismuth oxide particles, Mater. Lett. 61 (2007) 709–714. doi:10.1016/j.matlet.2006.05.048.

[223] S. Öz, J.C. Hebig, E. Jung, T. Singh, A. Lepcha, S. Olthof, F. Jan, Y. Gao, R. German, P.H.M. van Loosdrecht, K. Meerholz, T. Kirchartz, S. Mathur, Zero-dimensional (CH3NH3)3Bi2I9 perovskite for optoelectronic applications, Sol. Energy Mater. Sol. Cells. 158 (2016) 195–201. doi:10.1016/j.solmat.2016.01.035.

[224] W. Zhang, S. Pathak, N. Sakai, T. Stergiopoulos, P.K. Nayak, N.K. Noel, A.A. Haghighirad, V.M. Burlakov, D.W. DeQuilettes, A. Sadhanala, W. Li, L. Wang, D.S. Ginger, R.H. Friend, H.J. Snaith, Enhanced optoelectronic quality of perovskite thin films with hypophosphorous acid for planar heterojunction solar cells, Nat. Commun. 6 (2015) 10030. doi:10.1038/ncomms10030.

[225] X. Han, Y. Li, H. Wang, Q. Zhang, Controlled preparation of β-Bi2O3/Mg–Al mixed metal oxides composites with enhanced visible light photocatalytic performance, Res. Chem. Intermed. 46 (2020) 5009–5021. doi:10.1007/s11164-020-04237-1.

[226] S. Singh, R.K. Sahoo, N.M. Shinde, J.M. Yun, R.S. Mane, K.H. Kim, Synthesis of Bi2O3-MnO2 Nanocomposite Electrode for Wide-Potential Window High Performance Supercapacitor, Energies. 12 (2019) 3320. doi:10.3390/en12173320.

[227] S. Gupta, R. Singh, M.D. Anoop, V. Kulshrestha, D.N. Srivastava, K. Ray, S.L. Kothari, K. Awasthi, M. Kumar, Electrochemical sensor for detection of mercury (II) ions in water using nanostructured bismuth hexagons, Appl. Phys. A Mater. Sci. Process. 124 (2018) 1–6. doi:10.1007/S00339-018-2161-9/FIGURES/6.

[228] J. Tauc, Optical properties and electronic structure of amorphous Ge and Si, Mater. Res. Bull. 3 (1968) 37–46. doi:10.1016/0025-5408(68)90023-8.

[229] D. Phuyal, S.M. Jain, B. Philippe, M.B. Johansson, M. Pazoki, J. Kullgren, K.O. Kvashnina, M. Klintenberg, E.M.J. Johansson, S.M. Butorin, O. Karis, H. Rensmo, The electronic structure and band interface of cesium bismuth iodide on a titania

heterostructure using hard X-ray spectroscopy, J. Mater. Chem. A. 6 (2018) 9498–9505. doi:10.1039/c8ta00947c.

[230] L. Zeng, L. Tao, C. Tang, B. Zhou, H. Long, Y. Chai, S.P. Lau, Y.H. Tsang, High-responsivity UV-Vis Photodetector Based on Transferable WS2 Film Deposited by Magnetron Sputtering, Sci. Rep. 6 (2016) 20343. doi:10.1038/srep20343.

[231] B. Ghosh, B. Wu, H.K. Mulmudi, C. Guet, K. Weber, T.C. Sum, S. Mhaisalkar, N. Mathews, Limitations of Cs 3 Bi 2 I 9 as Lead-Free Photovoltaic Absorber Materials, ACS Appl. Mater. Interfaces. 10 (2018) 35000–35007. doi:10.1021/acsami.7b14735.

[232] D. Nath, F. Singh, R. Das, X-ray diffraction analysis by Williamson-Hall, Halder-Wagner and size-strain plot methods of CdSe nanoparticles- a comparative study, Mater. Chem. Phys. 239 (2020) 122021. doi:10.1016/j.matchemphys.2019.122021.

[233] O. V. Vakulenko, V.O. Gubanov, S. V. Kun, F. V. Motsnyi, E.Y. Peresh, V.A. Terekhov, Raman diagnostics of new types of A 3 B 2 X 9 layered crystals, in: S. V. Svechnikov, M.Y. Valakh (Eds.), Opt. Diagnostics Mater. Devices Opto-, Micro-, Quantum Electron. 1997, SPIE, 1998: p. 351. doi:10.1117/12.306241.

[234] B. Philippe, B.-W. Park, R. Lindblad, J. Oscarsson, S. Ahmadi, E.M.J. Johansson, H. Rensmo, Chemical and Electronic Structure Characterization of Lead Halide Perovskites and Stability Behavior under Different Exposures—A Photoelectron Spectroscopy Investigation, Chem. Mater. 27 (2015) 1720–1731. doi:10.1021/acs.chemmater.5b00348.

[235] D. Kim, J.-Y. Leem, Crystallization of ZnO thin films via thermal dissipation annealing method for high-performance UV photodetector with ultrahigh response speed, Sci. Rep. 11 (2021) 382. doi:10.1038/s41598-020-79849-z.

[236] A. Moyseowicz, Scalable one-pot synthesis of bismuth sulfide nanorods as an electrode active material for energy storage applications, J. Solid State Electrochem. 23 (2019) 1191–1199. doi:10.1007/S10008-019-04215-7.

[237] P.K. Panigrahi, A. Pathak, The Growth of Bismuth Sulfide Nanorods from Spherical-Shaped Amorphous Precursor Particles under Hydrothermal Condition, J. Nanoparticles. 2013 (2013) 1–11. doi:10.1155/2013/367812.

[238] H. Moreno-García, S. Messina, M. Calixto-Rodriguez, H. Martínez, Physical properties of chemically deposited Bi 2 S 3 thin films using two post-deposition treatments, Appl. Surf. Sci. 311 (2014) 729–733. doi:10.1016/j.apsusc.2014.05.147.

[239] N. Benramdane, M. Latreche, H. Tabet, M. Boukhalfa, Z. Kebbab, A. Bouzidi, Structural and optical properties of spray-pyrolysed Bi2S3 thin films, Mater. Sci. Eng. B. 64 (1999) 84–87. doi:10.1016/S0921-5107(99)00174-9.

[240] H. Song, X. Zhan, D. Li, Y. Zhou, B. Yang, K. Zeng, J. Zhong, X. Miao, J. Tang,

Rapid thermal evaporation of Bi2S3 layer for thin film photovoltaics, Sol. Energy Mater. Sol. Cells. 146 (2016) 1–7. doi:10.1016/J.SOLMAT.2015.11.019.

[241] S.Y. Wang, Y.W. Du, Preparation of nanocrystalline bismuth sulfide thin films by asynchronous-pulse ultrasonic spray pyrolysis technique, J. Cryst. Growth. 236 (2002) 627–634. doi:10.1016/S0022-0248(02)00846-1.

[242] A.A. Ramachandran, B. Krishnan, S. Devasia, D.A. Avellaneda, M.I. Mendivil Palma, J.A. Aguilar Martinez, S. Shaji, Photosensitive antimony triiodide thin films by rapid iodization of chemically deposited antimony sulfide, Mater. Res. Bull. 142 (2021) 111382. doi:10.1016/j.materresbull.2021.111382.

[243] S. Devasia, S. Shaji, D.A. Avellaneda, J.A. Aguilar Martinez, B. Krishnan, Tin antimony sulfide (Sn6Sb10S21) thin films by heating chemically deposited Sb2S3/SnS layers: Studies on the structure and their optoelectronic properties, J. Alloys Compd. 827 (2020) 154256. doi:10.1016/j.jallcom.2020.154256.

[244] H. Bao, X. Cui, C.M. Li, Y. Gan, J. Zhang, J. Guo, Photoswitchable Semiconductor Bismuth Sulfide (Bi2S3) Nanowires and Their Self-Supported Nanowire Arrays, J. Phys. Chem. C. 111 (2007) 12279–12283. doi:10.1021/JP073504T.

[245] Z. Li, X. Liu, C. Zuo, W. Yang, X. Fang, Supersaturation-Controlled Growth of Monolithically Integrated Lead-Free Halide Perovskite Single-Crystalline Thin Film for High-Sensitivity Photodetectors, Adv. Mater. 33 (2021) 2103010. doi:10.1002/adma.202103010.

[246] L. Li, G. Ye, T. Luo, X. Chen, G. Zhang, H. Wu, L. Yang, W. Zhang, H. Chang, Centimeter-Sized Stable Zero-Dimensional Cs 3 Bi 2 I 9 Single Crystal for Mid-Infrared Lead-Free Perovskite Photodetector, J. Phys. Chem. C. (2022) acs.jpcc.1c08815. doi:10.1021/acs.jpcc.1c08815.

ANNEX A:

TIN ANTIMONY SULFIDE ($Sn_6Sb_{10}S_{21}$) THIN FILMS BY HEATING CHEMICALLY DEPOSITED Sb_2S_3/SnS LAYERS: STUDIES ON THE STRUCTURE AND THEIR OPTOELECTRONIC PROPERTIES

A.1. Abstract

Tin antimony sulfide thin films ($Sn_6Sb_{10}S_{21}$) are formed by post-heating Sb_2S_3/SnS layers obtained by chemical bath deposition. This work is primarily focused on the systematic study of structure, composition, morphology, optical and electrical properties of the thin films obtained by low-vacuum annealing in the temperature of 300 – 450 ℃ range for 30 min as well as at 390 ℃ for 1, 2 and 3 h. When heated higher than 390 ℃, the crystallization of ternary $Sn_6Sb_{10}S_{21}$phase is revealed by X-ray diffraction and Raman spectra analyses. X-ray photoelectron spectroscopy recognized the Sn^{2+}, Sb^{3+} and S^{2-} states in the ternary phase, while the depth profile presented a uniform distribution of elements through the film thickness. Further, the as-deposited and annealed thin films are probed by scanning electron microscopy displaying a compact nanosheet morphology. Significant absorption properties are demonstrated by the thin films with absorption coefficients in the order of 10^5 cm^{-1} and the optical band gaps are estimated in the 1.26 – 1.45 eV range, suitable for photovoltaic devices. Moreover, the photoconductive thin film is incorporated into the photovoltaic structure, Glass/FTO/CdS/ASTS/C-Ag, yielding V_{oc}, J_{sc}, and FF values of 409 mV, 1.46 $mAcm^{-2}$ and 25 %, respectively.

Journal of Alloys and Compounds 827 (2020) 154256

Contents lists available at ScienceDirect

Journal of Alloys and Compounds

journal homepage: http://www.elsevier.com/locate/jalcom

Tin antimony sulfide ($Sn_6Sb_{10}S_{21}$) thin films by heating chemically deposited Sb_2S_3/SnS layers: Studies on the structure and their optoelectronic properties

Sebin Devasia [a], S. Shaji [a, b], D.A. Avellaneda [a], J.A. Aguilar Martinez [a, c], B. Krishnan [a, b, *]

[a] Facultad de Ingeniería Mecánica y Eléctrica, Universidad Autónoma de Nuevo León, San Nicolás de los Garza, Nuevo León, 66455, Mexico
[b] Centro de Innovación, Investigación y Desarrollo en Ingeniería y Tecnología (CIIDIT)- Universidad Autónoma de Nuevo León, Parque de Investigación e Innovación Tecnológica (PIIT), Apodaca, Nuevo León, 66600, Mexico
[c] Centro de Investigación e Innovación en Ingeniería Aeronáutica (CIIIA), Facultad de Ingeniería Mecánica y Eléctrica, Carretera a Salinas Victoria, Apodaca, Nuevo León, 66600, Mexico

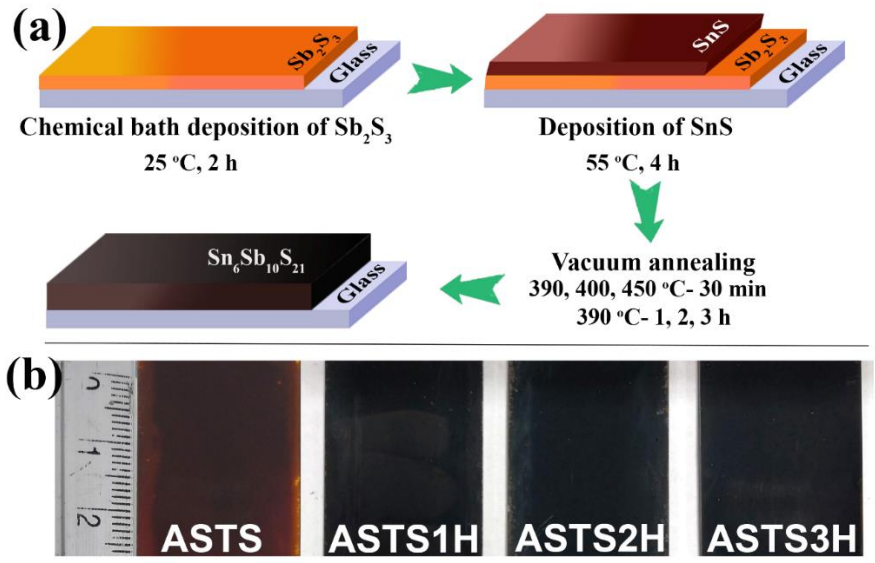

Figure A.1. (a) Schematic representation of the sequential deposition of Sb_2S_3, SnS and vacuum annealing to obtain $Sn_6Sb_{10}S_{21}$ thin films. (b) The as deposited Sb_2S_3/SnS (ASTS) thin film and samples annealed at 390°C for 1 h (ASTS1H), 2 h (ASTS2H) and 3 h (ASTS3H).

A.2. Structure

X-ray diffraction (XRD)

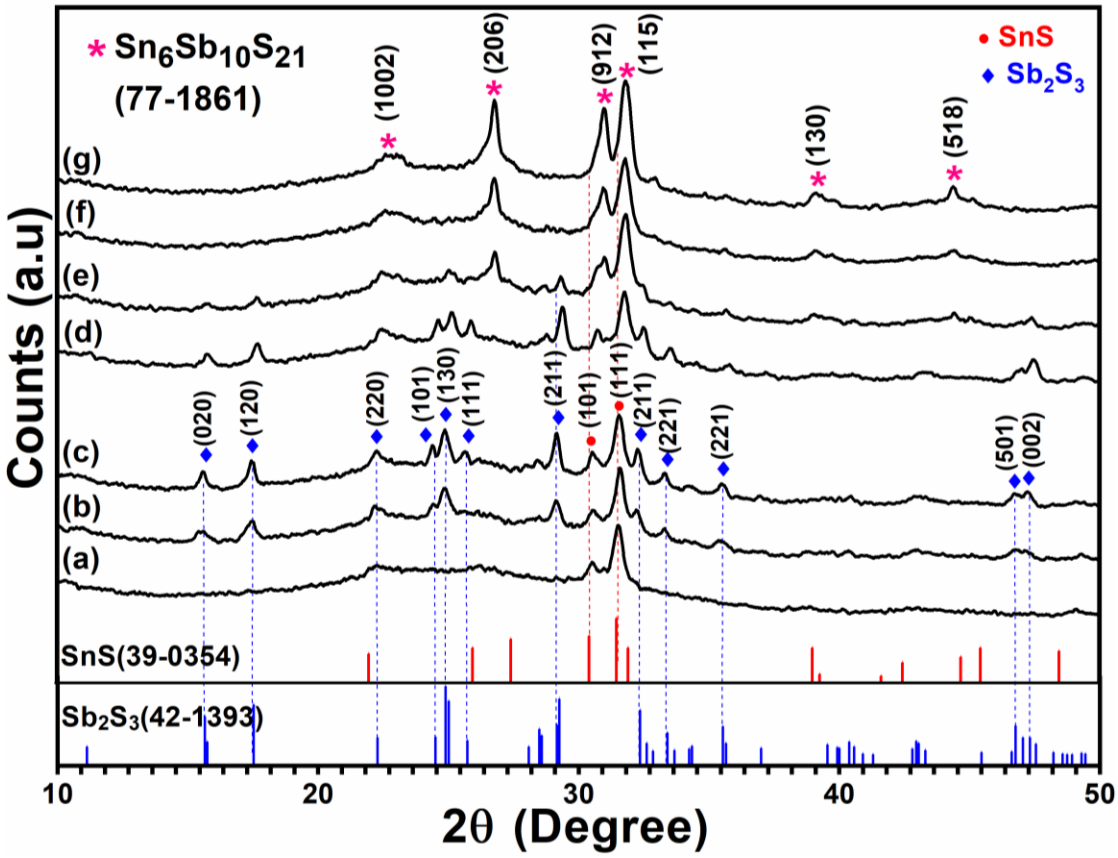

Figure A.2. X-ray diffractograms of (a) ASTS, (b) ASTS300, (c) ASTS350, (d) ASTS375, (e) ASTS390, (f) ASTS400 and (g) ASTS450.

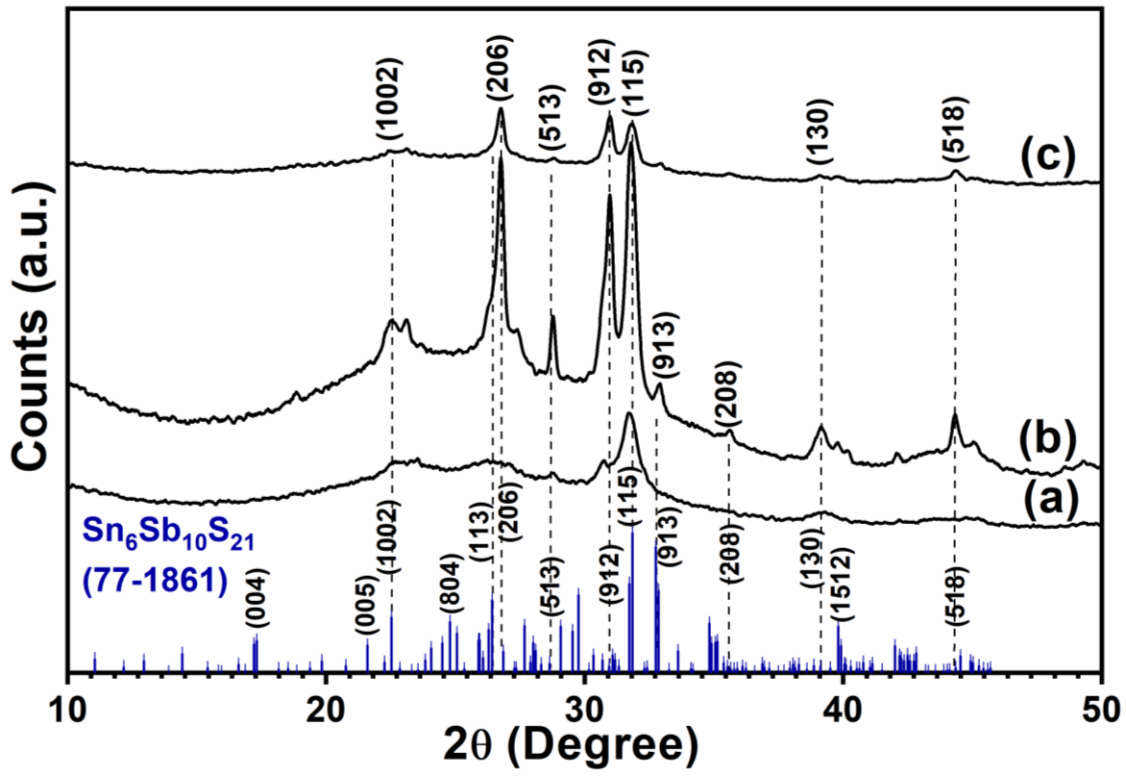

Figure A.3. XRD patterns of ASTS thin films annealed at 390 ℃ for (a) 1 h (ASTS1H), (b) 2 h (ASTS2H) and (c) 3 h (ASTS3H) durations.

Table A-1. The structural parameters of the ASTS thin films annealed at different temperatures for 30 minutes and different durations at 390 ℃.

Sample	2θ (º)	FWHM (º)	Average Crystallite size (nm)
ASTS	31.53	0.4917	16
ASTS300	31.59	0.4763	17
ASTS350	31.56	0.5203	15
ASTS375	31.77	0.5071	16
ASTS390	31.79	0.5513	15
ASTS400	31.77	0.5014	16
ASTS450	31.85	0.4854	17
ASTS1H	31.74	0.6793	12
	30.81	0.6751	
ASTS2H	31.80	0.4769	16
	30.93	0.5063	
	26.71	0.5475	
	31.81	0.4947	

ASTS3H	30.94 26.73	0.4670 0.4693	17

Raman Spectroscopy

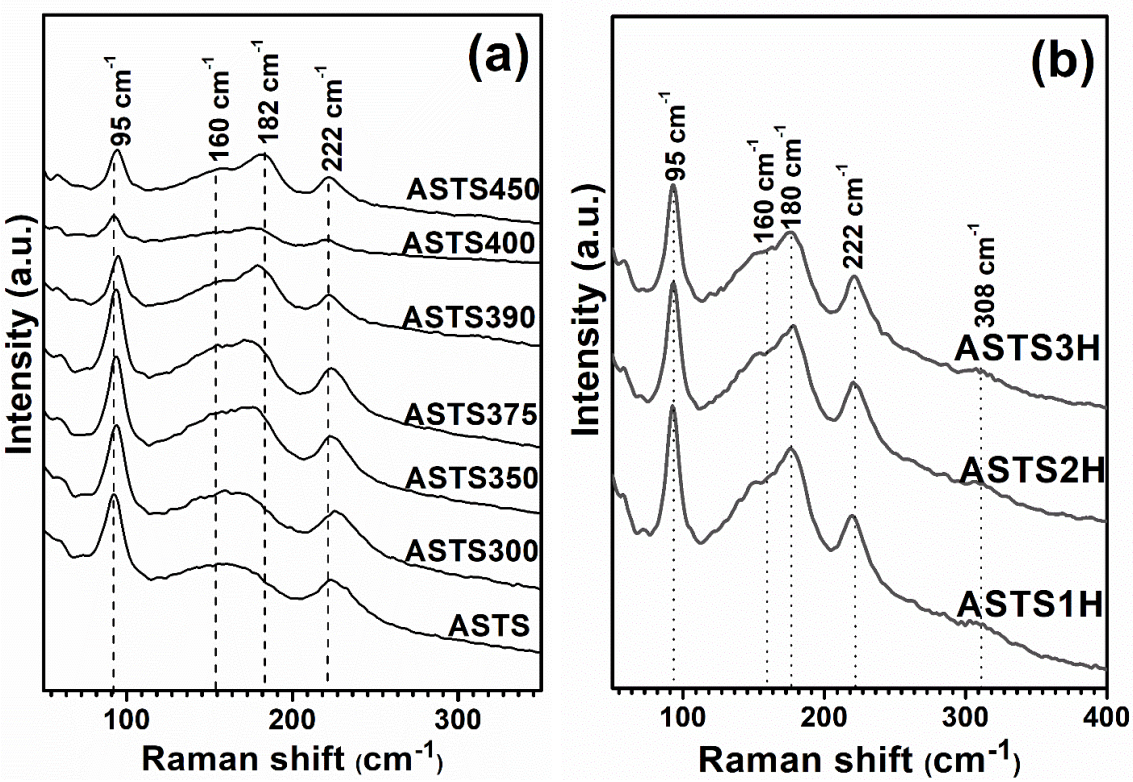

Figure A.4. Raman spectra of (a) as prepared ASTS samples as well as the samples annealed at various temperatures in vacuum. (b) ASTS thin films annealed at 390 ℃ for 1 h, 2 h and 3 h durations.

Table A-2. Raman shifts reported for Sn-Sb-S systems compared with the observed results.

Sn-Sb-S system	Raman shifts (cm^{-1})	Ref.
$SnSb_4S_7$	93, 164, 230 and 307	[1]
	306, 281, 241, 188 and 157 (powder)	[2]
	295.89, 220.87, 125.51, 165.45, 96.16, 77.88 and 67.69	[3]
$SnSb_2S_4$	92, 163, 229 and 307	[1]
	93, 160, 186 and 220	[4]
	305, 280, 235 and 194 (powder)	[2]
	313.01, 292.56, 246.88, 158.56, 119.68, 94.89 and 74.69	[3]
$Sn_2Sb_2S_5$	91, 163, 227 and 307	[1]
	93, 160, 186 and 220	[4]
	308, 276, 228 and 176 (powder)	[2]
	306, 227.73, 182.19, 148.78, 112.62, 92.02 and 72.49	[3]
$Sn_2Sb_6S_{11}$	117, 155,188, 250, 303, 371 and 450	[5]
	323.76, 309.74, 277.82, 233.45, 135.50, 94.64 and 74.18	[3]
$Sn_3Sb_2S_6$	93, 160, 186 and 220	[4]
	306, 271, 227 and 186 (powder)	[2]
	296.20, 217.12, 183.31, 152.31, 113.04, 91.84 and 72.35	[3]
$Sn_4Sb_6S_{13}$	305, 277, 236 and 197 (powder)	[2]
	312.44, 246.10, 160.23, 121.99, 97.69, 80.51 and 70.44	[3]
$Sn_6Sb_{10}S_{21}$	95, 160, 180, 222 and 308	Our work

A.3. Chemical states

X-ray Photoelectron Spectroscopy (XPS)

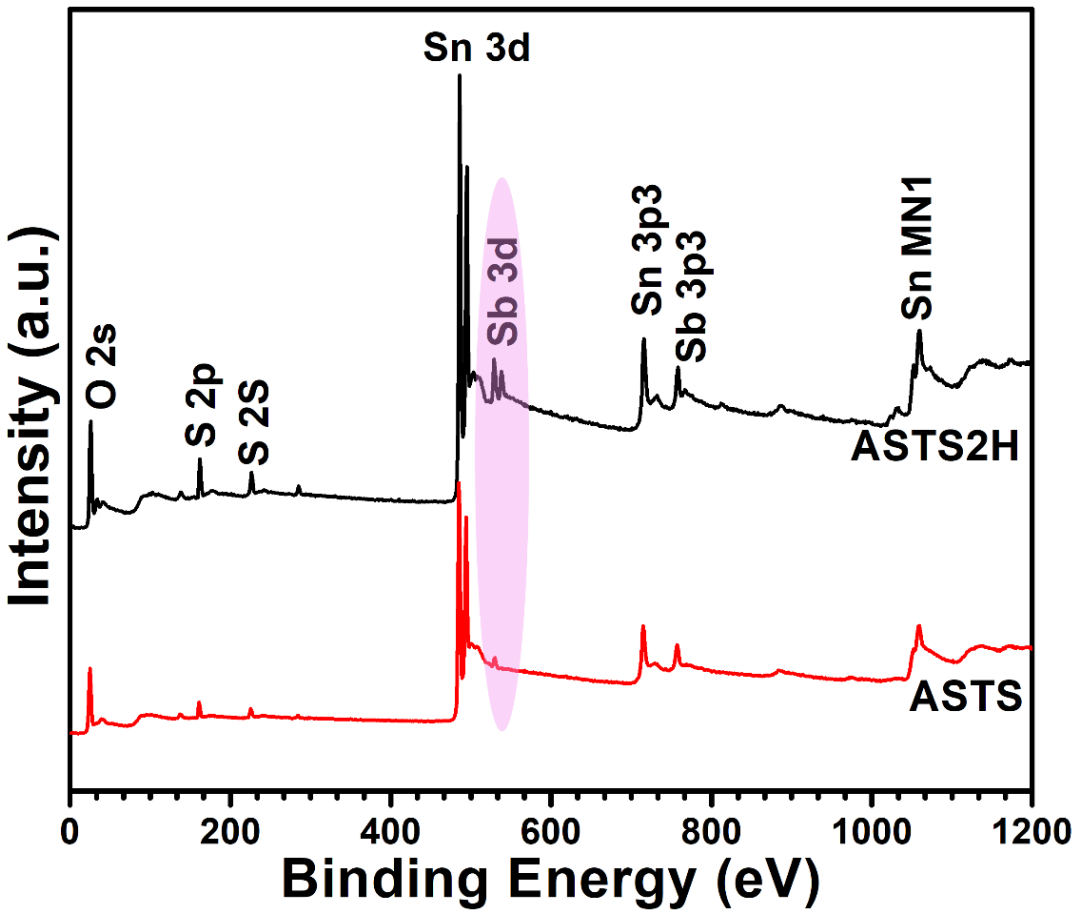

Figure A.5. XPS survey spectrum of the ASTS and ASTS2H thin film sample obtained after a soft surface etching.

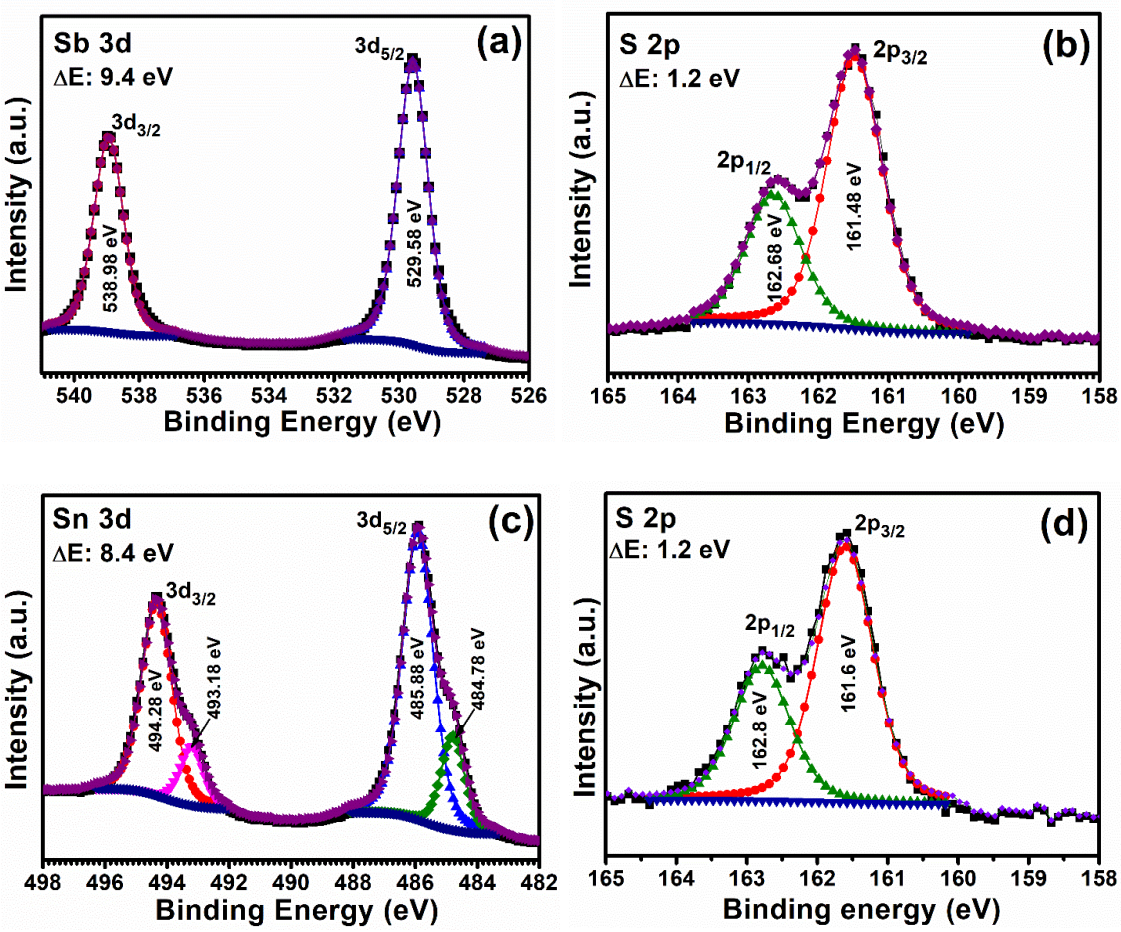

Figure A.6. XPS core level spectra of (a) Sb 3d and (b) S 2p in Sb2S3 layer and (c) Sn 3d and (d) S 2p in SnS layer in the as-deposited ASTS thin films prepared via CBD.

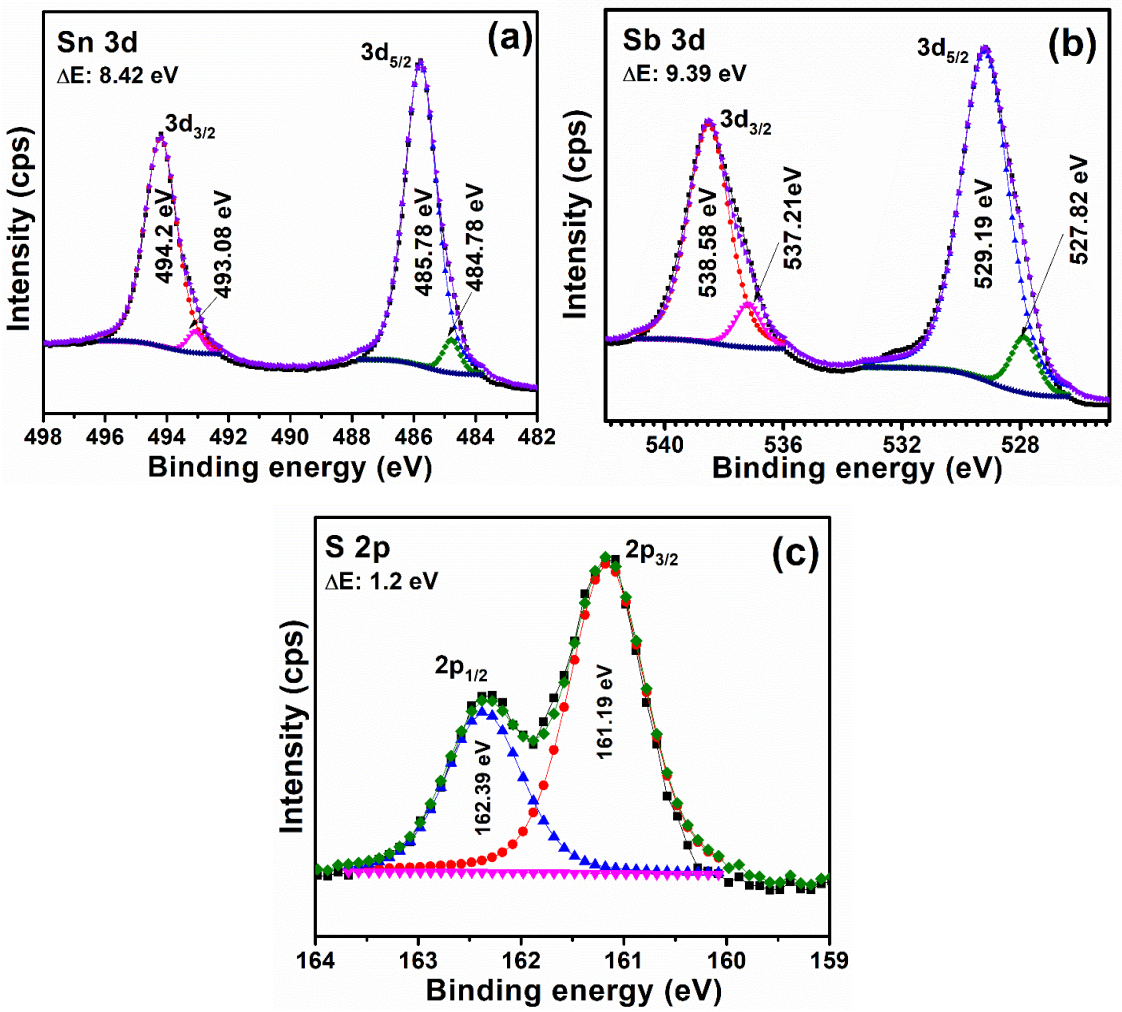

Figure A.7. XPS high resolution spectra of (a) Sn 3d, (b) Sb 3d and (c) S2p states in ASTS2H.

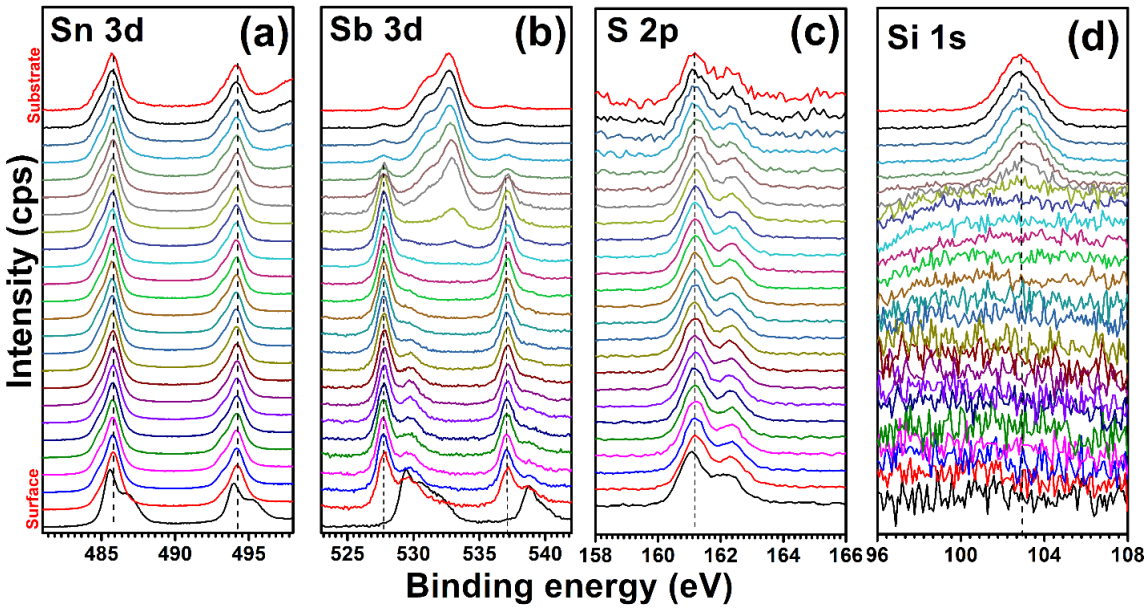

Figure A.8. XPS depth profile analysis in the (a) Sn 3d, (b) Sb 3d, (c) S 2p and (d) Si 1s regions for ASTS2H thin film from surface to glass substrate.

A.4. Morphology

Scanning Electron Microscopy (SEM)

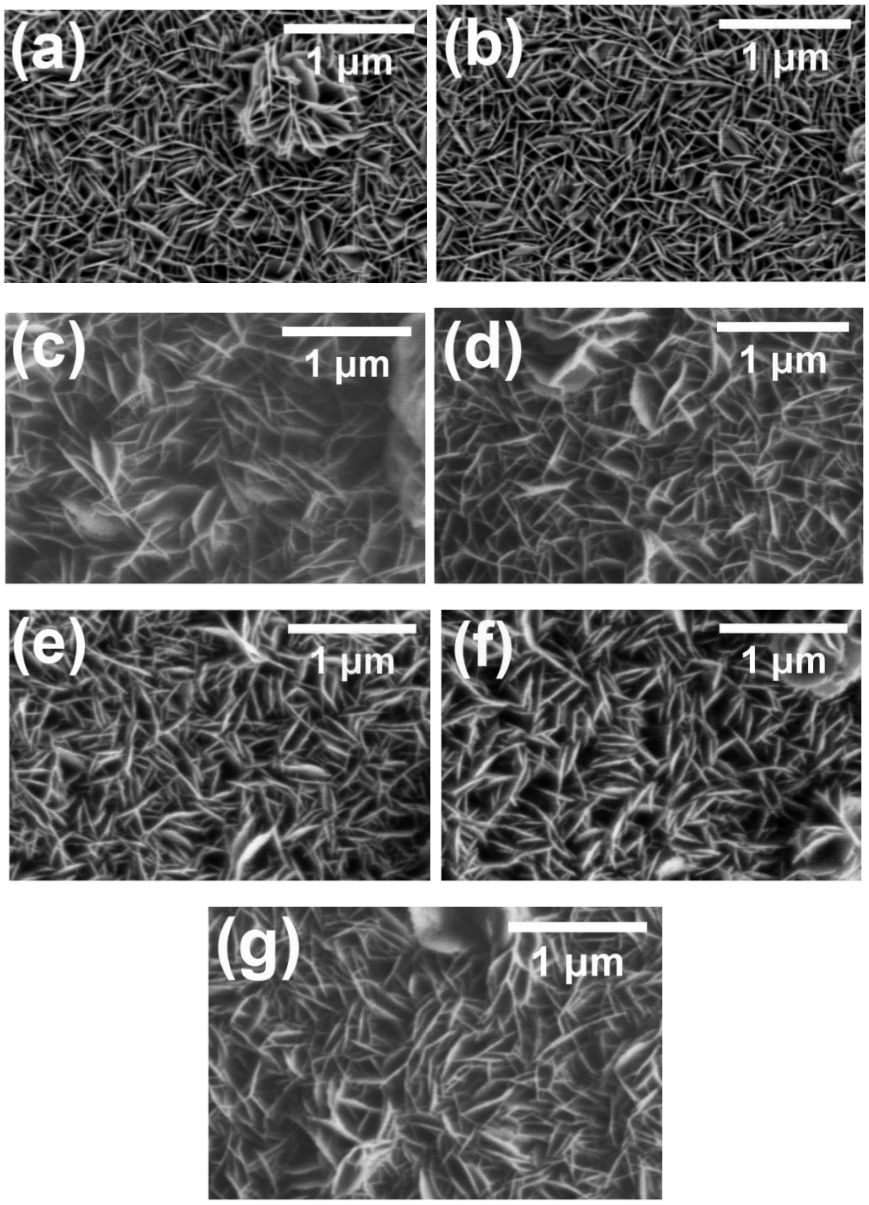

Figure A.9. SEM images of (a) ASTS (b) ASTS390 (c) ASTS400 (d) ASTS450 (e) ASTS1H (f) ASTS2H (g) ASTS3H thin films.

A.5. Optical properties

UV-Vis-NIR spectroscopy

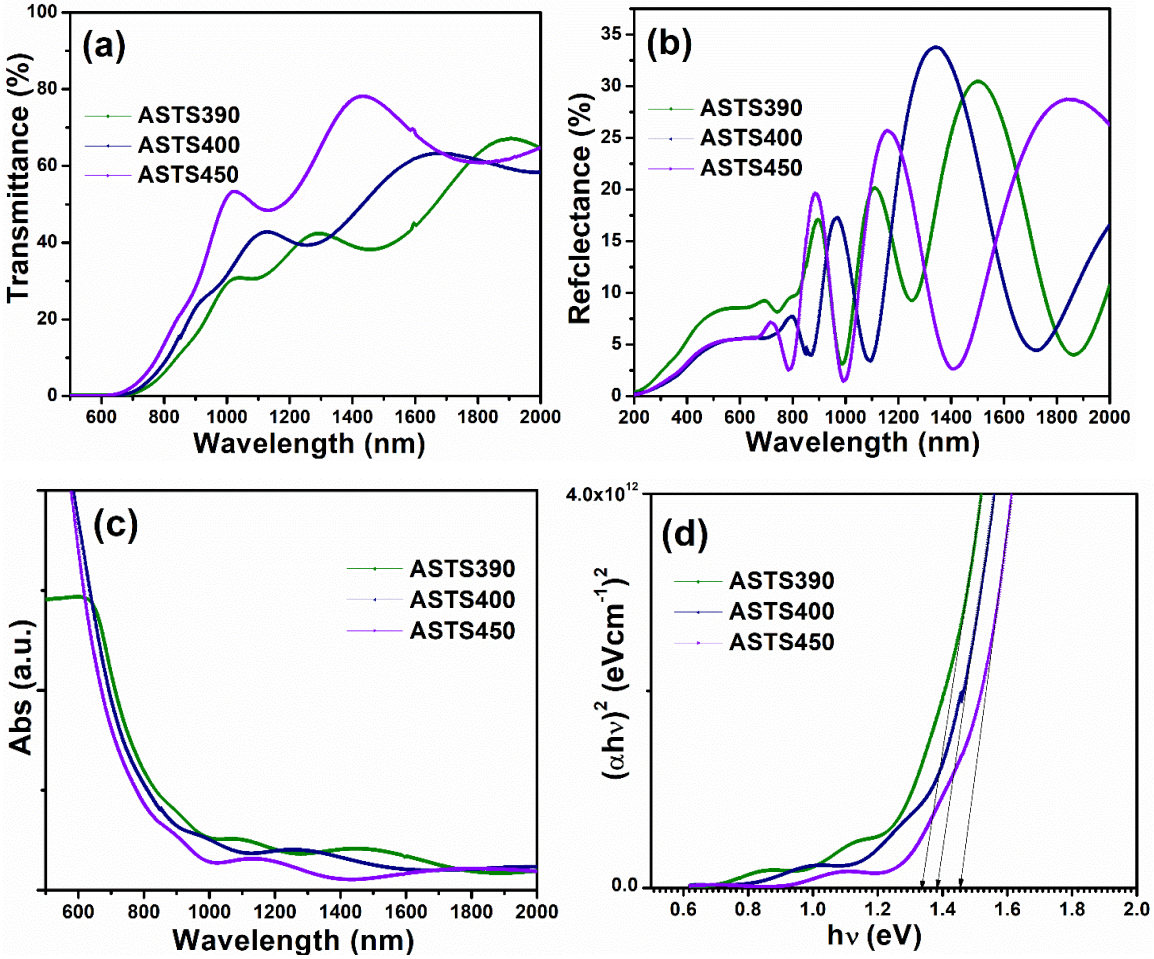

Figure A.10. The spectra of (a) transmittance (b) reflectance (c) absorbance measured for the ASTS thin films annealed at different temperatures (d) Tauc plot for calculation of the band gaps of thin films.

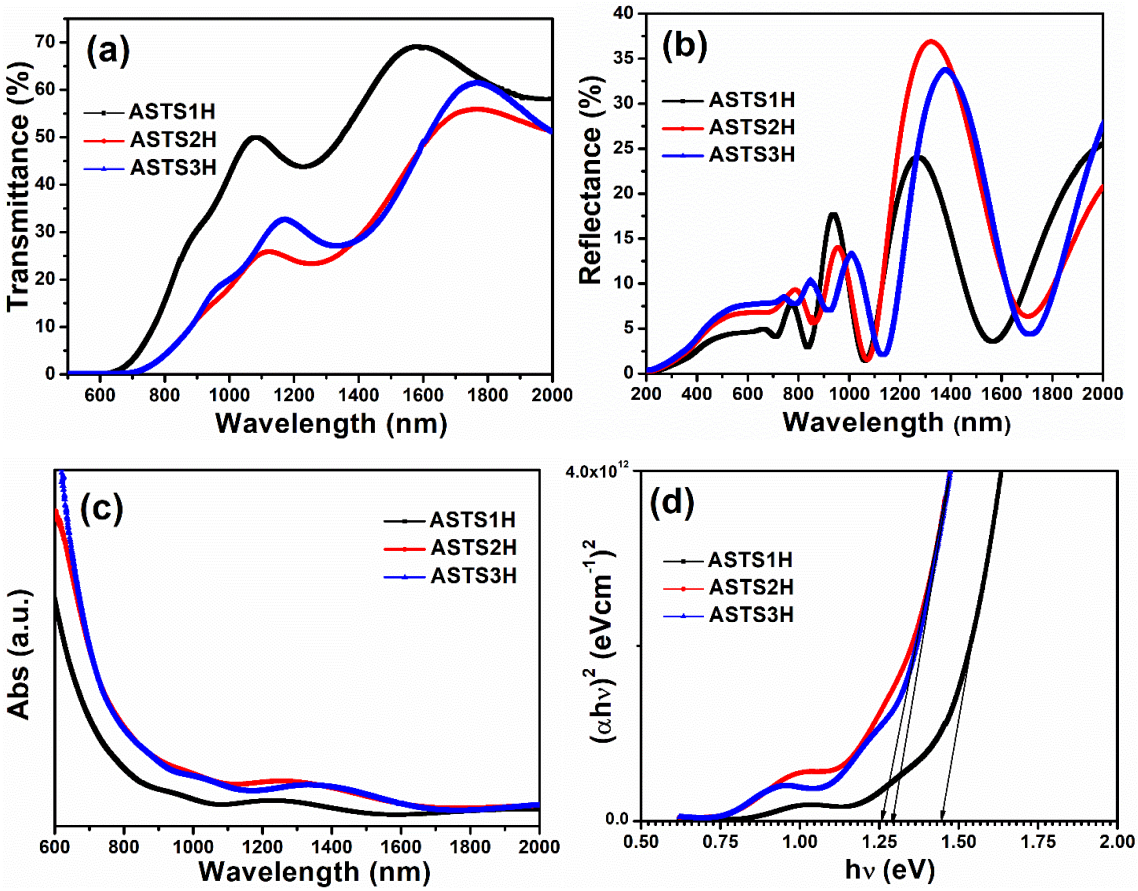

Figure A.11. The spectra of (a) transmittance (b) reflectance (c) absorbance for ASTS thin films annealed at 390 °C for 1 h, 2 h and 3 h. (d) Tauc plot for the calculation of band gaps of the thin films.

Table A-3. The optical band gap values from the literature for various Sn-Sb-S phases.

Composition	Optical band gap (eV)	
	Direct	Indirect
$SnSb_2S_4$	1.23 [6], 2.75-1.65 [7], 1.29 [1], 2.04 [3], 1.63 [4] 1.87-1.46 [8], 2.1-1.65 [9], 1.75-2.76 [10], 1.3 [11], 1.53-1.84 [12], 1.40-1.65 [13], , 2.4 [14]	1.82 [3], 1.71-1.31 [8]
$SnSb_4S_7$	1.52 [1], 2.11 [3], 1.45-1.92 [15]	1.87 [3]
$Sn_2Sb_2S_5$	1.60 - 1.80 [16], 1.28 [1], 1.70 [3], 1.52–1.78, 1.80-1.96 [17], 1.51 [4]	1.42 [3]
$Sn_2Sb_6S_{11}$	2.09 [3]	1.86 [3]

$Sn_3Sb_2S_6$	1.67 [3], 1.47 [4], 1.47-1.18 [18], 1.44 - 1.66 [19]	1.42 [3]
$Sn_4Sb_6S_{13}$	2.041.47 [4]	1.81 [3]
$Sn_6Sb_{10}S_{21}$	(Our result)	
ASTS390	1.33	
ASTS400	1.38	
ASTS450	1.45	
ASTS1H	1.44	
ASTS2H	1.26	
ASTS3H	1.31	

A.6. Photoresponse

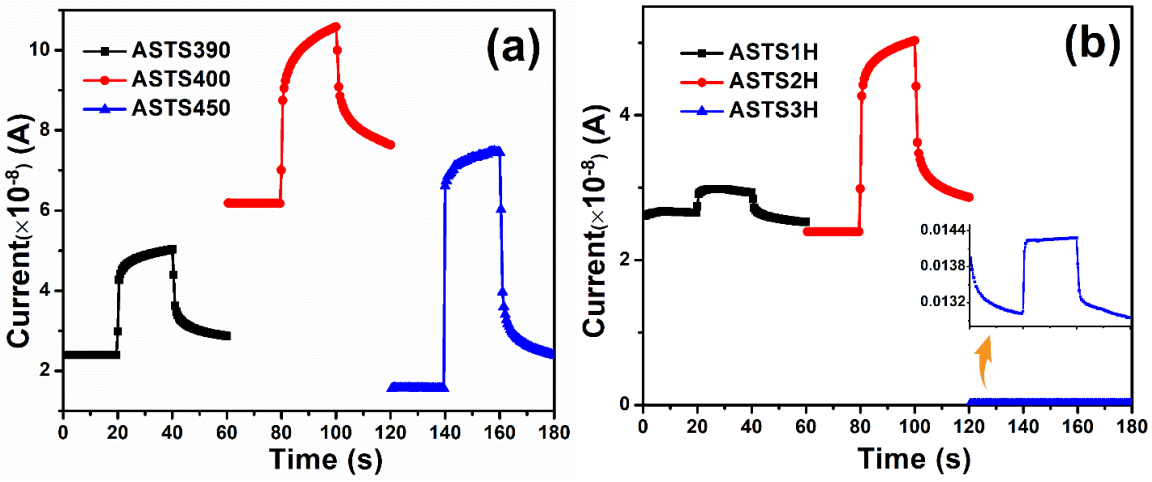

Figure A.12. The photoconductivity curves of ASTS thin film samples annealed at (a) 390, 400 and 450 ℃ for 30 minutes as well as (b) 390 ℃ for 1 h, 2 h and 3 h.

A.7. Photovoltaic device

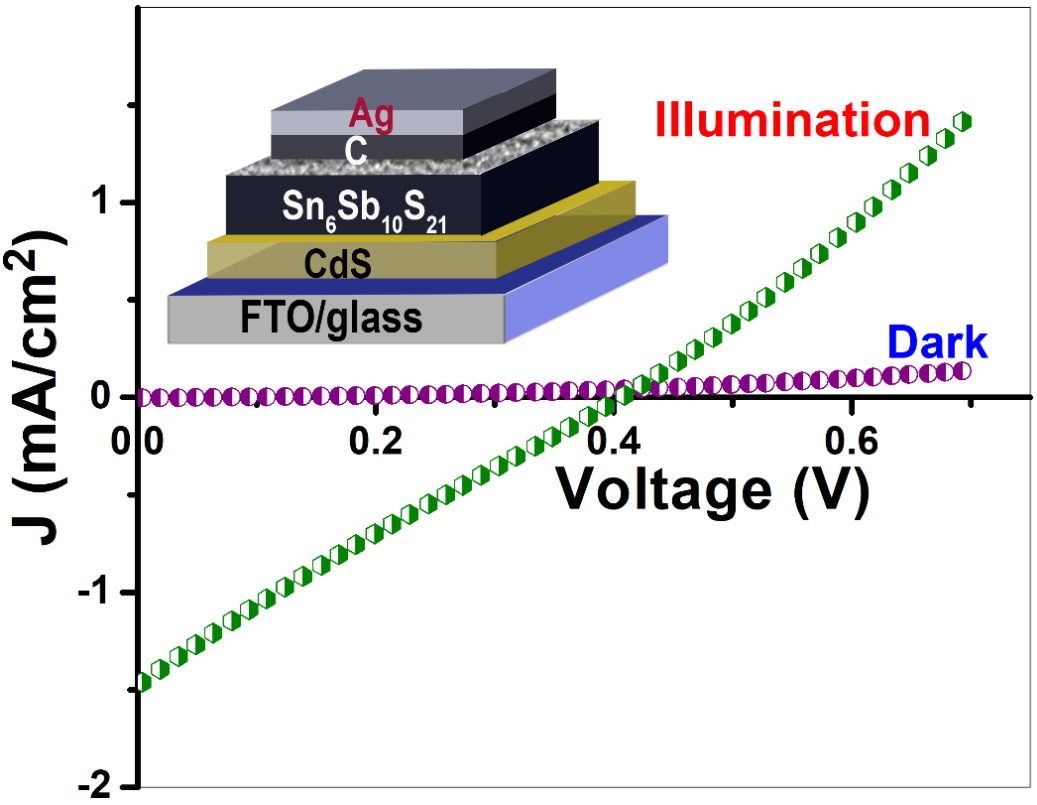

Figure A.13. The J-V characteristic curve of the photovoltaic device Glass/FTO/CdS/ASTS/C-Ag.

A.8. Conclusions

Sb_2S_3 and SnS were deposited subsequently over glass substrates by chemical bath deposition and the two layers were reacted through post-thermal treatments. The low-vacuum annealed thin films were analyzed systematically revealing the novel $Sn_6Sb_{10}S_{21}$ phase at temperatures above 390 °C. The thin films have interpenetrating vertically aligned nanosheets forming a compact and uniform surface morphology. The calculated band gap values were in the 1.3 – 1.5 eV range with the different annealing processes. These values are suitable for performing as a photoabsorber in photovoltaic devices. The solar cell glass/FTO/CdS/ $Sn_6Sb_{10}S_{21}$/C-Ag yielded an open circuit voltage (V_{OC}) of 409 mV and a current density (J_{SC}) of 1.46 $mAcm^{-2}$ with a fill factor (FF) of 25 %.

References

[1] D. Abdelkader, F. Chaffar Akkari, N. Khemiri, B. Gallas, F. Antoni, M. Kanzari, Structural and spectroscopic ellipsometry studies on vacuum-evaporated Sn<inf>2m-4</inf>Sb<inf>4</inf>S<inf>2m+2</inf> (m = 2.5, 3 and 4) thin films deposited on glass and Si substrates, J. Alloys Compd. 646 (2015) 1049–1057. doi:10.1016/j.jallcom.2015.06.114.

[2] D. Abdelkader, A. Jebali, A. Larbi, A. Harizi, M. Ben Rabeh, N. Khemiri, F. Antoni, M. Kanzari, Synthesis, characterization, structural and optical absorption behavior of SnxSbySz powders, Adv. Powder Technol. 27 (2016) 734–741. doi:10.1016/j.apt.2016.02.034.

[3] D. Abdelkader, F. Chaffar Akkari, N. Khemiri, R. Miloua, F. Antoni, B. Gallas, M. Kanzari, Effect of SnS addition on the morphological and optical properties of (SnS)m(Sb2S3)n nano-rods elaborated by glancing angle deposition, Phys. B Condens. Matter. 546 (2018) 33–43. doi:10.1016/j.physb.2018.05.016.

[4] M. Ben Rabeh, N. Khedmi, M. Kanzari, Prospect for SnmSb2nS3n+m (n = 1, m = 1, 2, 3) sulfosalt compounds, J. Mater. Sci. Mater. Electron. 26 (2015) 2002–2009. doi:10.1007/s10854-014-2531-9.

[5] N. Ben Mehrez, N. Khemiri, M. Kanzari, Study of structural and morphological properties of thermally evaporated Sn2Sb6S11 thin films, Mater. Chem. Phys. 182 (2016) 133–138. doi:10.1016/j.matchemphys.2016.07.014.

[6] N. Ali, Z. Ali, R. Akram, S.M. Aslam, M. Jabeen, M.N. Chaudhry, M.A. Iqbal, N. Ahmad, Study of Sb28.47Sn11.22S60.32 compound as thin film for photovoltaic applications, Chalcogenide Lett. 9 (2012) 329–335.

[7] N. Ali, S.T. Hussain, Y. Khan, N. Ahmad, M.A. Iqbal, S.M. Abbas, Effect of air annealing on the band gap and optical properties of SnSb 2S4 thin films for solar cell application, Mater. Lett. 100 (2013) 148–151. doi:10.1016/j.matlet.2013.02.097.

[8] D. Abdelkader, M. Ben Rabeh, N. Khemiri, M. Kanzari, Investigation on optical properties of SnxSbyS z sulfosalts thin films, Mater. Sci. Semicond. Process. 21 (2014) 14–19. doi:10.1016/j.mssp.2014.01.027.

[9] N. Khedmi, M. Ben Rabeh, M. Kanzari, Structural Morphological and Optical Properties of SnSb2S4 Thin Films Grown by Vacuum Evaporation Method, J. Mater. Sci. Technol. 30 (2014) 1006–1011. doi:10.1016/j.jmst.2014.03.019.

[10] N. Ali, S.T. Hussain, M.A. Iqbal, K. Hutching, D. Lane, Structural and optoelectronic properties of antimony tin sulphide thin films deposited by thermal evaporation techniques, Optik (Stuttg). 124 (2013) 4746–4749. doi:10.1016/j.ijleo.2013.01.086.

[11] A. Gassoumi, M. Kanzari, Growth and post-annealing effect on the properties of

the new sulfosalt SnSb2S4 thin films, Phys. E Low-Dimensional Syst. Nanostructures. 44 (2011) 71–74. doi:10.1016/j.physe.2011.07.007.

[12] Y. Fadhli, A. Rabhi, M. Kanzari, Annealing effects on the physical properties of thermally evaporated Sn2Sb2S5 thin films, 2014 1st Int. Conf. Green Energy, ICGE 2014. (2014) 124–128. doi:10.1109/ICGE.2014.6835409.

[13] M. Ben Rabeh, N. Khedmi, M. Kanzari, Vacuum annealing effects on the structural and optical properties of SnSb<inf>2</inf>S<inf>4</inf> thin films fabricated by thermal evaporation technique, Optik (Stuttg). 126 (2015) 3104–3109. doi:10.1016/j.ijleo.2015.07.093.

[14] A. Saeed, N. Alia, W.A. Syed, Photovoltaic effect in the metal based sulfosalt thin film deposited by physical vapor deposition technique, Chalcogenide Lett. 10 (2013) 143–150.

[15] A. Jebali, N. Khemiri, M. Kanzari, The effect of annealing in N 2 atmosphere on the physical properties of SnSb 4 S 7 thin films, J. Alloys Compd. 673 (2016) 38–46. doi:10.1016/j.jallcom.2016.02.159.

[16] M.A. Khan, A. Ahmed, N. Ali, T. Iqbal, A.A. Khan, M. Ullah, M. Shafique, Improved Optical Properties of Tin Antimony Sulphide Thin Films for Photovoltaics, Am. J. Mater. Sci. Eng. 4 (2016) 1–6. doi:10.12691/ajmse-4-1-1.

[17] A. Gassoumi, M. Kanzari, Optical, structural and electrical properties of the new absorber Sn2Sb2S5 thin films, Chalcogenide Lett. 6 (2009) 163–170. http://www.chalcogen.ro/163_Gassoumi.pdf (accessed August 8, 2019).

[18] A. Larbi, H. Dahman, M. Kanzari, Effect of substrate temperature on structural and optical properties of the new high absorbent Sn3Sb2S6 thin films, Vacuum. 110 (2014) 34–39. doi:10.1016/j.vacuum.2014.08.009.

[19] A. Larbi, F. Chaffar Akkari, H. Dahman, D. Demaille, B. Gallas, M. Kanzari, Structural, Morphological and Optical Properties of Sn3Sb2S6 Thin Films Synthesized by Oblique Angle Deposition, J. Electron. Mater. 45 (2016) 5487–5496. doi:10.1007/s11664-016-4714-z.